Durham University

Durham E-Theses

Floquet calculations of rates of frequency conversion and multiphoton Ionisation in intense laser field

Emine Mese

How to cite:

Mese, Emine (1997) Floquet calculations of rates of frequency conversion and multiphoton Ionisation in intense laser field. Doctoral thesis, Durham University.

Use policy

The full-text may be used and/or reproduced, and given to third parties in any format or medium, without prior permission or charge, for personal research or study, educational, or not-for-profit purposes provided that:

- a full bibliographic reference is made to the original source
- a https://etheses.durham.ac.uk/id/eprint/4697/ is made to the metadata record in Durham E-Theses
- the full-text is not changed in any way

The full-text must not be sold in any format or medium without the formal permission of the copyright holders.

Please consult the full Durham E-Theses policy for further details.

Academic Support Office, The Palatine Centre, Durham University, Stockton Road, Durham, DH1 3LE
e-mail: e-theses.admin@durham.ac.uk Tel: +44 0191 334 6107
https://etheses.durham.ac.uk

Floquet Calculations of Rates of Frequency Conversion and Multiphoton Ionisation in Intense Laser Field

The copyright of this thesis rests
with the author. No quotation
from it should be published
without the written consent of the
author and information derived
from it should be acknowledged.

by

Emine Meşe

A thesis submitted to the University of Durham in candidature for the degree of Doctor of Philosophy

March 1997

2 8 MAY 1997

Abstract

Nonperturbative rates of harmonic generation or frequency mixing and rates of multiphoton ionisation were obtained for atomic hydrogen and for a one-electron model of the negative hydrogen ion, using the Floquet-Sturmian method. The following cases were investigated: elliptically polarised, monochromatic incident field, two-colour incident field with incommensurable frequencies, coherent superposition of an incident field and its third harmonic, and superposition of a laser field and a static electric field.

For elliptical polarisation, the ellipticity angle of the harmonics differ from the ellipticity of the incident laser and we established that there is an offset angle between the major axis of the incident laser's polarisation ellipse and that of the harmonics generated. The variation is greatest in the plateau region.

Resonance-enhanced ionisation was studied when a high frequency field was applied in addition to a fundamental field. In contrast to these changes in the ionisation rate only small variations have been obtained in the harmonic generation rate. Results for frequency-mixing exhibit a difference in the strength of the harmonics, although the behaviour is the same in terms of the length of the plateau and the cut-off order. Also we found a marked change between sum-frequency and difference frequency processes, which depends on the harmonic order.

In addition to a strong production of even harmonics, it was found that the variation of the rate of ionisation and harmonic generation in the presence of a static field oscillates as a function of the strength of the latter. In the case of hydrogen, we observed dc-stark shift induced resonance enhancements. The results obtained for H^- are in very good agreement with those obtained for two colour $(\omega, 3\omega)$ mixing. We concluded that the application of a static field in general leads to a reduction in the conversion efficiency.

Acknowledgements

It is a great pleasure for me to acknowledge those people who contributed to the preperation of this thesis.

To start with I would like to thank to Dr. J. V. Major and Prof. D. R. Flower for accepting me as a research student in Durham and extend this thanks to Dr Major and his wife Helen for welcoming me to Durham and for opening their door to me whenever I have had difficulties over the period of studying in Durham.

I would like to give very special thanks to Dr. R. M. Potvliege for his friendly and tolerant approach to his students. Without his guidance and patience, not only would it not have been possible to carry out this task, but it would also have been impossible to start it. In this context I owe him more than I can express. I also thank him for providing the Floquet-Sturmian code for my research.

I sincerely thank Dr. Lydia Heck for her generous help and friendship. Without her it would have been much harder to solve the tedious computational problems and of course Latex. I would like to thank the other members of the atomic and molecular physics group.

I would like to give special thanks to Christian Caron: as a colleague for his useful comments and helpful discussions, as a friend in the University or out for his company, share, support and care.

While talking about friends I would like to thank my office mates Simon, Henry, Alex, Peter for correcting my English. Also my time in Durham has been made more enjoyable by Helen, Mirela, Hilary, Lars, Thomas for their company both in and out of university especially in moments of frustration.

I should not forget how much I owe to my corridor mates Alejandra, Kumiko, Medina, Undala and Theodara for their friendship and solidarity, especially during the process of writing up. How about some former corridor mates! I must mention Adnan and Marlene. I had great fun having them in the corridor and derived especially great pleasure from discussions with Adnan, who is a physicist, although in a different field.

Thanks should also go to all members of the technical staff of the department, especially Pat for nice teas and coffees; to Sharon, Penny and the other secretaries for typing forms from time to time; to Mike and Vicki for laminating the poster and helping to deal with the photocopier and fax machine and finally for promising to bind this thesis in just half an hour.

I am very happy to thank to my home university (University of Dicle) for providing me with a grant in order to study abroad.

More than anything else I would like to give my deepest thank to my parents, for their generous and endless love, and the education and the belief in humanity which they have provided us with which has led me to hold the pen as firmly as I can. I would also like to give my special thanks to my two brothers Hüseyin and Mustafa and my sisters Fatma (and her husband Selahattin), Sevinç and Ayşe for always doing their best to integrate this belief and to develop it. My thanks are extended to relatives and friends, especially, İbrahim Çiçek, Hasan Ç. Özen, Gülten Kavak, Yüksel Coşkun, Fikret Uyar, Rıdvan Şeşen, Süleyman Tarı and

many others, who have contributed to and/or integrated with this ideology over the years.

Finally I would like to thank my dear little niece Medya and to Medya for the love.

I also would like to mention that I will be very much greatful if this work will be a tiny contribution towards peace and humanity in the world, which we have been all the way worked for it.

Declaration

I declare that the work contained in this thesis has not been submitted for a degree at this University or any other. All the work presented here was conducted by the author, unless stated otherwise.

Emine Meşe

March 1997

Copyright ©1997 by Emine Meşe. The copyright of this document rests with the author. No quotation from it should be published without the author's prior written consent. Information derived from this thesis should be acknowledge.

To those two great people, who are the symbol of moral, labour and love;
my mum and dad.

Contents

Chapter 1

Introduction

The aim of this work is to study some aspects of multiphoton processes when an atom is in intense electromagnetic radiation. Exploring the atom through studying these processes has started since the early 1960's with the invention of the laser. Multiphoton ionisation (MPI) is one of the important process which occurs due to the interaction of the atomic or molecular system with intense radiation. It was predicted in the 1960's [1],[2] and observed first from a negative halogen by Hall *et al.* [3] and then from rare gases by Voronov and Delone [4] and Agostini *et al.* [5]. In the 1970's important results were obtained at Saclay and in Canada concerning the power-law dependence of the ionisation rate on the intensity of the radiation; for measured cross sections; for resonance-enhancement of MPI, etc [6]. Later on a new dimension was added to simplest understanding of multiphoton ionisation. It was discovered by Agostini *et al.* [7] that there are multiple channels of ionisation, in which the ejected electron could absorb more photons than the minimum number required for an MPI process [8]. Currently, this process is called *above threshold ionisation* (ATI). Today with ATI or other new aspects the MPI still preserves its central role within the area of multiphoton physics.

It is obvious that the behaviour of atom in intense radiation can be characterised by MPI. Another important aspect of the interaction is what happens to the radiation as a consequence of its encounter with atoms/molecules. It was noticed from the beginning that odd harmonics of the initial frequency might be generated and thus, the first discovery of third harmonic generation by New and Ward in 1967 [9], fifth harmonic generation by Reintjes in 1976 [10], and observation of higher orders (7th, 9th, 11th, 13th, 17th, 33rd, etc.) followed [10]-[14].

Today this number exceeds the order of 100, which is demonstrated in several laboratories as the result of the interaction of atoms with intense low-frequency pulses [15]-[17]. The biggest worry of the field until the discovery of the high harmonics (about 1988) was the low efficiency which was dropping down very rapidly with harmonic order, in accordance with perturbative predictions. One of the surprising aspects was that the production efficiency did not continue to drop off rapidly, but stayed approximately constant for a wide range of harmonics, called the plateau region, beyond this region the efficiency dropped very rapidly to an unobservable level. Since this phenomena could be not addressed by perturbative theory, it brought out the necessity of nonperturbative approaches.

Besides their fundamental importance (MPI and high harmonic generation (HHG)) some other new interesting features related to these processes became topics of active research. Some of many are as follows: MPI and HHG in the presence of two different laser fields, thus dichroism and ellipticity dependency of harmonic generation; production of even harmonics using mixing two different incommensurable or commensurable frequencies; effects of a static field in the presence of an electromagnetic field, etc.

These are the processes we aimed to study through this thesis using a non-perturbative method. The results are mainly produced for atomic hydrogen as it has been often used as a base for research in theoretical physics. For instance a group-theoretical analysis of hydrogen has been used in high energy physics (see [18],[19]). Hydrogen is nowadays very widely used for studying laser-atom interactions in the context of theoretical atomic physics [8],[20].

Nowadays, accurate *ab initio* calculations are possible for complex atoms (and molecules) in the absence of external fields [21] and also in the presence of electromagnetic field [22]-[25], but the theoretical and numerical difficulties, coming principally from the electron-electron interaction, keeps the place of hydrogen in the research arena constantly popular. Despite the fact that hydrogen has never been an ideal subjet for experiments, theoretical efforts have concentrated on the hydrogen atom and the results produced by these efforts have been successfully applied to interpret experimental results obtained for the noble gases (e.g. Helium[26], Neon[27],[28], Xenon[7],[29] or Argon[29]).

Several types of calculations are useful in interpreting the experiments. Calculations can be time-dependent or time-independent, and often it is instructive to perform calculations in both ways because the methodologies are often complementary and may highlight different physical aspects. One of the most successful time-independent approaches to multiphoton processes is the Floquet theory, especially when the processes do not depend crucially on temporal variation of the intensity of the incident laser field [30]-[35]. Although accurate *ab initio* calculations in complex atoms are now possible [36] they are still difficult and computationally demanding due to the electronic correlation. However, a large body of results have been collected for hydrogen using the Floquet approach incorporating a Sturmian basis set [37]. The computations of level shifts, ionisation rates and harmonic generation rates using such a basis are numerically stable for this atom and in many cases can be performed on ordinary workstations. Their main limitations, besides that inherent in any time-independent description, is the relatively small number of coupled partial waves one can retain in the spherical harmonic expansion of the wavefunction without having to deal with very large matrices [37]. The method is therefore not practical for dealing with processes induced by ultra-intense fields in the visible or in the infrared. Nevertheless, it allows a detailed, quantitative study of many processes of interest, over large ranges of frequency and intensity. Progress made by 1992 in this line of the research using the Sturmian-Floquet method have been reviewed in some detail [38], in particular, adiabatic stabilisation; the appearance of light-induced states; ionisation in the tunneling regime; ionisation by coherent superpositions of two harmonics of the same laser beam; and microwave ionisation of Rydberg states [37].

Note that for these processes, which have been studied using Sturmian-Floquet calculations, the laser fields are mainly linearly polarised. It will be one of the objectives of this thesis to handle the interaction of hydrogen with an elliptically polarised field (from which the phenomenon of dichroism arises) using the non-perturbative Floquet-Sturmian approach. The main body of the thesis will be concerned with the nonperturbative effects of dichroism. The application of the theory to hydrogen will be given in Chapter 4, which follows an exposotion of the basic principles of light-matter interaction (Chapter 2) and the Sturmian-Floquet

theory for elliptically polarised light (Chapter 3). An extension of Floquet theory to two-colour processes will be described in Chapter 5 together with an application to the hydrogen atom in a biochromatic field with incommensurable frequencies. Chapter 5 will mainly be concerned with resonance-enhanced ionisation due to a high frequency field, but will also address the influence of a weak high frequency field on harmonic generation. Frequency-mixing processes will be discussed in Chapter 6, with emphasis on the conversion-efficiency due to mixing two incommensurable frequencies. In the last chapter the effect of a static electric field acting in the presence of a laser field is reported. In the main, the response of hydrogen to simultaneously applied dc and ac-field is reported in this chapter, but response of the negative hydrogen ion via a one-electron model is also considered. Lastly, a two colour $(\omega, 3\omega)$ mixing is considered in complement of our calculation of harmonic generation in the presence of a static field.

Chapter 2

Basic Concepts

2.1 Basic principles of photon-atom interactions

Before introducing the main theory and its applications it is worth describing the basic principles and working frames. The fundamental Hamiltonian for the interaction of a nonrelativistic electron with an external electromagnetic field is

$$\mathrm{H}(\mathbf{r},t) = \frac{1}{2\mu}\Big[\mathbf{p} + \frac{e}{c}\mathbf{A}(\mathbf{r},t)\Big]^2 - e\phi(\mathbf{r},t) \tag{2.1}$$

where μ, e and p are the reduced mass, absolute charge and linear momentum, respectively, of the electron; $\phi(\mathbf{r},t)$ and $\mathbf{A}(\mathbf{r},t)$ are the scalar and vector potentials, respectively, of the external field, in Gaussian units.

2.1.1 Gauge transformation in the classical electromagnetic theory

In classical electromagnetic theory, a gauge transformation on the scalar potential $\phi(\mathbf{r},t)$ and, the vector potential $\mathbf{A}(\mathbf{r},t)$ is defined by the relations

$$\begin{aligned} \phi'(\mathbf{r},t) &= \phi(\mathbf{r},t) - \frac{\partial}{\partial t} f(\mathbf{r},t) \\ \mathbf{A}'(\mathbf{r},t) &= \mathbf{A}(\mathbf{r},t) + \nabla f(\mathbf{r},t) \end{aligned} \tag{2.2}$$

where $f(\mathbf{r},t)$ is an arbitrary differentiable scalar function of space and time. Since the fields are related to the potentials by

$$\begin{aligned} \mathbf{E}(\mathbf{r},t) &= -\nabla\phi(\mathbf{r},t) - \frac{1}{c}\frac{\partial}{\partial t}\mathbf{A}(\mathbf{r},t) \\ \mathbf{B}(\mathbf{r},t) &= \nabla \times \mathbf{A}(\mathbf{r},t) \end{aligned} \tag{2.3}$$

a gauge transformation of the potentials has no effect on the fields; that is; when ϕ and $\mathbf{A}$ are replaced by ϕ' and $\mathbf{A}'$, the fields are unchanged. Hence, the potentials are not determined uniquely and $\mathbf{E}(\mathbf{r},t)$ and $\mathbf{B}(\mathbf{r},t)$ as physically observable quantities are gauge invariant.

2.1.2 Gauge transformation in a quantum mechanical context

The time-dependent Schrödinger equation is

$$i\hbar\frac{\partial}{\partial t}\Psi(\mathbf{r},t) = H\Psi(\mathbf{r},t) \tag{2.4}$$

where H is the Hamiltonian given with Equation (2.1). A unitary operation O transforming $\Psi(\mathbf{r},t)$ into

$$\Psi'(\mathbf{r},t) = O\Psi(\mathbf{r},t) \tag{2.5}$$

changes H' into

$$H' = OHO^{\dagger} + i\hbar\frac{\partial O}{\partial t}O^{\dagger} \tag{2.6}$$

Now, let

$$O = \exp(-ief/\hbar), \qquad f \equiv f(\mathbf{r},t) \tag{2.7}$$

Using $\mathbf{p} = -i\hbar\nabla$, the Hamiltonian in Equation (2.1) is transformed into

$$\begin{aligned} H' &= \frac{1}{2\mu}\Big[\mathbf{p} + \frac{e}{c}(\mathbf{A} + \nabla f)\Big]^2 - e\Big(\phi - \frac{\partial f}{\partial t}\Big) \\ &= \frac{1}{2\mu}\Big[\mathbf{p} + \frac{e}{c}\mathbf{A}'\Big]^2 - e\phi' \end{aligned} \tag{2.8}$$

This shows that the operator O defined by Equation (2.7) acting through the transformation (2.6), generates a gauge transformation of the type of Equation (2.2) when the Hamiltonian has the form of Equation (2.1). This is the quantum mechanical counterpart to the classical gauge transformation. Since O is a unitary operator, its effect on the wavefunction Ψ is to alter the phase but not the absolute value. Therefore, the physically observable content of quantum mechanics cannot depend on the specific choice of the gauge function $f(\mathbf{r},t)$.

Let us consider an electron interacting with an electromagnetic field that has no scalar potential ($\phi = 0$). Then the field is described only by the vector potential. Therefore, the Hamiltonian (2.1) reduces to

$$H = \frac{1}{2\mu}\Big[\mathbf{p} + \frac{e}{c}\mathbf{A}(\mathbf{r},t)\Big]^2 \tag{2.9}$$

and the transformed Hamiltonian (2.8) reduces to

$$H' = \frac{1}{2\mu}\Big[\mathbf{p} + \frac{e}{c}(\mathbf{A} + \nabla f)\Big]^2 + e\frac{\partial f}{\partial t} \tag{2.10}$$

We choose a gauge function of the form such that the vector potential is independent of the spatial coordinates. Since we are dealing with atomic systems, it is sufficient for $\mathbf{A}$ not to vary over atomic dimensions. In other words, the wavelengths associated with $\mathbf{A}$ must be much longer than the scale of atomic dimensions, that is,

$$\mathbf{k}.\mathbf{r} \ll 1 \tag{2.11}$$

This condition is known as dipole approximation. Thus we may choose the gauge function as follows

$$f(r,t) = -\mathbf{A}(t)\cdot\mathbf{r} \tag{2.12}$$

Using this gauge function together with $\mathbf{E}(t) = -\partial\mathbf{A}/\partial t$ in the transformed Hamiltonian (2.10):

$$H' = \frac{p^2}{2\mu} + e\mathbf{r}\cdot\mathbf{E}(t) \tag{2.13}$$

Thus, the gauge transformation described above has eliminated the vector potential from the Hamiltonian. This frame is called the *length gauge* and the interaction term in the gauge-transformed Hamiltonian features the electronic dipole moment operator $\mathbf{d} = -e\mathbf{r}$. As the dipole approximation is valid for optical frequencies and beyond, this gauge is widely used in quantum optics. However, one should be aware that the length gauge may not always be the best one as far as numerical calculations are concerned (see e.g. Section 5.5.3).

Going back to Equation (2.9) the Hamiltonian includes the terms $\frac{e}{c}(\mathbf{p}\cdot\mathbf{A} + \mathbf{A}\cdot\mathbf{p})$. If $\psi(\mathbf{r},t)$ is an arbitrary function of time and position, $\mathbf{p}\cdot\mathbf{A}\psi(\mathbf{r},t) = \mathbf{A}\cdot[\mathbf{p}\psi(\mathbf{r},t)] + \psi(\mathbf{r},t)[\mathbf{p}\cdot\mathbf{A}]$ and we can use the gauge freedom to subject the vector potential to the condition $\nabla\cdot\mathbf{A} = 0$ (Coulomb gauge). Therefore, $\mathbf{p}\cdot\mathbf{A} = \mathbf{A}\cdot\mathbf{p}$ and the Hamiltonian in Equation (2.9) becomes

$$H = \frac{1}{2\mu}\Big[p^2 + \frac{2e}{c}\,\mathbf{p}\cdot\mathbf{A} + \frac{e^2}{c^2}A^2\Big] \tag{2.14}$$

This is the Hamiltonian in the *velocity gauge*. Furthermore in the dipole approximation the A^2 term can be removed with a contact transformation, given by

$$\Psi' = \Psi\ \exp\Big(-\frac{ie^2}{2\mu c^2\hbar}\int^t A^2(\tau)\mathrm{d}\tau\Big) \tag{2.15}$$

Therefore, we may use

$$H = \frac{1}{2\mu}\left[p^2 + \frac{2e}{c}\,\mathbf{p}\cdot\mathbf{A}\right] \tag{2.16}$$

instead 2.14 as long as we are in the dipole approximation. The velocity gauge is quite convenient to use, especially in connection with Floquet theory. Convergence can be obtained easily when working with a Sturmian basis set in the velocity gauge. Note that there is yet another gauge used in the literature. This frame is known as the moving frame or Kramers-Henneberger frame (equivalently, the *acceleration gauge*). The corresponding unitary operation is called the Kramers-Henneberger-Transformation. This gauge is for example used to investigate the stabilisation of atoms in intense laser fields. We have not used this gauge in our calculations. In the main we have used the velocity gauge to calculate the wavefunction, but we have also done some calculations in the length gauge (see Section 7.3).

2.2 Floquet theory

The Floquet formalism is a semiclassical approach to the theoretical problem of multiphoton processes. It has been used to describe multiphoton ionisation of the hydrogen atom by many workers such as Chu and Reinhardt [31]; Potvliege and Shakeshaft [32], [33]. It has also been used to describe harmonic generation by Potvliege and Shakeshaft [34], [35]. There has also been recent harmonic generation calculations using R-matrix-Floquet method by Burke *et al* [39], [40] (and related references therein).

Consider an atom in a monochromatic and spatially homogeneous laser field, which is treated classically. The time-dependent Schrödinger equation for this atomic system in the laser field is

$$i\hbar\frac{d}{dt}\left|\Psi(t)\right\rangle = \left[H_a + V(t)\right]\left|\Psi(t)\right\rangle \tag{2.17}$$

where $|\Psi(t)\rangle$ is the required solution, H_a is the field-free atomic Hamiltonian and $V(t)$ is the interaction of the field with the atom. The interaction potential can be expressed either in the length gauge or the velocity gauge. In our case the interaction of the nucleus with the field is ignored. Therefore $V(t)$ is the interaction of the field with the bound electron. We can set up equations for the hydrogen atom and the laser field system. From Equation 2.13 the interaction potential in the length gauge is

$$V(t) = -e\mathbf{E}(t).\mathbf{r} \tag{2.18}$$

where $\mathbf{E}(t)$ is the electric field vector of the incident wave and e is the electron charge. In the velocity gauge, $V(t)$ is given in terms of the corresponding vector potential of the field (from Equation 2.16)

$$V(t) = -(e/\mu c)\mathbf{A}(t).\mathbf{p} \tag{2.19}$$

where e and μ are the electron charge and reduced mass, $\mathbf{p}$ is the canonical momentum operator for the electron and $\mathbf{A}(t)$ is the vector potential for the field, which can be taken as $\mathbf{A}(t) = \mathbf{A_o}\sin(\omega t)$ or $\mathbf{A}(t) = \mathbf{A_o}\cos(\omega t)$. The potential does not include the $\mathbf{A}^2$ term since it can be removed by a gauge transformation which does not effect the value of any observable physical quantity as long as the field can be considered spatially homogeneous.

The Floquet method involves the substitution

$$|\Psi(t)\rangle \;=\; \exp(-i\varepsilon_i t/\hbar)\;|\psi_i(\tau)\rangle \tag{2.20}$$

where $|\psi_i(\tau)\rangle$ is periodic in $\tau = \omega t$, with period 2π, and ε_i is the atom quasi energy. Substituting this in equation (2.17) and making a Fourier expansion for (2.20) as

$$|\psi_i(\tau)\rangle \;=\; \sum_n \exp(-in\tau)|\psi_{i,n}\rangle \tag{2.21}$$

gives a set of time-independent coupled equations for the harmonic components:

$$(\varepsilon_i \;+\; n\hbar\omega \;-\; H_a)\;|\psi_{i,n}\rangle \;=\; V_+\;|\psi_{i,n-1}\rangle \;+\; V_-\;|\psi_{i,n+1}\rangle \tag{2.22}$$

where $n \;=\; 0,\; \pm 1,\; \pm 2, ...V_+$ and V_- are the Fourier components of the dipole interaction potential in the velocity gauge:

$$\begin{aligned} V(t) \;&=\; i(e\hbar A_o/\mu c)\mathbf{Im}\Big[\mathbf{e_i}\cdot\nabla\exp(-i\omega t)\Big] \\ &=\; V_+\exp(-i\omega t) \;+\; V_-\exp(i\omega t) \end{aligned} \tag{2.23}$$

where V_+ and V_- are the absorbtion and emission operators ($V_+ = V_-^\dagger$) and $\mathbf{e}_i$ is the polarisation vector of the incident wave:

$$\mathbf{e_i} = \cos(\xi/2)\hat{\mathbf{x}} \;+\; i\sin(\xi/2)\hat{\mathbf{y}} \tag{2.24}$$

The ellipticity is described by ξ and may change from 0 to $\pm\pi/2$. A value of $\xi = 0$ corresponds to linearly polarised light and $\xi = \pm\pi/2$ corresponds to circularly polarised light. If it is $+\pi/2$ that means that the light is left circularly polarised and if it is $-\pi/2$, the light is right circularly polarised. The unit vectors $\hat{\mathbf{x}}$ and $\hat{\mathbf{y}}$ define the polarisation plane. The eigenvalue ε_i (the quasi energy) is in general complex:

$$\varepsilon_i \;=\; E_i \;+\; \Delta_i \;-\; i\frac{\Gamma_i}{2} \tag{2.25}$$

where E_i is the unperturbed energy of the initial state in the absence of the field, Δ_i is the shift from the unperturbed bound-state eigenvalue E_i and includes a downward ponderomotive shift U_p, defined by $U_p = 2\pi e^2 I/\mu c\omega^2$ with intensity $I = \omega^2|A_o|^2/8\pi c$. If the electron is tightly bound in its initial state $\Delta_i = -U_p$. Γ_i is the induced width and is proportional to the photoionisation rate. While the shift Δ_i is dependent on the choice of gauge, Γ_i is invariant.

The solutions of equations (2.22) are constrained by the physical boundary conditions in coordinate space. These conditions are that each harmonic component $|\psi_{i,n}\rangle$ is regular at $r = 0$ and behaves as a superposition of outgoing waves as $r \to \infty$. If $\mathbf{x}$ is the electron coordinate and $r = |\mathbf{x}|$, each harmonic component satisfies

$$\langle \mathbf{x}|\psi_{i,n}\rangle \sim \sum_m f_{m,n}(\varepsilon_i, \hat{\mathbf{x}}) r^{i\nu_{i,m}} \exp(ik_{i,m}r)/r \tag{2.26}$$

where $k_{i,m} = \left[(2\mu/\hbar^2)(\varepsilon_i + m\hbar\omega)\right]^{1/2}$ and $\nu_{i,m} = Z/a_o k_{i,m}$ with $-Ze$ the charge of the residual ion. Thus, boundary condition is adequate in the velocity gauge, but not in the length gauge.

2.3 Method of Potvliege and Shakeshaft

The eigenvalue problem was solved numerically in position space by expanding each harmonic component $< \mathbf{x}|\psi_{i,n} >$ on a basis set consisting of spherical harmonics $Y_{lm}(\hat{\mathbf{r}})$ and the radial Sturmian functions $S^{\kappa}_{\nu l}(r)$:

$$\langle \mathbf{x}|\psi_{i,n}\rangle = \sum_{lm\nu} C^{(n)}_{lm\nu} Y_{lm} S^{\kappa}_{\nu l}(r)/r \tag{2.27}$$

Here the sum over l is restricted by parity consideration; if $\sigma(\equiv \pm 1)$ is the parity of the initially unperturbed bound level, we have $C_{lm\nu} = 0$ if $(-1)^n\sigma \neq (-1)^l$. The restrictions on m depends on other symmetry considerations and the polarisation of the light [20].

The complex Sturmian functions are defined as

$$S^{\kappa}_{\nu l}(r) = N^{\kappa}_{\nu l}(-2i\kappa r)^{l+1}\exp(i\kappa r)\ {}_1F_1(l+1-\nu; 2l+2; -2i\kappa r) \tag{2.28}$$

where ${}_1F_1$ is the confluent hypergeometric function, the wave number κ is complex with $0 < \arg(\kappa) < \pi/2$, and $N_{\nu l}$ is the normalisation constant and given by

$$\frac{1}{(2l+1)}\left(\frac{(\nu+l)!}{(\nu-l-1)!}\right)^{1/2} \tag{2.29}$$

The orthonormality property is

$$\int_0^{\infty} dr S^{\kappa}_{\nu' l}(r) S^{\kappa}_{\nu l}(r)/r = \delta_{\nu'\nu} \tag{2.30}$$

and for $r \to \infty$, $S^{\kappa}_{\nu l}(r)$ behaves like

$$S^{\kappa}_{\nu l}(r) \approx a_{\nu l} r^{\nu} \exp(i\kappa r) \tag{2.31}$$

where $a_{\nu l}$ is a constant. Any well-behaved function of r vanishing as r^{l+1} at the origin and behaving as an outgoing wave $\exp(ikr)$ at infinity can be expanded on the basis with converging coefficients provided that [32]:

$$| \, arg(k) - arg(\kappa) \, | < \pi/2 \tag{2.32}$$

Because of the inequality (2.32) and the boundary conditions we must choose κ to lie in the upper-right quadrant of the complex κ-plane (see figure 2.1) [32].

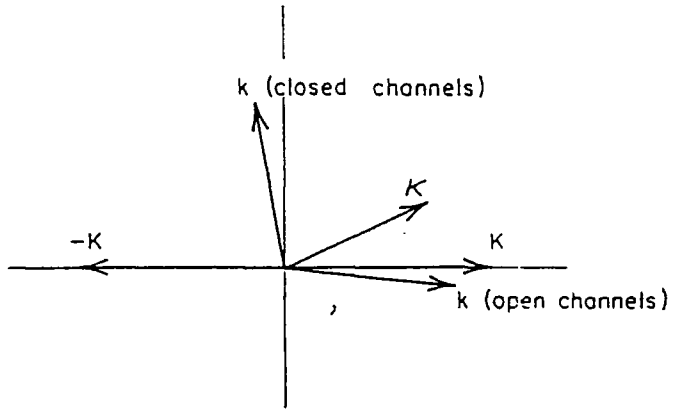

Figure 2.1: Illustration of κ parameter [32].

In addition to the fact the Sturmian basis set can represent the physical boundary conditions, it has other qualities which are useful for computation when a single value of κ is used [20]. It is easy to obtain simple analytical expressions for the matrix elements of the kinetic energy operator, of the Coulomb potential, of the Yukawa potential, and of the absorption-emission dipole operators $V_{\pm}$. The recurrence relations obeyed by the Sturmian functions are useful and the overlap matrix of the basis functions, and the matrix representing the $V_{\pm}$ operators are very sparse. Moreover, in the case of the hydrogen atom, the matrix representing of the field-free Hamiltonian is tridiagonal and so perturbative calculations of rates for high-order multiphoton ionisation and harmonic generation are fast. However, our calculations being nonperturbative and for either an elliptically polarised field, or a two-colour field, are much more demanding.

2.4 Normalisation of the Floquet wavefunction

Since the atom is initially in a bound state, its physical wave function must have a pure outgoing (+) wave behaviour in the open channels, which is described in Section 2.2 with the boundary condition (2.26):

$$\Psi^{(+)}(\mathbf{r},t) = \exp\left(-i\varepsilon_i t/\hbar\right) \sum_{n=-\infty}^{n=+\infty} \exp\left(-in\omega t\right) \times \sum_{lm\nu} C^{(n)}_{lm\nu} Y_{lm}(\mathbf{r}) S^{\kappa}_{\nu l}(r)/r \qquad (2.33)$$

Besides the Floquet wave function with outgoing wave behaviour, we also need the wave function with ingoing wave behaviour, $\Psi^{(-)}(\mathbf{r},t)$ [41]:

$$\Psi^{(-)}(\mathbf{r},t) = \exp\left(-i\varepsilon_i^* t/\hbar\right) \sum_{n=-\infty}^{n=+\infty} \exp\left(-in\omega t\right) \times \sum_{lm\nu} C^{(n)*}_{lm\nu} Y_{lm}(\mathbf{r}) \left[S^{\kappa}_{\nu l}(r)\right]^* /r \qquad (2.34)$$

The product $\Psi^{(-)*}(\mathbf{r},t)\Psi^{(+)}(\mathbf{r},t)$ is a periodic function of t and the cycle average of $\langle\Psi^{(-)*}(\mathbf{r},t)|\Psi^{(+)}(\mathbf{r},t)\rangle$ is constant in time.

$$\frac{\omega}{2\pi}\int_0^{2\pi/\omega} dt \langle\Psi^{(-)*}(\mathbf{r},t)|\Psi^{(+)}(\mathbf{r},t)\rangle = \sum_{n=-\infty}^{n=+\infty} \sum_{ll'mm'\nu\nu'} C^{(n)}_{lm\nu} C^{(n)}_{l'm'\nu'} \int_0^{\infty} dr S^{\kappa}_{\nu l}(r) S^{\kappa}_{\nu' l'}(r) \qquad (2.35)$$

Therefore, the normalisation of the Floquet wave function is

$$\sum_{n=-\infty}^{n=+\infty} \int \psi_n(\mathbf{r})\psi_n(\mathbf{r}) d\mathbf{r} = 1 \qquad (2.36)$$

where the ψ_n are the harmonic components of the Floquet wave functions defined in the Section 2.2 (for details see [41]) and the expansion of the Floquet harmonics on the Sturmian basis set has been given in Section 2.3.

2.5 Inverse iteration technique

The resulting matrix of the eigenvalue problem was solved by the inverse iteration technique. To describe this technique one can introduce the elements of the operator matrix,

$$H_{nn'} = (H_a - n\hbar\omega)\delta_{nn'} + V_+\delta_{n,n'+1} + V_-\delta_{n,n'-1} \qquad (2.37)$$

so equation 2.22 can be expressed as

$$\sum_{n'} H_{nn'}|\psi_n'\rangle = \varepsilon_i|\psi_n\rangle \qquad (2.38)$$

Projecting Equation (2.37) onto the basis set, which is given by Equation (2.27), the following set of coupled linear equations for the expansion coefficients $C_{lm\nu}^{(n)}$ of the harmonic components is obtained [20]:

$$\bar{\mathbf{H}}\mathbf{y} = \varepsilon_i \mathbf{N}\mathbf{y} \tag{2.39}$$

where $\mathbf{y}$ is the column vector which consists of the expansion coefficients, $\bar{\mathbf{H}}$ is the square matrix which is the basis-set representations of the operator matrix whose elements are $H_{nn'}$ and consists of blocks, each block being a square submatrix that represents the operator $H_{nn'}$. Also $\bar{\mathbf{H}}$ is a block-tridiagonal matrix, in other words, $\bar{\mathbf{H}}$ is a sparse matrix. $\mathbf{N}$ is the basis set representations of the identity operator.

In order to solve equation (2.39) one should iterate

$$(\bar{\mathbf{H}} - \varepsilon' \mathbf{N})\mathbf{y}^{k+1} = \mathbf{N}\mathbf{y}^{k} \tag{2.40}$$

with an initial guess value of ε' which is complex. When ε' is close-enough to the eigenvalue ε_i, each component of $\mathbf{y}^k$ converges towards the corresponding component of the eigenvalue ε_i by:

$$\mathbf{y}^{k+1} = (\varepsilon_i - \varepsilon')^{-1}\mathbf{y}^{k} \tag{2.41}$$

In our calculations the relative error is not more than 0.01 %. Although it is quite easy to achieve convergence in a few iterations for the nonresonant case, for the resonant case it is always difficult to find the right eigenvalue since several eigenvalues are close to each other. In this case it is necessary to make a good initial guess for ε'.

Chapter 3

Single Colour Processes

3.1 Multiphoton ionisation

This section provides an overview of the current understanding of multiphoton ionisation (MPI) of atoms, especially for the case of atomic hydrogen. MPI was first observed from negative halogen ions in the experiments of Hall, Robinson and Branscomb [3], then from rare gas atoms by Voronov and Delone [4] and Agostini *et al.* [5]. Later experiments by Agostini *et al.* measuring the energy of the photoelectrons produced by the MPI process showed that free-free transitions can accompany MPI, when electrons absorb additional photons, more than are required for ionisation [7]. This phenomenon is called above-threshold ionisation (ATI) and many experiments have been performed to study its details (for a review see [8]). Figure 3.1 illustrates a multiphoton ionisation process. Here, the absorption of 3-photons is required ($N_0 = 3$) in order to ionise the atom. However, the electron may continue to absorb further photons above the ionisation threshold. e.g. in Figure 3.1 this process may occur with $S = 1$ or $S = 2$, where S indicates the number of excess photons. Note that N_0 is not a fixed number and it may increase with increasing intensity, for a given laser wavelength, especially for ionisation from the ground-state which is always shifted downwards.

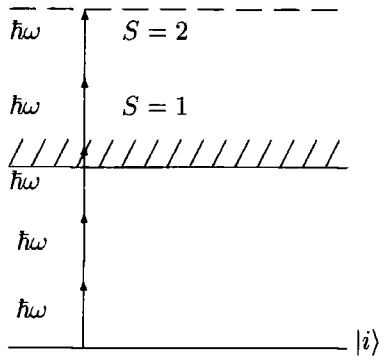

Figure 3.1: A schematic illustration of multiphoton processes: MPI and ATI

The photoelectron spectrum resulting from such transitions exhibits a series of peaks at photoelectron energies E_S, where

$$E_S = (N_0 + S)\hbar\omega - E_i + \Delta \tag{3.1}$$

where, N_0 is the minimum number of photons to obtain MPI, E_i is the field-free ionisation potential of the atom, Δ is the intensity dependent shift in the energy level $|i\rangle$ of the atom and S is any positive number, which shows the number of excess photons.

For a long time MPI of atoms was described successfully using perturbation theory with the laser electric field representing a perturbation with respect to the Coulomb field. When calculated using leading-order perturbation theory, the probability, P_N, of an N-photon transition occurring is proportional to the Nth power of the laser intensity, which is

$$P_N = a_N I^N \tag{3.2}$$

where a_N is some intensity-independent constant. Thus, a plot against $log(I)$ is a straight line and its gradient is $N = N_0 + S$, which is called the order of the process. Figure 3.2 shows the intensity dependence of the four first peaks of the Xe ATI spectrum (1064 nm) [42].

However, with increasing intensity at some point perturbative methods become impractical, and finally fail to describe the phenomena, accurately. At these intensities one has to turn to nonperturbative calculations. There are several nonperturbative techniques to solve the problem. Here we refer to some review

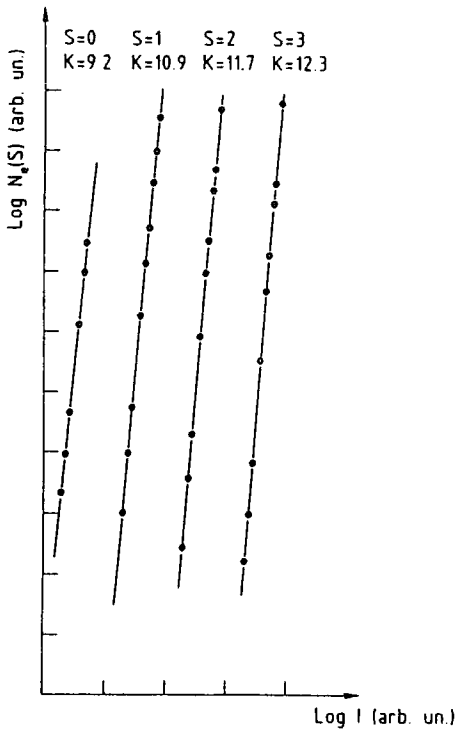

Figure 3.2: Intensity dependence of the four first peaks of the Xe ATI spectrum (1064 nm) [42].

articles: Floquet-type theories used for MPI by Giusti-Suzor and Zoller [43], Chu [44], Plummer and McCann [45], and Potvliege and Shakeshaft ([20], [35] and [46]). Kulander *et al.* [47] used time-dependent method to solve the Schrödinger equation as a partial differential equation on a grid and Burke *et al.* [22]-[23] applied the Floquet method to complex atoms. Parker *et al* [48] investigated multiphoton ionisation of helium at high laser intensities by direct numerical integration of the time-dependent two-electron Shrödinger equation on a Cray T3D. Also for time-dependent calculations see the references [8], [49]-[54].

In the following we shall give some results for the hydrogen atom in a laser field with a wavelength of 1064 nm from a nonperturbative calculation (see [20] and [35]). In later sections of this chapter we deal with harmonic generation from the same system and in the later chapters we investigate various other multiphoton processes of the hydrogen atom in the presence of laser fields mainly at this particular wavelength.

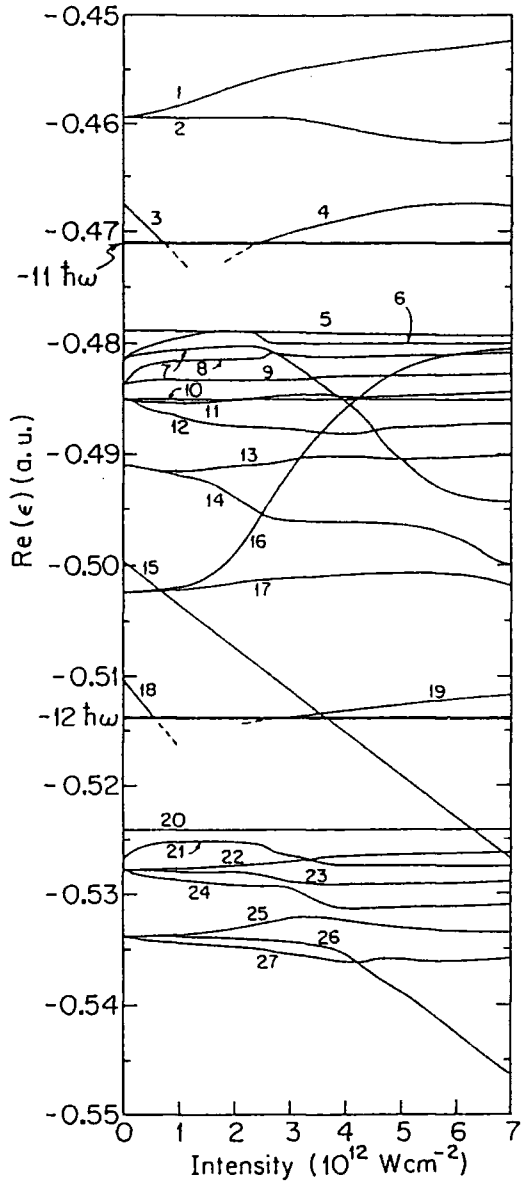

Figure 3.3: Real parts of various eigenvalues ε_j for H-atom irradiated by linearly polarised light of wavelength 1064 nm, where the integer index j labels the following atomic configurations (or superposition of configurations), where known, in the weak-intensity limit. (1-2): superpositions of $4s$ and $4d$, $N_{1,2} = 10$; (3): $2s$, $N_3 = 8$; (4): unknown; (5): superposition of $8p$, $8f$, $8h$ and $8j$, $N_5 = 11$; (6-7): superpositions of $7p$, $7f$ and $7h$, $N_{6-7} = 11$; (8-9): superpositions of $3s$ and $3d$, $N_{8-9} = 10$; (10-12): superpositions of $6p$, $6f$ and $6h$, $N_{10-12} = 11$; (13-14): superpositions of $5p$ and $5f$, $N_{13-14} = 11$; (15): $1s$, $N_{15} = 0$; (16-17): superpositions of $4p$ and $4f$, $N_{16-17} = 11$; (18): $2p$, $N_{18} = 9$; (19): unknown; (20): superpositions of $7s$, $7d$, $7g$ and $7i$, $N_{20} = 12$; (21): $3p$, $N_{21} = 11$; (22-24): superpositions of $6s$, $6d$ and $6g$, $N_{22-24} = 12$; (25-27): superpositions of $5s$, $5d$ and $5g$, $N_{25-27} = 12$; and note that the bold horizontal lines indicate multiphoton ionisation thresholds and note that the reduced mass effects are included, so that, for example, $\mathrm{Re}(\varepsilon_{15})$ approaches a value slightly above -0.5 a.u. in the zero-intensity limit [35].

The general features of the energy spectrum of atomic hydrogen as a function of intensity I for linearly polarised light of wavelength 1064 nm are given in Figure 3.3 [35]. All of the eigenvalues shown in this figure correspond to states which have parity $(-1)^{N_j}$ and which for $I \sim 0$, are detuned from an N_j-photon resonance with the $1s$ state by no more than $\hbar\omega$. In this figure $\mathrm{Re}(\varepsilon_j) - N_j\hbar\omega$ is displayed instead ε_j for convenience. In the figure ε is indicated by an integer index j. All the eigenvalues corresponding to atomic states with principal quantum number ≤ 6 when $I \sim 0$, and a few more besides. In the zero-field limit the eigenvectors are, in general, superpositions of atomic states with the same principal quantum number and parity, but different orbital angular momentum quantum numbers. Note that the absorption of twelve 1064 nm photons is required for weak-field ionisation from the $1s$ state, three photons from the $n = 2$ states, two photons from $n = 3$ states and only one photon from all states with principal quantum number $n \geq 4$. These eigenvalues have been calculated in the velocity gauge [1]. One might expect the shifts of the high Rydberg states to be small. This is indeed the case for many of these states; e.g. in the figure 3.3 ε_5, ε_{8-11}, ε_{17}, ε_{20}, and ε_{22} stay rather flat as I varies while some of the Rydberg states undergo large shifts, often because of strong coupling to the $2s$ or $2p$ states. For instance, as I increases ε_3, the eigenvalue originating from the $2s$ level, shifts downwards by roughly the ponderomotive energy P and passes below a multiphoton ionisation threshold at about 0.7×10^{12} W/cm^2. Therefore, the number of 1064 nm photons required to ionise an atom which is initially in the $2s$ state increases from 3 to 4 as this threshold is passed. Not far below the threshold, ε_3, undergoes a true crossing with an eigenvalue curve originating from a very high Rydberg level. Precisely which Rydberg level gives rise to the crossing is not clear. The reason lies in the fact that just below the multiphoton ionisation threshold an infinite number of Rydberg states accumulate and give rise to true and avoided crossings. However, when two eigenvalue curves undergo an avoided crossing, the character of the corresponding states interchange (see reference [35] for details). Thus, at first avoided crossing encountered by ε_3, the other curve (which originates from a very high Rydberg level) acquires $2s$ character, and at intensities above the crossing intensity this

[1] The A^2 term being removed.

second curve shifts downwards until (almost immediately) it encounters an avoided crossing with another curve originating from a high Rydberg level, and so on. The eigenvalue ε_6, originates from a level with principal quantum number 7. The $2s$ character acquired by ε_6 is almost immediately transferred to ε_7 as I increases, and ε_7 shifts downwards without interruption as it undergoes true crossings with ε_{8-13}, until the avoided crossing with ε_{14}. For the structure of the other eigenvalues see reference [35].

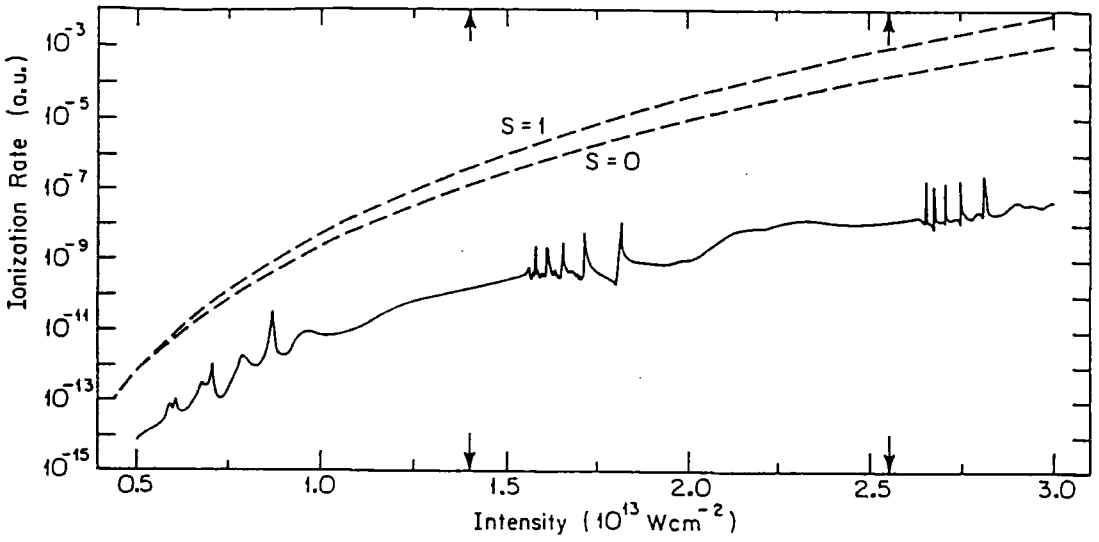

Figure 3.4: Total ionisation rate vs intensity for H($1s$) irradiated by linearly polarised light of wavelength 1064 nm. Dashed curves are partial rates for $(12+S)$-photon ionisation obtained within lowest-order perturbation theory. The arrows indicate the intensities at which the real part of the $1s$ Floquet eigenvalues crosses the 13- and 14-photon ionisation thresholds [35].

In Figure 3.4 total rates (which is Γ_{1s}) for ionisation of H($1s$) by 1064 nm radiation are given as a function of the laser-intensity [35]. These are the rates for ionisation from diabatic $1s$ state. Each of the peaks (or bumps) in rates can be correlated with one (or more) crossing of the real parts of the quasi-energies of this state and another state. For example the first group of resonances seen in Figure 3.4 is associated with the group of crossings of $\mathrm{Re}(\varepsilon_{15})$ (which shows the $1s$ state) with $\mathrm{Re}(\varepsilon_j)$ (with $j = 20-25, 27$ and 1) in the intensity range $6-10\times10^{12}$ W/cm^2. These resonances involve 11- or 12-photon transitions from the $1s$ state to highly excited states. However, not all of the crossings lead to an enhancement

of the width Γ_{15}, e.g. the crossing of $\mathrm{Re}(\varepsilon_{15})$ with $\mathrm{Re}(\varepsilon_{23})$ or $\mathrm{Re}(\varepsilon_{27})$. The middle group of resonances in Figure 3.4 involves 12− or 13-photon transitions from the $1s$ state to excited states, corresponding to crossings occurring in the intensity range $1.5 - 2 \times 10^{13}$ W/cm^2 where $\mathrm{Re}(\varepsilon_{15})$ crosses the group of curves $\mathrm{Re}(\varepsilon_{5-14})$ and $\mathrm{Re}(\varepsilon_{16-17})$ when this group is displaced downwards by $2\hbar\omega$, that is, when N_j is increased by 2 for $j = 5 - 14$ and $16 - 17$. The third group of resonances, occurring in the intensity range $2.7 - 3 \times 10^{13}$ W/cm^2, is a replication of the first group with the $\mathrm{Re}(\varepsilon_j)$ of the first group displaced downwards by $2\hbar\omega$. This group is again crossed by $\mathrm{Re}(\varepsilon_{15})$, the crossing which corresponds to 13− or 14−photon resonant transitions to the excited states of the first group.

3.2 Harmonic generation

Instead of escaping, as in MPI or ATI, the electron driven by the oscillating laser-field can come back close to the nucleus emit a photon with frequency that is an integer multiple of the fundamental's frequency. These photons are accordingly called harmonics. The general expression for the mechanism is

$$N\gamma(\omega) + X \longrightarrow \gamma'(N\omega) + X \tag{3.3}$$

where ω is the frequency of the fundamental and $N\omega$ is the energy of the harmonic. The energy-level diagram of this process for $N = 2$ is illustrated schematically in figure 3.5.

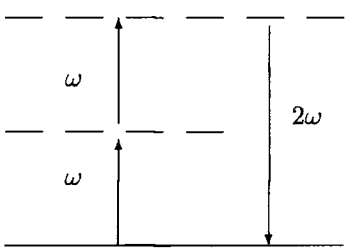

Figure 3.5: Illustration of second harmonic generation with one colour. The dashed levels may be virtual or real, and lie below or above ionisation threshold.

3.2.1 Overview of experiments

Harmonic generation was first demonstrated by Franken *et al.* [55]. They demonstrated second harmonic generation in a crystalline quartz sample. Maker *et al.* [56] reported a demonstration of second harmonic generation in crystals, glasses, and liquids. New and Ward [9] first put forward the idea of harmonic generation in a gas. Gases are homogeneous and isotropic which presents a great simplification for theoretical calculations. The advantage of using gaseous media lies in their transparency over broad frequency ranges, high resistance to radiation damage and recovery from breakdown and the possibility of continuously varying their composition and concentration. The ability to produce higher order harmonics was another reason to use gases, New and Ward were the first workers to detect

the third harmonic in gases. The gases used were mainly the rare gases in order to limit chemical reactions. The gases New and Ward studied were helium, neon, argon, xenon, krypton, molecular hydrogen, carbon dioxide, nitrogen, oxygen, ethylene, chlorine and air.

For the reasons outlined above harmonic generation in gases became very quickly a popular topic among active researchers. Fifth and higher-order harmonic generation was observed at several laboratories a few years later. Reintjes *et al.* (see [10] and [11]) reported the first observation of the fifth and the seventh harmonic generation from helium atom. It followed the 11th harmonic of a 1315 nm iodine laser reported by Wildenauer [12], the highest harmonic (17th) at that date from neon was reported by McPherson *et al.* [13] in addition to lower harmonics. In 1989 Li *et al.* [14] produced the 33rd harmonic of Nd-YAG from argon.

Very recently several groups performed experiments in which they observed generation of harmonics of the 100th order and higher. The highest harmonics observed so far are the 109th of an 806 nm Ti-sapphire laser and 135th of a 1053 nm Nd-glass laser, both in neon [16].

Harmonic generation experiments meausure simultaneously the single-atom response to the laser interaction and the many-atom response, that is the capability of the medium to ensure proper phase matching between the nonlinear polarisation induced by the incident field and the generated radiation.

The experiments soon showed that the harmonic spectra at sufficiently high intensities presented a characteristic distribution: a steep decrease for the first few orders, followed by a long plateau, which ends with a sudden cut-off. The width of the plateau increases with the laser power, up to the intensity at which the medium becomes ionised [29]. This new feature of the harmonic spectrum at higher intensity demonstrated the breakdown of (lowest order) perturbation theory. In order to have a correct description of these features new theoretical techniques (which are briefly described in section 3.2.2) needed to be devised to calculate the harmonic spectrum.

The experiments described above and most other research until recently in this area have been carried out using a linearly polarised incident field. However, it is

interesting to explore the influence of the ellipticity of the incident laser beam on harmonic production. The following picture has brought to the forefront the idea of considering various ellipticities of the incident field: When an atom is in an intense laser field, the electron can, in certain circumstances tunnel through the atomic potential. Its motion in the field is, to a good approximation, a free electron so it can be treated classically [15],[57]-[60]. Depending on the polarisation of the field the electron may follow a trajectory such that it returns to the nucleus where it can recombine and emit a harmonic photon. However, the electron may not return to the nucleus at all. The atom will then simply ionise and no harmonics will be produced. The way to control the trajectory of the electron is to change the polarisation of the incident beam.

Experiments have been performed in two different regimes - the tunnelling regime and the multiphoton regime. Although there is no definite boundary between the multiphoton and tunnelling regimes, in general it has been described in terms of the Keldysh parameter, $\gamma = (I_p/2U_p)^{1/2}$, where I_p is the atomic ionisation potential and U_p is the ponderomotive energy of the electron in the laser field. $\gamma>1$ corresponds to the multiphoton regime whereas $\gamma<1$ corresponds to the tunnelling regime.

The first experiment inducing harmonic generation with elliptically polarised laser pulses was performed by Chin *et al.* [57] in the multiphoton regime using argon gas. In this regime the quasi classical model described above does not hold and they confirmed that the data is in near agreement with perturbation theory. However, there were still differences between the perturbative theory and the experimental results.

Corkum *et al.* [58] examined the dependency of harmonic generation on the ellipticity of the driving field in the tunnelling regime. They used a Ti:sapphire laser system to obtain harmonic emission from Ne and Ar gases. Here too a discrepancy between the perturbative predictions and the experiment was observed. A similar experiment has been performed by Budil *et al.* [15] which probed both regimes.

Other more recent work exists exploring the ellipticity dependence of the harmonics for high intensity fields e.g. Burnett *et al.* [59], Weihe *et al.* [60], Weihe

et al. [61] and Kakehata *et al.* [62]. These experiments demonstrate that in general the harmonic efficiency decreases rapidly with increase in the ellipticity of the laser field. For linearly polarised light it reaches a maximum whereas for circularly polarised light it is zero (from the dipole transition selection rules, see Section 3.2.7). This decrease is valid for any order of harmonics but in general is more rapid for the higher harmonics.

There has also been some theoretical work done in order to understand the influence of the ellipticity of the incident field on harmonic generation and this will be discussed in subsection 3.2.3.

3.2.2 Overview of theory of harmonic generation for linearly polarised pump field

1- Numerical Solution of Time Dependent Schrödinger Equation:

Kulander and Shore [63]-[64], DeVries [65], LaGattuta [66], and Taylor *et al.* (see [25] and [48]) have obtained numerical solutions of the Time Dependent Schrödinger Equation (TDSE) in order to calculate the multiphoton absorption spectra for atomic systems.

Kulander and Shore followed an approach based on the evaluation of the atomic response by generating a numerical solution to a single active-electron approximation to the time-dependent Hartree-Fock (TDHF) equation for an atom in a time varying field. The model was successfully applied to Xe for 1064 nm radiation with intensities in the range $10^{13} - 10^{14}$ W/cm^2. The calculated spectrum displayed sharply defined optical harmonics up to order 61 [64].

DeVries [65] investigated the response of a hydrogen atom in an intense radiation field using numerical methods to solve the three-dimensional time-dependent Schrödinger equation. This nonperturbative calculation used an initial $1s$ state orbital which was then propagated in time under the influence of the driving field. The resulting wavefunctions were used to evaluate the time-dependent dipole-moment, from which the spectrum of generated light was obtained.

LaGattuta [66] solved the TDSE numerically as a set of coupled equations for an electron moving in three spatial dimensions, bound initially ($t \leq 0$) by a Coulomb potential, and acted on by a linearly polarised, monochromatic field

turned on at t=0.

Taylor *et al.* [25] and Parker *et al.* [48] investigated multiphoton processes in the helium atom by direct numerical integration of the time-dependent two-electron Schrödinger equation on a Cray T3D. They considered especially two-photon ionisation, double ionisation, high harmonic generation.

Rae and Burnett [49], Véniard *et al.* [50] and [51], Protopapas *et al.* and Sanpera [53] are also the workers of this line.

2- Floquet Techniques:

Potvliege and Shakeshaft [35] and Dörr *et al.* [67] employed the Floquet technique successfully to describe multiphoton processes. This technique involves a replacement of the semiclassical Hamiltonian of a quantum system in an oscillating field with a time-independent Hamiltonian represented by an infinite matrix.

There is also growing interest in treating multiphoton processes using a unified R-matrix-Floquet method especially in the case of complex atoms. This treatment is also a fully nonperturbative one. In the R-matrix method configuration space is divided into an internal and external region. This implies that in each region the most appropriate form of the laser-atomic system interaction Hamiltonian can be selected in a physically natural way by performing unitary transformations on the wavefunction. Some of the work using R-matrix-Floquet method is reported in the references [23], [68], [69], [70], [71] and in particular calculations for harmonic generation are presented in references [39] and [40].

3- Semi-analytical Models:

Lewenstein *et al.* [72] considered an atom in the single-electron approximation under the influence of a laser field based on the following assumptions.

(a) The contribution to the evolution of the system of all bound states except the ground state $|0\rangle$ can be neglected.

(b) The depletion of the ground state can be neglected ($U_p \ll U_{sat}$).

(c) In the continuum, the electron can be treated as a free particle moving in the electric field with no effect of the potential $V(\mathbf{x})$.

The results from these theoretical calculations display good agreement with experimental harmonic spectrums which has the characteristic, universal shape: The harmonic spectrum falls off for the first few harmonics, then exhibits a plateau

where all the harmonics have about the same strength, and it ends with a sharp cut-off. This cut-off in the harmonic spectrum occurs for a harmonic of order higher then

$$N_{max} \backsimeq \frac{\mathrm{I}_p + 3.17\mathrm{U}_p}{\omega} \tag{3.4}$$

In addition to these methods there are other model calculations which provide some insight into the physics involved, e.g. Becker *et al.* [16] have performed calculations using the δ-function potential.

3.2.3 Overview of theory of harmonic generation for elliptically polarised pump field

The work described previously considered the incident field as linearly polarised. However, recently there has been a growing interest exploring the influence of the ellipticity of the incident laser field on harmonic production. Methods from the literature are as follows.

1- Perturbative Method: Potvliege and Shakeshaft have calculated harmonic generation dependency on the ellipticity of the field using a lowest order perturbation theory. They report their results in [34] for three wavelengths: 265, 532, 1064 nm for the hydrogen atom. However, their results do not agree with experimental results at higher intensities because of being perturbative.

2- Analytical:

Manakov *et al.* [73] have obtained the polarisation vector of the emitted harmonics in terms of the susceptibility tensor for lowest order perturbation theory. They also calculated the first correction to this in order to obtain higher order effects. They noted the influence on harmonic generation rates and also the influence on the direction of the polarisation vector.

In general these calculations are in good agreement with experimental results for low intensities, but at higher intensities the agreement is not good.

As far as we are aware no nonperturbative calculations of harmonic generation rates for elliptically polarised incident fields have been performed so far, apart from the theory based on the Lewenstein model [74].

We have carried out a nonperturbative calculation of harmonic generation considering the laser field elliptically polarised. This work is a generalisation of

the nonperturbative theoretical work done by Potvliege and Shakeshaft for the linearly polarised case [35]. The formal exposition of this theory, its application to the hydrogen atom and a comparative discussion with the Lewenstein model [74] as well as with experimental results will be given in the following Sections of this Chapter and in Chapter 4.

3.2.4 Formal expressions for harmonic generation

Consider an atom immersed in a monochromatic laser beam of angular frequency ω. The component of the dipole moment which oscillates at frequency Ω, generates electric and magnetic fields which are given by the formulae below [75]:

$$\mathbf{B}(\mathbf{x}) = (\hat{\mathbf{n}} \times \mathbf{D})F(r) \tag{3.5}$$

and

$$\mathbf{E}(\mathbf{x}) = \mathbf{B}(\mathbf{x}) \times \hat{\mathbf{n}} \tag{3.6}$$

where $F(r) = (\Omega/c)^2 e^{i\Omega r}/r$ and $\hat{\mathbf{n}}$ is a unit vector which is along the direction of observation. The polarisation plane is perpendicular to $\hat{\mathbf{n}}$ and $\mathbf{E}(\mathbf{x})$ and $\mathbf{B}(\mathbf{x})$ both lie in this plane.

The unit polarisation vector $\mathbf{e}$ of the incident field is defined by Equation (2.24) and the atomic dipole moment induced by the incident field can be written in terms of the expectation value of the dipole operator $e\mathbf{x}$:

$$\mathbf{d}(t) \;=\; \langle \Psi_i(t) | (-e)\mathbf{x} | \Psi_i(t) \rangle \tag{3.7}$$

where $\Psi_i(t)$ is the wavefunction of the atomic system in the presence of the field and e is the electron charge. Making the Floquet ansatz and using Equations (2.20) and (2.21) give

$$\begin{aligned} \mathbf{d}(t) \;&=-\; \langle \psi_i(\tau) | e\mathbf{x} | \psi_i(\tau) \rangle \exp(-\Gamma_i t/\hbar) \\ &= \exp(-\Gamma_i t/\hbar) \sum_{n'} \sum_{n} \exp(-i(n' - n)\omega t) \langle \psi_{i,n'} | e\mathbf{x} | \psi_{i,n} \rangle \end{aligned} \tag{3.8}$$

define $N = n - n'$ and so $n' = n - N$

$$\mathbf{d}(t) \;=-\; \exp(-\Gamma_i t/\hbar) \sum_{N} \sum_{n} \exp(-iN\omega t) \langle \psi_{i,n-N} | e\mathbf{x} | \psi_{i,n} \rangle \tag{3.9}$$

then use

$$\mathbf{d}_{Nn} = -\langle \psi_{i,n-N} | e\mathbf{x} | \psi_{i,n} \rangle \tag{3.10}$$

$$\mathbf{d}_N = \sum_n \mathbf{d}_{Nn} \tag{3.11}$$

$$\mathbf{d}(t) = \exp(-\Gamma_i t/\hbar)\Big[\mathbf{d}_0 + \sum_{N>0} \mathbf{Re}(2\mathbf{d}_N \exp(-iN\omega t)\Big] \tag{3.12}$$

The rate for generating photons with frequency $\Omega = N\omega$ and polarisation $\mathbf{e}$ can be written

$$\frac{dR(\Omega, \hat{\mathbf{n}})}{d\hat{\mathbf{n}}} = \frac{\Omega^3}{8\pi\hbar c^3} |2\mathbf{d}_N.\mathbf{e}^\star|^2 \tag{3.13}$$

In fact $2\mathbf{d}_N$ is equal to the vector $\mathbf{D}$. The harmonic fields in general are elliptically polarised and the ellipticities of the harmonics are different from that of the incoming fields. Writing the dipole moment in Equation (3.13) as $\mathbf{d}_N = d_N \mathbf{e}_N$; $\mathbf{e}_N$ is the polarisation of the N-th harmonic:

$$\mathbf{e}_N = \cos(\eta_N/2)\hat{\mathbf{u}}_N + i\sin(\eta_N/2)\hat{\mathbf{v}}_N \tag{3.14}$$

where $\hat{\mathbf{u}}_N$ and $\hat{\mathbf{v}}_N$ are the unit vectors making an angle θ_N with $\hat{\mathbf{x}}$ and $\hat{\mathbf{y}}$, respectively. Restricting the ellipticity angles ξ and η_N to vary between $-\pi/2$ and $+\pi/2$, θ_N is the offset angle between the major axis of the polarisation ellipse of the N-th harmonic and the major axis of the polarisation ellipse of the incident field.

3.2.5 Ellipticity angle, offset angle and phase of the produced harmonic

As already mentioned we may investigate the case of general ellipticities by defining an offset angle θ and a change in ellipticity $\xi \rightarrow \eta$ for the generated harmonics. For a given harmonic N the angles and unit vectors are defined as follows (note: for simplifying the equations we leave the indices N out for a moment):

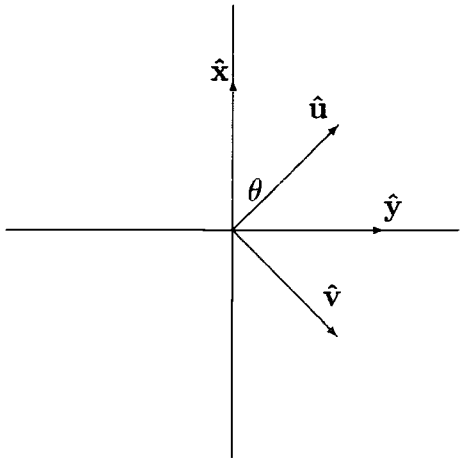

$$\hat{\mathbf{u}} = \cos\theta\hat{\mathbf{x}} + \sin\theta\hat{\mathbf{y}} \tag{3.15}$$

$$\hat{\mathbf{v}} = -\sin\theta\hat{\mathbf{x}} + \cos\theta\hat{\mathbf{y}} \tag{3.16}$$

$\hat{\mathbf{x}}$ || major axis of ellipse (fundamental)
$\hat{\mathbf{y}}$ || minor axis of ellipse (fundamental)
$\hat{\mathbf{u}}$ || major axis of ellipse (harmonic)
$\hat{\mathbf{v}}$ || minor axis of ellipse (harmonic)

Using Equation (3.14) for the polarisation of the harmonics and the orthogonality property of the unit vectors $\hat{\mathbf{u}}$ and $\hat{\mathbf{v}}$, the polarisation vector can be written in terms of the unit vectors $\hat{\mathbf{x}}$ and $\hat{\mathbf{y}}$.

$$\begin{aligned}\mathbf{e} &= (\cos(\eta/2)\cos\theta - i\sin(\eta/2)\sin\theta)\hat{\mathbf{x}} \\ &\quad +(\cos(\eta/2)\sin\theta + i\sin(\eta/2)\cos\theta)\hat{\mathbf{y}}\end{aligned} \tag{3.17}$$

If $-\pi/2 < \eta < +\pi/2$: the polarisation is elliptic with the major axis of the ellipse in the $\hat{\mathbf{u}}$ direction. If we expand the dipole moment vector as

$$\mathbf{d} = \mathrm{d}_x\hat{\mathbf{x}} + \mathrm{d}_y\hat{\mathbf{y}} \tag{3.18}$$

then we can write $\mathbf{d}$ in terms of η, θ and the phase ϕ:

$$\begin{aligned}\mathbf{d} &= |\mathbf{d}|e^{i\phi}\Big[(\cos(\eta/2)\cos\theta - i\sin(\eta/2)\sin\theta)\hat{\mathbf{x}} \\ &\quad +(\cos(\eta/2)\sin\theta + i\sin(\eta/2)\cos\theta)\hat{\mathbf{y}}\Big]\end{aligned} \tag{3.19}$$

We want to know ϕ, θ, η. Introduce a unit vector $\hat{\mathbf{b}} = \cos\delta\hat{\mathbf{x}} + \sin\delta\hat{\mathbf{y}}$.

$$\begin{aligned}\mathbf{d}.\hat{\mathbf{b}} &= |\mathbf{d}|e^{i\phi}\Big[(\cos(\eta/2)\cos\theta - i\sin(\eta/2)\sin\theta)\cos\delta \\ &\quad +(\cos(\eta/2)\sin\theta + i\sin(\eta/2)\cos\theta)\sin\delta\Big] \\ |\mathbf{d}.\hat{\mathbf{b}}|^2 &= |\mathbf{d}|^2\Big[\cos^2(\eta/2)\cos^2(\delta-\theta) + \sin^2(\eta/2)\sin^2(\delta-\theta)\Big]\end{aligned}$$

The extrema of $|\mathbf{d}.\hat{\mathbf{b}}|^2$ as a function of δ are given by

$$\begin{aligned}\frac{d}{d\delta}|\mathbf{d}.\hat{\mathbf{b}}|^2 &= |\mathbf{d}|^2\sin(2(\delta-\theta))\Big[\sin^2(\eta/2) - \cos^2(\eta/2)\Big] \\ &= -|\mathbf{d}|^2\sin(2(\delta-\theta))\cos\eta \\ &= 0 \text{ when } 2(\delta-\theta) = 0, \pm\pi, \pm 2\pi, \pm 4\pi, \ldots\end{aligned} \tag{3.20}$$

$|\mathbf{d}.\hat{\mathbf{b}}|^2$ is a maximum when $2(\delta - \theta) = 0, \pm\pi, \pm 2\pi, \pm 4\pi, \ldots$ provided $\cos\eta > 0$. Hence in order to find θ (assuming that $\cos\eta > 0$) we need to calculate

$$|\mathbf{d}.\hat{\mathbf{b}}|^2 = |\mathrm{d}_x \cos\delta + \mathrm{d}_y \sin\delta|^2$$

and find the maximum vs δ, then $\theta = \delta_{max}$. Analytically:

$$|\mathrm{d}_x \cos\delta + \mathrm{d}_y \sin\delta|^2 = |\mathrm{d}_x|^2 \cos^2\delta + 2\mathbf{Re}(\mathrm{d}_x^* \mathrm{d}_y)\cos\delta\sin\delta + |\mathrm{d}_y|^2 \sin^2\delta$$

Its derivative with respect to δ:

$$\frac{d}{d\delta}|\mathbf{d}.\hat{\mathbf{b}}|^2 = \sin(2\delta)(|\mathrm{d}_y|^2 - |\mathrm{d}_x|^2) + \cos(2\delta)2\mathbf{Re}(\mathrm{d}_x^*\mathrm{d}_y) \tag{3.21}$$

$$= 0 \qquad \text{for} \quad \delta = \delta_{max}(= \theta) \tag{3.22}$$

Finally, from 3.22 with some algebra we obtain

$$\theta = \frac{1}{2}\arctan\Big((\mathrm{d}_x^*\mathrm{d}_y + \mathrm{d}_x\mathrm{d}_y^*)/(|\mathrm{d}_x|^2 - |\mathrm{d}_y|^2)\Big) \tag{3.23}$$

Now, calculate η: Recall Equations (3.15), (3.16) and (3.18) in order to write the dipole moment $\mathbf{d}$ in the $(\hat{\mathbf{u}}, \hat{\mathbf{v}})$ basis

$$\mathbf{d} = \mathrm{d}_u\hat{\mathbf{u}} + \mathrm{d}_v\hat{\mathbf{v}} \tag{3.24}$$

where

$$\mathrm{d}_u = \mathbf{d}.\mathbf{u} = \mathrm{d}_x\cos\theta + \mathrm{d}_y\sin\theta \tag{3.25}$$

$$\mathrm{d}_v = \mathbf{d}.\mathbf{v} = -\mathrm{d}_x\sin\theta + \mathrm{d}_y\cos\theta \tag{3.26}$$

Then using Equations (3.15), (3.16), (3.25) and (3.26) we write $\mathbf{d}$ as

$$\mathbf{d} = |\mathbf{d}|e^{i\phi}\Big[\cos(\eta/2)\hat{\mathbf{u}} + i\sin(\eta/2)\hat{\mathbf{v}}\Big] \tag{3.27}$$

Hence

$$\mathrm{d}_u = |\mathbf{d}|e^{i\phi}\cos(\eta/2) \tag{3.28}$$

$$\mathrm{d}_v = -i|\mathbf{d}|e^{i\phi}\sin(\eta/2) \tag{3.29}$$

and finally,

$$\tan(\eta/2) = -i\mathrm{d}_v/\mathrm{d}_u \tag{3.30}$$

Knowing θ and η, one can obtain ϕ from

$$\mathrm{d}_x = |\mathbf{d}|e^{i\phi}\Big[\cos(\eta/2)\cos\theta - i\sin(\eta/2)\sin\theta\Big] \tag{3.31}$$

and

$$\mathrm{d}_y = |\mathbf{d}|e^{i\phi}\Big[\cos(\eta/2)\sin\theta + i\sin(\eta/2)\cos\theta\Big] \tag{3.32}$$

3.2.6 Perturbative limit for the dipole moment

In leading order perturbation theory the dipole moment of the N-th harmonic is

$$\mathbf{d}_N = (\cos\xi)^{(N-1)/2} A_o^N \alpha_N \mathbf{e}_i \tag{3.33}$$

and including the next - to - leading order correction,

$$\mathbf{d}_N = (\cos\xi)^{(N-1)/2} A_o^N \left[(\alpha_N + \beta_N A_o^2)\mathbf{e}_i + \gamma_N A_o^2 \cos\xi \mathbf{e^*}_i\right] \tag{3.34}$$

In this equation α_N, β_N and γ_N are frequency-dependent coefficients. Equation (3.34) was obtained by Manakov *et al.* [73] for the particular case of $N = 3$. Equation (3.34) is in fact also valid for $N > 3$ [76].

3.2.7 Selection rules and Parity consideration for the dipole moment

Here we are concerned with evolution of the $\mathbf{d}_{Nn} = \langle\psi_{i,n-N}|e\mathbf{x}|\psi_{i,n}\rangle$ which enter the expression of $\mathbf{d_N}$. The probability for electromagnetic transitions is governed by well known selection rules due to the Wigner-Eckart theorem. These are:

$$\Delta l = \pm 1, 0 \qquad (0 \nrightarrow 0) \tag{3.35}$$

$$\Delta m = \pm 1, 0 \tag{3.36}$$

for a one-photon transition within the dipole approximation for a nonrelativistic interaction ($\mathbf{j} = \mathbf{l}$). In Equation (3.35) l is the orbital angular momentum quantum number. Additionally, the basic Hamiltonian being parity invariant and taking the eigen states to be parity eigenstates, the parity given by l, all transitions $\Delta l = 0$ are forbidden. This leads to certain restrictions on the harmonic order which can be produced in a one-colour process. If the state i has a definite parity, $\sigma = \pm 1$, the function $\langle\mathbf{x}|\psi_{i,M}\rangle$ has a parity

$$\sigma(-1)^M \tag{3.37}$$

since $|\psi_{i,M}\rangle$ represents an electron which has absorbed M (real or virtual) photons, each of parity (-1). Then $\langle\psi_{i,n-N}|\mathbf{x}\rangle\langle\mathbf{x}|\psi_{in}\rangle$ has parity,

$$\sigma(-1)^{n-N}(-1)^n\sigma = (-1)^N \tag{3.38}$$

therefore $\mathbf{d}_{Nn}$ and $\mathbf{d}_N$ which are given by Equations (3.10) and (3.11), respectively, will vanish if N is even. Thus, only odd harmonics can be produced in a one-colour process.

Moreover, depending on the polarisation of the incident field there are additional restrictions on the magnetic quantum number. For a linearly polarised field one has $\Delta m = 0$ and for circular polarisation $\Delta m = \pm 1$.

3.2.8 Dipole moment without complex-conjugation

The scalar product in the expression of the dipole moment includes the complex conjugate of the Floquet wavefunction. Recalling (3.10)

$$\begin{aligned} \mathbf{d}_{Nn} &= \langle \psi_{i,n-N} | e\mathbf{x} | \psi_{i,n} \rangle \\ &= \int \psi^*_{n-N}(\mathbf{x}) e\mathbf{x} \psi_n(\mathbf{x}) d^3x \end{aligned} \tag{3.39}$$

in contrast to the expression for the normalisation of the Floquet wavefunction, given in Section 2.4.

However, one can also define the product in the expression of the dipole moment without introducing the complex conjugate as done in normalising the Floquet wavefunction :

$$\mathbf{d}'_{Nn} = \int \psi_{n-N}(\mathbf{x}) e\mathbf{x} \psi_n(\mathbf{x}) d^3x \tag{3.40}$$

The following reasons support why it makes sense to calculate the dipole moment in this way:

- There is no physical reason why $\mathbf{d}'_{Nn}$ should be better (or more accurate) than $\mathbf{d}_{Nn}$ [77].
- It turns out that $\mathbf{d}'_{Nn} \simeq \mathbf{d}_{Nn}$ to a very good approximation (see Table 3.1).

The reason for the latter most probably is as follows: $\mathbf{d}_{Nn}$ and $\mathbf{d}'_{Nn}$ are dominated by the contribution from the region of space close to the nucleus.

Thus, we calculate the dipole moment (d), ellipticity (η) and offset (θ) angle of harmonics and the phase (ϕ) of the dipole moment using both definitions of the dipole moment (Equations (3.39) and 3.40)). For the following laser-field parameters the results are exhibited in Table 3.1: The wavelength of the laser field is $\lambda = 1064$ nm, the intensity of the field is I= 10^{13} W/cm^2 and finally

the polarisation of the laser field is $\xi = 60^o$. In this table the variables with *prime* give the results from a calculation using the definition of dipole moment without introducing the complex conjugate of the wavefunction and the variables without *prime* give the results using the definition of dipole moment where the complex conjugate of the wavefunction is used (standard way). There is hardly any difference between these two sets of results in Table 3.1. The biggest relative difference between two different sets of results is 4.9×10^{-4} for the value of the dipole moment of the 3rd harmonic. For the other parameter the relative difference is nearly zero for all harmonics [2]

Table 3.1: Dipole moment (d), ellipticity (η) and offset angle (θ) of the harmonics, and phase (ϕ) of dipole moment using two different definitions in the calculation of dipole moment. The laser field used for these calculations has a wavelength $\lambda = 1064$ nm, intensity I= 10^{13} W/cm^2 and ellipticity angle $\xi = 60^o$.

.

Dipole moment with Two Different Definition				
N	η' (deg)	θ' (deg)	ϕ' (deg)	d'
3	0.59188 (2)	0.12016 (-2)	0.18067 (-2)	0.88634 (-4)
5	0.55307 (2)	0.72007 (0)	0.12025 (1)	0.12356 (-5)
7	0.41678 (2)	0.22651 (1)	0.25543 (2)	0.23865 (-6)
9	0.60180 (2)	-0.67435 (2)	0.99808 (2)	0.18802 (-6)
11	0.34713 (2)	-0.53520 (2)	-0.85876 (2)	0.50919 (-7)
13	0.72579 (2)	-0.54442 (1)	0.16904 (3)	0.13962 (-7)
15	0.52833 (2)	0.22836 (1)	-0.15553 (3)	0.63977 (-8)
17	0.56925 (2)	0.28934 (1)	-0.46284 (2)	0.87417 (-9)
19	0.59067 (2)	0.21283 (1)	0.68597 (2)	0.54143 (-10)
N	η (deg)	θ (deg)	ϕ (deg)	d
3	0.59188 (2)	0.12187 (-2)	-0.18000 (3)	0.88585 (-4)
5	0.55307 (2)	0.72007 (0)	-0.17880 (3)	0.12349 (-5)
7	0.41678 (2)	0.22650 (1)	-0.15446 (3)	0.23852 (-6)
9	0.60180 (2)	-0.67435 (2)	-0.80192 (2)	0.18792 (-6)
11	0.34713 (2)	-0.53520 (2)	0.94124 (2)	0.50891 (-7)
13	0.72579 (2)	-0.54442 (1)	-0.10955 (2)	0.13954 (-7)
15	0.52833 (2)	0.22836 (1)	0.24471 (2)	0.63942 (-8)
17	0.56925 (2)	0.28934 (1)	0.13372 (3)	0.87370 (-9)
19	0.59067 (2)	0.21284 (1)	-0.11140 (3)	0.54113 (-10)

[2]The difference between the two sets of results for the phase (ϕ) for each harmonic is equal to 180, which is effectively the same.

3.2.9 Different forms of dipole moment

Evaluation of the wavefunctions for all calculations have been performed in the velocity gauge apart from in Section 7.3 for a set of test calculations. However, calculation of the dipole moment were also performed using other forms of the dipole operator in order to check the gauge invariance. Besides the velocity form these were the length and acceleration forms. The general expression for the dipole moment is given by Equation (3.10) which is the length form of the dipole moment. For an arbitrary elliptical polarisation

$$\mathbf{d}_{Nn} = \langle\psi_{i,n-N}|ex|\psi_{i,n}\rangle\hat{\mathbf{x}} + \langle\psi_{i,n-N}|ey|\psi_{i,n}\rangle\hat{\mathbf{y}} \tag{3.41}$$

Considering the interaction potential in the velocity gauge (Equation (2.19) the velocity form of the dipole moment is as follows:

$$\mathbf{d}_{Nn} = \langle\psi_{i,n-N}|e\frac{\partial}{\partial x}|\psi_{i,n}\rangle\hat{\mathbf{x}} + \langle\psi_{i,n-N}|e\frac{\partial}{\partial y}|\psi_{i,n}\rangle\hat{\mathbf{y}} \tag{3.42}$$

One may derive the acceleration form of the dipole moment for a Coulomb potential using the absorption and emission components of the dipole interaction potential expressions in the velocity form. Consider ψ_i and ψ_c as eigenstates of the hydrogen atom with $E_c = E_i + \hbar\omega$ (first order perturbation theory).

$$\begin{aligned}\langle\psi_c|V_+|\psi_i\rangle &= (eF_0/2\mu\omega)\Big[\cos(\eta/2)\cos(\theta)\langle\psi_c|\frac{\partial}{\partial x}|\psi_i\rangle \\ &\quad + i\sin(\eta/2)\cos(\theta)\langle\psi_c|\frac{\partial}{\partial y}|\psi_i\rangle\Big]\end{aligned} \tag{3.43}$$

Now, consider each matrix elements in Equation 3.43 separately, so

$$E_i\langle\psi_c|\frac{\partial}{\partial x}|\psi_i\rangle = \langle\psi_c|\frac{\partial}{\partial x}H_{at}|\psi_i\rangle \tag{3.44}$$

where H_{at} is the atomic Hamiltonian. Using $H_{at} = \nabla^2 + V$, V is the Coulomb potential,

$$\begin{aligned}E_i\langle\psi_c|\frac{\partial}{\partial x}|\psi_i\rangle &= \langle\psi_c|\nabla^2\frac{\partial}{\partial x}|\psi_i\rangle + \langle\psi_c|\frac{\partial}{\partial x}V|\psi_i\rangle \\ &= \langle\psi_c|H_{at}\frac{\partial}{\partial x}|\psi_i\rangle + \langle\psi_c|\frac{\partial V}{\partial x}|\psi_i\rangle \\ &= E_c\langle\psi_c|\frac{\partial}{\partial x}|\psi_i\rangle + \langle\psi_c|\frac{\partial V}{\partial x}|\psi_i\rangle\end{aligned} \tag{3.45}$$

Therefore,

$$\langle\psi_c|\frac{\partial}{\partial x}|\psi_i\rangle = \frac{1}{E_i - E_c}\langle\psi_c|\frac{\partial V}{\partial x}|\psi_i\rangle \tag{3.46}$$

and so

$$\langle\psi_c|\frac{\partial}{\partial y}|\psi_i\rangle = \frac{1}{E_i - E_c}\langle\psi_c|\frac{\partial V}{\partial y}|\psi_i\rangle \tag{3.47}$$

$$\mathbf{d}_{Nn} = \langle\psi_{i,n-N}|e\frac{\partial V}{\partial x}|\psi_{i,n}\rangle\hat{\mathbf{x}} + \langle\psi_{i,n-N}|e\frac{\partial V}{\partial y}|\psi_{i,n}\rangle\hat{\mathbf{y}} \tag{3.48}$$

This can be generalised for a dressed state [78]. A set of results from calculations performed using the three forms of the dipole moment described above is given in Table 3.2 for an ac field with a wavelength $\lambda = 1064$ nm and intensity I= 10^{13} W/cm^2. In this table the first column represents the results using the velocity form of dipole moment and the second column the length form of dipole moment for an elliptically polarised incoming field with an ellipticity angle $\xi = 60^o$. In addition a set of results for linearly polarised field ($\xi = 0^o$) from calculations using the velocity form of the dipole moment and the acceleration form of the dipole moment are given in the third and fourth columns of this table, respectively, in order to present the consistency of the results from the three forms. The agreement is found to be very good. The results are identical for lower harmonics (up to 17th). There is about 0.16% of a relative difference for the 17th harmonic and 1.1% for the 19th harmonic in the case of comparison between the results from the velocity form and length form of the dipole moment. There is also about 0.61% of relative difference for the 19th harmonic between the results from the calculation with velocity and acceleration form of the dipole moment although the results for the other harmonics are identical.

3.2.10 Summation methods for calculating the dipole moment

In all calculations Sturmian functions defined in Section 2.3, are used in order to calculate the dipole moment. Because the sum over the Sturmian functions in the expression for the dipole moment $\left(\int \psi^*_{i,M-N}(\mathbf{x})\big(e\mathbf{x}\big)\psi_{i,M}(\mathbf{x})\mathrm{d}\mathbf{x}\right)$ converges slowly (or even diverges), one should use Padé (ε-algorithm) for summing up over the Sturmian coefficients [79].

Table 3.2: Harmonic generation rate with the different forms of the dipole moment for $\lambda = 1064$ nm, intensity I= 10^{13} W/cm^2 and $\xi = 0^o, 60^o$.

Gauge Invariance for HG Rates (a.u.)				
N	R_{vel1}	R_{len}	R_{vel2}	R_{acce}
3	0.357 (-0)	0.357 (-0)	1.470 (-0)	1.470 (-0)
5	0.321 (-3)	0.321 (-3)	0.610 (-2)	0.610 (-2)
7	0.328 (-4)	0.328 (-4)	0.244 (-2)	0.244 (-2)
9	0.433 (-4)	0.433 (-4)	0.635 (-2)	0.635 (-2)
11	0.581 (-5)	0.581 (-5)	0.190 (-1)	0.190 (-1)
13	0.720 (-6)	0.720 (-6)	0.123 (-1)	0.123 (-1)
15	0.232 (-6)	0.232 (-6)	0.299 (-2)	0.299 (-2)
17	0.631 (-8)	0.632 (-8)	0.545 (-3)	0.545 (-3)
19	3.420 (-9)	3.382 (-9)	0.164 (-4)	0.163 (-4)

This can be done before or after having sum coefficient of dipole moment over M, in

$$\sum_M \langle \psi_{i,M-N} | e\mathbf{x} | \psi_{i,M} \rangle \tag{3.49}$$

In addition Padé summation can be done in several ways. Substituting Equation(2.27) in the expression (3.10) of the dipole moment one obtains that

$$\langle \psi_{i,M-N} | e\mathbf{x} | \psi_{i,M} \rangle = \sum_{lmn} \sum_{l'm'n'} C^{(M-N)}_{lmn} Y_{lm} S^{\kappa}_{nl}(r)/r C^{(M)}_{l'm'n'} Y_{l'm'} S^{\kappa}_{n'l'}(r)/r \tag{3.50}$$

where the indices n and $n^{'}$ in Equation (3.50) are the indices of the Sturmian basis set. Padé summation is done over indices n and $n^{'}$. There are several ways of doing this summation: i.e.

- Sum over $n^{'}$, fixed n, then sum over n using Padé.
- Sum over all n and $n^{'}$ such that $n + n^{'} \leq \bar{n}$. This sum up to $\bar{n}$ gives a sequence of number where convergence is accelerated by Padé.

The Floquet code is able to sum up in both ways. Although both methods are used, in practice the latter one is more common because of the quicker convergence of the series. Table 3.3 shows some data produced using the Floquet code with these different summation methods. In this table each column presents

a harmonic generation rate with different options of summation methods (which are described above): $ioptio = 1$ means that Padé summation for summing up over the Sturmian coefficient has been done before having summed over the indices of dipole moment, in the dipole moment expression (3.49) while $ioptio = 2$ means the Padé summation for summing up over the Sturmian coefficients has been done after having summed over the indices of the dipole moment, in the dipole moment expression (3.49). In addition $isumtd = 1, 2$ stands for the items of Padé, defined in 3.2.10, respectively. Note that the incident field used for these results is a linearly polarised laser field with a wavelength $\lambda = 1064$ nm and an intensity I= 10^{13} W/cm^2. It is clear that the results for harmonic generation rates are consistent with each other regardless of summation method or technique.

Table 3.3: HG Rate from the different summation methods for the laser field with wavelength $\lambda = 1064$ nm and intensity $I = 10^{13}$ W/cm^2.

N	$isumtd = 1$ $ioptio = 1$	$isumtd = 1$ $ioptio = 2$	$isumtd = 2$ $ioptio = 1$	$isumtd = 2$ $ioptio = 2$
3	1.4650 (-0)	1.4656 (-0)	1.4656 (-0)	1.4656 (-0)
5	0.6095 (-2)	0.6095 (-2)	0.6095 (-2)	0.6095 (-2)
7	0.2437 (-2)	0.2437 (-2)	0.2437 (-2)	0.2437 (-2)
9	0.6352 (-2)	0.6352 (-2)	0.6352 (-2)	0.6352 (-2)
11	0.1898 (-1)	0.1898 (-1)	0.1898 (-1)	0.1898 (-1)
13	0.1226 (-1)	0.1226 (-1)	0.1226 (-1)	0.1226 (-1)
15	0.2988 (-2)	0.2987 (-2)	0.2988 (-2)	0.2987 (-2)
17	0.5450 (-2)	0.5450 (-2)	0.5450 (-2)	0.5450 (-2)
19	0.1627 (-2)	0.1627 (-2)	0.1627 (-2)	0.1627 (-2)

3.2.11 Convergence with basis set and further technical details for the calculations of dipole moments and harmonic generation rates

One has to check that the results (rate of harmonic generation) from the calculations are stable with respect to changes in the number of angular momenta used, are in the number of radial basis functions, in the number of harmonic components, and to values of κ over the allowed range. The convergence with respect to these parameters has been checked. Some results are given in Table 3.4, where

$\theta = \arg(\kappa)$, in order to see the convergence with respect to the θ parameter and in Table 3.5 in order to see the convergence with respect to the number of angular momenta, radial basis functions for various harmonic components. The tests reported in both tables are for a laser field with an intensity I= 10^{13} W/cm^2 and wavelength $\lambda = 1064$ nm and the ellipticity angle of the incident field is 60^o. Each column of Table 3.5 represents the following basis set: Rate_1: lmin=0, lmax=11, nbf=30, nflh=43, Rate_2: lmin=0, lmax=13, nbf=30, nflh=43, Rate_3: lmin=0, lmax=9, nbf=30, nflh=43, Rate_4: lmin=0, lmax=11, nbf=30, nflh=38, Rate_5: lmin=0, lmax=11, nbf=25, nflh=43 where lmin and lmax are the number of minimum and maximum angular momenta, respectively; nflh is the number the Floquet harmonics and nbf is the number of basis functions used for each test. As a results of such tests it is clear that the rate of harmonic generation is very well converged with respect to all parameters of the basis set: All the results are identical (better than 5 digits agreement) with the variation of the θ-parameter between $\theta = 15$ and $\theta = 25$ (see Table 3.4) and the data in Table 3.5 shows that a basis set that will yield use a set of converged results is lmax=11, nbf=30 and nflh=43 with any value of θ between 15^o and 25^o.

Table 3.4: The convergence of the harmonic generation rate according to $\theta = \arg(\kappa)$ parameter.

	Harmonic Generation Rates (a.u)		
N	$\theta = 15^o$	$\theta = 20^o$	$\theta = 25^o$
3	0.3569 (-00)	0.3569 (-00)	0.3569 (-00)
5	0.3210 (-03)	0.3210 (-03)	0.3210 (-03)
7	0.3286 (-04)	0.3286 (-04)	0.3286 (-04)
9	0.4335 (-04)	0.4335 (-04)	0.4335 (-04)
11	0.5805 (-05)	0.5805 (-05)	0.5805 (-05)
13	0.7204 (-06)	0.7204 (-06)	0.7204 (-06)
15	0.2324 (-06)	0.2324 (-06)	0.2324 (-06)
17	0.6315 (-08)	0.6315 (-08)	0.6315 (-08)
19	0.3382 (-10)	0.3382 (-10)	0.3382 (-10)

It is worth mentioning the memory needed and disk space, and also the computer time needed for such computationally demanding calculations. The code

Table 3.5: The convergence of the harmonic generation rate with the basis set.

Harmonic Generation Rates (a.u.)					
N	Rate_1	Rate_2	Rate_3	Rate_4	Rate_5
3	0.3570 (-0)	0.3570 (-0)	0.3570 (-0)	0.3570 (-0)	0.3570 (-0)
5	0.3200 (-3)	0.3210 (-3)	0.3210 (-3)	0.3210 (-3)	0.3210 (-3)
7	0.3260 (-4)	0.3285 (-4)	0.3284 (-4)	0.3286 (-4)	0.3287 (-4)
9	0.4000 (-4)	0.4330 (-4)	0.4320 (-4)	0.4330 (-4)	0.4330 (-4)
11	0.6280 (-5)	0.5810 (-5)	0.5820 (-5)	0.5810 (-5)	0.5810 (-5)
13	0.6960 (-6)	0.72040 (-6)	0.7200 (-6)	0.7208 (-6)	0.7208 (-6)
15	0.2280 (-6)	0.2324 (-6)	0.2322 (-6)	0.2323 (-6)	0.2323 (-6)
17	0.6220 (-8)	0.6315 (-8)	0.6312 (-8)	0.6340 (-8)	0.6312 (-8)
19	0.3340 (-10)	0.3382 (-10)	3381 (-10)	0.2940 (-10)	0.3380 (-10)

is able to calculate the matrix elements (see Section 2.5) in two ways in terms of memory and disk space usage: The first option requires more memory due to storing all the LU-factorised blocks in core. However, in the second option since the LU-factorised blocks are stored on the disk as a scratch file, smaller memory and larger disk space and longer running time is needed for the calculations. For example for a typical basis set: 11 angular momenta, 43 Floquet harmonics and 30 radial basis functions when the calculations is done with the first option the size of executable file is 1.13 Gb, however, this number reduces to 87 Mb but together with 1.1 Gb scratch disk space used during the calculations when the second option is used. Both these numbers are for an elliptically polarised incoming field. If the code is arranged for the linearly polarised field case there is a considerable reduction in memory and disk space required for the both cases. e.g. for the basis set defined above one obtains the required memory is 15.2 Mb storing the matrices in the core and 4.2 MB writing the matrices to scratch disk space with 500 Mb of disk scratch. The reason for this big difference is that when the field is elliptically polarised more partial waves contribute to the processes; the selection rules and parity considerations demonstrate more m values for a given l are involved in this case (see Section 3.2.7).

The computer time required for one set of calculation is roughly proportional to the number of harmonic components and to the cube of the size of the diagonal

blocks; therefore to the cube of the basis set number. For example for a basis set of 9 angular momenta, 43 Floquet harmonics and 30 radial basis functions the required computing time on a Convex machine is 18000 seconds and for a basis set with the same angular momenta but 20 radial basis functions only 5600 seconds are required on the same machine. The ratio of these two numbers is approximately equal to the ratio of the cubes of ratio of the required basis numbers. It can also be checked taking into account the required number of angular momenta. For example comparing the first basis set with a basis set of 11 angular momenta, 43 Floquet harmonics and 30 radial basis functions, which required 52000 seconds CPU time, again the ratio of the required CPU times is approximately equal to ratio of the cubes of the number of partial waves required (which for the first set is about 30 and for the second one is 42). Moreover, since the basis set required is always smaller for a linearly polarised field the computational time is also smaller compared with the elliptically polarised case.

Note that the technical details of the calculation given above come from a calculation which solves the matrix equation (see Section 2.5) using the LU-routines from reference [80]. It is also possible to do the matrix calculations using lapack and blas library routines instead. Although the size of the executable file and the disk space required do not change for a particular calculation using either the LU-routine from [80] or lapack and blas library routines, the running time of the calculation is faster using the libraries. This is due to the fact that these libraries are better optimised. e.g. with a basis set; 11 angular momenta, 43 Floquet harmonics and radial 30 basis functions 245 seconds CPU time are required for a calculation for a linearly polarised case when one uses LU-decomposition from reference [80] whereas 141 seconds (Note that this test in both case is done keeping the matrix elements in the core and using an IBM RS6000-515 workstation.).

Chapter 4

Results for Harmonic Generation

4.1 Application for linearly polarised field

It is well known that when the incident field is linearly polarised, the harmonics produced are also linearly polarised. In order to check whether our computer codes were correct we first of all calculated the harmonic generation rate for $\xi = 0$ (linearly polarised) and $\xi = 90^o$ (circularly polarised). For $\xi = 90^o$ the results were zero as expected. Also for $\xi = 0$ we obtained that $\eta = 0$ and the results for harmonic generation rate were identical to the results produced by the linear polarisation code. Using these results the behaviour of the harmonics with respect to harmonic order in perturbative and nonperturbative regions was checked in order to see the breakdown of perturbation theory at high intensities. To this end, the intensity of the field was varied from 10^{10} W/cm^2 to 1.4×10^{13} W/cm^2. We saw that perturbation theory yields a behaviour with respect to harmonic order which is reasonable for lower harmonics, but breaks down for high harmonics, and more seriously so at higher intensities. However, with increasing intensity this pattern also breaks down. A set of results for $\lambda = 1064$ nm and I= $10^{12}, 3 \times 10^{12}, 10^{13}, 1.2 \times 10^{13}$ and 1.4×10^{13} W/cm^2 is given in Figure 4.1 in order to demonstrate the breakdown.

Nonperturbative rates for harmonic generation at first decrease rapidly as the harmonic order increases until the order is slightly below N_0, which is the number of photons required for coupling of the $1s$ and $2p$ states for this particular case; they then exhibit a plateau picture; and finally decrease beyond a certain order of harmonic N_{max}, which is the cut-off point (see Figure 4.1). With increasing

intensity the length of the plateau tends to be longer and thus, the cut-off point occurs at higher harmonics. Note that the perturbative results do not exhibit a plateau; they rather peak at an order close to N_0, varying with the intensities [35].

From Figure 4.1 the cut-off occurs at $N_{max} = 11, 13, 15$, for intensities I= $10^{12}, 3 \times 10^{12}$ and 10^{13} W/cm^2, respectively, and for intensities I = 1.2×10^{13} and 1.4×10^{13} W/cm^2 although there is a minimum point in the plateau region, the actual cut-off occurs at $N_{max} = 17$. For comparison the value of N_{max} is calculated using Equation (3.4) and the ionisation potential for hydrogen $I_p = 0.5$ a.u. (field free) and E_b (ac-shifted). These results are given in Table 4.1 using the codes, 1 for the results from the numerical calculation (Figure 4.1), 2 for the results using the simple formula with the field free potential and 3 for the results using the simple formula with the ac shifts taken into account. In addition the corresponding intensities (I), ponderomotive shifts (U_p) and the ac shifted ground state energy are given in the first, second and third columns of the table, respectively.

Table 4.1: Cut-off

I(W/cm^2)	U_p(a.u.)	E_b (a.u.)	N_{max1}	N_{max2}	N_{max3}
1.0×10^{12}	0.389×10^{-2}	0.5037	11	11.9	12.0
3.0×10^{12}	0.117×10^{-1}	0.5116	13	12.5	12.8
1.0×10^{13}	0.389×10^{-1}	0.5389	15	14.4	15.5
1.2×10^{13}	0.467×10^{-1}	0.5467	17	14.9	16.2
1.4×10^{13}	0.544×10^{-1}	0.5546	17	15.5	16.9

Table 4.1 shows that for the lowest intensity the results from the numerical calculation agree with the simple formula using I_p, but for higher intensities the use of the ac shifted energy gives better agreement.

4.2 Application for elliptically polarised field

We have calculated the harmonic generation rate for $\lambda = 1064$ nm, $\lambda = 532$ nm and $\lambda = 354$ nm for some intensities: From very weak to relatively strong fields and for different ellipticity angles of the incident laser. We have investigated

nonperturbative effects in the harmonic generation rate, i.e. in the cut-off point N_{max}; in the ellipticity angle of the harmonics produced versus the variation of the ellipticity angle of the incident field.

4.2.1 Nonperturbative effects in harmonic generation rate with change in ellipticity

In order to see nonperturbative effects in the harmonic generation rate we wish first of all to give results in the perturbative region. Thus, a set of nonperturbative results is exhibited in Figure 4.2 with a set of perturbative results for comparison. Both results are for a wavelength $\lambda = 1064$ nm and an intensity I= 10^{10} W/cm^2. The points in this figure show the nonperturbative results and the lines the perturbative results.

As shown in this figure with increasing ellipticity of the incident laser the harmonic generation rate decreases and for higher harmonics decreases rapidly, which is consistent with the prediction in Equation 3.33 from which follows $R(\xi) \sim (\cos\xi)^{N-1}$, where $R(\xi)$ represents the rate of emmited photons. As we can see from Figure 4.2 the nonperturbative results are in very good agreement with the perturbative results for lower intensities. However, for higher intensities nonperturbative effects are found in the harmonic generation rate with change in ellipticity angle of the incident laser. Results are shown with respect to ellipticity angle of the incident laser for various intensities, but for fixed wavelength, in Tables 4.2 and 4.3 for $\lambda = 1064$ nm and in Table 4.4 for $\lambda = 532$ nm, in order to compare perturbative and nonperturbative results for harmonic generation rates. Note that these results are not the rates themselves but the ratio (in %) of the rate of generation of the Nth harmonic calculated nonperturbatively to the rate obtained from leading order of perturbation theory.

Let us first analyse the rate for $\lambda = 1064$ nm. For this wavelength, an incident intensity I= 10^{12} W/cm^2, is still more or less in the perturbative region, but it is already a high enough intensity that some perturbative effects are to be found in the harmonic generation rate; that is, the nonperturbative rates are rather higher than the perturbative rates. In fact there is a regularity in the change of the ratio with increasing harmonic number for this particular case. As the harmonic

number increases the ratio of the nonperturbative rate to the perturbative one increases for all ellipticity angles. For the 19th harmonic there is up to a factor 40 increase for ellipticity angles $\xi = 0^o, 20^o, 40^o$ and more than 40 for $\xi = 60^o$. However, one should point out that at 11th harmonic there is rather a decrease in the change of the ratio comparing with the 9th harmonic. This is due to this particular harmonic corresponds to the harmonic where the peak occurs at harmonic spectrum with respect to harmonic order (see Figure 4.1). The change at ratio with respect to ellipticity is a decrease with increasing ellipticity of the incident field for the harmonics smaller than 9th harmonic, but it is an increase at the 9th, harmonic where the peak occurs, and also afterwards.

With increasing intensity of the incident field one obtains an increase in the nonperturbative rate with respect to perturbative one both before and after plateau, but not in the plateau region itself. This is due to the breakdown of perturbation theory for higher intensities. For example for intensity of the incident field I= 3×10^{12} W/cm^2, although the plateau is narrow one can still observe this feature. In both regions (before and after the plateau) the ratio increases with increasing harmonic number N. Again before the 9th harmonic (where the plateau starts, N_0) the ratio decreases with increasing ellipticity angle for each harmonic number. However, at N_0 it increases with respect to ellipticity angle, but then the after N_0 there is a decrease at the ratio, and finally again after the plateau an increase is noted due to the decrease at the ratio in the plateau region the value of N_{max} is also decreasing with increasing ellipticity angle. For different intensities of incident field this behaviour is shown in Figure 4.3. In this Figure the ellipticity angle of the incident field is $\xi = 60^o$ and the intensities are I = $10^{12}, 3 \times 10^{12}, 10^{13}, 1.2 \times 10^{13}$ and 1.4×10^{13} W/cm^2. There is still a plateau for the elliptically polarised field. However, attention must be directed to the fact that the length of the plateau is getting shorter, and later the value of N_{max} is getting smaller with increasing ellipticity of the incident laser field (see Figure 4.3).

Going back to Tables 4.2 and 4.3 one should note that at an intensity I= 1.4×10^{13} W/cm^2 for $\lambda = 1064$ nm the change of the ratio with respect to ellipticity angle is still the same for harmonics smaller than 9th but for the 9th, $N = 11$th

and $N = 13$th harmonics the ratio increases with increasing ellipticity angle. This might be due to the fact that for this intensity the real part of the $1s$ Floquet eigenvalue crosses the 13th and 14th photon ionisation threshold (see Figure 3.3) [35].

For wavelength $\lambda = 532$ nm it is clear that for an intensity I= 2×10^{13} W/cm^2 the behaviour of the ratio is same as for $\lambda = 1064$ nm with intensity I=3×10^{12} W/cm^2. But the structure is more complicated at the I= 2.79×10^{13} W/cm^2. That is due to a resonance with the $n = 6$ manifold occurring at this particular intensity.

These results are in qualitative good agreement with experimental results although we cannot make a direct comparison with experiments for the following reasons. The experiments are performed with rare gases whereas our calculations were performed for the hydrogen atom and we are dealing with single atom multiphoton processes. For such comparison a set of results from experimental work together with perturbative results are given in Figure 4.4 for the 3rd, 5th, 7th, 9th and 11th harmonics [57].

In Figure 4.4 the points show experimental results, produced in argon gas with I= 10^{13} W/cm^2 laser intensity; the lines are perturbative results from the simple formula 4.1. (For details about this equation see references: [15], [57] and [73].)

$$I_N = \left[(1-\epsilon^2)/(1+\epsilon^2)\right]^{(N-1)} \tag{4.1}$$

where N is the harmonic number, I_N is the Nth harmonic intensity which is proportional to the harmonic generation rate and ϵ is the ellipticity of the incident field. The relation between the ellipticity angle (ϵ) occuring in this equation and ξ, which represents the ellipticity angle of the incident field for our results, is given by Equation 4.2. Note that this relation comes from the different definition of the polarisation vector (see Equation 3.14 and the references mentioned above).

$$\cos(\xi) = \frac{1-\epsilon^2}{1+\epsilon^2} \tag{4.2}$$

The experimental data show that there is conversion rate which is greater than the perturbative rate for the 3rd and 5th harmonics, but smaller for the harmonics the 7th, 9th and 11th harmonics. This is what we have obtained from

Table 4.2: Ratio (in %) of the rate of generation of the Nth harmonic calculated nonperturbatively to the rate obtained in the leading order of the perturbation theory for different ellipticities and intensities of the incident laser at $\lambda = 1064$ nm.

Harmonic Generation Rates									
ξ(deg)	$N=3$	$N=5$	$N=7$	$N=9$	$N=11$	$N=13$	$N=15$	$N=17$	$N=19$
Wavelength : 1064 nm Intensity : 10^{10} W/cm^2									
0	99.225	95.429	98.713	98.233	101.493	101.808	102.741	104.900	105.884
20	99.210	95.406	98.715	98.191	101.545	101.801	102.778	104.914	105.747
40	99.247	95.426	98.686	98.116	101.717	101.907	102.738	104.932	105.626
60	99.225	95.405	98.661	97.952	101.835	101.892	102.721	104.915	105.563
Wavelength : 1064 nm Intensity : 10^{12} W/cm^2									
0	100.465	103.644	122.928	306.700	134.990	256.835	518.057	1322.411	3733.267
20	100.439	103.485	121.963	315.844	131.420	258.254	524.182	1342.979	3796.268
40	100.383	103.139	119.705	339.893	121.048	261.179	539.927	1392.341	3953.291
60	100.279	102.767	117.147	367.747	107.126	263.023	555.986	1446.556	4128.272

Table 4.3: Same as Table 4.2, but with different intensity of the laser fields as given.

Harmonic Generation Rates									
ξ(deg)	$N=3$	$N=5$	$N=7$	$N=9$	$N=11$	$N=13$	$N=15$	$N=17$	$N=19$
Wavelength : 1064 nm Intensity : 3×10^{12} W/cm^2									
0	103.102	114.830	193.121	68.005	6.500	46.759	128.840	401.575	1344.502
20	103.025	114.328	192.199	73.315	6.397	46.432	128.749	403.394	1354.041
40	102.741	113.026	187.352	82.705	6.032	45.010	127.233	403.774	1368.037
60	102.413	111.549	177.869	83.218	5.451	42.558	123.555	398.891	1368.919
Wavelength : 1064 nm Intensity : 1.4×10^{13} W/cm^2									
0	120.972	241.102	1396.414	89.545	0.223	0.006	0.248	6.658	86.855
20	120.128	233.873	1533.814	97.850	0.253	0.005	0.233	6.544	86.745
40	118.256	218.609	1443.731	108.163	0.273	0.010	0.164	5.859	83.708
60	116.098	199.173	1049.084	65.882	0.195	0.027	0.110	3.989	64.011

Table 4.4: Ratio (in %) of the rate of generation of the Nth harmonic calculated nonperturbatively to the rate obtained in the leading order of perturbation theory for different ellipticities, and intensities of the incident laser at $\lambda = 532$ nm.

Harmonic Generation Rates									
ξ(deg)	$N=3$	$N=5$	$N=7$	$N=9$	$N=11$	$N=13$	$N=15$	$N=17$	$N=19$
Wavelength : 532 nm Intensity : 2×10^{13} W/cm^2									
0	358.041	23.466	64.229	75.320	82.231	88.150	94.620	110.642	172.049
20	347.326	21.230	62.191	74.087	81.566	88.059	94.895	111.509	176.011
40	303.872	15.843	56.556	70.090	78.881	86.456	94.181	112.354	182.610
60	238.129	10.754	50.233	64.996	74.848	83.279	91.857	111.239	186.928
Wavelength : 532 nm Intensity : 2.79×10^{13} W/cm^2									
0	122.520	0.877	32.259	60.909	161.527	423.713	791.584	1423.048	4372.219
20	146.734	1.083	33.755	63.194	157.684	397.957	741.188	1202.135	4051.416
40	294.419	1.736	39.594	69.526	139.080	295.195	543.388	730.956	2609.302
60	688.882	2.953	46.806	50.769	53.090	57.163	57.504	82.735	334.785

our calculations too (as discussed above). For a comparison with experimental results a set of results from our calculations for an intensity of I= 10^{13} W/cm^2 and wavelength $\lambda = 1064$ nm together with results from leading order perturbative calculations are given in Figure 4.5 for harmonics from the 3rd to the 19th and in order to see the change clearly, for the smallest harmonics ($N = 3, 5$) in Figure 4.6; for harmonics with order $N = 7, 9, 11$ in Figure 4.7; and for higher order harmonics $N = 13, 15, 17, 19$ in Figure 4.8. In these figures the points indicate the results from this calculation and the lines results from leading order perturbation theory. The results for $N = 13, 15, 17, 19$ harmonics can be compared with the results from experiments by L'Huillier *et al.*. As they have also pointed out, we see that for high harmonics beyond $N = 17$ (in fact depending on the system) the dependency on ellipticity is practically independent of the harmonic order (see Figures 4.9 and 4.8 and the reference [15]).

Furthermore, one may analyse the harmonic rates produced in the x-direction and y-direction, separately, as Kakehata *et al.* [62] did in analysing the results of their experiments. They measured systematically the ellipticity of the high order harmonics from He, Ne, Ar, and Kr using a 150 fs, 785 nm Ti:sapphire laser, (with maximum focused intensity $\sim 3 \times 10^{15}$ W/cm^2 in vacuum.). They observed an anomalous ellipticity dependence having a maximum at a nonzero ellipticity for the 11th and 13th harmonics from Ne and for the 7th and the 9th harmonics from Ar and Kr. The authors suggest that the anomalous dependence observed is due to the near-resonant multiwave mixing process an even number of linearly polarised photons with a single circularly polarised photon in the neutral atomic gases [62]. The experiment was performed in the high-intensity regime where rare gas atoms could be fully ionised in an incident laser pulse. Thus, He and Ne atoms would be ionised through tunneling in the region of the Keldisyh parameter $\gamma \ll 1$. For He and Ne the corresponding Keldisyh parameter values are $\gamma = 0.38$ and 0.47, respectively, the tunneling regime in both cases. On the other hand, for Ar and Kr atoms $\gamma = 0.90$ and 0.75, respectively. Having the value of Keldisyh parameter so close to the border between the tunneling and multiphoton regimes leads the authors to interpret the observed behaviour in the ellipticity-dependent harmonic generation as a phenomenon of the multiphoton regime.

Although we did not find such type of anomalies, our results support their results if a comparison is made taking into account the proportion of harmonics produced vertically (y-direction) to those produced horizontally (x-direction). Table 4.5 presents this proportion for the ellipticity angle $\xi = 20^o$. The data of this table show that the contribution of the vertical component (y-) is rather higher particularly for the 9th, 11th, 13th harmonics. This supports the Kakehata *et al.*' interpretation. However, the intensity region we are dealing is smaller than used in their experiment. That might be the reason not to obtain the anomalies they obtained.

Table 4.5: The proportion of harmonics produced in the vertical direction to the horizontal direction for a laser field with an intensity I= 10^{13} W/cm^2, and wavelength $\lambda = 1064$ nm and ellipticity $\xi = 20^o$.

	Harmonic Generation rate (a.u.)		
N	rate(x)	rate(y)	rate(y)/rate(x)
3	1.25 (-0)	0.366 (-1)	3.0%
5	4.52 (-3)	0.997 (-4)	2.2%
7	1.52 (-3)	0.378 (-4)	2.5%
9	3.23 (-3)	0.263 (-3)	8.1%
11	6.80 (-3)	0.171 (-2)	25.0%
13	3.50 (-3)	0.721 (-3)	21.0%
15	2.00 (-3)	0.126 (-4)	0.6%
17	2.70 (-4)	0.236 (-5)	0.9%
19	6.16 (-6)	0.947 (-7)	1.5%

4.2.2 Variation of the ionisation rate with respect to ellipticity of the incident field

The variation of total rate of photoionisation versus ellipticity of the incident field has also been considered. However, it has been found that the change with the total photoionisation rate vs ellipticity of the incident field is often small compared to the change in the harmonic generation rate (see table 4.6).

Note that in Table 4.6 the columns (a), (b), (c), (d) represent the ionisation rate for the following fields:

(a) Wavelength : 1064 nm Intensity : 10^{13} W/cm^2

Table 4.6: Total rate of photoionisation, in 1/sec, for different ellipticities, wavelengths and intensities of the incident field. The numbers between brackets indicate the power of 10.

Ionisation Rate (1/sec)				
ξ(deg)	(a)	(b)	(c)	(d)
0	2.976(5)	6.798(6)	2.289(10)	1.154(11)
20	2.157(5)	5.135(6)	1.853(10)	1.459(11)
40	7.336(4)	1.906(6)	1.007(10)	1.784(11)
60	1.355(4)	3.197(5)	3.742(9)	1.271(11)

(b) Wavelength : 1064 nm Intensity : 1.4×10^{13} W/cm^2

(c) Wavelength : 532 nm Intensity : 2.0×10^{13} W/cm^2

(d) Wavelength : 532 nm Intensity : 2.79×10^{13} W/cm^2

4.2.3 Nonperturbative effects in ellipticity and offset angles of the produced harmonics

In this section we aim to show using our nonperturbative approach that when the incident field is elliptically polarised, there is in general an offset angle between the major axis of the incident laser's polarisation ellipse and that of the ellipse for the harmonics generated and also to prove that the ellipticity of each harmonic generated is different from the ellipticity of the incident field.

Thus, the values of the $\hat{\mathbf{x}}$ and $\hat{\mathbf{y}}$ components of the dipole moment were calculated numerically. Equations (3.23), (3.30) and (3.31) or (3.32) were used to calculate the ellipticity (η) and offset angle (θ) of the harmonics as well as the phase (ϕ) as a function of the ellipticity angle of the incident field and the components of the dipole moment. The ellipticity angle and offset angle of the produced harmonics vary with the ellipticity angle of the incident field. The variation of the ellipticity angle as well as the offset angle of the harmonics vs harmonic number is illustrated in Figures 4.10, 4.11, 4.12, 4.13 for the following ellipticity angles of the incident field: $\xi = 0$, 20^o, 40^o, 60^o, for different intensities and wavelengths of the incident field.

It is clear that the variation depends on harmonic number and also on the intensity of the incident field for a fixed wavelength. For lower intensities the variation on ellipticity angle with respect to harmonic number is small and smooth for all harmonics except for the one equal to N_0. For example for $\lambda = 1064$ nm for incident field intensities I= 10^{12} W/cm^2 and I= 3×10^{12} W/cm^2 there is a rapid change (that is an increase for the former intensity and a decrease for the later one) at $N = 9$ in the variation of the ellipticity angle as well as in that of the offset angle with respect to harmonic number. In the previous subsection it was shown that this harmonic corresponds to the peak of the harmonic generation rate the variation with respect to harmonic number due to the ionisation. After this harmonic there is also a sudden change at the 11th harmonic due to the same reason. For higher intensities, where one could observe a plateau in the harmonic generation rate with respect to harmonic number, there is not only one peak, but peaks at the harmonics of this plateau region.

The change in ellipticity angle and offset angle of the harmonics with respect to ellipticity of the incident field is given in Figures 4.14, 4.15 and 4.16 for laser fields with $\lambda = 1064$ nm and the following intensities: 3×10^{12} W/cm^2; 10^{13} W/cm^2 and 1.4×10^{13} W/cm^2, respectively. These Figures show that the change in ellipticity angle and offset angle of the harmonics with respect to ellipticity of the incident field is in general either monotonically increasing or decreasing at lower intensities for all harmonics apart from for N_0 (harmonic where the peak occurs in the harmonic generation rate). In fact the change with respect to the ellipticity angle of incident field is in general, linear. At higher intensities the change in the ellipticity and the offset angle of harmonics vs the ellipticity of the incident field is still linear for harmonics which are not in the plateau region, but in the plateau region there is no linearity with respect to N neither in the ellipticity angle nor in the offset angle of the harmonics with respect to the ellipticity angle of the incident field. A similar set of results from the experimental study by Weihe *et al.* [61]-[60] is given in Figure 4.17. In Figure 4.17 the ϵ is identical to the ϵ defined by Equation 4.2 in subsection 4.2.1. Note that the light source used for these measurements is a Ti:sapphire oscillator-chirped-pulse amplification laser system delivering a 10-Hz train of 785 nm, 1.5 mJ, 200 fs pulses. The laser is

tunable and the light is focused using a 0.2 m focal-length lens. Thus, with a simple calculation using the intensity-power-energy relation per focusing area (in cm^2) the intensity of the field used for this experiment is about 10^{15} W/cm^2. In addition they observed harmonics in both Argon and Nitrogen gases.

Our results for lower intensity fields agree with the results Weihe *et al.* obtained from their experiment: the polarisation of high harmonics generated by intense, short, elliptical polarised laser pulses is rotated with respect to the incident laser polarisation [61]-[60]. However, Weihe *et al.* restricted themselves to relatively small ellipticity angles comparing with ours. They varied the ellipticity angle of the incident field between 0^o and 44^o. This was due to the fact that the efficiency of harmonic generation drops off quickly as a function of incident field ellipticity, so that data cannot be reliably collected for incident field ellipticities beyond 40^o [60]. This difficulty is only experimental, not computational. They obtained a linear change in the ellipticity and offset angle of the harmonics with respect to the ellipticity of the incident field, in agreement with the results we have obtained for low intensity laser fields and also any intensity but for the harmonics which are not in the plateau region. On the other hand, we cannot in general compare our results with the experimental results directly for the following reasons: Experiments involved rare gases, whereas hydrogen was used for our calculations. Also we deal with the single atom response rather than the overall response of nonlinear media, i.e. phase matching has not been taken into account in our calculations. Lewenstein *et al.* [74] in their calculations for single atom response obtained results similar to ours. However, when they took propagation effects into account the nonlinearity of the change in the ellipticity and the offset angle of the harmonics vs the ellipticity angle of the incident field disappeared.

4.3 Conclusions

In this chapter we have reported an investigation of the interaction of the hydrogen atom with an elliptically polarised laser field. The system has been treated nonperturbatively using Floquet-Sturmian method. The conclusions drawn from the results are briefly as follows. Nonperturbative effects were obtained in harmonic generation rates and multiphoton ionisation rates for all ellipticity angles

of the incident laser field, although in the latter case they were small. The non-perturbative effects in harmonic generation rate have been found to increase with increasing intensity of the incident laser and for the higher intensities the effects are greater in the plateau region and beyond. It has also been noticed that the contribution to the harmonic generation rate from the horizontal-direction is in general higher than the contribution from the vertical-direction and this disparity is greatest in the plateau region. The ellipticity angle (η) of the harmonics differ from the ellipticity angle (ξ) of the incident laser and there is an offset angle (θ) between the major axis of the incident laser's polarisation ellipse and that of each harmonic generated. The variation of both (η and θ) with respect to polarisation of the incident laser also depends on the order of the harmonics. The variation is greatest in the plateau region.

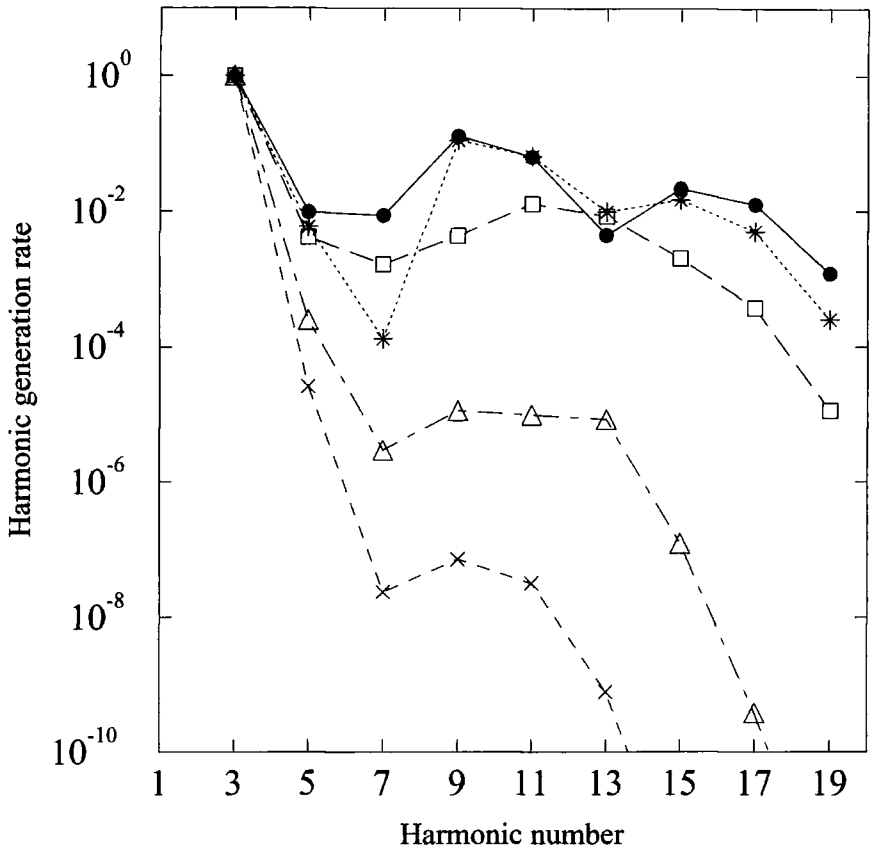

Figure 4.1: Non perturbative results for harmonic generation rate from H(1s) vs harmonic number for different incident fields with a wavelength $\lambda = 1064$ nm and intensities: I= 10^{12} W/cm^2 ($\times$), 3×10^{12} W/cm^2 ($\triangle$), 10^{13} W/cm^2 ($\square$), 1.2×10^{13} W/cm^2 ($*$), and 1.4×10^{13} W/cm^2 ($\bullet$).

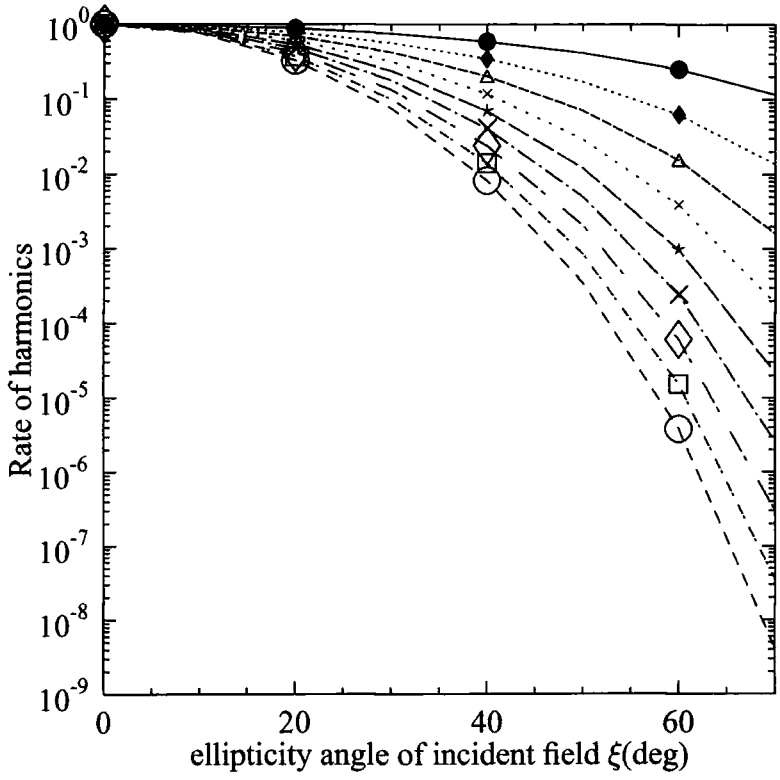

Figure 4.2: Harmonic generation rate from H(1s) vs ellipticity angle of the incident field when the intensity of the incident field is low enough that the rate for HG is in the perturbative limit ($\lambda = 1064$ nm and I= 10^{10} W/cm^2). In this figure the lines are perturbative results; respectively for $N = 3, 5, 7, 9, 11, 13, 15, 17, 19$ starting from the solid line and symbols are nonperturbative results from our calculations; $\bullet : N = 3, \blacklozenge : N = 5, \triangle : N = 7, \times : N = 9, \star : N = 11, big\times : N = 13, \Diamond : N = 15, \square : N = 17, \bigcirc : N = 19$.

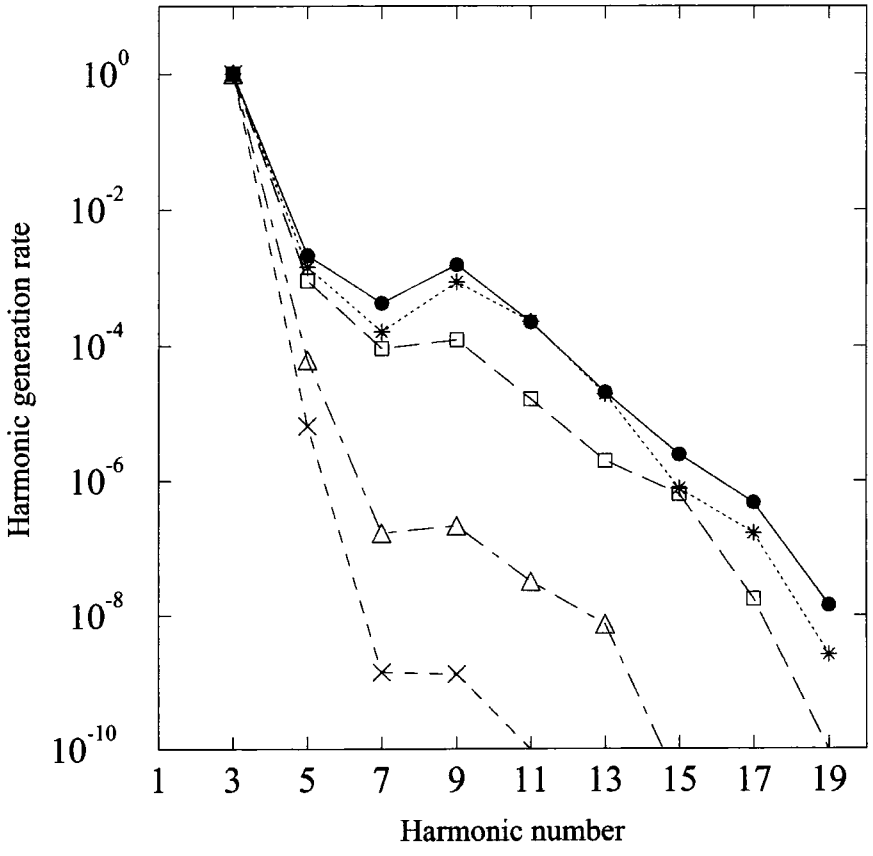

Figure 4.3: Harmonic generation rate from H(1s) vs harmonic number for ellipticity angle of the incident field $\xi = 60^o$, $\lambda = 1064$ nm and intensities I= $10^{12}, 3 \times 10^{12}, 10^{13}, 1.2 \times 10^{13}$ and 1.4×10^{13} W/cm^2. The notation is the same as in Figure 4.1.

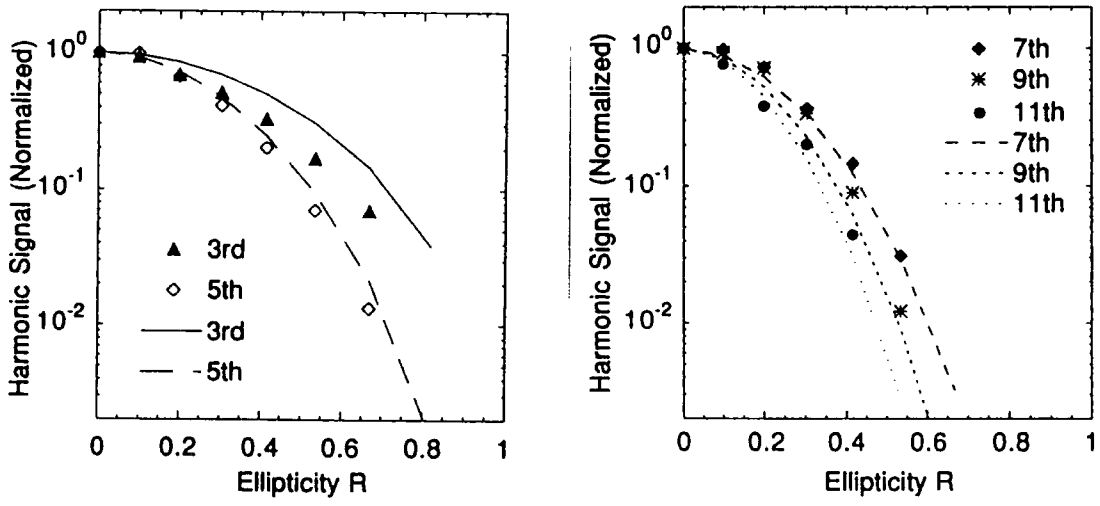

Figure 4.4: The polarisation dependence of harmonic signals in an argon jet. The points represent the experimental data of the 3rd, 5th, 7th, 9th and 11th harmonics. Each datum is the mean of 300 shots with the laser intensity in the range of 10^{13} W/cm^2 and wavelength is 594 nm. The lines are perturbative theoretical results [57].

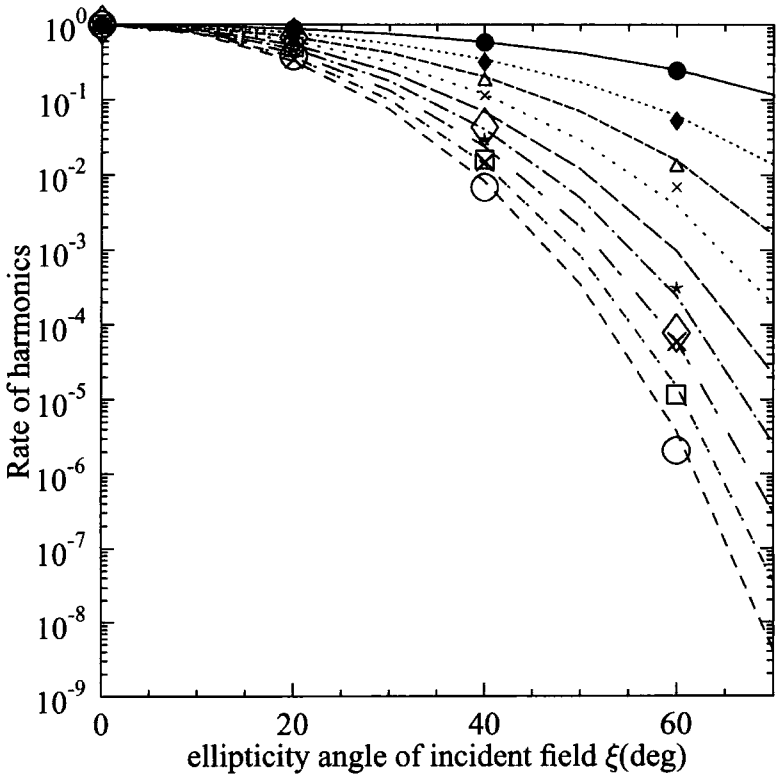

Figure 4.5: Harmonic generation rate with respect to ellipticity angle of the incident field, λ = 1064 nm and I= 10^{13} W/cm^2 for the harmonics with order of $N = 3, 5, 7, 9, 11, 13, 15, 17, 19$th. The points indicate the results from this nonperturbative calculation and the lines from the leading order perturbative calculation. respectively for $N = 3, 5, 7, 9, 11, 13, 15, 17, 19$ starting from the solid line and the symbols are nonperturbative results from our calculations; $\bullet : N = 3, \blacklozenge : N = 5, \triangle : N = 7, \times : N = 9, \star : N = 11$, big $\times : N = 13, \Diamond : N = 15, \square : N = 17, \bigcirc : N = 19$.

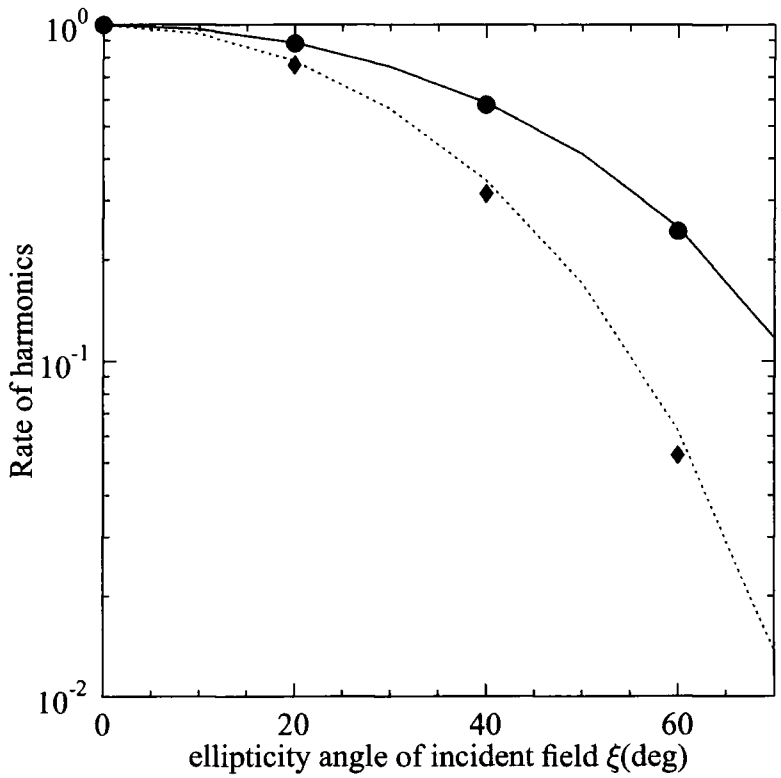

Figure 4.6: Harmonic generation rate with respect to ellipticity angle of the incident field, $\lambda = 1064$ nm and I= 10^{13} W/cm^2. for the harmonics with order of $N = 3, 5$th. The points indicate the results from this nonperturbative calculation: i.e. •: 3rd harmonic and ♦: 5th harmonic ; the lines from the leading order perturbative calculation.

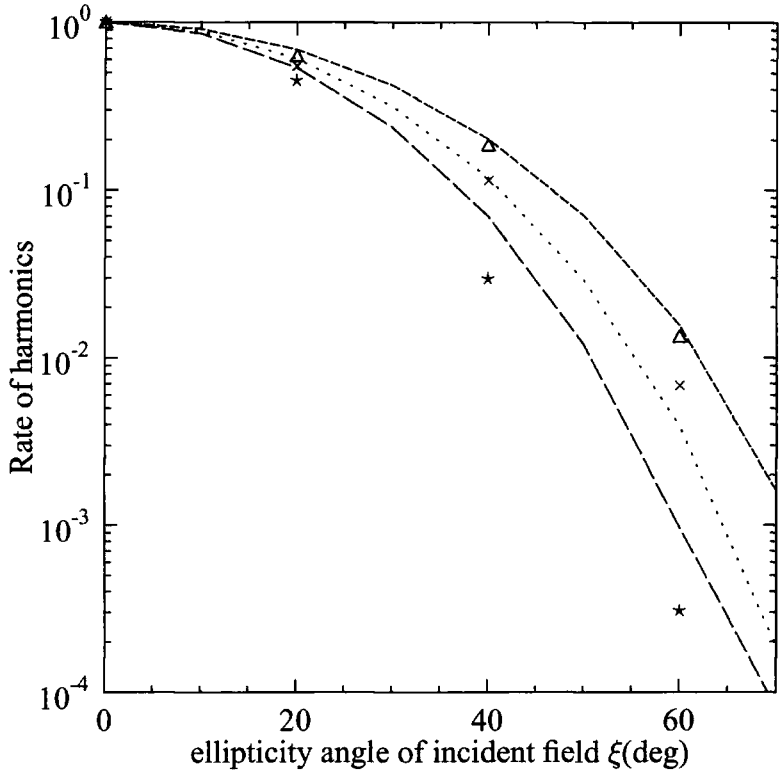

Figure 4.7: Harmonic generation rate with respect to ellipticity angle of the incident field, $\lambda = 1064$ nm and I= 10^{13} W/cm^2 for the harmonics with order of $N = 7, 9, 11$th. The points indicate the results from this nonperturbative calculation, respectively, $\triangle : N = 7, \times : N = 9, \star : N = 11$ and the lines from the leading order perturbative calculation.

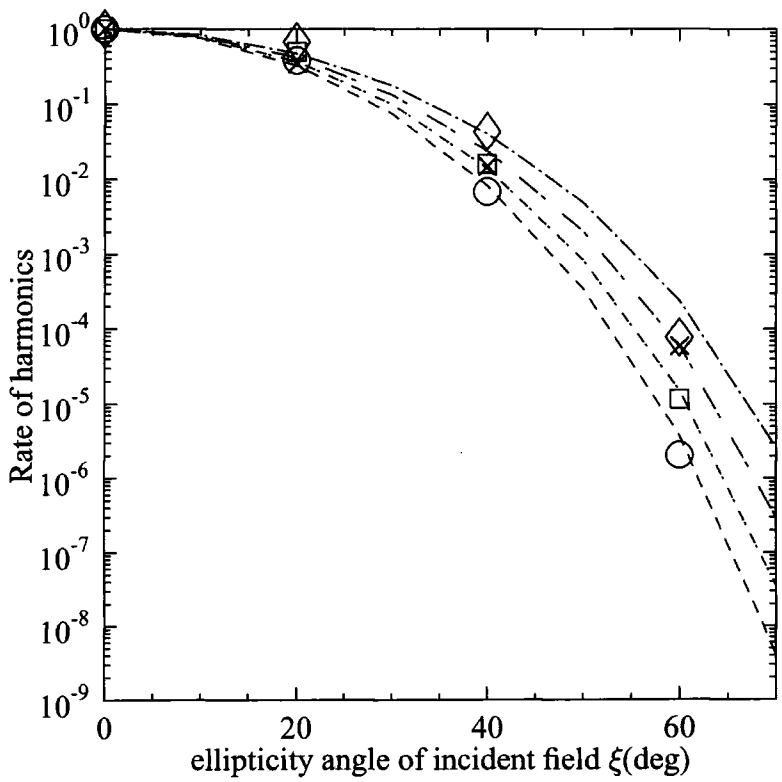

Figure 4.8: Harmonic generation rate with respect to ellipticity angle of the incident field, $\lambda = 1064$ nm and I= 10^{13} W/cm^2 for the harmonics with order of $N = 13, 15, 17, 19$th. The points indicate the results from this nonperturbative calculation, respectively, big $\times : N = 13, \Diamond : N = 15, \Box : N = 17, \bigcirc : N = 19$ and the lines from the leading order perturbative calculation.

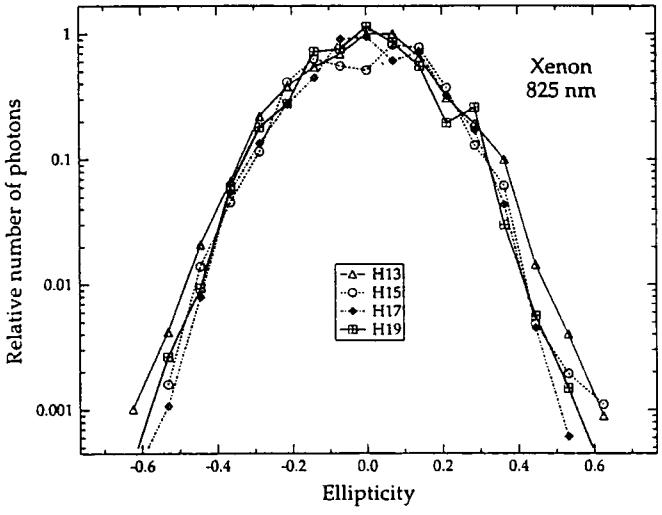

Figure 4.9: Harmonic produced in Xenon with the Cr:LiSAF laser system as a function of ellipticity, normalised to 3.5×10^9 photons at the 13th harmonic, 2.2×10^9 photons at the 15th harmonic, 5×10^8 photons at the 17th harmonic, 3.5×10^7 photons at the 19th harmonic. The laser intensity is 1.2×10^{13} W/cm^2 [15].

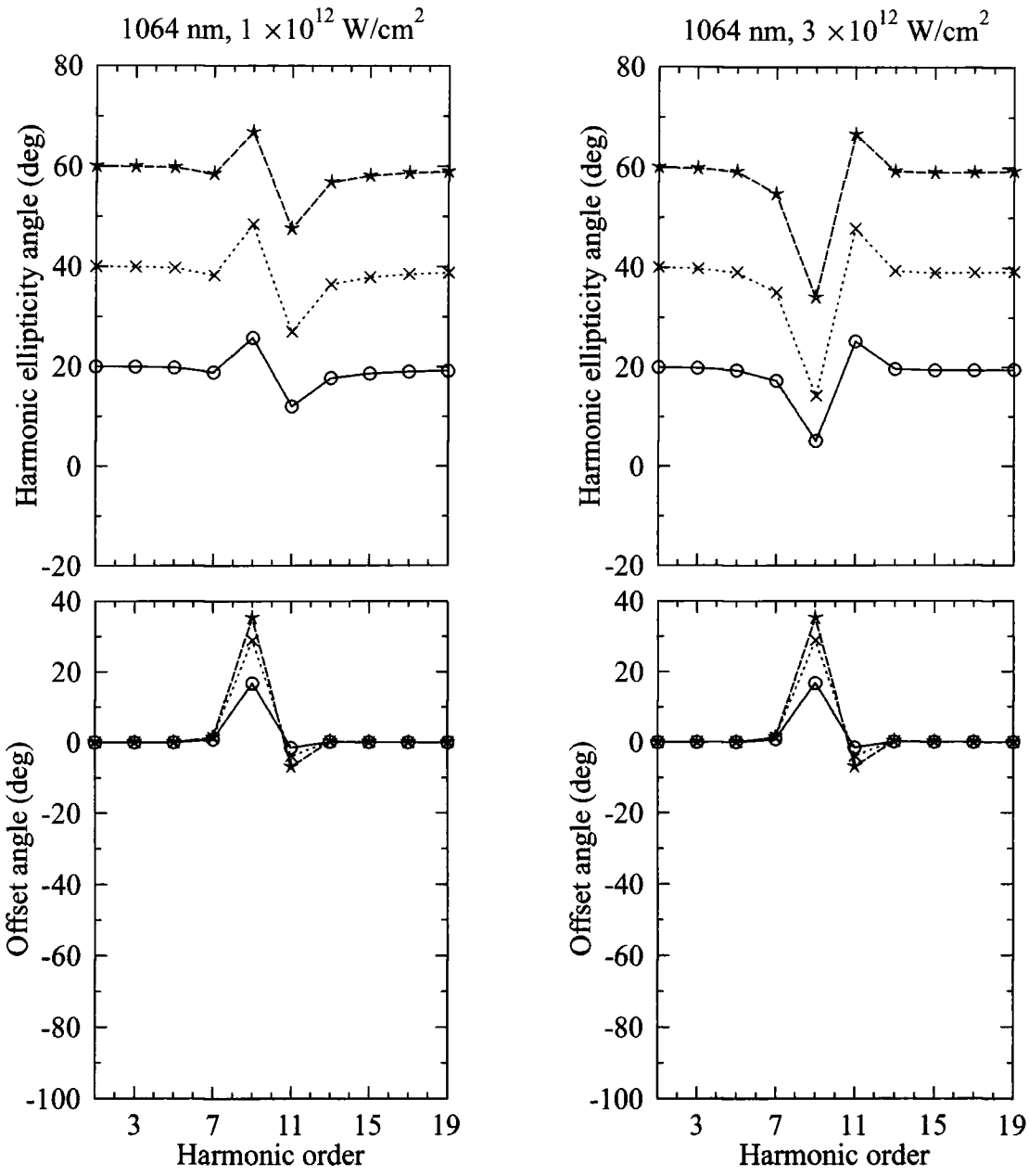

Figure 4.10: The ellipticity angle (η) and offset angle (θ) of the harmonics vs harmonic number for (a) intensity I= 10^{12} W/cm^2 and wavelength $\lambda = 1064$ nm, (b) intensity I= 3×10^{12} W/cm^2 and wavelength $\lambda = 1064$ nm

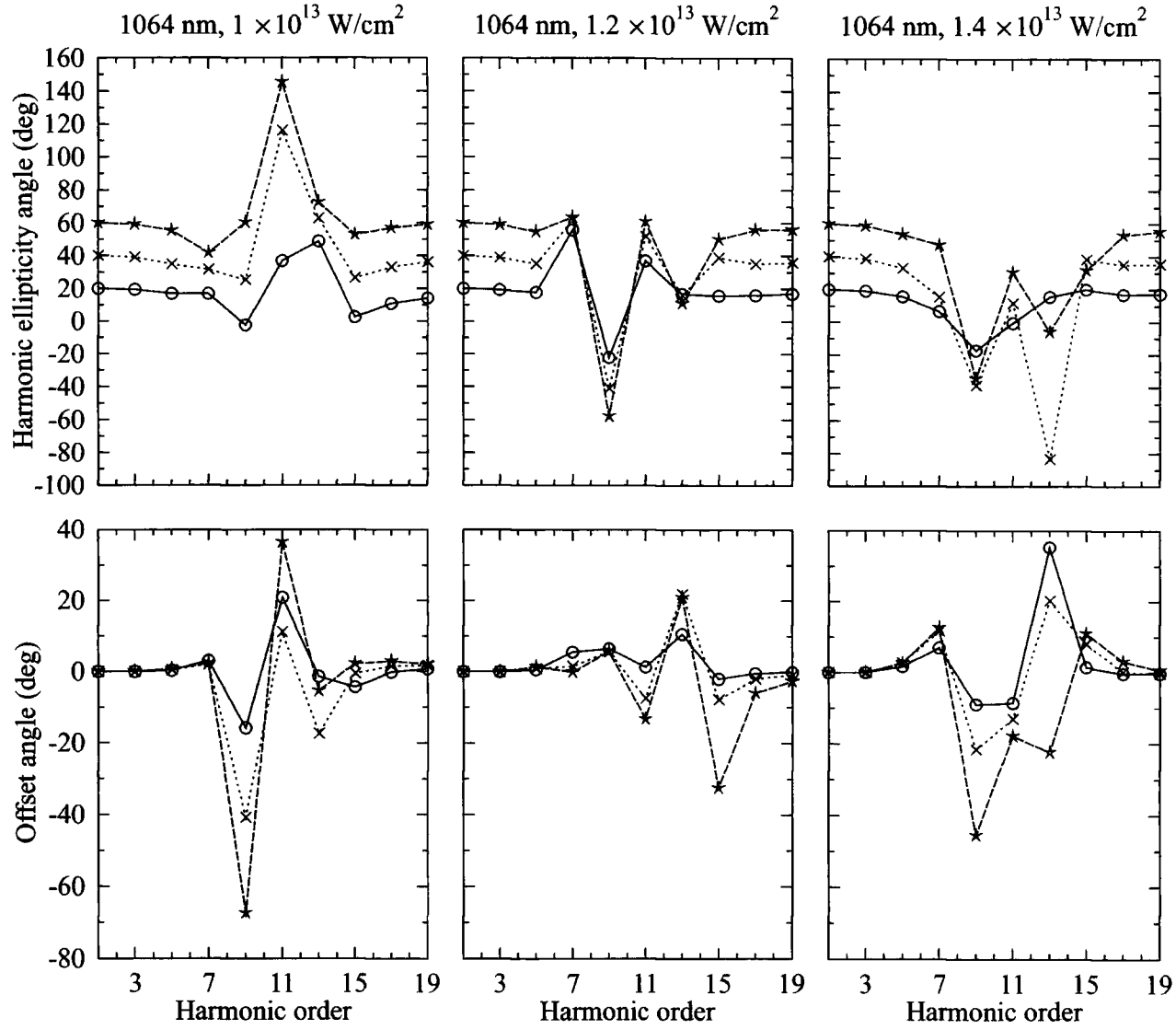

Figure 4.11: Same as Figure 4.10 but for different intensities of the incident field.

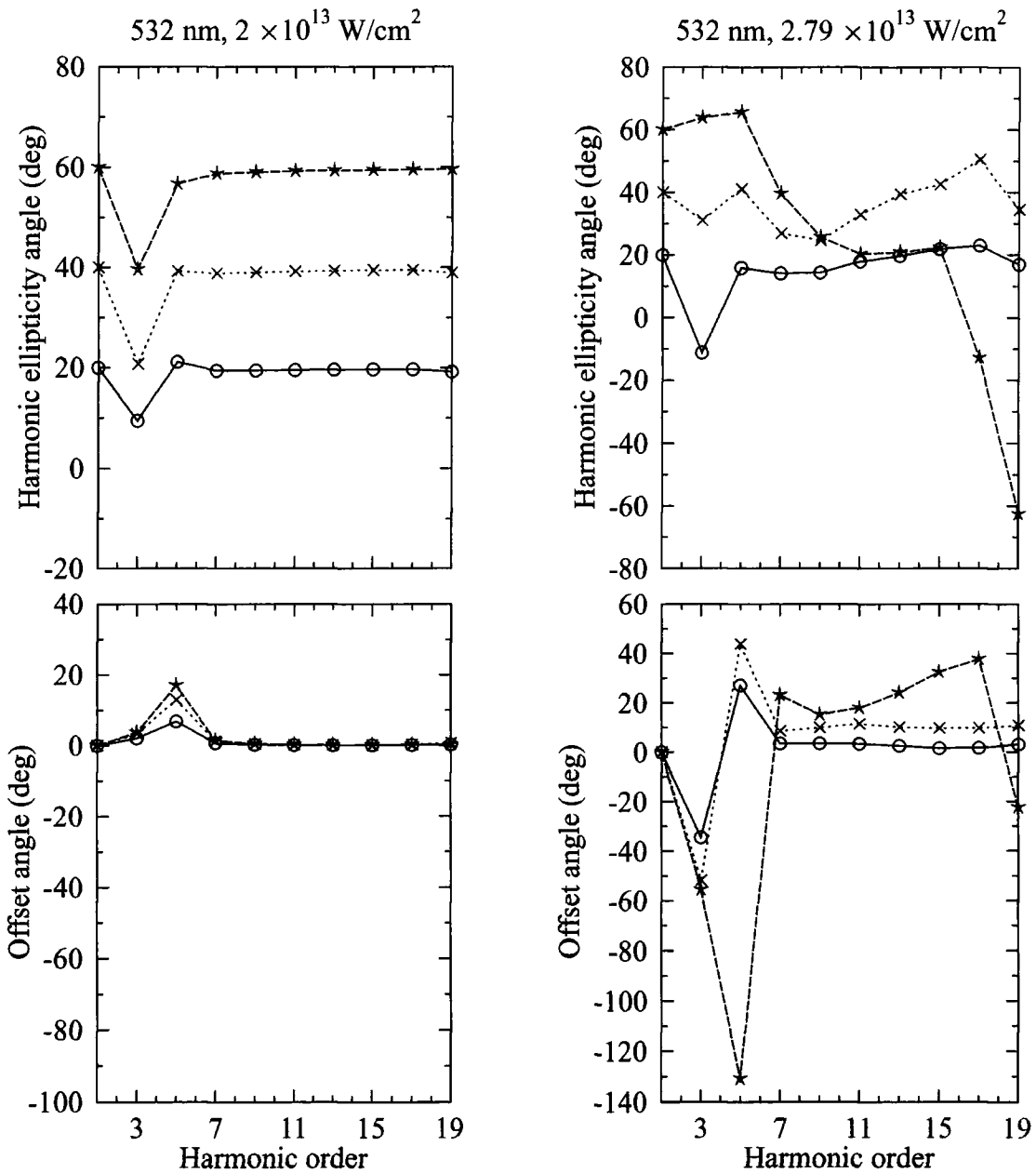

Figure 4.12: The ellipticity angle (η) and offset angle (θ) of the harmonics vs harmonic number for (a) intensity I= 2×10^{13} W/cm^2 and wavelength $\lambda = 532$ nm, (b) intensity I= 2.79×10^{13} W/cm^2 and wavelength $\lambda = 532$ nm

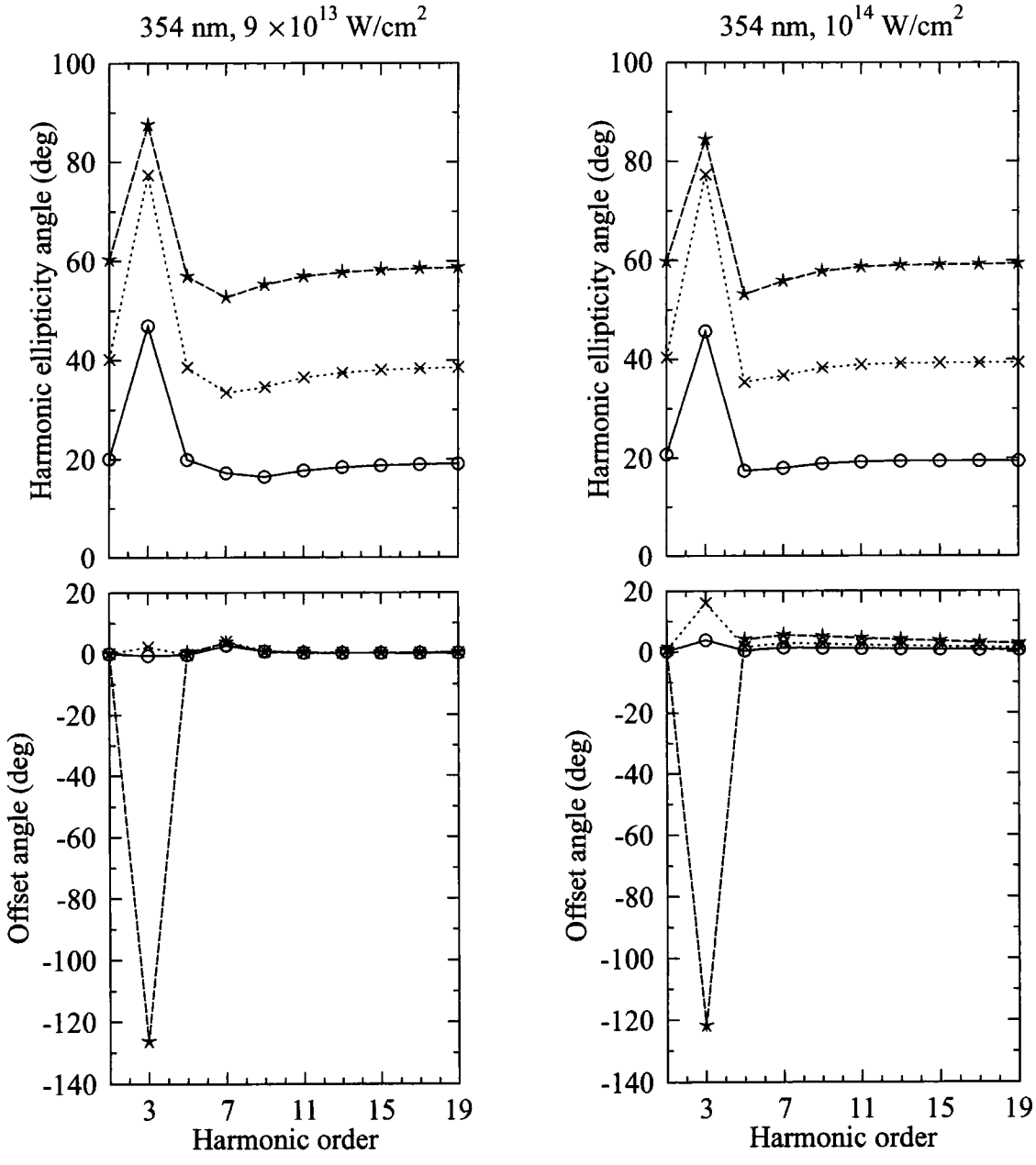

Figure 4.13: The ellipticity angle (η), offset angle (θ) of the harmonics vs harmonic number for (a) intensity I= 9×10^{13} W/cm^2 and wavelength $\lambda = 354$ nm, (b) intensity I= 10^{14} W/cm^2 and wavelength $\lambda = 354$ nm

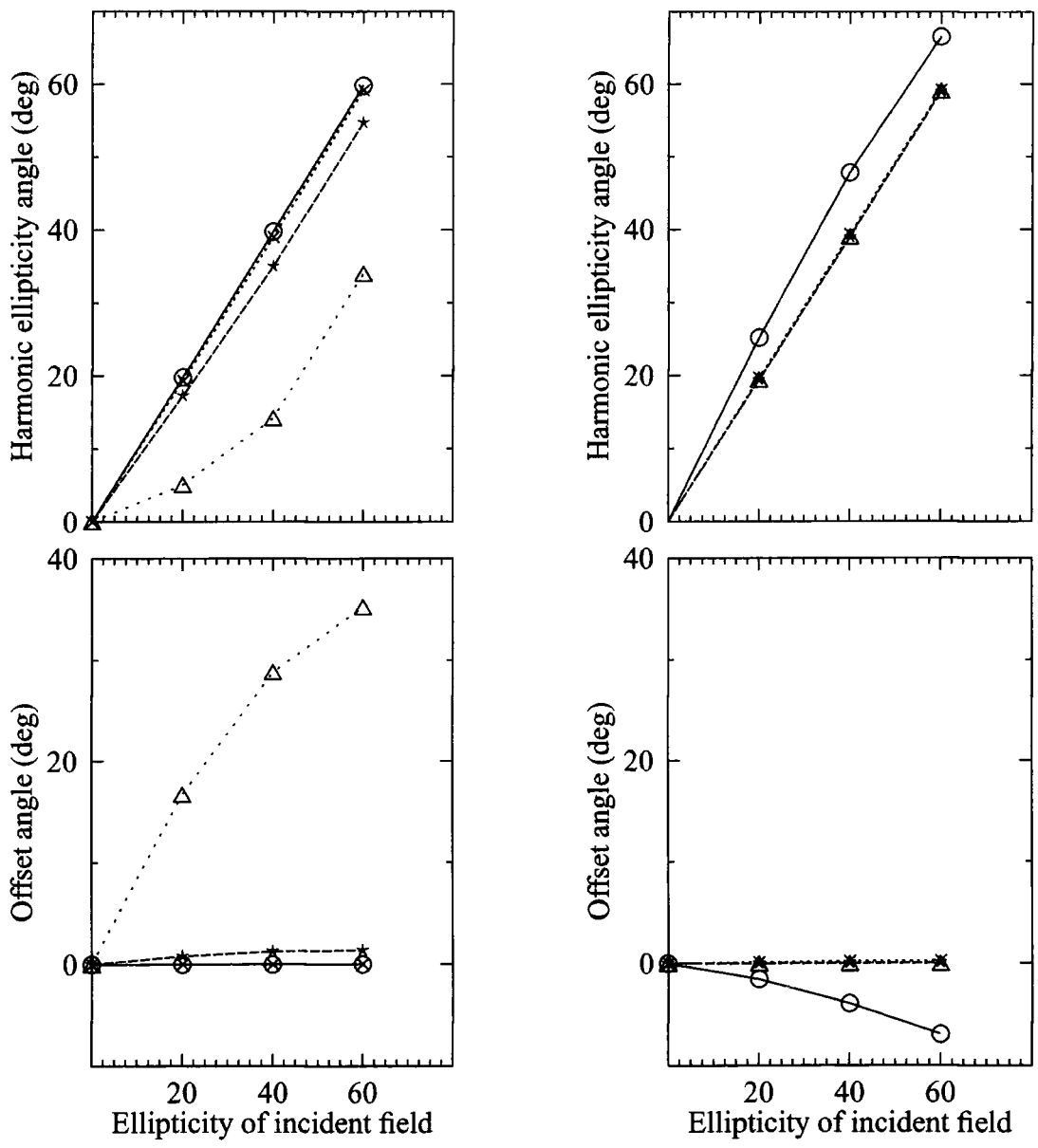

Figure 4.14: Ellipticity angle of the harmonics generated vs ellipticity angle of the incident field, $\lambda = 1064$ nm and I$= 3 \times 10^{12}$ W/cm^2 for harmonics of order $N = 3, 5, 7, 9, 11, 13, 15, 17$th.

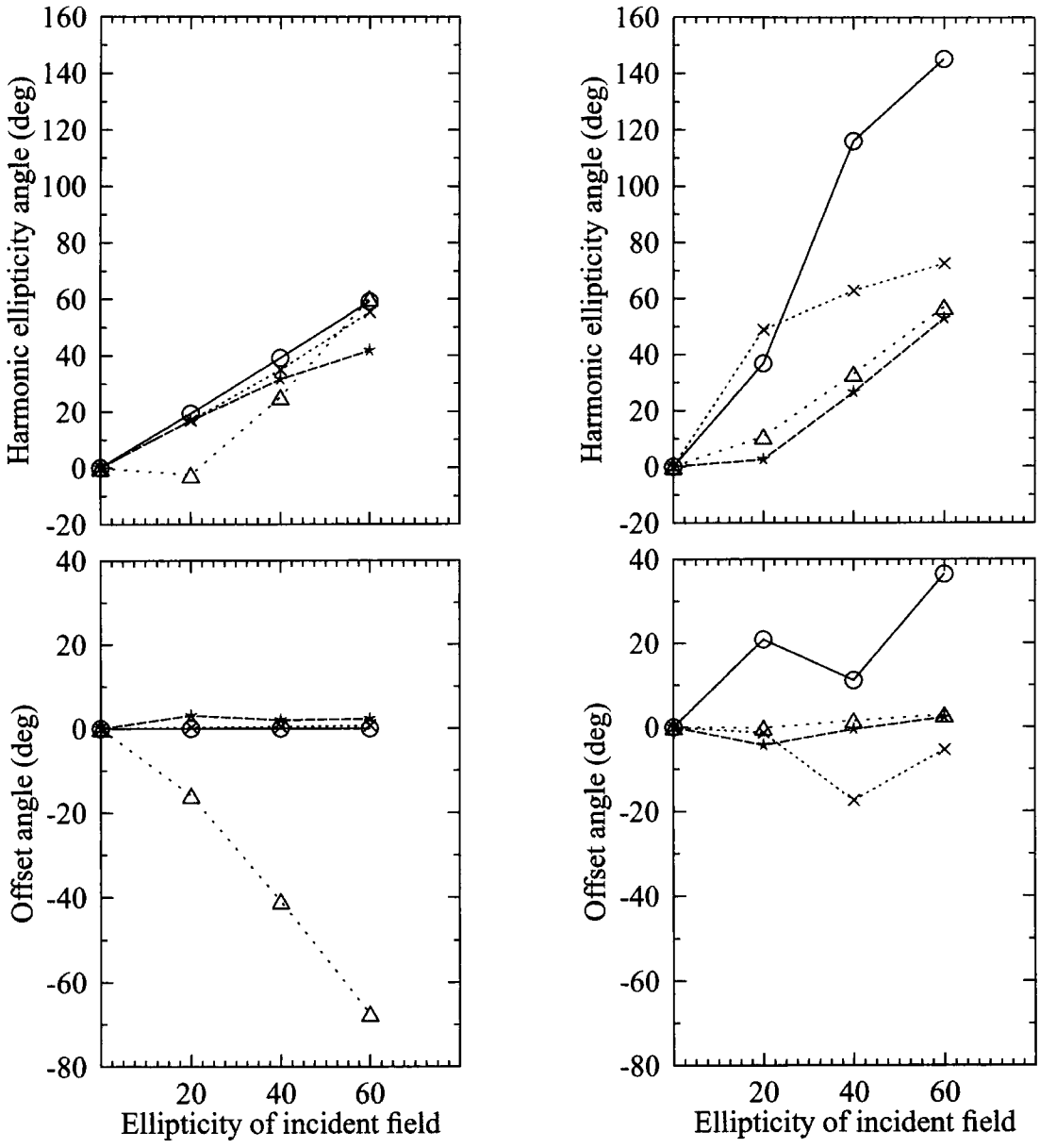

Figure 4.15: Ellipticity angle of the harmonics generated vs ellipticity angle of the incident field, $\lambda = 1064$ nm and I= 10^{13} W/cm^2 for harmonics of order $N = 3, 5, 7, 9, 11, 13, 15, 17$th.

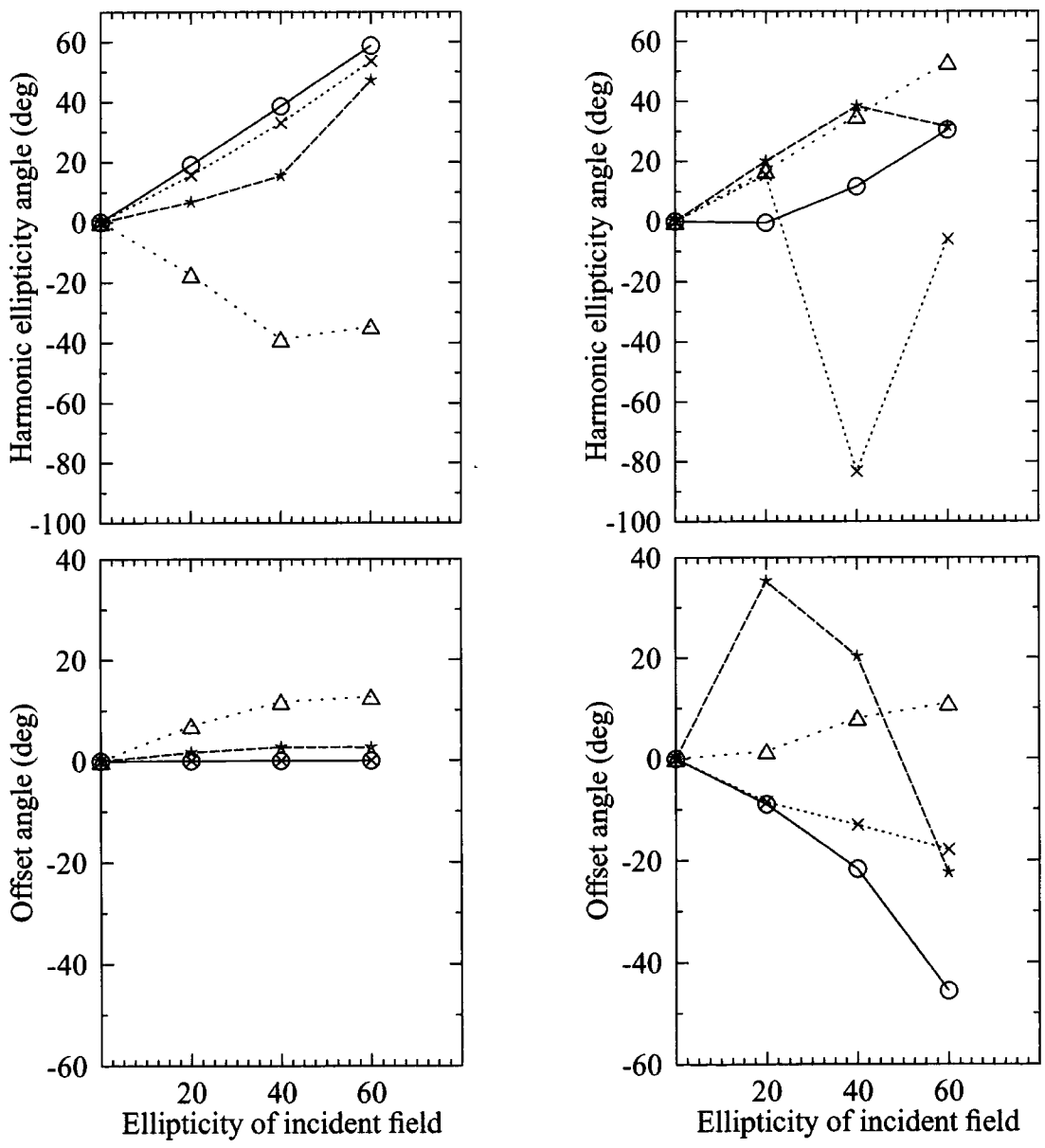

Figure 4.16: Ellipticity angle of the harmonics generated vs ellipticity angle of the incident field, $\lambda = 1064$ nm and I= 1.4×10^{13} W/cm^2 for harmonics of order $N = 3, 5, 7, 9, 11, 13, 15, 17$th.

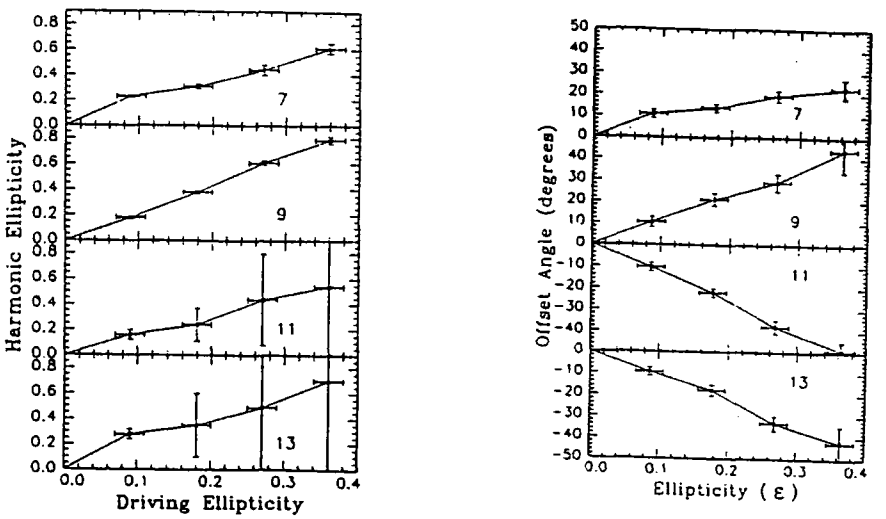

Figure 4.17: (a)Ellipticity and (b) Offset angle of the harmonics generated vs ellipticity angle of the incident field, λ = 785 nm and I$\sim$ 10^{15} W/cm^2, for the harmonics seventh through the thirteenth in Argon [61].

Chapter 5

Two Colour Processes

5.1 General description and overview

Studies of high-order multiphoton processes have been limited mainly to monochromatic laser fields, especially the studies of harmonic generation (HG) processes in strong fields. However, atomic and molecular multiphoton processes in two strong laser fields with different frequencies has recently received attention from the experimentalists [81] and theoreticians [82]- [84]. In this chapter a special case of two colour harmonic generation is considered; the emitted photons are odd multiple of the fundamental of the first field, the high intensity field. The second field, of lower intensity, acts as a perturbation and some number of photons from this field are absorbed and emitted during the HG process. This is illustrated in Figure 5.1 (b). We will also study two-colour multiphoton ionisation, as shown schematically in Figure 5.1 (a). Note that these are only the first order processes which contribute to the ionisation and harmonic generation process but they are not the only ones: there are many other orders of processes which contribute to the ionisation and the harmonic generation phenomena.

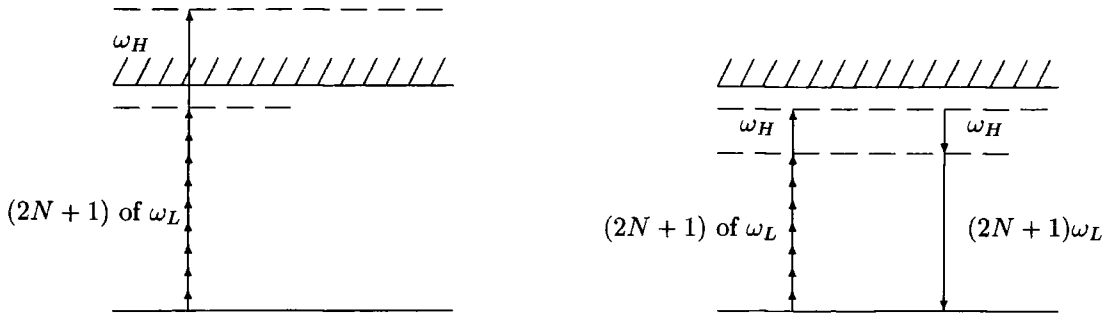

(a) Two colour ionisation

(b) Two colour harmonic generation

Figure 5.1:

The study of two colour processes has shown that having a second field has a relatively big influence on the harmonic generation rate, the total ionisation rate, the electron energy and the angular distribution during the ionisation process. This influence also depends on whether the frequencies of the two fields are commensurable, that is, frequencies whose ratio can be expressed as $p/q = r$ where p, q and r are integers. However, whether commensurable or not, the investigations have shown that several effects occur due to the second colour.

In the case of two colour processes with commensurable frequencies the total ionisation rate, the electron energy and the angular distribution depend strongly on the relative intensity and phases of the two fields [83]. The reason for this dependency is the interference between the two fields [83]-[84].

Two colour interference affects harmonic production, as observed by experimentalists [92] and also described by theoreticians [87]. Both the theoreticians and the experimentalists used a strong laser field and its third harmonic in their studies. So far not many Floquet calculations considering incommensurable frequencies have been carried out apart from the following studies: Chu *et al.* [86] studied the non-linear multiphoton excitation dynamics of two-level systems under the influence of two strong linearly polarised fields for the first time using semiclassical many-mode Floquet theory. Dörr *et al.* [88] investigated the ionisation rate of atomic hydrogen in its ground state in the presence of a relatively weak high frequency field and a relatively strong low frequency field. They also formulated the problem within the Floquet frame-work by making a double-Fourier-series expansion in both frequencies. The method was applied to the following three processes: Resonance-enhanced ionisation, via levels that are Stark mixed and substantially

shifted relative to the ground state by an infrared laser field; Laser modification of the continuum, including population trapping; Nonresonant one-photon ionisation, in a regime where, despite the fact that the infrared field significantly shifts the spectrum to the continuum, it only distributes the photoelectrons over the low frequency channels. The calculations were carried out for a realistic configuration of laser pulses, and it was found that the choice of the pulse configuration can have a significant effect on the profile of the ionisation rate.

van der Hart [89] extended the R-matrix Floquet approach to treat multiphoton processes involving two incommensurate laser frequencies. The approach is illustrated with an example of light-induced continuum structure in He, linking the $1s^2$ ground state with the 1s2s state.

In this study we will use the method of Dörr *et al.* [88] in order to investigate the following processes:

- Harmonic generation rate for a low frequency ($\lambda = 532$ nm), high intensity field and a high variable frequency, low intensity field;
- Rate of harmonic generation and multiphoton ionisation for an infrared field with $\lambda = 1064$ nm and a second field for various wavelengths (including a wavelength which is in the infrared region but has a slightly different value of wavelength companed to that of the first field) and variable intensity;
- Resonance-enhanced ionisation for a low frequency ($\lambda = 532$ nm), high intensity field and a low intensity field with variable high frequency.

The following sections include the formulation of Floquet theory for a two colour process, transition rules in the dipole approximation and the application of the theory to a hydrogen atom when it is in a two colour field. Note that theory is set out for incommensurable frequency fields incommensurable and the application will perform using incommensurate lasers parameters.

5.2 Generalising Floquet techniques for two colour processes

The time dependent Schrödinger equation for an atomic system in a laser field is

$$i\hbar\frac{d}{dt}\,|\Psi(t)\rangle \;=\; [H_a + V(t)]\,|\Psi(t)\rangle \tag{5.1}$$

where $H_a \;=\; \mathbf{p}^2/2\mu \;-\; e^2/r$ is the Hamiltonian of field-free atomic hydrogen and $V(t)$ is the interaction of the atom with the radiation field. In the velocity gauge the interaction potential is equal to $(-e/\mu c)\mathbf{A}(t)\,\cdot\,\mathbf{p}$, where e, μ and $\mathbf{p}$ are the charge, the reduced mass, and the canonical momentum of the electron in the centre of mass frame respectively, and $\mathbf{A}(t)$ is the classical vector potential of the field in the dipole approximation. The expression for the vector potential is :

$$\mathbf{A}(t) \;=\; \mathrm{Re}\,(\mathbf{A}_{0H}\,e^{-i\omega_H t}) \;+\; \mathrm{Re}\,(\mathbf{A}_{0L}\,e^{-i\omega_L t}) \tag{5.2}$$

where ω_L and ω_H are the incommensurable high and low frequencies. As a consequence of Equation (5.2) the interaction potential is given by

$$V(t) \;=\; V_{H+}\,e^{-i\omega_H t} \;+\; V_{H-}\,e^{i\omega_H t} \;+\; V_{L+}\,e^{-i\omega_L t} \;+\; V_{L-}\,e^{i\omega_L t} \tag{5.3}$$

where

$$V_{H+} \;=\; (-e/2\mu c)\,\mathbf{A}_{0H}\,\cdot\mathbf{p} \tag{5.4}$$

and

$$V_{L+} \;=\; (-e/2\mu c)\,\mathbf{A}_{0L}\,\cdot\mathbf{p} \tag{5.5}$$

with $V_{H-} \;=\; V_{H+}^{\dagger}$ and $V_{L-} \;=\; V_{L+}^{\dagger}$. A particular solution of Equation (5.1) has the form

$$|\Psi(t)\rangle \;=\; e^{-iE_i t/\hbar}\sum_m\sum_n e^{-i(m\omega_H + n\omega_L)t}\,|\psi_{i,m,n}\rangle \tag{5.6}$$

where the subscript i denotes the initial bound state. Substitution of this expression into the time-dependent Schrödinger Equation (5.1) will give a set of time-independent coupled equations for the harmonic components $|\psi_{i,m,n}\rangle$:

$$\begin{aligned}(E_i \;+\; m\,\hbar\omega_H \;+\; n\,\hbar\omega_L \;-\; H_a)\,|\psi_{i,m,n}\rangle \;&=\; V_{H+}\,|\,\psi_{i,m-1,n}\rangle \\ &+\; V_{H-}\,|\psi_{i,m+1,n}\rangle \;+\; V_{L+}\,|\psi_{i,m,n-1}\rangle \;+\; V_{L-}\,|\psi_{i,m,n+1}\rangle.\end{aligned} \tag{5.7}$$

The necessary physical boundary conditions on the harmonic components in position space require the harmonic components to be regular at $r = 0$ and to behave as a superposition of outgoing waves as $r \to \infty$:

$$\langle \mathbf{x}|\psi_{i,m,n}\rangle = \sum_{m'} \sum_{n'} f_{m'n'mn}(\hat{\mathbf{x}}, E_i) r^{i\nu_{m'n'}} e^{ik_{m'n'}(E_i)r}/r \tag{5.8}$$

where $\hat{\mathbf{x}} = \mathbf{x}/r$, and where the wavenumber $k_{m'n'}$ of the (m,n)th channel is defined as

$$k_{mn}(E) = \left[(2\mu/\hbar^2)\left(E + m\hbar\omega_H + n\hbar\omega_L\right)\right]^{1/2}. \tag{5.9}$$

The harmonic component $|\psi_{i,m,n}\rangle$, with photon indices m and n, represent the absorption of m high frequency and n low frequency real or virtual photons; $f_{m'n'mn}(\hat{\mathbf{x}}, E_i)$ is the amplitude for absorbing m' high frequency and n' low frequency real photons in the channel m, n. Equation (5.7), together with the boundary conditions (5.8), is an eigenvalue problem with E_i a complex quasi-energy eigenvalue. In order to solve this equation each harmonic component is expanded in position space on a basis of complex Sturmian functions and spherical harmonics. The quasi-energy E_i is expressed as $E_i = E_i^0 + \Delta_i - i\Gamma/2$, where E_i^0 is the field free atomic energy, Δ_i is the shift and Γ_i is the width of this level and their values are calculated by the method of inverse iteration as in the case of one colour processes. The shift Δ_i includes a contribution $-P_L$, where $P_L = (e^2/4\mu c^2)\,|\mathbf{A}_{0L}|^2$ is the ponderomotive energy due to the low frequency field.

The interaction potential 5.3 does not include the quadratic term of the vector potential which has been removed by a gauge transformation. Hence the continuum threshold does not shift.

Note that the total ionisation rate, integrated over all directions of the emergent photoelectron, and summed over all channels, is $\Gamma_i/\hbar$. In fact $\Gamma_i/\hbar$ is the instantaneous ionisation rate averaged over a long time interval. It is important that this averaging should be performed over the longest important beat period in the problem. The period of the cycle of beat frequency $q\omega_H - p\omega_L$, due to the absorption of q high frequency photons and the emission of p low frequency photons, is $2\pi/(q\omega_H - p\omega_L)$ and the longest important beat period is the one associated with the smallest important non-zero beat frequency. Although ω_H and ω_L are incommensurable there are always sufficiently large integers p and q for which the

beat frequency $q\omega_H - p\omega_L$ is relatively small; however, the absorption of q high frequency photons and emission of p low frequency photons is not probable if p or q are very large, and so very small beat frequencies are irrelevant. On the other hand, if $\Gamma_i/\hbar$ is comparable to the smallest relevant beat frequency, the atom completely ionises in a time that is less than the longest important cycle, $\Gamma_i/\hbar$ cannot be interpreted as a cycle-averaged ionisation rate, and the lifetime of the atom must depend on the relative phase of the two fields. A cycle-averaged rate cannot depend on this relative phase. The eigenvalue E_i is also independent of the phase of either field when the frequencies are incommensurable. The following test makes this clear: First of all replace $\mathrm{Re}\,(\mathbf{A}_{0H}\, e^{-i\omega_H t})$ by $\mathrm{Re}\,(\mathbf{A}_{0H}\, e^{-i\omega_H t - i\phi_H})$. The effect of this is a change in Equation (5.7), which will bring an extra term $e^{\mp i\phi_H}$ to the $V_{H,\pm}$. However, transformation of $|\psi_{i,m,n}\rangle$ to $|\psi'_{i,m,n}\rangle = e^{im\phi_H}|\psi_{i,m,n}\rangle$ removes the presence of ϕ_H and the transformed set of equations is identical to the original one; therefore, E_i is independent of ϕ_H [88].

5.3 Calculating the rate for harmonic generation and the dipole moment

The rate for generating photons with frequency $\Omega = N\omega$ is calculated using Equation (3.13) but the dipole moment for two colour processes is calculated from Equation (5.10) using the two colour Floquet techniques.

$$\mathbf{d}_N = \sum_{n,m} \langle \psi_{n-N,m} | e\mathbf{x} | \psi_{n,m} \rangle \tag{5.10}$$

In this equation the harmonic component $|\psi_{n,m}\rangle$, with photon indices n and m, represents the absorption of m high-frequency and n low-frequency real or virtual photons; and N is the harmonic order.

5.4 Selection rules

Before starting application of the theory it is worth mentioning the transition rules so that it will be easy to explain the possible transitions during the processes. Consider both laser fields to be linearly polarised in the same direction and their frequencies to be incommensurable. For a one photon transition, as

a consequence of the Wigner-Eckart theorem and parity considerations, in the dipole approximation the following selection rules have to be satisfied:

$$\Delta l = l_f - l_i = \pm 1 \tag{5.11}$$

$$\Delta m = m_f - m_i = 0 \tag{5.12}$$

For two photon transitions this implies for each photon: $\Delta l_1 = \pm 1, \Delta l_2 = \pm 1$. The total orbital angular momentum $\Delta l_T = \Delta l_1 + \Delta l_2$ so for $\Delta l_1 = 1$ and $\Delta l_2 = 1$; $\Delta l_T = 2$, for $\Delta l_1 = 1$ and $\Delta l_2 = -1$; $\Delta l_T = 0$, for $\Delta l_1 = -1$ and $\Delta l_2 = 1$; $\Delta l_T = 0$ and for $\Delta l_1 = -1$ and $\Delta l_2 = -1$; $\Delta l_T = -2$. Thus, two photon transitions are restricted to

$$\Delta l^{(2)} = 0, \pm 2 \tag{5.13}$$

where the upper indices shows the number of photons involved in the transition. It follows that the three photon transition rule is: Each value of $\Delta l^{(2)}$ should be added to the allowed change in angular momentum caused by emission and absorbtion of the third photon, which is $\Delta l_3 = \pm 1$. Thus the rule for three-photon transitions is :

$$\Delta l^{(3)} = \pm 1, \pm 3 \tag{5.14}$$

and for 4-photon transitions $\Delta l^{(4)} = 0, \pm 2, \pm 4$ and so on.

5.5 Applications and results

For these applications we assumed both laser fields are linearly polarised along the same direction. Otherwise the computations would be far more demanding, owing to the additional coupling between partial waves with different magnetic quantum numbers. The code which has been used for this calculation is based on Floquet theory as described above and the wave function has been calculated in the velocity gauge. The dipole moment is calculated in three different ways using the velocity, length and acceleration forms as described in Section 3.2.9. The results presented in this section are in general calculated using the velocity form. In order to show the consistency of the results from different forms of dipole moment a set of results from the three forms will be given in a table in

the subsection 5.5.4. In addition one should point out that it is easier to obtain convergence in velocity and acceleration forms of the dipole moment rather than in the length form.

5.5.1 Resonance-enhanced ionisation for a low frequency (λ = 532 nm), high intensity field and a high frequency, low intensity field

In this section the ionisation rate is computed for the hydrogen atom in the two colour field described in section 5.5.3. Calculations were performed for the following low frequency fields

- $\lambda_L = 532$ nm and $I_L = 10^{13}$ W/cm^2,
- $\lambda_L = 532$ nm and $I_L = 2 \times 10^{13}$ W/cm^2,
- $\lambda_L = 532$ nm and $I_L = 3 \times 10^{13}$ W/cm^2,
- $\lambda_L = 532$ nm and $I_L = 3.5 \times 10^{13}$ W/cm^2,
- $\lambda_L = 532$ nm and $I_L = 4 \times 10^{13}$ W/cm^2,

superposed with a high frequency field with a low intensity of $I_H = 10^{10}$ W/cm^2 and a frequency chosen in the range 0.2 a.u to 0.6 a.u.

The following basis set was used in order to achieve convergence for the ionisation rate. It was found that the number of angular momenta, Floquet harmonics and basis functions in the basis set needed for convergence of the ionisation rate is always less than that needed for convergence of the harmonic generation rate. In our conclusion of latter,

- the number of Floquet harmonics used was 15,
- the number of maximum angular momenta used was 11,
- the number of basis functions used was 30,
- the number of Floquet harmonics for the high frequency field was taken from 0 to 1, a one-photon absorption, since I_H was sufficiently weak.

Results obtained showed that in contrast to the harmonic generation rate, the ionisation rate is strongly affected when the second colour is applied to the system (see Table 5.1). For example for the particular system given in Table 5.1 the ionisation rate is increased by about 20% with the application of the high frequency field whereas in this particular example the highest change in harmonic generation rate appears at 9th harmonic with only a 2% increase. It is expected that the newly possible transitions between the ground state and the excited states are responsible for the rapid change in the rate of ionisation with the application of the high frequency field. Schematical presentation of the possible transitions with 1-photon (ω_H), 2-photon ($\omega_H + \omega_L$) and 3-photon ($2\omega_L + \omega_H$) are respectively given in Figure 5.2, 5.3 and 5.4.

Table 5.1: Comparison of Harmonic generation rate and ionisation rate for one colour process ($I_L = 4 \times 10^{13}$ W/cm^2 and $\lambda_L = 532$nm) and two colour process (the first field together with a field $I_H = 10^{10}$ W/cm^2 and $\omega_H = 0.3750$ a.u). Rate is given in (a.u.).

N	Rate for One-Colour	Rate for Two Colour
3	1.03(+04)	1.02(+04)
5	8.28(+04)	8.29(+04)
7	1.72(+04)	1.72(+04)
9	1.60(+03)	1.63(+03)
11	1.58(+01)	1.58 (+01)
ionisation	3.53(+11)	4.42(+11)

In order to understand the change in the ionisation rate when the high frequency field is applied to the system in addition to the fundamental field, the shifted energy levels of the hydrogen atom in the fundamental field were calculated. The results of the ionisation rate from the calculations for different intensity of the fundamental field ($I_{L1} = 10^{13}$, $I_{L2} = 2\times10^{13}$, $I_{L3} = 3\times10^{13}$, $I_{L4} = 3.5\times10^{13}$, $I_{L5} = 4 \times 10^{13}$ W/cm^2) are given in Table 5.2. In order to calculate and plot the change in the real part of the quasi energies of the levels versus I_L when $I_H = 0$, a very small intensity value was used for each level and then the adiabatic curve was followed. The identification of each Floquet state was done according to the contribution of each Floquet harmonic $\langle\psi_{Nl}|\psi_{Nl}\rangle$ (which is expressed in %) to the

normalised Floquet state

$$\sum_{Nl}\langle\psi_{Nl}|\psi_{Nl}\rangle = 1 \tag{5.15}$$

Depending on intensity, some states are rather mixed and some are pure. For the lower intensities, we found the lower states (such as 2s, 2p, 3s, 3p) are fairly pure; however, as the intensity increases ($> 10^{13}$ W/cm^2) through absorption and subsequent emission (or vice versa) of photons the field breaks the spherical symmetry and these states becomes more strongly mixed. In contrast, the levels with higher orbital-angular-momentum quantum numbers l become clearer. For example, for an intensity $I_L = 10^{13}$ W/cm^2 the contribution of $l = 0$ to the 2s state, which has an energy value -0.1278158 a.u, is 38% while for $I_L = 4 \times 10^{13}$ W/cm^2 it is less than 20% and the energy value of the state for this intensity is -0.129114 a.u. On the other hand for the state with n=7 for $I_L = 10^{13}$ W/cm^2 the contribution of $l = 0$ is 94.6% and this percentage is reduced to 56.5 % for $I_L = 4 \times 10^{13}$ W/cm^2 with energy value -0.00853 a.u. It should be pointed out that since there is parity conservation, only states with either even l or odd l are mixed. For example if $I_L = 4 \times 10^{13}$ W/cm^2 the level with energy value -0.1291 a.u. is a mixed state of the 2s with 4p+ω_L.

Now, in light of this information it is possible to analyse the effect of the high frequency field on the ionisation rate. Trends in the ionisation rate (for various intensities of the low frequency fields) with respect to frequency of the high frequency field are given in Figures 5.5, 5.6, 5.7, 5.8 and 5.5. In the figures the transitions between the ground and excited states are indicated by arrows, the corresponding couplings are written in the brackets and the indices of the brackets show the number of low-frequency photons. The analysis of the figures is as follows.

Table 5.2: The shifted energy levels for the fundamental field: $\lambda_L = 532$ nm and the intensities $I_{L1} = 1 \times 10^{13}$ W/cm^2, $I_{L2} = 2 \times 10^{13}$ W/cm^2, $I_{L3} = 3 \times 10^{13}$ W/cm^2, $I_{L4} = 3.5 \times 10^{13}$ W/cm^2, $I_{L5} = 4 \times 10^{13}$ W/cm^2.

	Shifted Energy Level				
States	I_{L1}	I_{L2}	I_{L3}	I_{L4}	I_{L5}
1s	-0.509783	-0.519843	-0.529909	-0.534946	-0.539983
2s	-0.127816	-0.128493	-0.128981	-0.129092	-0.129114
2p	-0.123832	-0.123941	-0.124015	-0.123841	-0.123508
3s	-0.055147	-0.051474	-0.054270	-0.051061	-0.050291
3p	-0.060973	-0.064980	-0.058453	-0.055562	-0.054122
3d	-0.063353	-0.067065	-0.069868	-0.069869	-0.069891
4s	-0.030896	-0.030301	-0.029111	-0.028373	-0.028084
4p	-0.041851	-0.042847	-0.043336	-0.043446	-0.043469
4d	-0.038187	-0.038295	-0.038369	-0.038196	-0.037863
4f	-0.031584	-0.031990	-0.032364	-0.032495	-0.032564
5s	-0.019754	-0.019399	-0.018667	-0.018206	-0.018079
5p	-0.027551	-0.026409	-0.026017	-0.025938	-0.025899
5d	-0.025603	-0.024249	-0.023819	-0.023600	-0.023292
5f	-0.020229	-0.020534	-0.028323	-0.020942	-0.021002
5g	-0.020046	-0.020103	-0.020162	-0.020191	-0.020221
6s	-0.013083	-0.013275	-0.013224	-0.012558	-0.011819
6p	-0.018477	-0.017622	-0.017294	-0.017226	-0.017200
6d	-0.017933	-0.016662	-0.016185	-0.016000	-0.015755
6f	-0.014045	-0.014272	-0.014504	-0.014595	-0.014656
6g	-0.013916	-0.013950	-0.013986	-0.014004	-0.014022
7s	-0.009581	-0.009849	-0.009865	-0.009283	-0.008526
7p	-0.009110	-0.008577	-0.008247	-0.008160	-0.008054
7d	-0.008994	-0.008072	-0.007867	-0.008616	-0.009488
7f	-0.009629	-0.009914	-0.01027	-0.01046	-0.01067
7g	-0.009375	-0.009421	-0.009469	-0.009493	-0.009518

In Figure 5.5 the total rate for two colour ionisation of H(1s) versus ω_H is shown for a fixed value of I_H ($= 10^{10}$ W/cm^2) and for a low frequency field with $\lambda_L = 532$ nm and $I_L = 10^{13}$ W/cm^2. From Table 5.2 we see that when the hydrogen atom is subject only to the fundamental field ($\lambda_L = 532$ nm and $I_L = 10^{13}$ W/cm^2) the shifted 1s state energy level is at -0.5097828 a.u ($\omega_H = 0.509782$ a.u.), shown as the 1st order threshold in Figure 5.5. Thus (the value of ω_H is given),
the 2nd threshold is: $0.5097828 - 0.085654 = 0.42413$ a.u,
the 3rd threshold is: $0.5097828 - 2 \times 0.085654 = 0.3385$ a.u,
the 4th threshold is: $0.5097828 - 3 \times 0.085654 = 0.253$ a.u
All the thresholds are indicated by vertical short-broken lines in Figure 5.5. From Table 5.2 the energy difference between the 1s and 2p state is equal to 0.386 a.u. Therefore, one would expect that with application of the high frequency field ($\omega_H = 0.386$ a.u) there should be a coupling between the 1s and 2p states with absorption of one high frequency photon. Figure 5.5 displays the highest peak at $\omega_H = 0.386$ a.u; thus the coupling between the 1s and 2p states with a high frequency ($\omega_H = 0.386$ a.u.) photon absorption causes a sharp rise (resonance) in the total ionisation rate. The 1s-3p coupling occurs at $\omega_H = 0.4488$ a.u. as one would expect according to Table 5.2. However, the peak at $\omega_H = 0.448$ a.u. is rather broadened. This structure is believed to exist because it represents the first resonance peak after the second threshold. As shown in Figure 5.5 the first peak after each threshold has a wider structure. Furthermore it is shown later in Figures 5.6, 5.7, 5.8 and 5.9, that as the intensity of the low frequency field is increased this structure becomes more complicated, which has interesting physical consequences, especially after the third threshold. The peaks on the right hand side of the 3p resonance peak in Figure 5.5 correspond respectively to the 1s-4p, 1s-5p, 1s-6p and 1s-7p couplings with a high frequency photon absorption. The value of ω_H for each case is equal to the energy difference between the 1s state and the other state: 1s-4p; $\omega_H = 0.468$ a.u, 1s-5p; $\omega_H = 0.482$ a.u, 1s-6p; $\omega_H = 0.491$ a.u, and 1s-7p; $\omega_H = 0.497$ a.u. For a schematic representation of this type of transition see Figure 5.2.

Figure 5.2: 1photon (ω_H) transitions: 1s-np where n=2,3,...

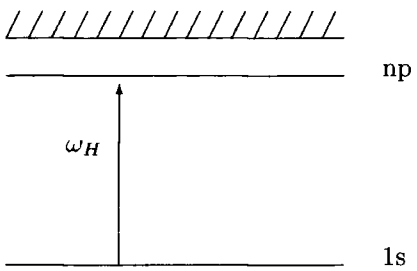

The shoulder just after the 2p resonance peak in Figure 5.5 is due to 2-photon coupling ($\omega_L + \omega_H$) of the 1s-4s states (in the dipole approximation the possible 2-photon transitions from the 1s state should be either to an ns state or an nd state, where n$\geqslant$ 2) : $\omega_H = 0.5097828 - 0.085654 - 0.0308962 = 0.393$ a.u.. 2-photon coupling ($\omega_L + \omega_H$) of 1s-4d contributes to a sudden minimum of 1s-2p resonances. However, 1s-4s coupling pushes it to a shoulder. The peaks on the right hand side of this shoulder until the second threshold are due to 2-photon ($\omega_L + \omega_H$) couplings of the 1s state with 5d, 5s, 6d, 6s, 7d and 7s states, respectively. The absorbed high frequency photon for each case is given by :

1s-5d: $\omega_H = 0.5097828 - 0.085654 - 0.0256034 = 0.3985$ a.u.

1s-5s: $\omega_H = 0.5097828 - 0.085654 - 0.0197539 = 0.4044$ a.u.

1s-6d: $\omega_H = 0.5097828 - 0.085654 - 0.0179325 = 0.3864$ a.u.

1s-6s: $\omega_H = 0.5097828 - 0.085654 - 0.0130830 = 0.4110$ a.u.

1s-7d: $\omega_H = 0.5097828 - 0.085654 - 0.0089942 = 0.4151$ a.u.

1s-7s: $\omega_H = 0.5097828 - 0.085654 - 0.0091100 = 0.4150$ a.u.

On the other hand the 2-photon ($\omega_L + \omega_H$) coupling of 1s-3s/3d contribute to the wider peak after the third threshold. In fact we believe that there is further coupling due to the Rydberg states, which contributes to the wider structure. See Figure 5.3 for the schematic representation of this type of 2-photon ($\omega_L + \omega_H$) transition.

Figure 5.3: 2-photon $(\omega_L + \omega_H)$ transitions: 1s-ns/nd where for ns; n=2,3,... and for nd; n=3,4,...

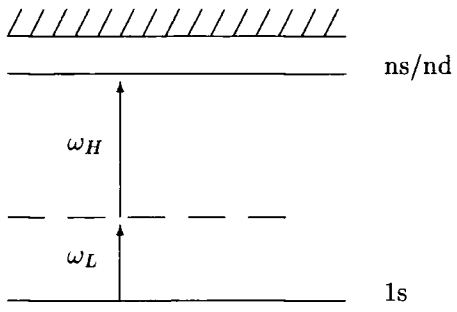

The peaks between the third and fourth thresholds starting from the first peak on the right hand side of the third threshold show the following resonances due to couplings with the 1s state:

1s-3p: 3-photon coupling $(2\omega_L + \omega_H)$ where $\omega_H = 0.2775$ a.u.

1s-2s: 2-photon coupling $(\omega_L + \omega_H)$ where $\omega_H = 0.2963$ a.u.

1s-4p: 3-photon coupling $(2\omega_L + \omega_H)$ where $\omega_H = 0.2966$ a.u. (this coupling causes a sudden minimum).

1s-4f: 3-photon coupling $(2\omega_L + \omega_H)$ where $\omega_H = 0.3069$ a.u.

1s-5p: 3-photon coupling $(2\omega_L + \omega_H)$ where $\omega_H = 0.311$ a.u.

1s-5f: 3-photon coupling $(2\omega_L + \omega_H)$ where $\omega_H = 0.318$ a.u.

1s-6p: 3-photon coupling $(2\omega_L + \omega_H)$ where $\omega_H = 0.320$ a.u

1s-6f: 3-photon coupling $(2\omega_L + \omega_H)$ where $\omega_H = 0.324$ a.u.

See Figure 5.4 for the schematic representation of this type of coupling (3-photon).

Figure 5.4: 3-photon $(2\omega_L + \omega_H)$ transitions: 1s-np/nf where for np; n=3,4,..., and for nf; n=4,5,...

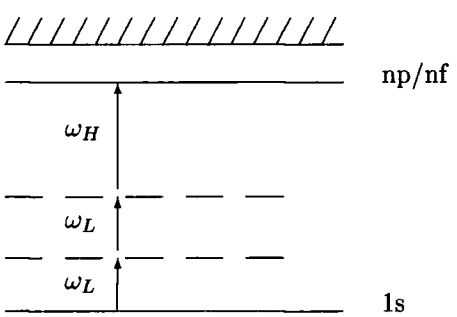

The resonances due to these types of coupling are shown in Figure 5.5 and each transition is indicated in the figure. Remember that in this figure and others (5.6, 5.7, 5.8, 5.9) the number of low-frequency photons is marked as an sub-script on each bracket.

The discussed transitions above have been investigated for higher intensities of the fundamental fields. Results are given in Figures 5.6, 5.7, 5.8 and 5.9 for intensities: $I_L = 2 \times 10^{13}$ W/cm^2, $I_L = 3 \times 10^{13}$ W/cm^2, $I_L = 3.5 \times 10^{13}$ W/cm^2, $I_L = 4 \times 10^{13}$ W/cm^2, respectively.

Analysing the figures shows that with increasing intensity of the fundamental field the location of the threshold, and therefore each series of the peaks between two thresholds, moves towards to the right. For example in the previous case (i.e. when $I_L = 10^{13}$ W/cm^2) the second threshold was at 0.42413 a.u., however now it appears at the following frequencies: $\omega_L = 0.4342$ a.u., 0.4443 a.u., 0.4493 a.u. and 0.4543 a.u when the intensity of the low-frequency field increased to $I_L = 2 \times 10^{13}$ W/cm^2, $I_L = 3 \times 10^{13}$ W/cm^2, $I_L = 3.5 \times 10^{13}$ W/cm^2, $I_L = 4 \times 10^{13}$ W/cm^2, respectively.

This analysis also shows that at lower intensities of the fundamental field some peaks apparently correspond to more than one transition: For example in Figure 5.5 (1s-ns) and (1s-nd), where n>1 , couplings are not split whereas for higher intensities these couplings are split: e.g. for $I_L = 3.5 \times 10^{13}$ W/cm^2 fundamental field in Figure 5.8 and for $I_L = 4 \times 10^{13}$ W/cm^2 in Figure 5.9, each (1s-ns) coupling causes a minimum whereas each (1s-nd) coupling causes a maximum (apart from (1s-3s) and (1s-3d) couplings). Since the energy needed for these two particular transitions are very close to the third threshold, their occurrence is more complicated. We will consider these two states in detail later. If we look at the coupling due to 3-photon transitions (1s-np) and (1s-nf), with increasing intensity these two couplings present structure similar to that product by (1s-nd) and (1s-ns) couplings.

With increasing intensity of the fundamental field more Rydberg states contribute to the ionisation processes. For example, while in Figure 5.5 we can at most observe 3-photon transitions, (nf states coupling with the ground state), in Figure 5.9 there is 4-photon coupling with a contribution of ng states as well

as previous couplings. In addition with increasing intensity of the low frequency field further peaks occur at frequencies $\omega_H > \omega_0$ and $\omega_H < \omega_4$, where ω_0 and ω_4 are the first and fourth threshold frequencies of the that particular field. The peaks at $\omega_H > \omega_0$ at high intensity of the low frequency field are also due to 2-photon coupling of (1s-ns/nd) states, where n$\geq$ 3. However, these couplings are not $(\omega_H + \omega_L)$ 2-photon couplings, but $(\omega_H - \omega_L)$ couplings. Starting from the first peak after the first threshold, each peak respectively corresponds to the couplings of the (1s-3s/3d), (1s-4s/4d), (1s-5s/5d), (1s-6s/6d) states. Note that the maximums points are corresponds to a d-state coupling and minimum s-state coupling.

However, whereas at lower fundamental field intensities 1-photon coupling is clearly distinguishable, as the intensity increases this type of coupling cannot be observed so easily. In addition they are not exactly at a maximum or a minimum, rather they occur between a maximum and a minimum.

Now, let us pay attention to the most crucial two transitions (1s-3d) and (1s-3s). In Figure 5.5 both transitions are inside the widest peak and they are not split although they have slightly different values and one of them close to the value of the minimum point with a value of $\Delta E - \omega_L = 0.369$ a.u. (the minimum is at $\omega_H = 0.370$ a.u.) and the other one to the maximum with a value of $\Delta E - \omega_L =$ 0.361 a.u. (the maximum is at $\omega_H = 0.361$ a.u.). With increasing intensity of the fundamental field these two values increase and for (1s-3d) the transition is close to the minimum point whereas for (1s-3s) to the maximum point for the fundamental field intensities $I_L = 10^{13}, 2 \times 10^{13}$, and 3×10^{13} W/cm^2, see Figures, 5.5, 5.6 and 5.7, respectively. In addition that with further increase in intensity we observed two small peaks in this region, where the wider peak is located. To analyse this region we first increased the intensity of the fundamental field to $I_L = 3.5 \times 10^{13}$ W/cm^2. The first small peak occurs at $\omega_H = 0.376$ a.u. with a maximum value of ionisation rate and then there is a shoulder, which continues with a very sharp fall to a minimum at $\omega_H = 0.401$ a.u. The value of $\Delta E - \omega_L$ is equal to 0.3794 a.u. for (1s-3d) coupling which is a value between the small peak and the shoulder. On the other hand $\Delta E - \omega_L = 0.398$ a.u. for (1s-3s) is after the shoulder and closer to the value of the sharp minimum. When the intensity I_L increases to the value

$I_L = 4 \times 10^{13}$ W/cm^2 the shoulder becomes a peak. Therefore we observe two minima and two maxima in this region. The value of $\Delta E - \omega_L$ for both transitions are between one maximum and one minimum (relatively close to the minimum) as indicated in Figures 5.8 and 5.9. Therefore, we think that these two small peaks are split due to (1s-3s) and (1s-3d) couplings. They are not very dominant due to being close to the third threshold, where we expect many more couplings of ground state and Rydberg states contribute to the wider structure in this region.

Furthermore, it is worth mentioning that the minimum value of the ionisation rate is not zero because of the background coupling to the continuum by the fundamental field (see Figures 5.5,5.6, 5.7, 5.8 and 5.9). When the fundamental field is applied alone the ionisation rate for intensities, $I_L = 1 \times 10^{13}$ W/cm^2, $I_L = 2 \times 10^{13}$ W/cm^2, $I_L = 3 \times 10^{13}$ W/cm^2, $I_L = 3.5 \times 10^{13}$ W/cm^2 and $I_L = 4 \times 10^{13}$ W/cm^2, are 1.712×10^{-8}, 5.534×10^{-7}, 1.03×10^{-6}, 1.581×10^{-6} and 8.530×10^{-6} (in a.u.), respectively.

5.5.2 Ionisation rate for an infrared field together with another field

The ionisation rate was investigated for a two-colour processes where the fundamental field is an infrared field with a wavelength 1064 nm and intensity $I = 10^{13}$ W/cm^2 with a second field whose frequency is incommensurable with the fundamental field. Two different cases were considered for this calculation. In the first one the wavelength of the second field was varied from the visible region ($\lambda = 530$ nm) to the infrared region ($\lambda = 1053$) with a fixed intensity I= 10^{10} W/cm^2. In the second the wavelength of the second field was kept fixed ($\lambda = 1053$ nm) and the intensity was varied; I=10^5, 10^6, 10^9 and 10^{10} W/cm^2. The results are given in Table 5.3.

It is clear that there is a 10^{-5} magnitude order of shift in the energy level of the 1s-state with application of the second field. In fact this shift gradually increase in the negative direction with increasing wavelength of the second field from 580 nm towards the infrared region, into the intensity of the second field kept fixed. When the wavelength of the second field is kept fixed at 1053 nm and the intensity of the second field is decreased from 10^{10} W/cm^2 to 10^5 W/cm^2, the

change in the real part of the quasienergy is consistant with the expected results; a gradual decrease of the order of 10^{-5} in the negative direction.

The change for ionisation is compatively important in contrast to the situation for harmonic generation (see subsection 5.5.4). There is a strong decrease in the ionisation rate when the second field (wavelength 580 nm (visible light) and 10^{10} W/cm^2 intensity) is applied, the rate dropps by a factor of $\sim$ 60, approximately. In addition the ionisation rate decreases as the wavelength of the second field increases (wavelength of the second fields between 580 nm and 600 nm with fixed intensity I= 10^{10} W/cm^2). However there is a rapid increase (a factor of $\sim$ 100) when the wavelength of the second field is 620 nm. At this point the ionisation rate is higher than the one without application of the second field. After this wavelength again the ionisation rate decreases as the wavelength of the second field increases towards the infrared. When the wavelength 1053 nm is reached, which is slightly different than the wavelength of the fundamental field the difference between the ionisation rate without application of second field and with application of second field is rather small (about 1.6% increase). However, decreasing the intensity of the second field from 10^{10} W/cm^2 towards 10^5 W/cm^2 causes a decrease in the relative change. When the intensity of the second infrared field is 10^5 W/cm^2, there is hardly any difference in the ionisation rate between the results with application of the second field and without application of the second field (about the order of 10^{-5} magnitude).

Table 5.3: The shifted energy of H-atom (1s-state) in a two colour field. The fundamental field is an infrared field with a wavelength of 1064 nm and intensity 10^{13} W/cm^2. The wavelength and intensity of the second field is given with the first and second column, respectively and the third column shows the real part of the quasi energy and the last column the corresponding ionisation rate.

Ionisation Rates (in a.u.)			
λ_2 (A^o)	I_2	Re(QE)	ionisation rate
0.0000 (00)	0.0 (10)	-0.5389216	0.7197312 (-11)
0.5800 (04)	1.0 (10)	-0.5389335	0.1164920 (-10)
0.5820 (04)	1.0 (10)	-0.5389335	0.1146030 (-10)
0.5840 (04)	1.0 (10)	-0.5389336	0.1128517 (-10)
0.5860 (04)	1.0 (10)	-0.5389337	0.1112194 (-10)
0.5880 (04)	1.0 (10)	-0.5389338	0.1096649 (-10)
0.5900 (04)	1.0 (10)	-0.5389339	0.1081780 (-10)
0.5920 (04)	1.0 (10)	-0.5389339	0.1067018 (-10)
0.5940 (04)	1.0 (10)	-0.5389340	0.1051917 (-10)
0.5960 (04)	1.0 (10)	-0.5389341	0.1036243 (-10)
0.5980 (04)	1.0 (10)	-0.5389342	0.1019588 (-10)
0.6000 (04)	1.0 (10)	-0.5389343	0.1002010 (-10)
0.6020 (04)	1.0 (10)	-0.5389344	0.9837696 (-11)
0.6040 (04)	1.0 (10)	-0.5389344	0.9656431 (-11)
0.6060 (04)	1.0 (10)	-0.5389345	0.9486365 (-11)
0.6080 (04)	1.0 (10)	-0.5389346	0.9335151 (-11)
0.6100 (04)	1.0 (10)	-0.5389347	0.9207974 (-11)
0.6120 (04)	1.0 (10)	-0.5389348	0.9104203 (-11)
0.6140 (04)	1.0 (10)	-0.5389349	0.9022767 (-11)
0.6160 (04)	1.0 (10)	-0.5389349	0.8959769 (-11)
0.6180 (04)	1.0 (10)	-0.5389350	0.8909863 (-11)
0.6200 (04)	1.0 (10)	-0.5389351	0.8870328 (-11)
0.6200 (04)	1.0 (10)	-0.5389351	0.8870328 (-11)
0.6220 (04)	1.0 (10)	-0.5389352	0.8838390 (-11)
0.6240 (04)	1.0 (10)	-0.5389353	0.8810479 (-11)
0.6260 (04)	1.0 (10)	-0.5389354	0.8786125 (-11)
0.6280 (04)	1.0 (10)	-0.5389354	0.8764460 (-11)
0.6300 (04)	1.0 (10)	-0.5389355	0.8744179 (-11)
0.6300 (04)	1.0 (10)	-0.5389355	0.8744179 (-11)
0.7000 (04)	1.0 (10)	-0.5389387	0.8121384 (-11)
0.8000 (04)	1.0 (10)	-0.5389438	0.7700806 (-11)
0.9000 (04)	1.0 (10)	-0.5389492	0.7775842 (-11)
0.1000 (05)	1.0 (10)	-0.5389514	0.7458444 (-11)
0.1053 (05)	1.0 (10)	-0.5389419	0.7311172 (-11)
0.1053 (05)	1.0 (09)	-0.5389243	0.7258132 (-11)
0.1053 (05)	1.0 (06)	-0.5389216	0.7197501 (-11)
0.1053 (05)	1.0 (05)	-0.5389216	0.7197786 (-11)

5.5.3 Harmonic generation rate for a fundamental field together with a high frequency field

For this calculation the following fields were used:

1. Fundamental field: This field has a low frequency and a high intensity: $\lambda_L = 532$ nm ($\omega_L = 0.085654$ a.u.) and $I_L = 4 \times 10^{13}$ W/cm^2

2. High frequency field with a low intensity: $I_H = 1 \times 10^{10}$ W/cm^2 and various frequencies much higher than ω_L.

First of all, the calculations have been done for a high frequency field having a frequency value $\omega_H = 0.37501470$ a.u. This particular frequency is chosen anticipating a resonance because of 1s-2p coupling brought up by a high frequency photon. However, the calculated results display little difference in harmonic generation rates between application of one field or two fields simultaneously. The results are given for one colour as well as for the two colour case in Table 5.4. The effect is largest for the third harmonic, 0.3% and with for the 19th harmonic, 0.2%. For the other harmonics it is either 0.1% or less. Even in the case of the 13th and the 15th harmonics no effect is recorded with the application of the second field.

In addition we have obtained that for this particular system, in fact, due to the ac-Stark shift, the 1s-2p coupling occurs at $\omega_H = 0.416475$ a.u. (see 5.5.1). Thus, the calculations were performed for $\omega_H = 0.416475$ a.u. in addition to the following frequencies: (the frequency region where resonances occurs due to 2-photon coupling of (1s-3s) and (1s-3d) states-see 5.5.1) for high frequency field:
$\omega_H = 0.379$ a.u.; maximum
$\omega_H = 0.384$ a.u.; (1s-3d)
$\omega_H = 0.387$ a.u.; minimum
$\omega_H = 0.393$ a.u.; maximum
$\omega_H = 0.404$ a.u.; (1s-3s)
$\omega_H = 0.405$ a.u.; minimum
These are the frequency regions where resonances occur due to 2-photon coupling of (1s-3s) and (1s-3d) states for this particular system. The frequency $\omega_H = 0.384$ a.u. is equal to $\Delta E - \omega_L$ where ΔE is the energy difference between the shifted

Table 5.4: The harmonic generation rate for one colour and two colour processes with the fundamental field with $\lambda_L = 532$ nm, intensity $I_L = 4 \times 10^{13}$ W/cm^2 and the high frequency field $\omega_H = 0.3750147$ a.u., intensity $I_H = 10^{10}$ W/cm^2.

Harmonic Generation Rates (a.u)		
q	One colour fundamental field	Two colour harmonic field
3	0.1024 (+05)	0.1027 (+05)
5	0.8281 (+05)	0.8287 (+05)
7	0.1724 (+05)	0.1725 (+05)
9	0.1604 (+04)	0.1606 (+04)
11	0.1583 (+02)	0.1584 (+02)
13	0.0439 (+00)	0.0439 (+00)
15	0.5223 (-04)	0.5223 (-04)
17	0.3331 (-07)	0.3335 (-07)
19	0.1315 (-10)	0.1318 (-10)

ground and 3s states in the absence of the high frequency field and $\omega_H = 0.404$ a.u. is the same for (1s-3d) coupling. The other four frequencies are the extreme points of the resonance occurring due to these transitions (see subsection 5.5.1 for details.). However, even for these particular frequencies, where resonances occur (see 5.5.1), the results show that there is not a dominant effect in the harmonic generation rate with the application of the high frequency field. Especially when the frequency of the high frequency field has the values $\omega_H = 0.405$ a.u. and $\omega_H = 0.404$ a.u., no effect is recorded apart from for the third harmonic (0.2%). The results for other high frequency fields are given in the table 5.5. These results are in percent with the definition: $(R_1 - R_2) \times 100/R_1$ where R_1 is the rate with the absence of the high frequency field and R_2 is the rate with application of the high frequency field. The highest effect occurs when the frequency of the high frequency field is $\omega_H = 0.416475$ a.u. (with 0.66% at 17th harmonic).

Moreover, there was a convergence problem between the results using the velocity form of dipole moment and using the length form of the dipole moment although the results from the velocity and acceleration forms agreed with each other and the results from both the acceleration and velocity form calculations

Table 5.5: The relative change in the harmonic generation rate for two- colour processes compare to one colour processes. The fundamental field has a wavelength $\lambda = 532$ nm and an intensity I$= 4 \times 10^{13}$ W/cm^2 ; the high frequency field has an intensity I$=10^{10}$ W/cm^2 and the following frequencies: $\omega_H = 0.379$ a.u., $\omega_H = 0.384$ a.u., $\omega_H = 0.387$ a.u., $\omega_H = 0.393$ a.u. and $\omega_H = 0.416475$ a.u.

Harmonic Generation Rates (in %)					
N	P_1	P_2	P_3	P_4	P_5
3	0.1	0.1	0.2	0.37	0.0
5	0.1	0.1	0.1	0.11	0.13
7	0.06	0.06	0.06	0.06	0.12
9	0.12	0.12	0.12	0.12	0.12
11	0.06	0.06	0.06	0.06	0.13
13	0.11	0.11	0.09	0.11	0.14
15	0.1	0.12	0.1	0.12	0.12
17	0.15	0.15	0.15	0.15	0.66

were converged in terms of the basis set. A set of results from the three forms of the dipole moment is given in Table 5.6 in order to see the consistency of the results from three different forms. The discrepancy between the results from the length form and the other two comes from the lack of convergence in terms of the basis set for the length form.

The basis set used for the results in table 5.6, 5.4 and 5.5 is given as follows:

- the number of Floquet harmonics used for the fundamental field is 43
- 13 angular momenta
- 45 basis functions
- Since I_H has been chosen sufficiently weak so that it is necessary to include only the harmonic components $|\psi_{i,m,n}\rangle$ with the high frequency photon index m equal to 0 or 1. Thus we take into account the resonant part of the ac-Stark shift due to the high frequency field (the Rabi-coupling energy) but we only partially take into account the non-resonant part; however, we expect this non-resonant shift to be negligible. In fact, when the high frequency field is non-resonant, it may be treated perturbatively, that is, we can ignore

(though we do not) the back-coupling between the harmonic components $|\psi_{i,1,n}\rangle$ and $|\psi_{i,0,n}\rangle$.

Table 5.6: The harmonic generation rate in a two colour processes with the fundamental field in three gauges with $\lambda_L = 532$ nm, intensity $I_L = 4 \times 10^{13}$ W/cm^2 and the high frequency field $\omega_H = 0.393$ a.u., intensity $I_H = 10^{10}$ W/cm^2.

Harmonic Generation Rates (a.u.)			
q	Velocity form	Length form	Acceleration form
3	0.1029 (+05)	0.1756 (+05)	0.1028 (+05)
5	0.8286 (+05)	0.8221 (+05)	0.8289 (+05)
7	0.1725 (+05)	0.1707 (+05)	0.1725 (+05)
9	0.1605 (+04)	0.1599 (+04)	0.1605 (+04)
11	0.1584 (+02)	0.1591 (+02)	0.1584 (+02)
13	0.4395 (-01)	0.4370 (-01)	0.4395 (-01)
15	0.5229 (-04)	0.5110 (-04)	0.5229 (-04)
17	0.3335 (-07)	0.3300 (-07)	0.3336 (-07)

5.5.4 Harmonic generation rate for an infrared field together with another field

The following three different types of processes were investigated considering an infrared field as a fundamental field.

The harmonic generation rate was calculated for an infrared field together with another infrared field, which has a slightly different wavelength. The first field is the fundamental field; it has a wavelength $\lambda = 1064$ nm and intensity I= 10^{13} W/cm^2 and the second field has a wavelength $\lambda = 1053$ nm and various intensities : I=10^5, 10^6, 10^9 and 10^{10} W/cm^2. The calculated results demonstrate that in this case the change in harmonic generation rate is nearly non existent for the lower intensity of the high frequency field (I=10^5 and I=10^6 W/cm^2.). However, with increasing intensity of high frequency field some change was found in the harmonic generation rate when the second field was applied. This effect was largest when the intensity of high frequency field was $I_H = 10^{10}$ W/cm^2 (among the the intensities we examined), and for this particular field it gradually increased as the harmonic

number increased (apart from in the case of the 15th harmonic): 0.1%, 1%, 3%, 3%, 5%, 11%, 7%, 12% and 20% for the 3rd, 5th, 7th, 9th, 11th, 13th, 15th, 17th and 19th, respectively (see Table 5.7).

Table 5.7: The harmonic generation rate for one colour and two- colour processes. The fundamental field has a wavelength $\lambda = 1064$ nm and an intensity I=10^{13} W/cm^2. The second field has a slightly different wavelength ($\lambda = 1053$) nm and varying intensity: $I_1 = 10^5$ W/cm^2, $I_2 = 10^6$ W/cm^2, $I_3 = 10^9$ W/cm^2, and $I_4 = 10^{10}$ W/cm^2.

Harmonic Generation Rates (a.u.)					
	One-Colour	Two Colour			
N	I	I_1	I_2	I_3	I_4
3	0.1466 (+01)	0.1466 (+01)	0.1466 (+01)	0.1465 (+01)	0.1464 (+01)
5	0.6095 (-02)	0.6095 (-02)	0.6095 (-02)	0.6089 (-02)	0.6038 (-02)
7	0.2437 (-02)	0.2437 (-02)	0.2437 (-02)	0.2422 (-02)	0.2367 (-02)
9	0.6352 (-02)	0.6352 (-02)	0.6352 (-02)	0.6408 (-02)	0.6166 (-02)
11	0.1898 (-01)	0.1898 (-01)	0.1898 (-01)	0.1898 (-01)	0.1795 (-01)
13	0.1226 (-00)	0.1226 (-01)	0.1226 (-01)	0.1191 (-01)	0.1088 (-01)
15	0.2988 (-02)	0.2988 (-02)	0.2988 (-02)	0.3014 (-02)	0.2773 (-02)
17	0.5449 (-03)	0.5449 (-03)	0.5449 (-03)	0.5428 (-03)	0.4799 (-03)
19	0.1636 (-04)	0.1636 (-04)	0.1636 (-04)	0.1565 (-04)	0.1307 (-04)
21	0.1462 (-06)	0.1462 (-06)	0.1465 (-06)	0.2946 (-06)	0.3670 (-06)

In addition to that of the fundamental field the intensity of the second field was fixed and the wavelength was varied from the visible region to the infrared region. The results of this calculation demonstrated that the enhancement of the harmonic generation rate with application of the second infrared field was rather small for the high frequency field with $\lambda_H = 700$ nm and $\lambda_H = 800$ nm. The largest effect for the former one was obtained to be a 2.2% change at 13th harmonic and for the latter one a 4.4% change at the 15th harmonic. However, for the high frequency field with $\lambda_H = 900$ nm and $\lambda_H = 1000$ nm the effect was bigger: 8% at 9th harmonic for $\lambda_H = 900$ nm and 24.44% at 11 harmonic for $\lambda_H = 1000$nm higher frequency field. Table 5.8 shows the effect for each case for each harmonic.

Finally, the expectation that in the resonant region the harmonic generation

rate might be enhanced led us to the following calculations in order to check whether there actually was a dominant enhancement of the harmonic generation rate. This calculation was done in the region where one would expect resonances to occur; i.e. λ between 580 nm and 630 nm [90] with a fixed intensity I= 10^{10} W/cm^2. However, the effects were relatively small. The results as percentage are given in Table 5.9 for various wavelengths.

The basis set used for the calculations was the same as the one described in section 5.5.3. However, with increasing intensity it was necessary to use a larger basis set in order to achieve good convergence. In addition the number of Floquet harmonics for the second field was taken from -1 to 1 which means there was one high frequency photon absorption as well as emission.

Table 5.8: The relative change in harmonic generation rate for two- colour processes to one colour processes. The fundamental field has a wavelength $\lambda = 1064$ nm and an intensity I= 10^{13} W/cm^2 ; the second field has an intensity I=10^{10} W/cm^2 and various wavelengths: $\lambda_1 = 700$ nm, $\lambda_2 = 800$ nm, $\lambda_3 = 900$ nm and $\lambda_4 = 1000$ nm.

Harmonic Generation Rates (in %)				
N	P_1	P_2	P_3	P_4
3	0.07	0.07	0.14	0.07
5	0.53	0.53	0.4	0.3
7	0.62	0.34	2.34	5.7
9	0.46	0.61	7.92	6.77
11	1.9	1.84	5.8	21.55
13	2.2	1.3	3.34	24.44
15	0.3	4.4	4.35	2.4
17	0.1	3.0	3.5	14.55
19	0.0	2.93	2.8	20.0
21	0.68	2.1	2.94	6.0

Table 5.9: The relative change in the harmonic generation rate for two- colour process to one colour process. The fundamental field has a wavelength $\lambda = 1064$ nm and intensity I=10^{13} W/cm^2. The second field has an I=10^{10} W/cm^2 various various wavelengths (in resonance region): $\lambda_1 = 580$, λ_2=586, λ_3=592, λ_4=598, λ_5=606, λ_6=614, λ_7=622, λ_8=630 nm.

Harmonic Generation Rates (in %)							
N	P_1	P_2	P_3	P_4	P_5	P_6	P_7
3	0.0	0.07	0.07	0.07	0.07	0.07	0.0
5	0.0	0.02	0.08	0.33	0.46	0.46	0.39
7	0.3	0.93	2.2	3.8	3.5	2.4	1.5
9	0.8	1.53	2.1	2.5	2.75	3.15	3.55
11	0.16	0.62	1.0	1.6	1.6	1.1	1.0
13	0.98	1.88	2.3	1.63	0.8	0.7	0.9
15	0.22	0.19	1.0	1.2	1.9	2.0	2.1
17	0.47	0.85	1.27	1.4	1.0	0.54	0.36
19	0.55	1.04	1.65	2.1	1.7	1.2	1.0
21	0.83	1.2	2.0	2.4	1.6	0.9	1.2

5.6 Conclusions

In this Chapter the rate for harmonic generation and for the ionisation was computed for the hydrogen atom in the two colour field described in section 5.5.3. Calculations were performed for various low frequency intense fields superposed with a high frequency weak field. Calculations have been performed for two low frequency fields, in the infrared or visible. The results obtained showed that there is no dominant effect in the harmonic generation rate on application of the high frequency field. In contrast to the harmonic generation rate, the ionisation rate was strongly affected with application of the high frequency field, especially in the case of visible light taken as the low frequency field. It has been shown that series of resonances occur due to coupling of 1s and some excited states when the high frequency field was applied to the system. These couplings have been shown in Figures 5.5, 5.6, 5.7, 5.8 and 5.9, respectively for $I_L = 10^{13}$ W/cm^2, $I_L = 2 \times 10^{13}$ W/cm^2, $I_L = 3 \times 10^{13}$ W/cm^2, $I_L = 3.5 \times 10^{13}$ W/cm^2 and $I_L = 4 \times 10^{13}$ W/cm^2. It has been shown that after each threshold the peak has a wide structure but the other peaks are rather sharp. With increasing intensity this wider structure splits into other peaks which cannot be observed clearly at low intensity of low frequency fields. e.g. at lower intensities it was not possible to observe 3s and 3d couplings separately (they both are in the same wide peak after the third threshold) while at higher intensities these two couplings clearly can be seen. It is clear that even more states contribute to this wide structured peak. With increasing intensity of the fundamental field more Rydberg states contribute to the ionisation processes. For example, while in Figure 5.5 we can at most observe 3-photon transitions, (nf states coupling with the ground state), in Figure 5.9 there is 4-photon coupling with a contribution of ng states as well as previous couplings. In addition the transitions for more than one photon at low intensity field are the lowest order transitions. With increasing intensity the higher order transitions appear as resonances in addition to the previous resonances due to lowest order. For example at I= 10^{13} W/cm^2 intensity of the low frequency field the observed 2-photon transitions are the transitions between the ground state and ns/nd (n$\geq$ 3) state with $(\omega_H + \omega_L)$. However, at higher intensities the transitions with $(\omega_H - \omega_L)$ also appear, which is the next order process.

Figure 5: Ionisation Rate of H-atom in two colour field:
λ_L=532 nm and $I_L=10^{13}$ W/cm^2 ; $I_H=10^{10}$ W/cm^2

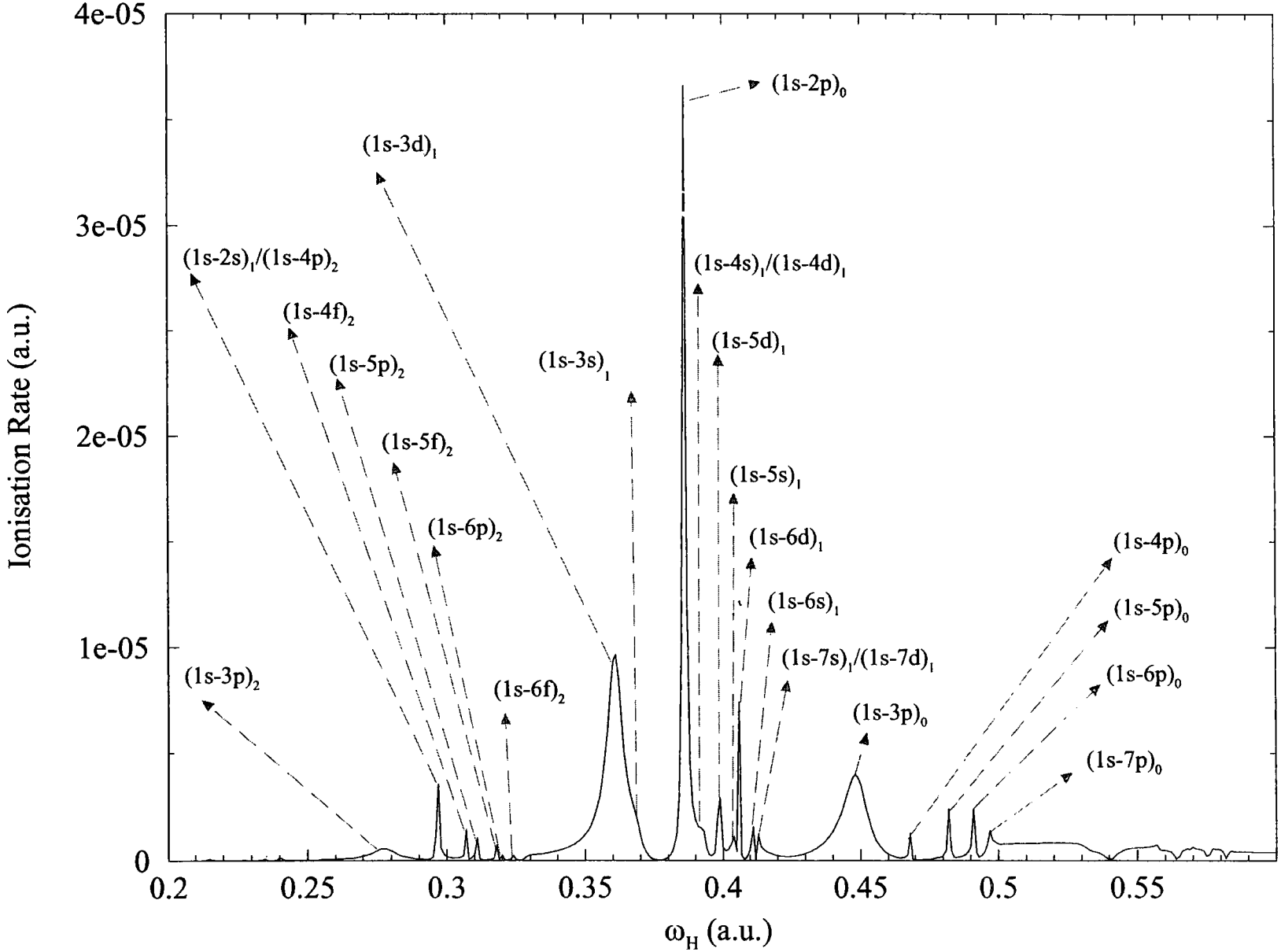

Figure 6: Ionisation Rate of H-atom in two colour field:
λ_L=532 nm and I_L=2.10^{13} W/cm^2 ; I_H=10^{10} W/cm^2

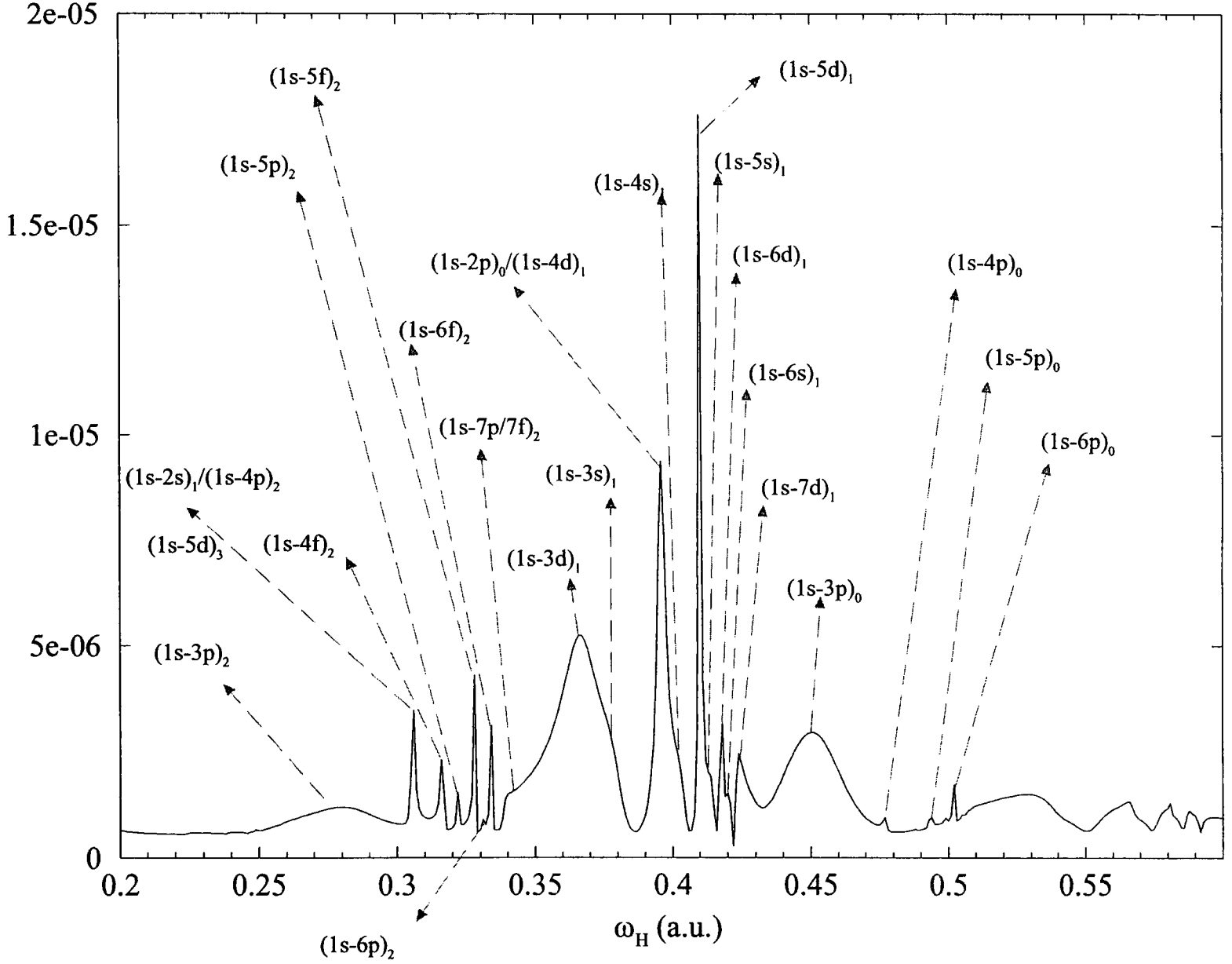

Figure 7: Ionisation Rate of H-atom in two colour field:
λ_L=532 nm and I_L=3.10^{13} W/cm^2 ; I_H=10^{10} W/cm^2

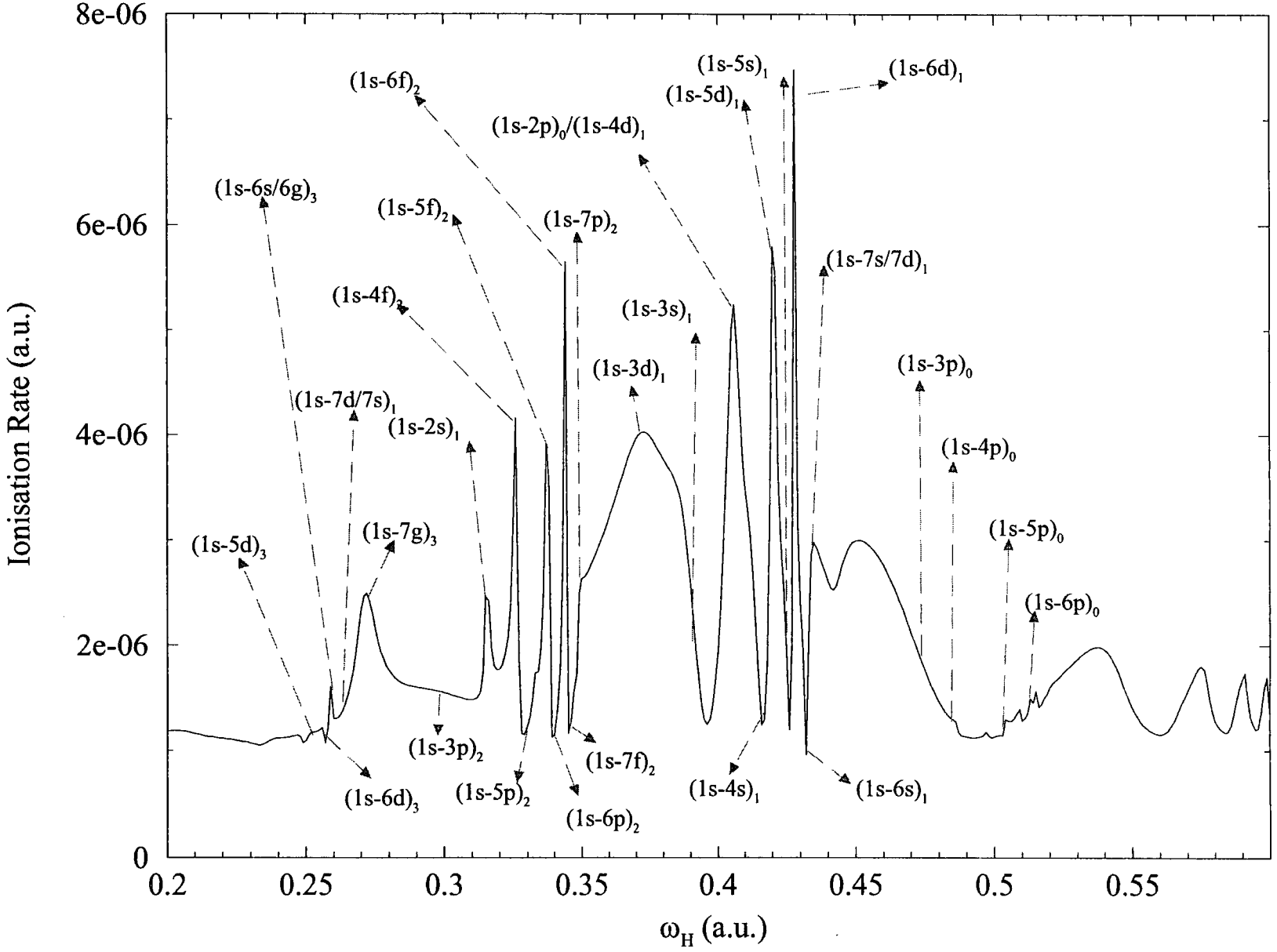

Figure 8: Ionisation Rate of H-atom in two colour field:
λ_L=532 nm and I_L=3.5X10^{13} W/cm^2 ; I_H=10^{10} W/cm^2

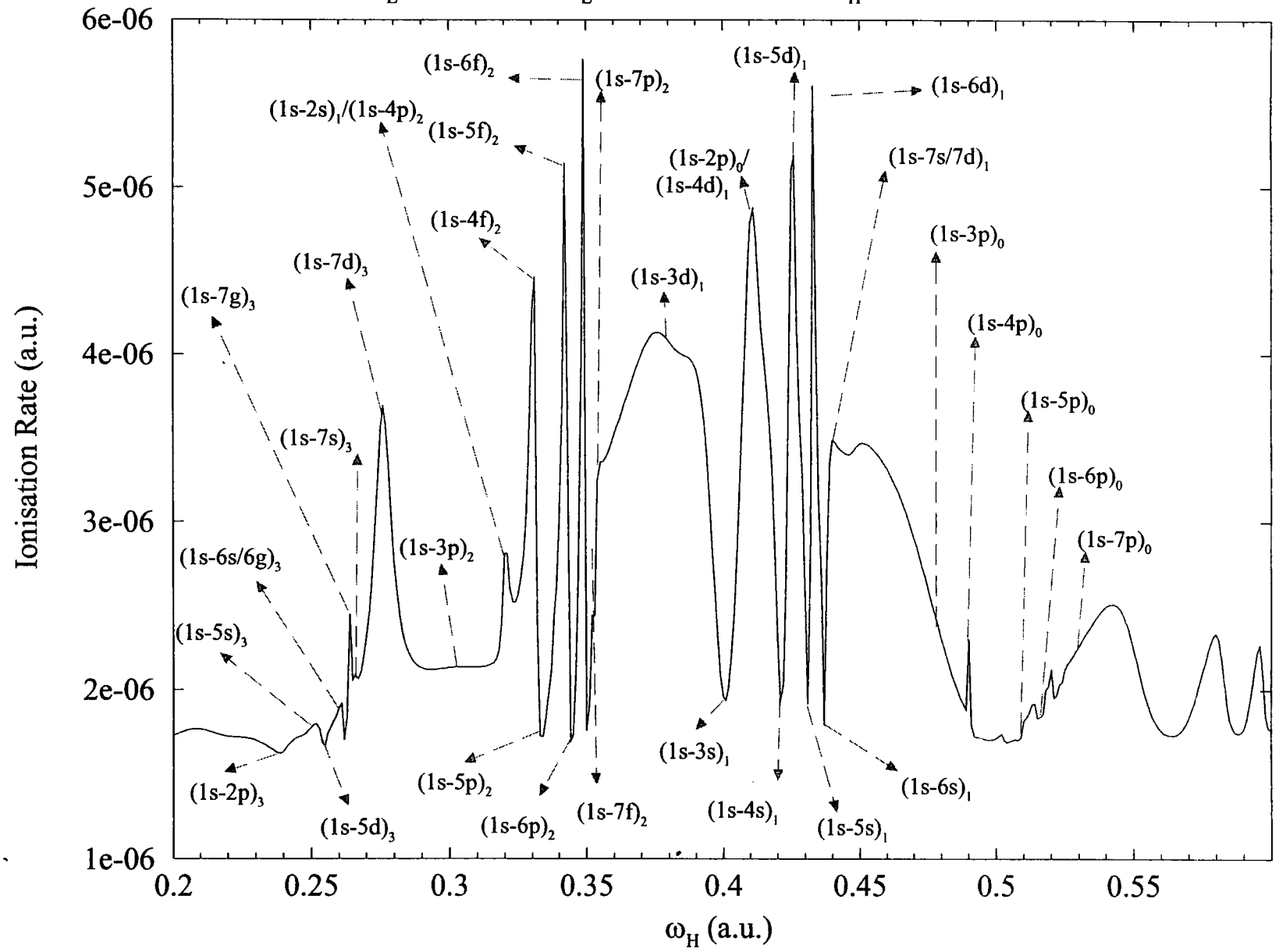

Figure 9: Ionisation Rate of H-atom in two colour field:
λ_L=532 nm and I_L=4.10^{13} W/cm^2; I_H=10^{10} W/cm^2

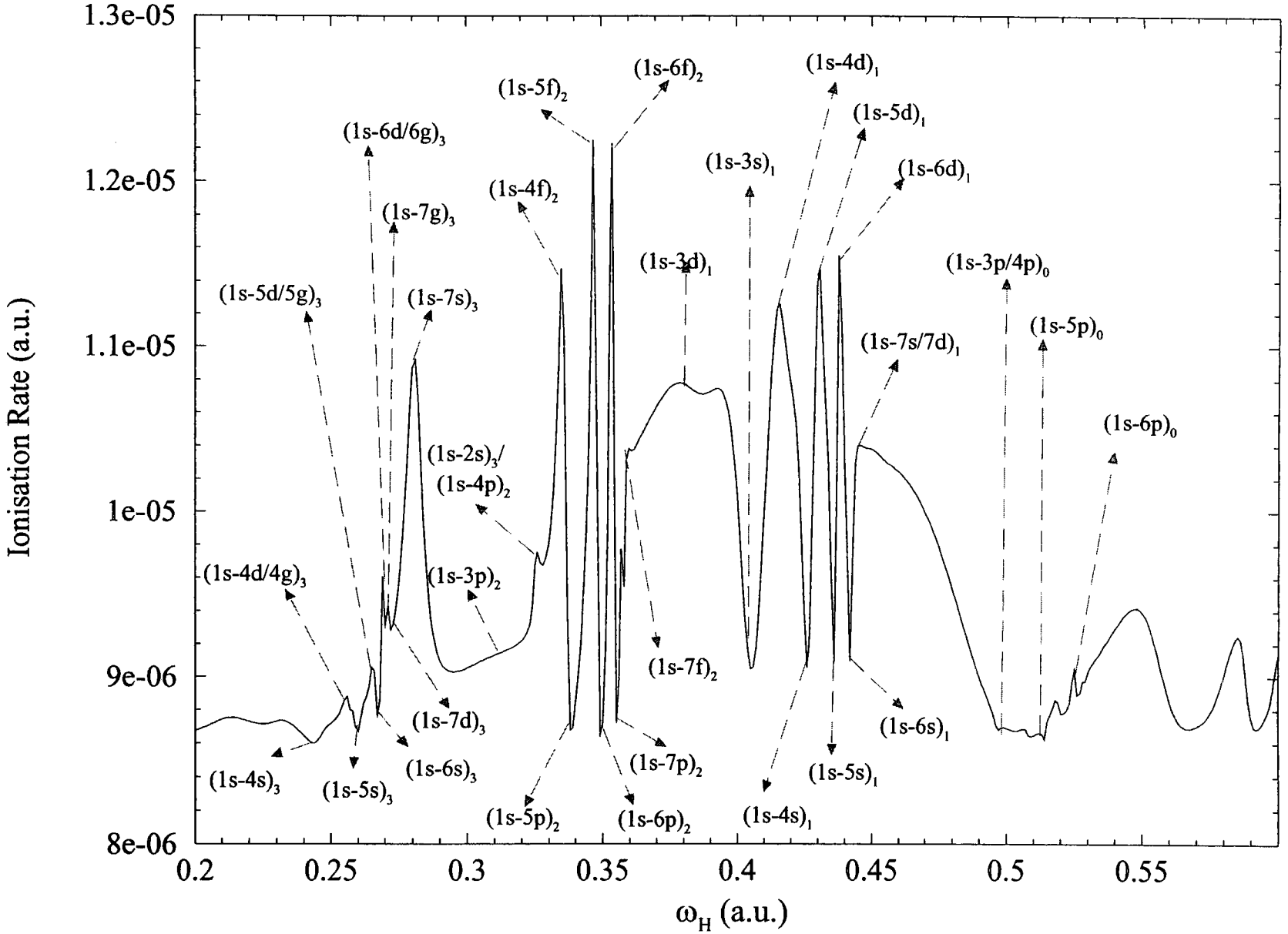

Chapter 6

Frequency mixing processes

6.1 Overview

Frequency mixing processes (sum and difference) in rare gaseous has recently taken the attention of experimentalists (see [91], [92], [93], [94], [95] and [96]) and theoreticians (see [86], [97], [52], [98], [99], [100], [101] and [102]). Most of the experiments have been performed by mixing light from high- power short-pulse laser and its second or third harmonic. For example Perry and Crane [91] were the first workers who performed a high order degenerate mixing experiment using a high power laser (ω_p, 1053 nm) and its second harmonic ($2\omega_p$, 527 nm). They observed even harmonics which in some cases had a strength almost comparable to that of the odd-order ones. They also found, that by controlling the relative polarisation of the two fields it is possible to control the mixing efficiency and to produce coherent extreme ultraviolet (XUV) radiation polarised orthogonally to the strong driving field. The experiments by Watanable *et al.* [92] were also frequency mixing processes with two commensurable frequencies. They performed experiments in the tunnelling regime, mixing the third harmonic with its fundamental. They observed the two-colour interference and controlled it by varying the phase between the two fields. This experiment was the first demonstration of two-colour phase control in the tunneling regime by mixing light with its third harmonic.

Eichmann *et al.* [94] reported a high-order frequency mixing experiment using the radiation of a high-power Ti:sapphire laser and its second harmonic. The earlier experiments were performed used linear polarisations for both fields, one

field being significantly weaker than the other. Eichman *et al.* [94] however considered two-colour mixing experiments with laser fields of comparable intensity and various polarisations. Finally, Meyer *et al.* [95] recently reported experimental results about the generation of coherent extreme ultraviolet radiation by phase-matched high-order difference frequency mixing in a plasma. The plasma was produced by optical field ionisation of atomic and molecular gaseous in an intense laser field. Phase matching for the high-order two-colour $(\omega, 2\omega)$ mixing processes, $9\omega = 6(2\omega) - 3\omega$, was demonstrated by them for the first time.

Zhang *et al.* [103] experimentally demonstrated a sum-frequency generation process using electromagnetically induced transparency with atomic hydrogen as a test medium (to the best of my knowledge, this is the only experiment in hydrogen published so far). The transparency was created by strong coupling through the photoionisation-decay channel which inevitably accompanies the strong laser coupling [103]. They generated Lyman-β coherent radiation at 103 nm with a conversion efficiency of 10^{-4}. They carried out the experiments using two single-longitudinal-mode (SLM) dye laser system and a cw atomic beam apparatus. The two dye lasers were pumped by second and third harmonics of an injection-seeded Nd:YAG laser to generate 656 and 486 nm radiation.

Also experiments have been performed by mixing light from an intense fixed-frequency laser with a tunable light source, leading to tunable radiation in the XUV region. Eichmann *et al.* [93] were the first group, to demonstrate the feasibility of such an experiment using light from a Ti:S laser mixing it with tunable radiation from an optical parametric generator (OPG). They generated tunable radiation up to $\sim$ 31 eV, with a tuning range of about 30% between consecutive harmonics. There are several advantages of using an OPG for the frequency mixing as compared to using the second or third harmonic. One of them is the aspect of tunability and the second is the possibility of identifying and thus studying sum-frequency mixing versus difference-frequency mixing since the two processes lead to different generated wavelengths when the two fields have non-commensurate frequencies. Gaarde *et al.* [96] performed an experiment by mixing light from a terawatt, sub-picosecond Ti:S laser and that from an OPG pumped by the Ti:S laser and compared the efficiencies for these mechanisms in

different gaseous, i.e. in different conditions of laser intensities and wavelengths ranges [96].

Most of the theoretical calculations for frequency mixing processes were performed using numerical integration of the Schödinger equation for a single atom or for a model potential and these studies were mainly for the mixing of two commensurable frequencies.

Lago *et al.* [97] presented a general theoretical analysis of optical-frequency mixing of the radiation of n different laser beams in gaseous media, so they calculated phase-matching conditions for third and fifth order sum and difference frequency mixing between the induced nonlinear polarisation and the generated optical radiation. That was the first theoretical analysis of frequency mixing in an inhomogeneous gas.

Protopapas *et al.* [52] solved the one dimensional Schrödinger equation. They used the Kramers-Hanneberger frame and a model potential for the case of excitation by two commensurable (third harmonic with its fundamental) intense fields. They obtained a strong dependence of the atomic evolution and high-harmonic generation on the relative phase between the two fields.

Ivanov *et al.* [100] considered a semi-classical model solution for H_2^+ and showed how to generate single subfemtosecond pulses and to control harmonic generation by varying the relative phase of the two fields. In their model calculation they dealt with the wave-mixing processes, restricting themselves to the tunneling regime [100]. They illustrated control of phases of the high harmonics using an example of the interaction with intense fundamental radiation and its weak second harmonic, which is linearly polarised along the same axis of the fundamental field.

Protopapas *et al* [99] and Véniard *et al* [101] used a time-dependent method, and Potvliege and Smith [83], [84], and Telnov *et al.* [86] used the Floquet method to study the hydrogen atom in a mixed field. However, these studies were also with commensurable frequencies. Potvliege *et al.* [88] studied the same problem for incommensurable frequencies but for only harmonic generation as in the case we have studied in Chapter 5 for different wavelength of low frequency and high frequency fields. In addition Long *et al.* [98] used a model potential to study

mixing commensurable and incommensurable fields but for harmonic generation.

The main motivation for this study was received from the experiment of Gaarde *et al.* [96] and hence the advantages of using incommensurable fields for a frequency mixing process, such as access to new frequencies, not obtainable by harmonic generation. In addition so far there is no such theoretical study using the Floquet approach. In our calculations we deal with single atom processes and obtained good agreement with the results from the above mentioned experimental study [96] although the experiments were performed in rare gaseous. Note that a very recent publication by Gaarde *et al.* [102], involving similar calculations used a different method. They considered single atom response as well as propagation effects, but for Neon. They solved the time dependent Schrödinger equation with the following basic assumptions; they considered the ground state of the atom to be the only bound state, depletion of the ground state was neglected and as soon as the electron reached in the continuum, it was treated as a particle moving freely in the electromagnetic field, i.e. they neglected the influence of the atomic potential.

In the following sections we will give a general description for a frequency mixing processes and present our applications, results and a discussion involving the experimental results by Gaarde *et al.* [96] and the theoretical results by Gaarde *et al.* [102].

6.2 General description

A multiphoton wave mixing process is either a sum or a difference frequency process. The energy-level diagrams for both sum and difference-frequencies are given in Figure 6.1.

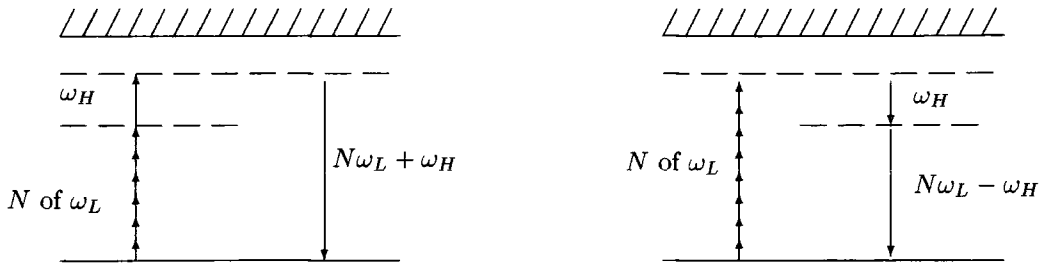

(a) Sum-frequency mixing

(b) Difference-frequency mixing

Figure 6.1:

Generalisation of the Floquet method to a two colour processes is described in Chapter 5. The only thing to change is the calculation of the dipole moment for which the expression now is:

$$\mathbf{d}_{N,\pm 1} = \sum_{n,m} \langle \psi_{n-N,m\mp 1} | e\mathbf{x} | \psi_{n,m} \rangle \tag{6.1}$$

In equation (6.1) $\mathbf{d}_{N,+1}$ is for the sum frequency process, $\mathbf{d}_{N,-1}$ is for the difference frequency process and N is even.

6.3 Applications, results and discussion

In this chapter we report studies of frequency mixing processes when two fields have non-commensurable frequencies. In particular we concentrated on studying sum versus difference frequency generation since this was one of the possibilities offered by using incommensurable frequencies as compared to mixing a field with one its harmonics. In addition to studying the variation of the strength of the dipole moment for the frequency mixing processes, we also studied the variation of the phase of the dipole moment. For both cases we have considered various applications and in all applications we assumed the fields linearly polarised in the same direction.

6.3.1 Rate for three different processes: harmonic generation, sum-frequency mixing, and difference-frequency mixing

First of all, we mixed light from an infrared source with a wavelength of $\lambda_L = 1064$ nm and intensity of $I_L = 10^{13}$ W/cm^2 together with light from a high frequency laser source (Ti:S) with wavelength $\lambda_H = 800$ nm (as well as for $\lambda_H = 700$ nm). We varied the intensity of the high frequency field in the perturbative region $I_H = 10^4 - 10^{10}$ W/cm^2. Figures 6.2 and 6.3 show the results from this set of calculations with $\lambda_H = 800$ nm for various intensities of the high frequency field. Note that Figure 6.2 presents the results for harmonic and for the sum-frequency mixing process and that Figure 6.3 presents results for harmonic generation and for difference-frequency mixing process. Since in these calculations the intensity of the high frequency field is always in the perturbative region we obtain the same trend for all values of I_H, which shows the consistency of the results from each calculation for different intensity of the high frequency field. This behaviour might change if we increase the intensity of the high frequency field further so that it enters the nonperturbative regime. However, as this may cause various computational difficulties, we refrained from attempting these calculations at this stage.

The results obtained so far can be summarised as follows: both sum and difference-frequency mixing processes exhibit the same plateau and cut-off behaviour as does the harmonic generation process. However, the strengths of the signal for both sum and difference frequency processes are lower than the strengths of the harmonics for harmonic generation. As the intensity of the high frequency field increases, the differences in both case decrease. For example when the intensity of the high frequency field is 10^4 W/cm^2 roughly there is roughly a factor of 10^6 difference between the harmonic signals and the frequency mixing signals. On the other hand the difference is only about a factor of 50 when the intensity of the high frequency field is 10^{10} W/cm^2. In fact the change also depends on the energy of the photon. The reason for that there is also a marked change in the strength of the $+1$ (sum frequency) and -1 (difference frequency) signals and this difference is varying as the photon energy (in another word the order of process) is increas-

ing. In general when the photon energy is smaller the difference between the sum-frequency signal and the difference-frequency signal is higher. In the plateau region and afterwards the difference between sum and difference-frequency signals nearly vanishes. The reason for this change with respect to the order of process is as follows: when the number of low-frequency photon N increases the ratio of the frequency of the high frequency field to that of the low frequency field is decreases and so $N\omega_L + \omega_H$ does not differ much from $N\omega_L - \omega_H$.

In order to emphasise the change in the relative strength of the $+1$ signals and -1 signals the following calculations were made: We kept the intensity of the high-frequency field fixed at a value in the perturbative regime ($I_H = 10^6$ W/cm^2) and we chose various wavelength the high-frequency field in the optical spectrum region (λ_H=600, 700, 750, 800, 850 and 900 nm). Figures 6.4 (a) and (b), 6.4 (a) and (b) and 6.6 (a) and (b) present the absolute value of the dipole moment for the three processes versus to photon energy. The corresponding wavelengths of the high frequency field are given above each figure. In each example we obtained the change in the relative strength of the two signals. We also found that the lower the wavelength of the high frequency field the greater the difference between the sum frequency signal and the difference frequency signal. For a high frequency field with a wavelength $\lambda_H = 600$ nm the difference between the sum-frequency mixing signal and difference-frequency signal is greatest and this does not vary very much with respect to the order of the process (see Figure 6.4 (a)). That is due to the frequency of the high frequency field is enough high to be effective. However, as the wavelength of high-frequency field increases the difference between the two signals in the plateau region and beyond gets smaller as expected.

In addition we made a calculation taking the frequency of the second field to be close to the frequency of the fundamental field: for the fundamental field we used $\lambda = 1064$ nm and intensity I= 10^{13} W/cm^2 and for the second field $\lambda = 1053$ nm and intensity I= 10^6 W/cm^2. The results of this calculation are given in Figures 6.4 (a). Although the wavelengths of the two fields were nearly identical, neverthless since the intensity of the second field was much lower, we could still identify sum and difference frequency processes observed a rather small difference between the two signals. However, in the plateau region and beyond the rates for

both processes were nearly identical, as expected.

Furthermore we have decreased the wavelength of the second field to a lower value than that of the fundamental field in order to examine the difference for an infrared field as in the first option with superposition of a lower frequency field ($\lambda = 10.6$ μm and I= 10^6 W/cm^2) in contrast to the first two cases (for results of this calculation see Figure 6.4 (b)). Figure 6.4 (b) shows that the rate for sum and difference frequency processes are identical since the influence of the second field is very small. This is due to the ratio ω_1/ω_2 being nearly zero and the intensity of the second field being still perturbative.

As a final test we took the frequency of the fundamental field as a high frequency with a wavelength $\lambda = 532$ nm and with an intensity I= 10^{13} W/cm^2 and the wavelength of the second field to be either $\lambda = 800$ nm or $\lambda = 1053$ nm with a fixed intensity I= 10^6 W/cm^2. A set of result is given in Figure 6.8 (a).

The results we obtained are in good agreement with the experimental results obtained by Gaarde *et al.* [96] and with the results from the calculations done by Gaarde *et al.* [102]. The experimental results and some results from the calculations of Gaarde *et al.* are given in Figures 6.9, 6.10 and 6.11 for comparison. The only difference between our results and the latter two (experiment as well as theoretical results) is the magnitude of the difference between the harmonic signal and the mixed frequency signal. We obtained - depending on the intensity and wavelength of the second field- that the harmonic signal differs from the mixed signal by between a factor of $50 - 10^4$. In fact the difference Gaarde *et al.* [102] obtained is a factor of 10 to 50, which agrees with the experimental results [96]. We believe that the reason for this discrepancy is not a fundamental problem. In addition to using a different atomic system it is caused by working in a different regime. In all our calculations the parameters of the first field place it in the multiphoton regime ($\gamma \gg 1$) but the intensity of the second field is perturbative. However, Gaarde *et al* [102] are dealing with the same problem in the tunneling regime ($\gamma \ll 1$; which shows the tunability of the light) using the following parameters for the first field. In the case of neon the intensity of the first field is $I_1 = 2.2 \times 10^{14}$ W/cm^2 (or higher) and the wavelength $\lambda_1 = 790$ nm. In addition the intensity of the second field they used is also higher ($I_2 = 10^{11}$

W/cm^2 and $\lambda_2 = 500$ nm) compared to the intensity of the second field we have been using for our calculations. They also concluded that with increasing intensity of the second field the conversion efficiency of the mixing process increases, which adds weight to our argument. Note that the system Gaarde *et al.* investigate in their calculations is the same as that in the experiments [96].

6.3.2 Phase of dipole moment

We also calculated the variation in phase of the dipole moment. These results are given in Tables 6.1, 6.2, 6.3, 6.4, 6.5 and 6.6 for the following fields and processes: in the case of the first three Tables the fundamental field is an infrared field with a wavelength 1064 nm and intensity 10^{13} W/cm^2, and the wavelength of the high frequency field is fixed at 800 nm but each column shows the phase for a given intensity of high frequency field, which is always in the perturbative region. The first three Tables 6.1, 6.2 and 6.3 present the results for harmonic generation, sum-frequency mixing and the difference-frequency mixing, respectively. The last three Tables 6.4, 6.5 and 6.6 present the results that arise from versus wavelengths of the high frequency field with a fixed intensity 10^6 W/cm^2; $\lambda_H = 600, 700, 750, 800, 900, 1053$ nm and 10.6μm. Again each table corresponds to a different process; so Table 6.4, 6.5 and 6.6 are for harmonic generation, sum-frequency mixing and difference-frequency mixing, respectively. Comparing all the results from Tables 6.1, 6.2, 6.3, 6.4, 6.5 and 6.6 we see that for each particular case and for each order of process the phase of the dipole moment in the harmonic generation process differs to that in the sum-frequency mixing process and to that in the difference frequency mixing processes. In other words considering a particular case with a a low-frequency field and a second field shows that for each order of process the phase of the dipole moment for the harmonic generation process is different that in either mixing frequency process. Also the phase of the dipole moment for the sum-frequency mixing process turns out to be different from that for the difference frequency process. This is true no matter whether the frequency of the second field is higher or lower than the fundamental.

Moreover, analysing Tables 6.1, 6.2 and 6.3 one sees that for each processes (harmonic generation, sum-frequency mixing and difference-frequency mixing) for

each order of process the phase of the dipole moment hardly changes with change in intensity of the high frequency field in the intensity region $10^4 - 10^{10}$ W/cm^2. This is due to this intensity range being perturbative However, when the intensity of the high frequency field is kept fixed at 10^6 W/cm^2 and the wavelength of the high frequency field is varied, we have found that the phase of the dipole moment changes in the case of sum and difference frequency generation but not for harmonic generation (see Tables 6.4, 6.5 and 6.6). This is again due to the second field being weak enough so that it does not affect the the dipole moment. But the frequency mixing processes occur due to the second field, and so we expect that the phase of the dipole moment to change with a change in the wavelength of the second field.

Gaarde *et al.* [102] also obtained differences between the phase of the dipole moment for three different processes. They studied the change in the dipole phase that resulted from changing the intensity of the low-frequency field.

6.4 Conclusions

In conclusion, we have studied sum and difference frequency processes in hydrogen atom using incommensurable fields. In the main we have considered a strong infrared field as the fundamental field and conversion efficiency for harmonic generation, sum-frequency and difference frequency processes have been studied for a weak high frequency field. We have found that adding such a field to the system does not significantly alter the strengths of the harmonics of the fundamental field. But it produces frequency mixing signals which exhibit the same plateau and cut-off behaviour as the harmonics. However, the strength of the frequency mixing signals is weaker than the harmonic signals. The difference varies with intensity and wavelength of both fields. The strength of the sum and the difference-frequency mixing also differ from each other. Usually the strength of the sum-frequency signal is higher than that of difference frequency. In fact this difference also depends on the frequency and intensity of the second field and therefore on the order of the process. When the ratio of the frequency of the fundamental field to the frequency of the second field is small, then for higher order of processes, this ratio decreases even more because the term $N\omega_L + \omega_H$ be-

comes nearly identical to the term $N\omega_L - \omega_H$. As a consequence of this equality the difference between the sum frequency signal and difference frequency signal decreases, sometimes even the strengths of the two signals become identical for these higher order of processes.

Moreover, the behaviour of the phase of the dipole moment also differs from one process to the other. Varying the intensity of the high frequency field in the perturbative regime (from 10^4 W/cm^2 to 10^9 W/cm^2) does not much change the phase of the dipole moment for harmonic generation and mixing frequency process. Varying the frequency of the high frequency field at fixed intensity resulted in no changes in the phase of the dipole moment for harmonic generation. However, it changes in the case of frequency mixing processes. This is again a consequence of producing new frequencies during the frequency mixing process.

Finally we believe that studying the mixing processes helps one to understand the production of harmonics and moreover allows one to obtain photon frequencies which cannot be obtained through harmonic generation.

Table 6.1: Change in the phase of the dipole moment for harmonic generation with change in intesity of the high-frequency field. The fundamental field has a wavelength $\lambda_L = 1064$ nm and an intensity I= 10^{13} W/cm^2. The high frequency field has a wavelength $\lambda_H = 800$ nm; its intensity is indicated at the top of each column.

	Phase of Dipole Moment (deg)					
N	10^4 W/cm^2	10^5 W/cm^2	10^6 W/cm^2	10^7 W/cm^2	10^8 W/cm^2	10^9 W/cm^2
3	0.5976 (-02)	0.5976 (-02)	0.5976 (-02)	0.5976 (-02)	0.5979 (-02)	0.6003 (-02)
5	0.1487 (+01)	0.1487 (+01)	0.1487 (+01)	0.1487 (+01)	0.1487 (+01)	0.1491 (+01)
7	0.2193 (+02)	0.2193 (+02)	0.2193 (+02)	0.2193 (+02)	0.2193 (+02)	0.2194 (+02)
9	0.1020 (+03)	0.1020 (+03)	0.1020 (+03)	0.1020 (+03)	0.1020 (+03)	0.1019 (+03)
11	0.9763 (+01)	0.9763 (+01)	0.9763 (+01)	0.9762 (+01)	0.9758 (+01)	0.9710 (+01)
13	0.1675 (+03)	0.1675 (+03)	0.1675 (+03)	0.1675 (+03)	0.1675 (+03)	0.1674 (+03)
15	-.1777 (+03)	-.1777 (+03)	-.1777 (+03)	-.1777 (+03)	-.1778 (+03)	-.1780 (+03)
17	-.7418 (+02)	-.7418 (+02)	-.7418 (+02)	-.7419 (+02)	-.7420 (+02)	-.7437 (+02)
19	0.4533 (+02)	0.4533 (+02)	0.4533 (+02)	0.4533 (+02)	0.4532 (+02)	0.4517 (+02)
21	0.1695 (+03)	0.1695 (+03)	0.1695 (+03)	0.1695 (+03)	0.1694 (+03)	0.1693 (+03)
23	-.6393 (+02)	-.6393 (+02)	-.6393 (+02)	-.6393 (+02)	-.6390 (+02)	-.6406 (+02)
25	0.6903 (+02)	0.6903 (+02)	0.6903 (+02)	0.6903 (+02)	0.6442 (+02)	0.6424 (+02)

Table 6.2: Change in phase of the dipole moment for sum-frequency mixing process with change in intensity of the high-frequency field. The fundamental field has a wavelength $\lambda_L = 1064$ nm and an intensity I= 10^{13} W/cm^2. The high frequency field has a wavelength $\lambda_H = 800$ nm; its intensity is indicated at the top of each column.

	Phase of Dipole Moment (deg)					
N	10^4 W/cm^2	10^5 W/cm^2	10^6 W/cm^2	10^7 W/cm^2	10^8 W/cm^2	10^9 W/cm^2
2	0.1524 (-01)	0.1524 (-01)	0.1524 (-01)	0.1520 (-01)	0.1487 (-01)	0.1220 (-01)
4	0.1817 (+01)	0.1817 (+01)	0.1817 (+01)	0.1817 (+01)	0.1817 (+01)	0.1813 (+01)
6	0.1596 (+02)	0.1596 (+02)	0.1596 (+02)	0.1596 (+02)	0.1597 (+02)	0.1595 (+02)
8	0.1336 (+03)	0.1336 (+03)	0.1336 (+03)	0.1336 (+03)	0.1336 (+03)	0.1332 (+03)
10	0.1691 (+03)	0.1691 (+03)	0.1691 (+03)	0.1691 (+03)	0.1691 (+03)	0.1691 (+03)
12	0.1604 (+03)	0.1604 (+03)	0.1604 (+03)	0.1604 (+03)	0.1604 (+03)	0.1604 (+03)
14	-.1114 (+03)	-.1114 (+03)	-.1114 (+03)	-.1114 (+03)	-.1115 (+03)	-.1115 (+03)
16	-.7492 (+01)	-.7492 (+01)	-.7492 (+01)	-.7492 (+01)	-.7511 (+01)	-.7502 (+01)
18	0.8420 (+02)	0.8420 (+02)	0.8420 (+02)	0.8420 (+02)	0.8419 (+02)	0.8437 (+02)
20	-.1787 (+03)	-.1787 (+03)	-.1787 (+03)	-.1787 (+03)	-.1787 (+03)	-.1786 (+03)
22	-.6329 (+02)	-.6329 (+02)	-.6329 (+02)	-.6329 (+02)	-.6328 (+02)	-.6325 (+02)
24	0.6395 (+02)	0.6395 (+02)	0.6395 (+02)	0.6395 (+02)	0.6275 (+02)	0.6270 (+02)

Table 6.3: Change in phase of the dipole moment for difference-frequency mixing process with change in intensity of the high-frequency field. The fundamental field has a wavelength $\lambda_L = 1064$ nm and an intensity I= 10^{13} W/cm^2. The high frequency field has a wavelength $\lambda_H = 800$ nm; its intensity is indicated at the top of each column.

	Phase of Dipole Moment (deg)					
N	10^4 W/cm^2	10^5 W/cm^2	10^6 W/cm^2	10^7 W/cm^2	10^8 W/cm^2	10^9 W/cm^2
2	0.7126 (-02)	0.7133 (-02)	0.7204 (-02)	0.8007 (-02)	0.1799 (+03)	0.1800 (+03)
4	0.4680 (+00)	0.4680 (+00)	0.4680 (+00)	0.4681 (+00)	0.4689 (+00)	0.4759 (+00)
6	0.1497 (+02)	0.1497 (+02)	0.1497 (+02)	0.1497 (+02)	0.1497 (+02)	0.1505 (+02)
8	0.1435 (+03)	0.1435 (+03)	0.1435 (+03)	0.1436 (+03)	0.1436 (+03)	0.1438 (+03)
10	-.1319 (+03)	-.1319 (+03)	-.1319 (+03)	-.1319 (+03)	-.1319 (+03)	-.1319 (+03)
12	-.1626 (+03)	-.1626 (+03)	-.1626 (+03)	-.1626 (+03)	-.1626 (+03)	-.1626 (+03)
14	-.1306 (+02)	-.1306 (+02)	-.1306 (+02)	-.1306 (+02)	-.1307 (+02)	-.1309 (+02)
16	0.1581 (+02)	0.1581 (+02)	0.1581 (+02)	0.1581 (+02)	0.1580 (+02)	0.1571 (+02)
18	0.1333 (+03)	0.1333 (+03)	0.1333 (+03)	0.1333 (+03)	0.1332 (+03)	0.1331 (+03)
20	-.9872 (+02)	-.9872 (+02)	-.9872 (+02)	-.9872 (+02)	-.9873 (+02)	-.9884 (+02)
22	0.3302 (+02)	0.3302 (+02)	0.3302 (+02)	0.3302 (+02)	0.3301 (+02)	0.3289 (+02)
24	0.1676 (+03)	0.1676 (+03)	0.1676 (+03)	0.1676 (+03)	0.1671 (+03)	0.1670 (+03)

Table 6.4: Change in phase of the dipole moment for harmonic generation with change in wavelength of the high-frequency field. The fundamental field has a wavelength $\lambda_L = 1064$ nm and an intensity I= 10^{13} W/cm^2. The high frequency field has an intensity I=10^6 W/cm^2; its wavelength is indicated on the top of each column.

	Phase of Dipole Moment (deg)						
N	600 nm	700 nm	750 nm	800 nm	900 nm	1053 nm	10.6μm
3	0.5976 (-02)	0.5976 (-02)	0.5976 (-02)	0.5976 (-02)	0.5976 (-02)	0.5976 (-02)	0.5976 (-02)
5	0.1487 (+01)	0.1487 (+01)	0.1487 (+01)	0.1487 (+01)	0.1487 (+01)	0.1487 (+01)	0.1487 (+01)
7	0.2193 (+02)	0.2193 (+02)	0.2193 (+02)	0.2193 (+02)	0.2193 (+02)	0.2193 (+02)	0.2193 (+02)
9	0.1020 (+03)	0.1020 (+03)	0.1020 (+03)	0.1020 (+03)	0.1020 (+03)	0.1020 (+03)	0.1020 (+03)
11	0.9763 (+01)	0.9763 (+01)	0.9763 (+01)	0.9763 (+01)	0.9763 (+01)	0.9765 (+01)	0.9763 (+01)
13	0.1675 (+03)	0.1675 (+03)	0.1675 (+03)	0.1675 (+03)	0.1675 (+03)	0.1675 (+03)	0.1675 (+03)
15	-.1777 (+03)	-.1777 (+03)	-.1777 (+03)	-.1777 (+03)	-.1777 (+03)	-.1777 (+03)	-.1777 (+03)
17	-7418 (+02)	-.7418 (+02)	-.7418 (+02)	-.7418 (+02)	-.7418 (+02)	-.7418 (+02)	-.7418 (+02)
19	0.4533 (+02)	0.4533 (+02)	0.4533 (+02)	0.4533 (+02)	0.4533 (+02)	0.4533 (+02)	0.4533 (+02)
21	0.1695 (+03)	0.1695 (+03)	0.1695 (+03)	0.1695 (+03)	0.1695 (+03)	0.1695 (+03)	0.1695 (+03)
23	-.6388 (+02)	-.6388 (+02)	-.6388 (+02)	-.6393 (+02)	-.6388 (+02)	-.6388 (+02)	-.6388 (+02)
25	0.6444 (+02)	0.6444 (+02)	0.6444 (+02)	0.6903 (+02)	0.6444 (+02)	0.6444 (+02)	0.6444 (+02)

Table 6.5: Change in phase of the dipole moment for sum-frequency generation with change in wavelength of the high-frequency field. The fundamental field has a wavelength $\lambda_L = 1064$ nm and an intensity I= 10^{13} W/cm^2. The high frequency field has an intensity I=10^6 W/cm^2; its wavelength is as indicated on the top of each column.

	Phase of Dipole Moment (deg)						
N	600 nm	700 nm	750 nm	800 nm	900 nm	1053 nm	10.6μm
2	0.8969 (-01)	0.4649 (-01)	0.2410 (-01)	0.1524 (-01)	0.2621 (-01)	-.2932 (-02)	-.1684 (-01)
4	0.5244 (+01)	0.8206 (+01)	0.4111 (+01)	0.1817 (+01)	0.4664 (+01)	-.4538 (+00)	-.7302 (+01)
6	-.1615 (+03)	0.7594 (+02)	0.8745 (+02)	0.1596 (+02)	0.4370 (+02)	-.8737 (+01)	-.5218 (+02)
8	0.1817 (+02)	-.5842 (+02)	-.1849 (+02)	0.1336 (+03)	-.1635 (+03)	-.5952 (+01)	-.1946 (+02)
10	-.9774 (+02)	-.1351 (+03)	-.1413 (+03)	0.1691 (+03)	0.3495 (+02)	-.8668 (+02)	-.4213 (+02)
12	-.1438 (+03)	0.1790 (+03)	-.1773 (+03)	0.1604 (+03)	0.1618 (+03)	0.1058 (+03)	0.1564 (+03)
14	-.3801 (+02)	-.1021 (+03)	-.1301 (+03)	-.1114 (+03)	-.1716 (+03)	-.1730 (+03)	0.1536 (+03)
16	0.8041 (+02)	-.1506 (+01)	-.2403 (+02)	-.7492 (+01)	-.6643 (+02)	-.9696 (+02)	-.1174 (+03)
18	-.1572 (+03)	0.1083 (+03)	0.9353 (+02)	0.8420 (+02)	0.5391 (+02)	0.1973 (+02)	0.5408 (+01)
20	-.3250 (+02)	-.1355 (+03)	-.1446 (+03)	-.1787 (+03)	0.1791 (+03)	0.1459 (+03)	0.1374 (+03)
22	0.9295 (+02)	-.1470 (+02)	-.2039 (+02)	-.6329 (+02)	-.5302 (+02)	-.8426 (+02)	-.8494 (+02)
24	-.1538 (+03)	0.1093 (+03)	0.1049 (+03)	0.6395 (+02)	0.7659 (+02)	0.4782 (+02)	0.5706 (+02)

Table 6.6: Change in phase of the dipole moment for difference- frequency generation. The fundamental field has a wavelength $\lambda_L = 1064$ nm with change in wavelength of the high-frequency field and an intensity I= 10^{13} W/cm^2. The high frequency field has an intensity I=10^6 W/cm^2; its wavelength indicated on the top of each column.

	Phase of Dipole Moment (deg)						
N	600 nm	700 nm	750 nm	800 nm	900 nm	1053 nm	10.6μm
2	0.1687 (-01)	0.9006 (-02)	0.6978 (-02)	0.7204 (-02)	0.5351 (-02)	0.1800 (+03)	0.2183 (-01)
4	0.3742 (+00)	0.3790 (+00)	0.4122 (+00)	0.4680 (+00)	0.4922 (+00)	-.2478 (+00)	0.3869 (+01)
6	0.9466 (+01)	0.9746 (+01)	0.1200 (+02)	0.1497 (+02)	0.1303 (+02)	-.2835 (+02)	0.1735 (+03)
8	0.3460 (+02)	-.2695 (+00)	0.5942 (+02)	0.1435 (+03)	-.9486 (+02)	-.8995 (+02)	-.1217 (+03)
10	-.1272 (+03)	-.1052 (+03)	-.1312 (+03)	-.1319 (+03)	-.4768 (+02)	-.3031 (+02)	0.1333 (+03)
12	-.1211 (+03)	-.1368 (+03)	-.1594 (+03)	-.1626 (+03)	-.1044 (+03)	-.1273 (+03)	0.3708 (+02)
14	-.6813 (+02)	-.3049 (+02)	-.2665 (+02)	-.1306 (+02)	0.1962 (+02)	0.4608 (+02)	0.3071 (+02)
16	-.2386 (+01)	-.1778 (+02)	-.3099 (+01)	0.1581 (+02)	0.8708 (+02)	-.2448 (+02)	0.1297 (+03)
18	0.1248 (+03)	0.9901 (+02)	0.1139 (+03)	0.1333 (+03)	-.1529 (+03)	0.1304 (+03)	-.1070 (+03)
20	-.1044 (+03)	-.1346 (+03)	-.1190 (+03)	-.9872 (+02)	-.2522 (+02)	-.9085 (+02)	0.2394 (+02)
22	-.1565 (+02)	-.4725 (+01)	0.1175 (+02)	0.3302 (+02)	0.1041 (+03)	0.4900 (+02)	0.1593 (+03)
24	0.2373 (+02)	0.1273 (+03)	0.1448 (+03)	0.1676 (+03)	-.1262 (+03)	-.1696 (+03)	-.6251 (+02)

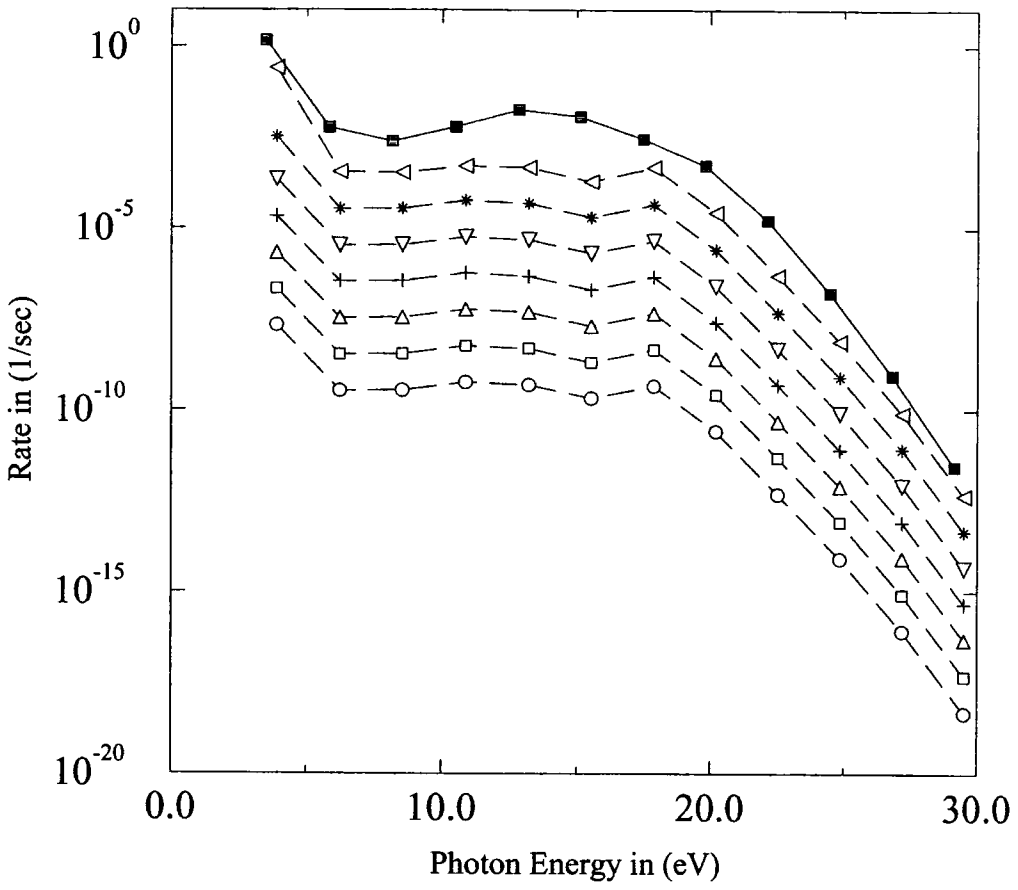

Figure 6.2: The strength of the dipole moment with respect to the photon energy for two colour harmonics generation and sum-frequency geneartion for the following laser field parameters (Note L, indicates the low-frequency and H, indicates the high frequency field): the wavelengths $\lambda_L = 1064$ nm and $\lambda_H = 800$ nm; the intensities $I_L = 10^{13}$ W/cm^2 and I_H is varying. The solid curve with ■ presents the results from harmonic generation for all I_H. The other curves with markers show the results for sum-frequency. The markers identify the results from the different intensity of the high frequency field: ○; 10^4 W/cm^2, □; 10^5 W/cm^2, △; 10^6 W/cm^2, +; 10^7 W/cm^2, ▽; 10^8 W/cm^2, ∗; 10^9 W/cm^2, ◁; 10^9 W/cm^2.

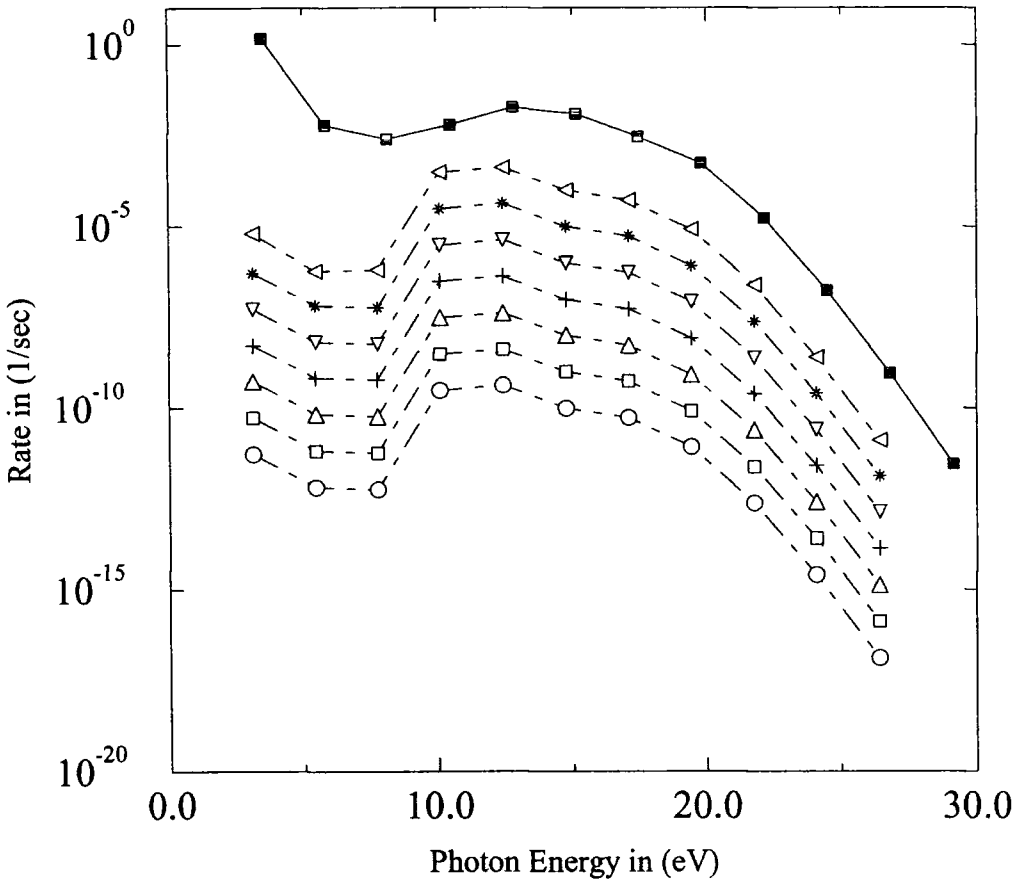

Figure 6.3: The strength of the dipole moment with respect to the photon energy for two colour harmonics generation and difference-frequency generation for the following laser field parameters (Note L, indicates the low-frequency and H, indicates the high frequency field): the wavelengths $\lambda_L = 1064$ nm and $\lambda_H = 800$ nm; the intensities $I_L = 10^{13}$ W/cm^2 and I_H is varying. The solid curve with ■ presents the results from harmonic generation for all I_H. The other curves with markers show the results for sum-frequency. The markers identify the results from the different intensity of the high frequency field: ○; 10^4 W/cm^2, □; 10^5 W/cm^2, △; 10^6 W/cm^2, +; 10^7 W/cm^2, ▽; 10^8 W/cm^2, ∗; 10^9 W/cm^2, ◁; 10^9 W/cm^2.

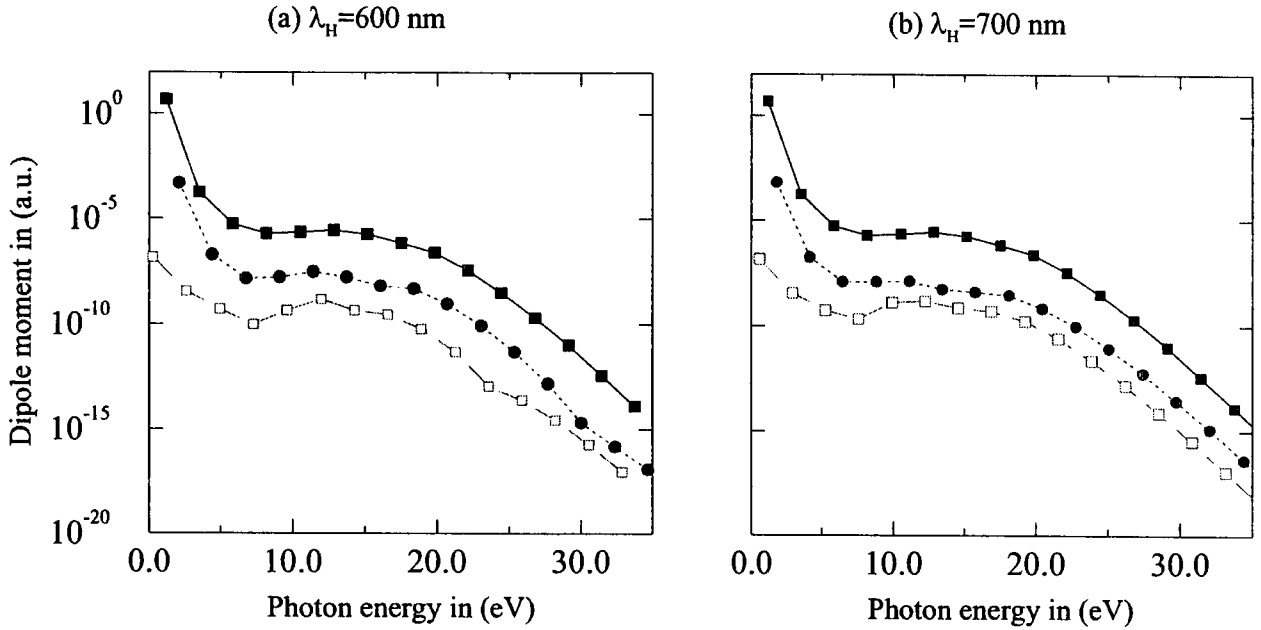

Figure 6.4: The strength of the dipole moment with respect to the photon energy for the mixing frequency processes for the following fields: Low-frequency field; wavelength $\lambda_L = 1064$ nm and intensity $I_L = 10^{13}$ W/cm^2. The intensity of the high frequency field $I_H = 10^6$ W/cm^2 for both figures (a), (b) and the wavelengths are given above each figures. The solid curve with the ■ presents the results from the harmonic generation, dotted curves with filled ○ presents the results from the sum-frequency signals and the dashed line with □ presents the results from the difference-frequency signals.

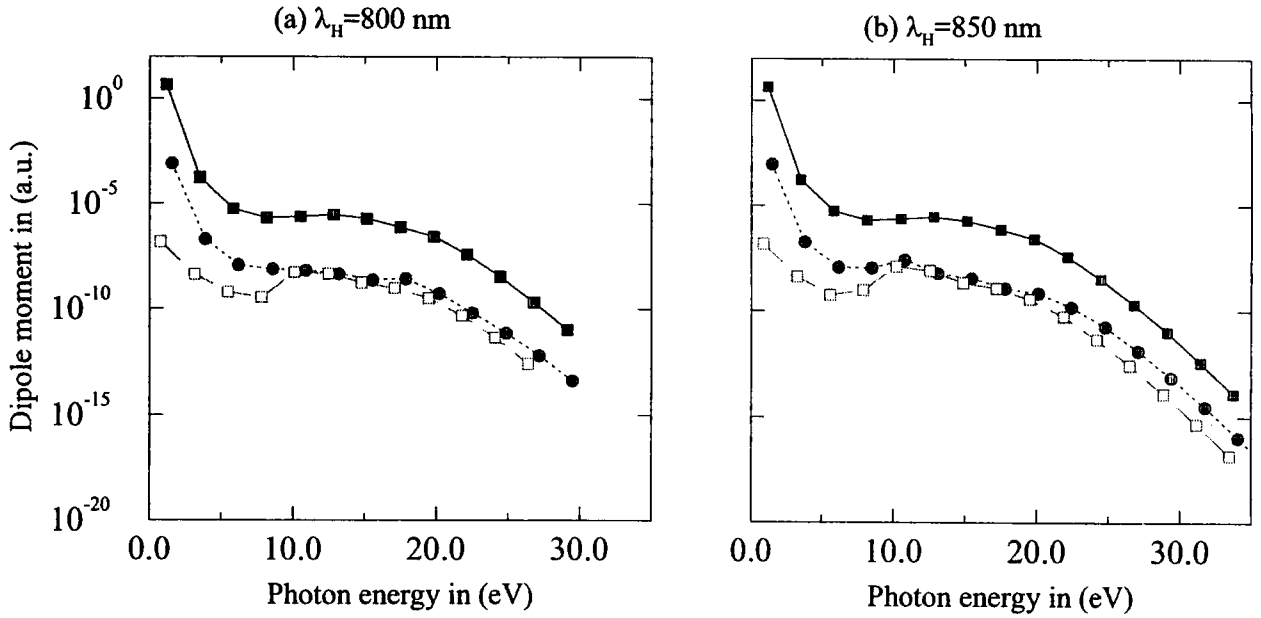

Figure 6.5: The same as Figure 6.4 (a-b) but for different wavelengths of the high frequency fields. The wavelengths of the high frequency field are given at top of each figure.

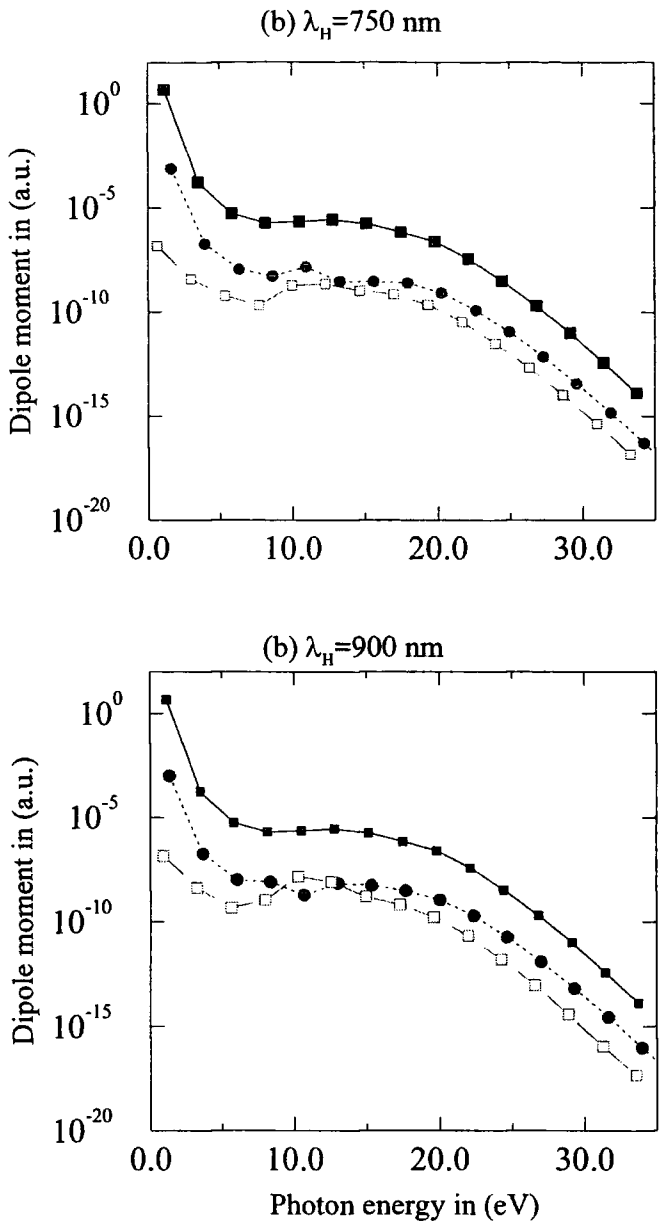

Figure 6.6: The same as Figure 6.4 (a-b) but for different wavelengths of the high frequency fields. The wavelengths of the high frequency field are given at top of each figure.

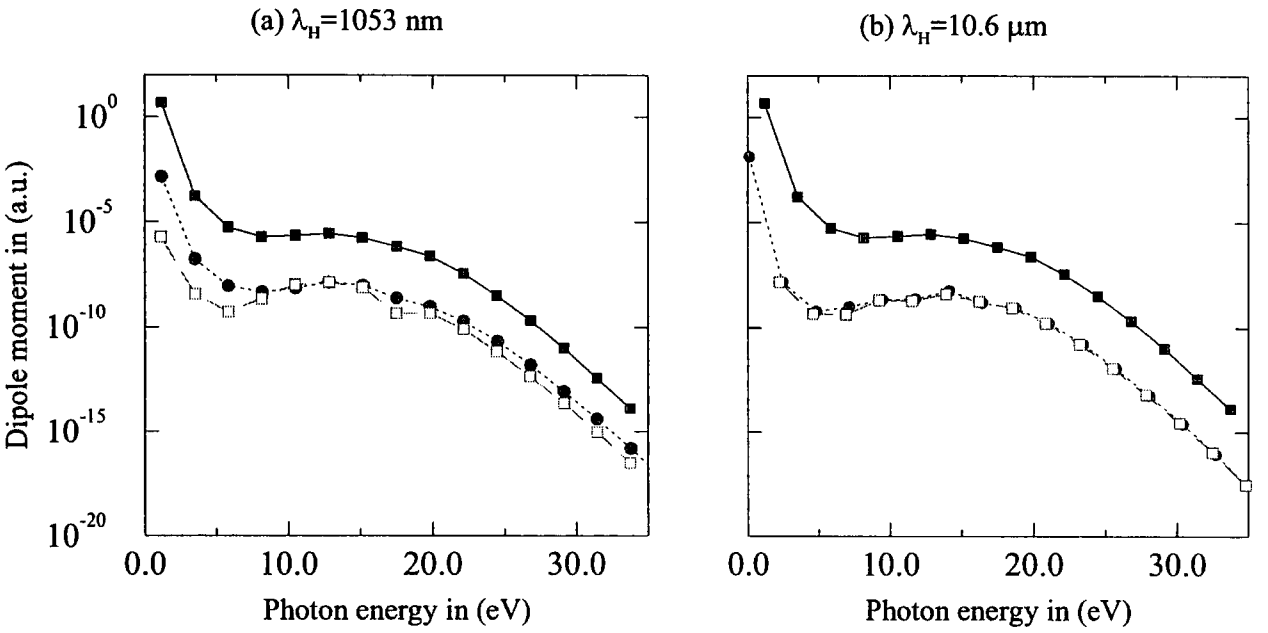

Figure 6.7: The same as Figure 6.4 (a-b) but for different wavelengths of the high frequency fields. The wavelengths of the high frequency field are given at top of each figure.

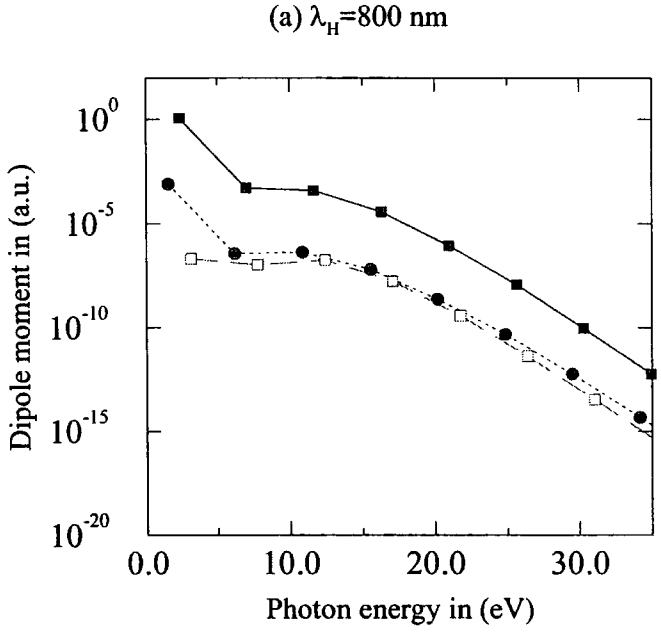

Figure 6.8: The same as Figure 6.4 (a-b) but wavelengths of the fundamental field is 532 nm. The wavelengths of the second field is given at top.

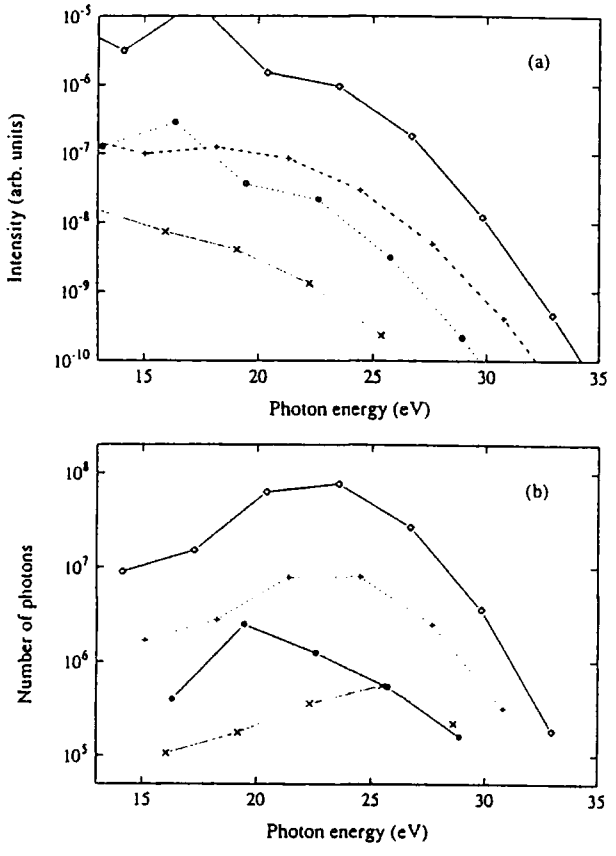

Figure 6.9: Results of mixing frequency processes from the experimental study of the Gaarde *et al.* [89] and the theoretical calculations by Gaarde *et al.* [96]. The intensity of the fields is as follows: the results are for Xenon, $I_1 = 0.87 \times 10^{14}$ W/cm^2 and $I_2 = 10^{11}$ W/cm^2. The notations of the markers are as follows: $\diamond$; harmonic generation, +; the sum-frequency, • difference- frequency and $\times$ sum-frequency process with 2-photons.

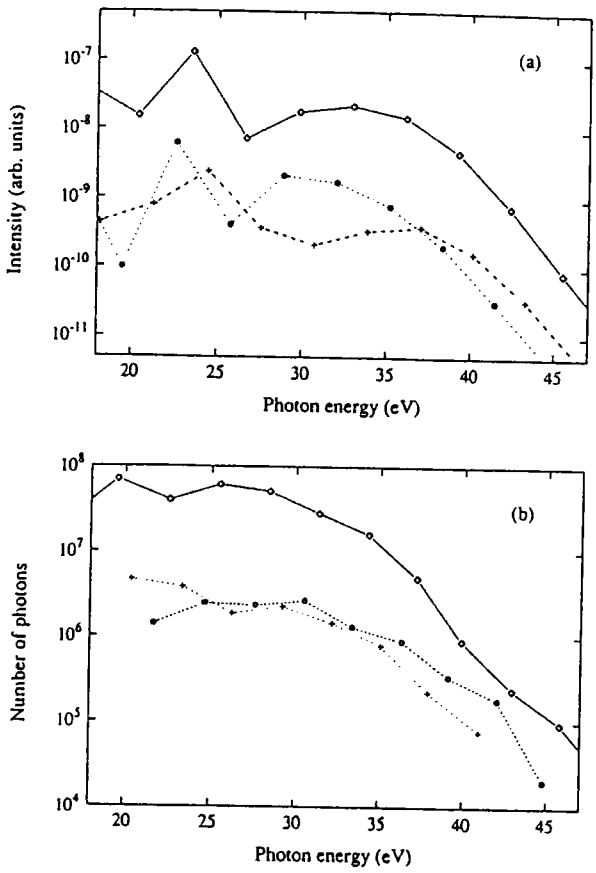

Figure 6.10: The same as Figure 6.9 but for Argon with the folowing laser parameters. $I_1 = 1.6 \times 10^{14}$ W/cm^2 and $I_2 = 10^{11}$ W/cm^2.

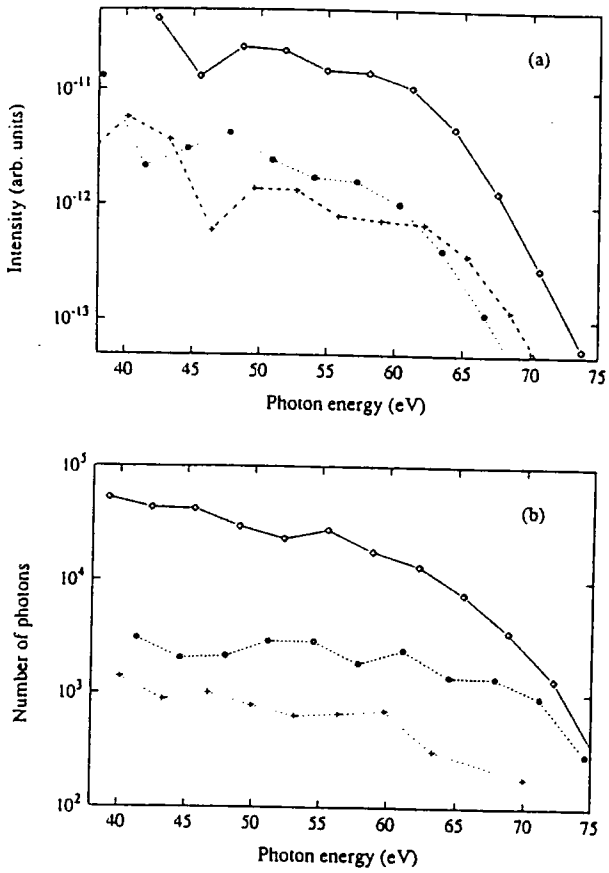

Figure 6.11: The same as Figure 6.9 but for Ne with the folowing laser parameters. $I_1 = 3.1 \times 10^{14}$ W/cm^2 and $I_2 = 10^{11}$ W/cm^2.

Chapter 7

Application of a static field in addition to an ac-field

7.1 Overview

The main motivation for this chapter came from the work by Bao and Starace [104]. In that paper they presented the rates of high harmonic generation from single-atom or ions in the presence of a static electric field in addition to the laser field. They did the calculation using an extension of the zero-range potential model treatment of Becker *et al.* [16] and they presented their results for two cases: harmonic generation by H^- using a CO_2 laser and by Ar using a Nd:YAG laser. For a static field of 100 kV/cm they found strong production of even harmonics and the intensities of odd harmonics near the low-order end of the plateau were increased by one or more orders of magnitude [104]. However, the finding for the odd harmonics disagrees with the results from the two-colour experiment of Perry *et al.* [91]. In fact it is expected that the effect of a dc-field on multiphoton processes would be similar to the effect of a two-colour field (whose frequencies are commensurable) due to the following reason. The variation of the fundamental field is nearly constant when compared to the variation of the harmonic field.

We mainly studied the harmonic generation rate from the hydrogen atom in the presence of a static electric field using the Floquet technique. In the literature there is another study considering a hydrogen atom. This has been done by Hakuta *et al.* [105] and [106]. However, this study was restricted to second order harmonic generation. They have shown theoretically and experimentally that a transparency can be induced using dc-electric field coupling and have proven the

possibility of obtaining high conversion efficiency for second harmonic generation (SHG) of Lyman-α radiation in atomic hydrogen. They applied a dc-field to dress the 2s and 2p states, and observed the reduced absorption and the enhanced nonlinear susceptibility when the dc coupling exceeded the Doppler broadening of the SHG radiation [105], [106].

There is also a model calculations that has been done by Thomas [107],[108]. In this model the author adopted the two-level system as the simplest model with which one can test the influence of a static field on the multiphoton processes induced by an oscillating field, the incorporation of further levels being merely a computational problem [107]. The author carried out an analytic treatment of the effects of the static field on the multiphoton spectrum of a degenerate two-level system. Then, that is followed by the numerical treatment of a nondegenerate two-level system. The model two-level system has energy levels $E_2 = -E_1 = 0.5 \times 10^{-3}$ and the dipole transition matrix elements $\mu_{11} = \mu_{22} = 0$ and $\mu_{12} = \mu_{21} = 1 = \mu$, so that the states $|1\rangle$ and $|2\rangle$ are of opposite parity and the allowed transition between the levels are governed by atomic selection rules. The peak value of the oscillating field strength used in the calculations was 5×10^{-4} a.u. ($\simeq 3 \times 10^8$ V/m) [107]. The result of the calculations confirmed that the enhancement of the multiphoton spectrum whose resonances are more power broadened and will appear at higher frequencies than it would be in the absence of the static field [107], [108]. One should also mention that some of the earliest work which had been done using a classical model by Noid and Stine [109] and a semiclassical model by Chu *et al.* [110], both for multiphoton excitation of the HF molecule, confirmed the enhancement of collisionless multiphoton excitation of HF molecule in an external static electric field with various nonlinear optical effects appearing at much lower oscillating field strengths than they would in the absence of the static field.

We also have done a set of calculations using a Yukawa potential as a model potential in order to do a comparison between our Floquet results and Bao and Starace's results. In this model of H^- the Yukawa potential is

$$V(r) = -\beta \frac{\exp(-r/a_0)}{r} \tag{7.1}$$

where $\beta = 1.100854$ a.u. and $a_0 = 1.0$ a.u. This model was used previously to

discuss multiphoton detachment of H^- by Shakeshaft *et al.* [111] and by Potvliege *et al.* [112]. The potential $V(r)$ supports only one bound state, with a binding energy of -0.0275654 a.u., that is, about -0.750 eV, close to the binding energy -0.7551 eV for the real H^-. Furthermore, the solution of the Schrödinger equation for an electron moving in $V(r)$ yields a radial probability distribution close to the distribution obtained by integrating an accurate two-electron probability density for H^- over the coordinates of one of the electrons [112]. First of all, we calculated the multiphoton detachment rate and harmonic generation rate for a Yukawa potential H^- in a CO_2 laser field alone and compared the rate for multiphoton detachment with the results obtained by Potvliege *et al.* [112] and the rate for harmonic generation rate with the results from the literature such as [113], [114] and [104]. We then added the static electric field to observe its influence on the harmonic generation.

In fact before analysing and calculating the influence of the static field on the harmonic generation rate it is interesting to analyse the influence of a static electric field on the rate of ionisation/detachment of atoms or ions in the laser field. There are several work in the literature that have been done in order to investigate the influence of a static electric field on the photodetachment rate. As far as we are aware, Arutyunyan and Askaryan [115] have given the first qualitative overview of the general process of multiphoton detachment in the presence of a static uniform electric field. They focused on the dependence of the detachment process on the laser frequency and on the field intensities. Nikishov [116] gave a general formal solution for the multiphoton transition rates using a gauge in which both fields are described by a vector potential. The author present detailed results of the influence of the static electric field on the multiphoton detachment process, however, for only two cases: the case of laser photons that are linearly polarised perpendicular to the static field and the case of the low-frequency limit. Slonim and Dalidchik [117] have treated both single photon and multiphoton detachment of negative ions in a static uniform electric field. For the single-photon case, they treated the coupling of the negative ion to the electromagnetic field perturbatively for arbitrarily polarised incident photons. For the multiphoton case, only circularly polarisation was considered. They treated the effects of both a static

uniform electric field and a circularly polarised electromagnetic field nonperturbatively. Manakov and Fainshtein [118] also considered the decay of a weakly bound electron in both a static uniform electric field and a circularly polarised electromagnetic field. They showed that the presence of the electromagnetic field could increase the rate of decay by tunneling by several orders of magnitude.

More recent works in this field are the researches on multiphoton detachment of the H^- ion (see [119]- [122]). Among these the first one is more general and closer to our work. In this paper Gao and Starace presented a theory of single-photon and multiphoton detachment processes in the presence of a static uniform electric field for a s-electron bound initially in a short-range potential. Their calculations were not restricted to weak laser intensities or to weak static-field strengths and depended only on (a) the dipole approximation and (b) the approximation that the final state electron-atom interactions were ignored. They considered only the case of H^- in both a linearly polarised light along the static-field direction and a circularly polarised light propogated along the static-electric field direction.

For the circularly polarised case they showed that the static and laser field effect were uncoupled and that near the threshold, weak static-electric field modulation factors for $N-$photon detachment cross sections were dependent on N.

For the linearly polarised case, which is the most interesting case the following processes were observed. First, the effects of a weak static electric field on N-photon detachment cross sections near threshold were shown to be described by two modulation factors, one for odd N and one for even N, which depended only on a scaled energy. Second, for photodetachment in a static electric field, effects of static-field-induced electron-photon interactions were demonstrated. It was shown that the photodetachment cross section oscillates with respect to the field strength of the static electric field. Third, the life time against field ionisation was presented. It was shown that the lifetime τ of H^- in an external static uniform electric field decreases with increasing field strength of the static field. Finally, the cross section for electric-field-induced stimulated emission of photons was obtained and it was shown that the stimulated emission cross section increases with increasing field strength of the static-electric-field and the stimulated emission cross section can be much larger for longer wavelengths.

Furthermore we have studied multiphoton processes for a two-colour process with commensurable frequencies for a comparison of our dc-field results and those two-colour results.

7.2 Theory

We have calculated the rate for harmonic generation as well as for ionisation for an H-atom in the presence of a static electric field together with an ac-field. The laser field and the static field are described by

$$\mathbf{E}(t) = (E_S + E_L \sin \omega t)\hat{\mathbf{k}} \tag{7.2}$$

and the vector potential is

$$\mathbf{A}(t) = c\Big(\frac{E_L}{\omega} \cos \omega t - E_S t\Big)\hat{\mathbf{k}} \tag{7.3}$$

where c is the velocity of light, ω is the laser frequency, and E_S and E_L are the amplitudes of the static and laser fields.

Recall the time-dependent Schrödinger equation 2.17 for this atomic system,

$$i\hbar \frac{d}{dt} |\Psi(t)\rangle \; = \; [H_a + V(t)] \, |\Psi(t)\rangle \tag{7.4}$$

where $|\Psi(t)\rangle$ is the required solution, H_a is the field free atomic Hamiltonian and $V(t)$ is the interaction of the field with the atom. The interaction potential should be expressed in the length gauge, because, the dipole moment for a dc-field can not be treated in the velocity gauge. Thus,

$$V(t) = -e\mathbf{E}(t).\mathbf{r} \tag{7.5}$$

Although test calculations have been done treating both fields in the length gauge, due to the convergence difficulties in the length gauge we have decided to use a mixed-gauge in a way that the dc-field is treated in the length gauge and the ac-field in the velocity gauge. A set of results from the two calculations, in order to demonstrate their agreement, and a numerical discussion about convergence, in order to argue the convenience of using a mixed gauge, will be given later.

Before making the Floquet ansatz and and Fourier expansion in order to pass to the time-independent theory, note that there have been two different ways of treating the interaction potential:

- The interaction due to the ac-field is treated nonperturbatively by the inverse iteration technique, as in the case when there is no contribution from the dc-field, and then the effect of the dc-field interaction is obtained using Jacobi iteration on this system.

- The interaction potential from ac-field plus dc-field is treated fully nonperturbatively.

A set of results from both calculations as well as the advantages and disadvantages of both methods will be given later. However, the main calculations have been done using the latter method.

7.3 Choosing a suitable gauge

All the way through this thesis the calculations of wave functions have been done in the velocity gauge because the Floquet-Sturmian technique is not so good in the length gauge. However, the velocity gauge is not convenient to use in order to calculate the wave function and the quasi-energy for a dc-field. As a consequence of this we have done various tests in the length gauge in order to ascertain the convergence of the ionisation rate and the harmonic generation rate with respect to the θ- parameter and the basis set used. The first set of tests were for an infrared field with $\lambda = 1064$ nm and intensity I= 10^{13} W/cm^2. This particular laser was chosen in view of its practical use. First of all we tried to obtain stability of the ionisation rate with respect to the θ-parameter. From the tests we observed that even though one may reach stability in a particular region of the θ-parameter (in its allowed range), changing the basis set destroys this stability: e.g. for the basis set lmax=15, nflh=43, nbf=30 (see Section 3.2.11 for the definition of these parameters), the ionisation rate seems to be stable in the range of $15^o \leq \theta \leq 20^o$, however, for the basis set lmax=17, nflh=81, nbf=40 the ionisation rate is very unstable in this θ region. For the latter basis set the rate seems to be more stable for smaller θ-parameter (e.g. $\theta < 15^o$). In addition the results from tests of other parameters of the basis set are not consistent with each other in terms of angular momenta, Floquet harmonics and the basis functions. There is a significant difference between any set of these results and the converged

results from the velocity gauge calculation. In order to show the poor convergence some results together with converged results are given in Figure 7.1.

Furthermore, it is not possible to use larger basis sets to check convergence because of limitation in memory and disk space on the IBM RISC 6000 workstations used for our calculations.

We have done calculations with the various options defined in Chapter 3 in order to see which one is more convenient for length gauge calculations. The results from such technical tests are as follows:

1. Calculating the dipole moment using velocity, and acceleration form of the dipole moment is more convenient despite fact that the wavefunctions are calculated in the length gauge.

2. Using the options defined in Section 3.2.10, summing up over the Sturmian coefficient after having summed coefficients of the dipole moment or before having summed coefficients of the dipole moment does not affect the final result significantly.

3. The choice of Padé summation methods, defined in Section 3.2.10 is normally not very effective when the dipole moment is calculated using definition (3.39), which involves a complex conjugated wavefunction.

4. However, in the case of calculating the dipole moment with the definition of dipole moment given by Equation (3.39) or (3.40) affects the results in contrast to velocity gauge calculations. The former definition, which involves the complex conjugated wavefunction, gives better results than the latter one using any option mentioned above. However, the latter one is quite satisfactory when the velocity or the acceleration form of the dipole moment is used with the second Padé summation method defined in Section 3.2.10, which sums over all n and n' indices such that $n + n' \leq \bar{n}$, where the sum up to $\bar{n}$ gives a sequence of number where the convergence is accelerated by Padé.

It has already been mentioned that these difficulties related to convergence in the length gauge are a feature of the Sturmian basis functions (see Section 2.3). In order to avoid these difficulties we decided to use a mixed-gauge approach. In this gauge the ac-field is treated in the velocity gauge and the dc-field in the length gauge. We believe that such a mixed-gauge treatment is physically an appropriate

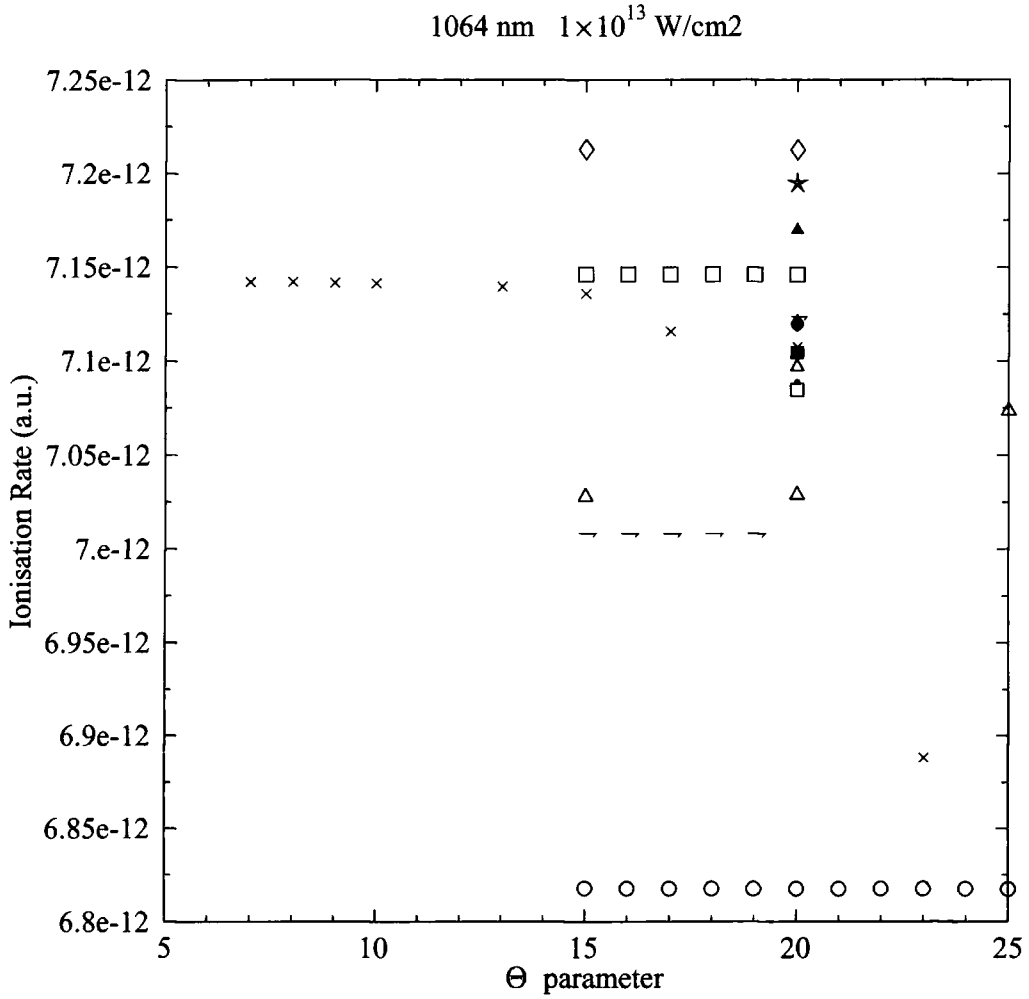

Figure 7.1: The ionisation rates with respect to θ-parameter and other parameters of the basis set. Note that these results are for a hydrogen atom in a laser field (λ = 1064 nm and I= 10^{13} W/cm^2) and the notations are as follows. $\star$; converged results, $\times$; lmax=17, nflh=81, nbf=40, $\square$; lmax=15, nflh=43,nbf=30, $\triangle$; lmax=17, nflh=61, nbf=50, $\diamond$; lmax=17, nflh=43, nbf=30, $\circ$; lmax=11, nflh=43, nbf=30, $\rightharpoonup$; lmax=13, nflh=43, nbf=30, smaller $\square$; lmax=17, nflh=74, nbf=50, $\bullet$; lmax=17, nflh=79, nbf=50, smaller $\triangle$; lmax=17, nflh=83, nbf=50, filled $\square$; lmax=17, nflh=87, nbf=50, filled $\circ$; lmax=19, nflh=61, nbf=50, filled $\triangle$; lmax=21, nflh=61, nbf=50.

treatment. However, for comparison we needed a set of converged results obtained in a pure length gauge treatment. Thus, since it is easier to obtain convergence for the laser with shorter wavelength, the length gauge tests have been done for λ = 355 nm with an intensity of I= 10^{13} W/cm^2. As expected it was easier to obtain convergence in ionisation rate. Convergence in the harmonic generation rate was achieved for the lowest harmonics (3, 5, 7 and 9th). The basis set and the θ-parameter used for the converged results are nbf=45,lmax=11, nflh=47 and 20^o, respectively.

After obtaining converged results for an ac-field with λ = 355 nm and I= 10^{13} W/cm^2 in the length gauge, a dc-field with $F_0 = 10^{-4}$ a.u. (0.5 MV/cm) was applied to the system in order to see its influence. We managed to obtain convergence for the first few harmonics (2-10). It was necessary to use a very big basis set to obtain convergence: lmax=21, nflh=43, nbf=45 and $\theta = 20^o$.

The application of a dc-field in addition to the ac-field had important physical effects. These effects are a significant change in the ionisation rate, production of even harmonics and some significant effects on production of the odd harmonics. The significance of the effects depends on the field strength of the dc-field in addition to the system we are working with. Detailed discussion and complete results will be given in the next section, however, a set of results from this test calculation are given in Table 7.1.

One must point out that the convergence for the harmonics greater than 10 was not good enough and also we were short of memory and disk space on the cluster (which is an IBM RISC 6000 workstation) for a further test. For example obtaining the results giving in Table 7.1 took 34 Mb. of memory and 370 Mb of scratch disk space was required when the code used the option of writing the LU-factorised blocks on disk during the running process and 395 Mb of memory was required if the code used the option of storing the LU-factorised in RAM. Note that the largest executable that could be run on the IBM workstation was 260 Mb. Thus it was not possible to use the second option for the calculation. Increasing the size of the basis set in order to obtain better convergence for higher harmonics required larger memory and larger scratch disk space. The first option (keeping the the LU-factorised blocks on the disk) does not require a big memory,

Table 7.1: Comparison of Harmonic generation rate and ionisation rate for few harmonics for an ac-field ($I_L = 10^{13}$ W/cm^2 and $\lambda_L = 355$nm) with a dc-field, which has the field strength 10^{-4} a.u (0.5 MV/cm) and without dc-field effect. Rates for the harmonics are given in (1/sec).

N	Rate without dc-field	Rate with dc-field
2		0.1226 (02)
3	0.5540 (06)	0.5529 (06)
4		0.9097 (02)
5	0.3894 (03)	0.3892 (03)
6		0.1140 (-01)
7	0.1841 (-01)	0.1842 (-01)
8		0.0276 (-05)
9	0.2435 (-06)	0.2521 (-06)
10		0.0731 (-09)
ionisation	0.5440 (-05)	0.5544 (-05)

but larger disk space, which may cause problems. For this particular case since the disk space required was not very large, it was thought it would be possible to obtain convergence. However, for another system such as a Yukawa potential case or for the H-atom case with Nd:YAG laser much larger basis set would be required to obtain convergence as already indicated above. Furthermore, sometimes using such a large basis set in the length gauge causes loss of accuracy and overflows. Moreover, one should point out that using such large basis sets is time consuming, both in CPU time and in real time.

All these disadvantages led us to a mixed-gauge calculation based on treating the ac-field in the velocity gauge and the dc-field in the length gauge.

Using the mixed-gauge saved us from needing a large basis set, thus, from large memory, disk space and time consumption (both CPU and real). For example when the above calculation was done using a mixed-gauge it was enough to use 13 angular momenta to obtain convergence. Of course this was much a smaller number than would have been necessary in length gauge calculations. Thus, this reduced, dramatically, the required memory, disk space, CPU time and real time for the calculations. In addition the for harmonic generation rates were converged up to the 21st harmonic in contrast to the case of the length gauge which converged

only the first 10 harmonics.

7.4 Different methods for treating the interaction potential

Two different iteration techniques have been used to solve the eigenvalue equation for an atomic system in an ac+dc field calculation. These are:

- a fully nonperturbative treatment, using inverse iterations for the full interaction potential,
- treating the ac-field nonperturbatively, solving the equation using inverse iteration technique and then treating the dc-field using leading order perturbation theory using Jacobi iteration for the solution.

The fully nonperturbative treatment using inverse iteration technique is very well known, and has been used through out this thesis and described in Section 2.5. With an added static-field potential the equation requiring solution is as follows:

$$(H_{ac} + V_{dc} - \sigma)\,\psi^{(n)} = \psi^{(n-1)} \tag{7.6}$$

Due to LU-factorisation this equation requires a big matrix to represent $(H_{ac} + V_{dc} - \sigma)$ over the basis set. This is difficult because the block-structure of the matrix is spoiled by the static-field potential V_{dc}. Thus, it requires larger memory and disk space and CPU time for this treatment.

Thus an alternative technique is required. One way of avoiding this difficulty if the static field strength is weak (i.e. V_{dc} is small) is for the influence of the interaction potential due to dc-field to be treated by Jacobi iteration while the ac-field is still treated using the inverse iteration technique. For this purpose for each inverse iteration, Equation (7.6) should be solved by Jacobi iteration, thus,

$$(H_{ac} - \sigma)\,\psi_m^{(n)} = \psi^{(n-1)} - V_{dc}\psi_{m-1}^{(n)}, \tag{7.7}$$

where m shows the order of Jacobi iteration and n shows the order of inverse iteration. Starting with $\psi_0^{(n)}$ being a solution of

$$(H_{ac} - \sigma)\,\psi_0^{(n)} = \psi^{(n-1)}, \tag{7.8}$$

next one

$$(H_{ac} - \sigma)\,\psi_1^{(n)} = \psi^{(n-1)} - V_{dc}\psi_0^{(n)} \tag{7.9}$$

and one more step

$$(H_{ac} - \sigma)\,\psi_2^{(n)} = \psi^{(n-1)} - V_{dc}\psi_1^{(n)} \tag{7.10}$$

so on. until it converges. At the convergence one has

$$(H_{ac} - \sigma)\,\psi^{(n)} = \psi^{(n-1)} - V_{dc}\psi^{(n)} \tag{7.11}$$

which is identical to the equation of nonperturbative inverse iteration treatment.

As expected, this new technique reduced the memory and disk space required. As an example, a test calculation has been done in order to demonstrate this. The following fields and basis set have used for this test: the ac-field 355 nm wavelength and 10^{13} W/cm^2 intensity, the dc-field which has 2×10^{-6} a.u. (0.1 MV/cm) field strength ; the basis set included 11 angular momenta, 31 Floquet harmonics and 30 basis functions.

The memory required for this calculation was 21 Mb and 38.24 Mb using Jacobi iteration and fully nonperturbative inverse iteration, respectively. In addition this also affected the CPU time and real time required for a complete set of results: about 4.00 minutes and 6.2 minutes, respectively, with Jacobi iteration and fully nonperturbative, inverse iteration. These calculation have been carried out on IBM RISC workstations, with 64 Mb of memory and 196 Mb of paging space. Note that for this particular test matrix elements of LU-decompositions were kept in the core, during the calculations not on the disk. In fact these numbers indicate big computational advantages, especially for systems which requires larger basis sets.

However, for higher dc-field strength Jacobi iteration was not sufficient to obtain converged results. We varied the strength of dc-field from 2×10^{-6} a.u. (0.01 MV/cm) to 10^{-4} a.u. (0.5 MV/cm) in order to find the limit of the validity. We obtained converged results when the field strength of the dc-field was smaller than 10^{-4} a.u. However, for this particular system 10^{-4} a.u. field strength was already high enough not to be able to obtain a set of converged results. Thus, this method was not sufficient for high dc-field strength. A set of results from the test calculations mentioned above is given in Table 7.2 for ionisation rate as well

as for generation rates for a few harmonics in order to show agreement between two sets of results although these results are fully converged in terms of the basis set. In this table we considered hydrogen atom in an ac-field with an intensity I= 10^{13} W/cm^2, a wavelength $\lambda = 355$ nm and a dc-field with 2×10^{-6} a.u. (0.01 MV/cm) of field strength.

Table 7.2: Comparison of rate of ionisation and harmonic generation for few harmonics for an ac-field ($I_L = 10^{13}$ W/cm^2 and $\lambda_L = 355$nm) with a dc-field field, which has a field strength 6×10^{-5} a.u (0.31 MV/cm) using inverse iteration technique and Jacobi iteration technique. Rates for harmonic are given in (1/sec).

N	Fully Inverse iteration	Jacobi iteration together
2	0.4913692 (-02)	0.4913692 (-02)
3	0.5539971 (06)	0.5539970 (06)
4	0.3643524 (-01)	0.3643524 (-01)
5	0.3894061 (03)	0.3894060 (03)
6	0.4580132 (-05)	0.4580132 (-05)
7	0.1841508 (-01)	0.1841508 (-01)
8	0.1138939 (-09)	0.1138939 (-09)
9	0.2435297 (-06)	0.2435297 (-06)
10	0.1092100 (-14)	0.1092293 (-14)
ionisation	0.5439380 (-05)	0.5439380 (-05)

7.5 Applications, results and discussion

Three different types of calculations have been performed in order to observe the effects of a dc-field on multiphoton processes and to be able to gain physical insight from the results obtained. The first applications were done for the hydrogen atom in a dc-field together with a laser field. In order to understand the results of these calculations and to compare our results with the results in the literature [104] it was necessary to perform a set of calculations for a system with only one bound state. Thus, a set of calculations was performed for H^- using the model potential of Equation (7.1). Finally, a set of calculations was done for the H^- ion in a two-colour field (whose frequencies are commensurable). The reason for this final calculation is as follows. The variation of the fundamental field is nearly negligible in comparison to the harmonic field. Thus, the effect of the fundamental field on the processes might be as a dc-field. The fields used for the case of the hydrogen atom were as follows:

- A high frequency field with wavelength $\lambda = 355$ nm and intensity I= 10^{13} W/cm^2 together with a static field of field strength 2×10^{-5} a.u. (0.1 MV/cm), 10^{-4} a.u. (0.5 MV/cm), 10^{-3} a.u. (5.0 MV/cm) and 2×10^{-3} a.u. (10.0 MV/cm).
- The intensity of the previous high frequency field was increased to I= 2×10^{13} W/cm^2 and the field strength of the dc-field was taken as 10^{-3} a.u. (5.0 MV/cm), 2×10^{-3} a.u. (10.0 MV/cm) and 3×10^{-3} a.u. (15.0 MV/cm).
- A high frequency field with wavelength $\lambda = 532$ nm and intensity I= 2×10^{13} W/cm^2 together with a static field of 10^{-3} a.u. (5.0 MV/cm), 2×10^{-3} a.u. (10.0 MV/cm).
- For an infrared field with a wavelength $\lambda = 1064$ nm and intensity I= 10^{13} W/cm^2 together with a static electric field with the following field strengths. 1.2×10^{-5} a.u., (0.06 MV/cm), 2.0×10^{-5} a.u., (0.1 MV/cm), 1.2×10^{-4} a.u., (0.6 MV/cm), 2.5×10^{-4} a.u., (1.25 MV/cm), 0.5×10^{-3} a.u., (2.5 MV/cm), 0.75×10^{-3} a.u., (3.75 MV/cm), 10^{-3} a.u. (5.0 MV/cm).
- A more detailed calculation for the infrared field has been performed with the field strength of the dc-field varied in steps of 10^{-5} a.u. between 2.0×10^{-5}

a.u. (0.1 MV/cm) and 2.5×10^{-4} a.u. (1.25 MV/cm).

The fields used for the case of H^- ion were as follows:

- a CO_2 laser ($\lambda = 10.6\mu$m) with an intensity of I= 5×10^{10} W/cm^2 and the dc-field with a dc-field strength $F_o = 2 \times 10^{-5}$ a.u. (0.1 MV/cm)
- a CO_2 laser ($\lambda = 10.6\mu$m) with an intensity of I= 2.5×10^{10} W/cm^2 and the dc-field with a dc-field strength $F_o = 2 \times 10^{-5}$ a.u. (0.1 MV/cm)
- A detailed was calculation performed for the second field with varying the field strength of the dc-field with a step of 10^{-6} a.u. between 0.5×10^{-5} a.u. (0.025 MV/cm), 1.5×10^{-5} a.u. (0.075 MV/cm).

and finally for the two-colour calculation in H^-,

- A low frequency field with wavelength $\lambda = 31.8$ μm and an intensity I= 1.4×10^7 W/cm^2 and its third harmonic (the wavelength of the third harmonic is $\lambda = 10.6$ μm and the intensity I= 2.5×10^10 W/cm^2). The calculations were performed for the phase between the fundamental and the harmonic field as $\phi = 0^o$ or 180^o. Note that the electric field amplitude of the low frequency field is identical to the dc-field strength used in the first and second options of the Yukawa potential calculations.
- The previous calculation was repeated for I= 2.81×10^7 W/cm^2 intensity of the harmonic field. For this intensity, the root-mean-square electric field amplitude was identical to the dc-field strength used in the first and second option of the Yukawa potential calculations.

The corresponding Keldysh parameters and ponderomotive shifts for these systems are given in Table 7.3. From the tables it is clear that we are mainly dealing with the multiphoton regime ($\gamma > 1$), apart from one set of calculation for the negative hydrogen ion, which was in the tunneling regime ($\gamma < 1$). In order to analyse the results from these calculations some of these results are exhibited through out this chapter. The rate of harmonic emission with respect to harmonic order is presented in Figures 7.2, 7.3, 7.4, 7.5 and 7.6; the first two for the hydrogen atom and the others for the negative hydrogen ion; the last two are for the two-colour process. The ac-fields used for the processes in these figures were as follows: an ac-field with 355 nm wavelength was used in both pictures of Figure 7.2, but the first one has an intensity 10^{13} W/cm^2 and second one 2×10^{13} W/cm^2. A laser

Table 7.3: Value of Keldysh parameter γ and Ponderomotive shift (P) for the hydrogen atom and for the negative hydrogen ion with respect to the laser parameters.

H-atom			
I (W/cm^2)	λ (nm)	γ	P
1.0×10^{13}	355	7.578	4.354 (-03)
2.0×10^{13}	355	5.358	8.710 (-03)
2.0×10^{13}	532	3.576	1.960 (-02)
1.0×10^{13}	1064	2.530	3.910 (-02)
H^--ion (Yukawa Potential)			
2.5×10^{10}	10600	1.190	0.970 (-02)
5.0×10^{10}	10600	0.840	0.194 (-01)

with 532 nm wavelength and 2×10^{13} W/cm^2 intensity was used for the first picture of Figure 7.3 and a laser with 1064 nm wavelength, 10^{13} W/cm^2 intensity was used for the second picture of the same figure. The field strengths of the dc-field used for the both pictures of Figure 7.2 and first (from left) pictures of Figure 7.3 were $F_o = 0.0, 1.0 \times 10^{-3}, 2.0 \times 10^{-3}$ a.u. and for the second picture of Figure 7.3 were $F_o = 0.0, 0.5 \times 10^{-3}, 1.0 \times 10^{-3}$ a.u. For both pictures of Figure 7.4 the wavelength of CO_2 laser was used. The intensity of the lasers was 2.5×10^{10} W/cm^2 for the picture above and 5.0×10^{10} W/cm^2 for the picture below. The dc-field strength for both pictures of this figure is $F_o = 2 \times 10^{-5}$ a.u. In Figures 7.5 and 7.6 the wavelength of CO_2 laser was also used (with I= 1.4×10^7 W/cm^2 and I= 2.81×10^7 W/cm^2 intensities, respectively). In these two figures the phase between the harmonic field and its fundamental was 180^o for the upper pictures and 0^o for the lower pictures. The ionisation rates with respect to dc-field strength for all processes mentioned so far are given in Table 7.4.

In addition, in order to see the detail of the calculations a set of results is given in Table 7.5 for the hydrogen atom. These tables include the rate for harmonic generation and quasienergies of the system. The ac-field used in Table 7.5 was a Nd:YAG laser with 10^{13} W/cm^2 intensity, and the following dc-field strengths $F_o = 0.0, 1.2 \times 10^{-5}$ a.u., 2.0×10^{-5} a.u., 1.2×10^{-4} a.u., 2.5×10^{-4} a.u., 0.5×10^{-3} a.u., 0.75×10^{-3} and 1.0×10^{-3} a.u.

The results show that the application of a static field in addition to an ac-field produces even harmonics in addition to affecting the strength of the odd harmonics. However, the spectrum of harmonics is similar to that obtained in the absence of dc-field in respect to plateau, cut-offs, etc (see Figures 7.2, 7.3 and 7.4).

In Figure 7.2 the strength of the even harmonics are in general decreasing with increasing dc-field strength. When the laser parameters were 355 nm and intensity I= 10^{13} W/cm^2 this occured for all harmonics (see the first picture in Figure 7.2) but when the laser intensity was increased to I= 2×10^{13} W/cm^2 there was no decrease for the 2nd and 4th harmonics (see the second picture in Figure 7.2). When the laser field had a wavelength 532 nm and an intensity I= 2×10^{13} W/cm^2 in contrast the strength of the even harmonics increased with increasing dc-field strength (see the first picture of Figure 7.3). In addition when the laser field had a wavelength $\lambda = 1064$ nm and an intensity I= 10^{13} W/cm^2 conversion efficiencies of the even harmonics are in general increasing with increased dc-field strength (see the scond picture of Figure 7.3). However, for this system for some even harmonics there was an increase in conversion efficiency. e.g. when the strength of dc-field F_o increased from 0.5×10^{-3} a.u. to 1.0×10^{-3} a.u. the conversion efficiencies for the 8th and 12th harmonics decreased (see Figure 7.3 and Table 7.5).

The effect on the strength of the odd harmonics was as follows. In Figure 7.2 the lower harmonics (such as 3, 5, 7, etc) were generated with lesser efficiency and the higher harmonics ($N \geq 9$) have generated with higher efficiency than in the absence of the dc-field. In addition with increasing dc-field strength the efficiency in generation of odd harmonics decreased for both laser intensity for the 355 nm laser. However, for the lasers with wavelength 532 nm or 1064 nm the variation of odd harmonics strength with respect to dc-field strength was more complicated (see Figure 7.4 and Table 7.5).

The same type of anomalies were obtained in the variation of the ionisation rate from the hydrogen atom with respect to dc-field strength (see Tables 7.4 and 7.5).

Detailed calculations were performed in order to elucidate this abnormal behaviour. They were performed for 1064 nm wavelength and an intensity of 10^{13} W/cm^2; the field strength of the dc-field was varied by small steps (10^{-5} a.u.) between 2.0×10^{-5} a.u. and 2.5×10^{-4} a.u.

The results from this calculation for the variation of the ionisation rate with respect to dc-field strength are presented in Figure 7.7 and for the variation of rate for each harmonic are presented in Figures 7.8-7.19. The variation of the odd harmonic's strength is given in Figures 7.8-7.13 and of the even harmonic's strength is given in Figures 7.14-7.19.

The ionisation rate and photoemission rate for each harmonic oscillates with respect to the field strength of the dc-field is made clear in these figures. Let us first concentrate on the variation of ionisation rate with respect to dc-field strength. In Figure 7.7 the imaginary part of the quasi energy peaks about $2F_o = 2.4$ a.u. and then continues oscillating, which follows a second peak. We believe that this trend is a resonance feature between the ground state and an excited state due to the effect of the dc-field. It has been expected that there might be a crossing of ground state and an excited state when the atom is in the dc-field in addition to the ac-field. This is a new feature we have obtained (so far there is no information in the literature to the best of my knowledge). A set of calculations for the $n = 4$ state of hydrogen with the same laser parameters has been performed by Povliege [123]. A results of this calculations, it has been found that with varying field strength of the dc-field at $2F_o = 2.4$ a.u. real part of quasienergy for the state 1 (according to the indication made Figure 3.3 in the section 3.1 of Chapter 4), which corresponds to a state with $4s/4d$ character is nearly identical to the quasienergy of the ground state when the field strength of the dc-field is about $2F_o = 2.4$ a.u. This shows a crossings of the ground state (15 with the notation used in Figure 3.3 in the section 3.1 of Chapter 4) and state 1.

One can generalise this feature to the other peaks, too, but further calculations would be required to analyse the other crossings. Thus, the oscillations of the variation of the emission rate with respect to dc-field strength is a consequence of these resonances caused by the crossings of ground and excited states under the dc-Stark shift.

Similar results have been obtained in the case of the Yukawa potential under the dc-field in addition to the laser field. Calculations were performed for a dc-field strength of $F_o = 2 \times 10^{-5}$ a.u. for two different intensities of the laser field; I= 2.5×10^{10} W/cm^2 and I= 5×10^{10} W/cm^2. The results of there calculations are illustrated in Figure 7.4. It is clear that for this particular dc-field strength there is a decrease in harmonic generation rate and in ionisation rate for both intensities of the ac-field. The results we have obtained for this particular dc-field strength agree with the results we obtained from the two-colour, $(\omega, 3\omega)$ mixing, calculation which had the same parameters as the dc-field. The results of the two-colour calculations are given in Figure 7.5 and 7.6, two different intensities of the ac-field (for two different phases; $\phi = 0^o, 180^o$). Remember that in Figure 7.5 the intensity of the harmonic field is I= 1.4×10^7 W/cm^2. The electric amplitude of this field is identical to the field strength of the dc-field. For Figure 7.6 the root-mean-square of the intensity (I= 2.81×10^7 W/cm^2) is identical to the field strength of the dc-field. Having the same parameters of the dc-field for the harmonic field and due to the fact that the variation of the electric field of the fundamental field was nearly negligible in comparison to the variation of its third harmonic field is the reason both dc-field and $(\omega, 3\omega)$ mixing give the same effects in the harmonic generation rate. Perry *et al.* [91] also obtained a decrease in the rate of harmonics generation in their two-colour experiment, which is done using an $(\omega, 3\omega)$ mixing.

However, our results for this particular system disagree with the results obtained by Bao and Starace [104]. Bao and Starace [104] calculated harmonic generation rate in the presence of the a dc-field. Their calculation is an extension of the zero-range potential model treatment of Becker *etal.* [16]. They presented two sets of results for harmonic generation. One is from H^- using a CO_2 laser and the other is from Ar using an Nd:YAG laser. For both case the static field they used had a strength 0.1MV/cm (which is 2×10^{-5} a.u.). For both laser systems they rather obtained an increase in the stength of the odd harmonics with the application of the dc-field, although their first work was for exactly the same laser system and with the same dc-field strength as we have discussed above. On the other hand our results for harmonic emission rate in the absence of the dc-field agree with the results obtained by them and reported by other workers in the

literature (e.g. [113] and [114]).

Moreover, for the case of Yukawa potential a set of detailed calculations was also performed in order to see the variation of the rate of photodetachment and emission with respect to dc-field strength. In this calculation a wavelength of CO_2 laser with an intensity of 2.5×10^{10} W/cm^2 was used and the field strength of the dc-field was varied from $2F_o = 1.0 \times 10^{-5}$ a.u. to $2F_o = 3.0 \times 10^{-5}$ a.u. in steps of 10^{-6}. The variation of photodetachment rate with respect to dc-field strength is presented in Figure 7.20 and the variation of the photoemission rate with respect to dc-field strength for each harmonic is presented in Figures 7.21-7.32 (for odd harmonics Figures 7.21-7.26 and for even harmonics Figures 7.27-7.32).

The Yukawa potential is a model potential for a system with only one bound state, thus one does not expect Stark-shift-induced resonances. Still, Figure 7.20 shows oscillation structure in the photodetachment rate. We believe that this structure results from the nonperturbative coupling of the static uniform electric field and the laser field, both being polarised along the same direction. Indeed, Gao and Starace [119] have shown analytically using the exact wavefunction for an electron in both fields, that the corresponding photodetachment cross-section (in the case of a weak laser-field) consists of two terms of which the second arises due to the nonperturbative treatment when including the static electric field. As both terms arise from a sum of distinct quantum mechanical amplitudes [119] the structures are thus induced through constructive and destructive interference between different pathways of the escaping electron. This interference effect is also responsible from the oscillations in Figures 7.21-7.32.

Note that the convergence of the results have been checked very carefully in order to prevent the results obtained being consequence of numerical error in dealing with very tedious numerical problems. In order to present the convergence of the results obtained some sets of results are given in the following tables. For the hydrogen atom case; Tables 7.6 and 7.7 presents the convergence of the harmonic emission rate and quasienergy for $2F_o = 2.0 \times 10^{-3}$ a.u. and $2F_o = 2.4 \times 10^{-4}$ a.u., dc-field strengths and in Yukawa potential case the same type of results are presented in Tables 7.8 and 7.9 for $2F_o = 3.0 \times 10^{-5}$ a.u. and $2F_o = 2.0 \times 10^{-5}$ a.u. dc-field strengths.

7.6 Conclusion

To conclude, the effect of a static electric field on hydrogen in the ground state and a Yukawa potential with only one bound state has been studied in this chapter. In addition to a strong production of even harmonics a marked change has been obtained in the rate of harmonic emission and ionisation.

For the case of the hydrogen atom it has been found that the ionisation rate oscillates with respect to the dc-field strength. It has been shown that this is a resonance feature and this resonance happens due to a dc-Stark shift. This resonance also affects the variation in the harmonic emission rate versus dc-field strength. Thus, we have found that this variation is also an oscillation.

For the case of the Yukawa potential, in general, the harmonic emission rate decreases with application of dc-field. For a particular case a set of results have been produced from a two-colour calculation, $(\omega, 3\omega)$ mixing, and it has been found that the results obtained from the dc-field calculations are in very good agreement with those obtained from the two-colour calculations.

For the case of Yukawa potential varying the dc-field strength showed that there is an oscillation in the photodetachment and photoemission rates due to the constructive and destructive interference between different pathways of the escaping electron.

Table 7.4: Rate of ionisation for hydrogen atom and rate of detachment for negative hydrogen ion, which are in a dc-field in addition to an ac-field, with respect to dc-field strength and rate of detachment for negative hydrogen ion, in a two-colour field, whose frequencies are commensurable ($\omega = 31.8$ μm, $(3\omega) = 10.6$ μm mixing) is given in the last 4 rows of the table. The intensity of the harmonic field in the first column and the phase (ϕ) between the harmonic field and its fundamental are given in the second column of this part of table.

H-atom		
ac-field (355 nm)	F_o (a.u.)	Γ (a.u.)
1.0×10^{13} W/cm^2	0.0 (-00)	0.5440 (-05)
1.0×10^{13} W/cm^2	2.0 (-05)	0.5440 (-05)
1.0×10^{13} W/cm^2	1.0 (-04)	0.5444 (-05)
1.0×10^{13} W/cm^2	1.0 (-03)	0.4288 (-05)
1.0×10^{13} W/cm^2	2.0 (-03)	0.1665 (-05)
2.0×10^{13} W/cm^2	0.0 (-03)	0.8682 (-05)
2.0×10^{13} W/cm^2	1.0 (-03)	0.1068 (-04)
2.0×10^{13} W/cm^2	2.0 (-03)	0.9024 (-05)
2.0×10^{13} W/cm^2	3.0 (-03)	0.1064 (-04)
ac-field (532 nm)	F_o (a.u.)	Γ (a.u.)
2.0×10^{13} W/cm^2	0.0 (-00)	0.5534 (-06)
2.0×10^{13} W/cm^2	1.0 (-03)	0.8489 (-06)
2.0×10^{13} W/cm^2	2.0 (-03)	0.1005 (-05)
ac-field (1064 nm)	F_o (a.u.)	Γ (a.u.)
1.0×10^{13} W/cm^2	0.0 (-00)	0.7197 (-11)
1.0×10^{13} W/cm^2	0.5 (-03)	0.6090 (-11)
1.0×10^{13} W/cm^2	1.0 (-03)	0.7813 (-11)
H^--ion		
ac-field (10.6 μm)	F_o (a.u.)	Γ (a.u.)
2.5×10^{10} W/cm^2	0.0 (-00)	0.6128 (-07)
2.5×10^{10} W/cm^2	2.0 (-05)	0.5015 (-07)
5.0×10^{10} W/cm^2	0.0 (-00)	0.9553 (-06)
5.0×10^{10} W/cm^2	2.0 (-05)	0.9542 (-06)
H^--ion		
ac-field (3.18 μm)	ϕ (deg)	Γ (a.u.)
1.40×10^{7} W/cm^2	0.0 (-00)	0.5804 (-07)
1.40×10^{7} W/cm^2	1.8 (+02)	0.5452 (-07)
2.81×10^{7} W/cm^2	0.0 (-00)	0.5748 (-07)
2.81×10^{7} W/cm^2	1.8 (+02)	0.4962 (-07)

Table 7.5: Harmonics emission rate from H-atom for different value of dc-field strength ($2F_o$) and the quasienergy of the ground state of the system. The input value of laser field and the dc-field ($2F_o$) are given on the top of each column with together other parameters for getting converged results. The corresponding quasienergies for each system is given at the end of the table.

input:	input:	input:	input:
6 40 11 -23 23	6 40 11 -25 25	7 40 13 -25 25	7 40 13 -25 25
1064 nm 1.0D+13	1064 nm 1.0D+13	1064 nm 1.0D+13	1064 nm 1.0D+13
25 -2.0D-01	20 -2.0D-01	20 -2.0D-01	33 -2.0D-01
-0.539 -3.7D-12	-0.539 -3.7D-11	-0.539 -3.7D-11	-0.539 -3.7D-11
0.00	-2.4D-05	-4.0D-05	-2.40D-04
HG	HG	HG	HG
3 1.466	3 1.466	3 1.466	1.466
5 0.610E-02	5 0.610E-02	5 0.610E-02	0.612E-02
7 0.244E-02	7 0.244E-02	7 0.244E-02	0.259E-02
9 0.635E-02	9 0.638E-02	9 0.643E-02	0.107E-01
11 0.190E-01	11 0.190E-01	11 0.190E-01	0.118E-01
13 0.123E-01	13 0.123E-01	13 0.122E-01	0.105E-01
15 0.299E-02	15 0.298E-02	15 0.296E-02	0.406E-03
17 0.545E-03	17 0.543E-03	17 0.540E-03	0.262E-03
19 0.163E-04	19 0.162E-04	19 0.161E-04	0.114E-04
21 0.172E-06	21 0.171E-06	21 0.170E-06	0.157E-06
23 0.778E-09	23 0.870E-09	23 0.866E-09	0.100E-08
	25 0.284E-11	25 0.283E-11	0.373E-11
	25 0.284E-11	25 0.283E-11	0.373E-11
	(dc+ac)	(dc + ac)	(dc + ac)
	2 0.645E-05	2 0.179E-04	0.645E-03
	4 0.599E-07	4 0.167E-06	0.703E-05
	6 0.122E-06	6 0.343E-06	0.184E-04
	8 0.326E-05	8 0.892E-05	0.113E-03
	10 0.331E-05	10 0.925E-05	0.405E-03
	12 0.719E-04	12 0.201E-03	0.864E-02
	14 0.605E-05	14 0.167E-04	0.188E-02
	16 0.405E-05	16 0.114E-04	0.867E-03
	18 0.247E-06	18 0.694E-06	0.368E-04
	20 0.414E-08	20 0.116E-07	0.474E-06
	22 0.294E-10	22 0.823E-10	0.268E-08
	24 0.111E-12	24 0.311E-12	0.817E-11

QE: (-0.538921587605767027,-0.359872106628154709E-11)
QE: (-0.538921587937819635,-0.360189933421918263E-11)
QE: (-0.538921588528136208,-0.360809916879352156E-11)
QE: (-0.538921620810842272,-0.347732833907631215E-11)

input:	input:	input:	input:
12 55 23 -25 25	12 55 23 -25 25	12 55 23 -25 25	12 55 23 -30 30
1064 nm 1.0D+13	1064 nm 1.0D+13	1064 nm 1.0D+13	1064 nm 1.0D+13
33 -2.0D-01	33 -2.0D-01	33 -2.0D-01	33 -2.0D-01
-0.539 -3.7D-11	-0.539 -3.7D-11	-0.539 -3.7D-11	-0.538921 -3.6D-12
-5.0D-04	-1.0D-03	-1.50D-03	-2.0D-03
HG	HG	HG	HG
3 1.466	3 1.467	3 1.469	1.472
5 0.605E-02	5 0.621E-02	5 0.633E-02	0.646E-02
7 0.211E-02	7 0.305E-02	7 0.386E-02	0.459E-02
9 0.305E-02	9 0.951E-02	9 0.223E-01	0.194E-01
11 0.386E-02	11 0.349E-03	11 0.756E-02	0.157E-01
13 0.118E-02	13 0.452E-02	13 0.269E-02	0.240E-02
15 0.677E-02	15 0.283E-02	15 0.814E-03	0.142E-02
17 0.821E-03	17 0.256E-03	17 0.217E-04	0.110E-03
19 0.225E-04	19 0.699E-05	19 0.567E-05	0.864E-05
21 0.242E-06	21 0.121E-06	21 0.233E-06	0.190E-06
23 0.1303E-08	23 0.141E-08	23 0.326E-08	0.155E-08
25 0.443E-11	25 0.912E-11	25 0.208E-10	0.599E-11
(dc + ac)	(dc + ac)	(dc + ac)	(dc + ac)
2 0.280E-02	2 0.112E-01	2 0.252E-01	0.448E-01
4 0.288E-04	4 0.111E-03	4 0.257E-03	0.471E-03
6 0.374E-04	6 0.279E-04	6 0.649E-04	0.177E-03
8 0.148E-02	8 0.202E-02	8 0.154E-02	0.975E-03
10 0.655E-03	10 0.128E-04	10 0.123E-02	0.106E-02
12 0.741E-02	12 0.125E-01	12 0.673E-02	0.379E-02
14 0.637E-03	14 0.885E-04	14 0.220E-03	0.549E-03
16 0.170E-03	16 0.499E-03	16 0.913E-03	0.824E-03
18 0.174E-04	18 0.528E-04	18 0.114E-03	0.893E-04
20 0.364E-06	20 0.159E-05	20 0.391E-05	0.230E-05
22 0.296E-08	22 0.224E-07	22 0.562E-07	0.220E-07
24 0.124E-10	24 0.168E-09	24 0.412E-09	0.970E-10

QE: (-0.538921731726348607,-0.354264584383306691E-11)
QE: (-0.538922164094739475,-0.304475124248828667E-11)
QE: (-0.538922884718673778,-0.302739738980051238E-11)
QE: (-0.538923893616123251,-0.390863565224797086E-11)

Table 7.6: A set of results for a convergence test for the harmonics emission rate from H-atom for the dc-field strength $2F_o = 2.0 \times 10^{-3}$ a.u. and the quasienergy of the ground state of the system. The input parameters are given on the top of each column. The corresponding quasienergies for each system is given at the end of the table.

input:	input:	input:	input:	input:	input:	input:
9 45 17 -23 23	9 45 17 -21 21	9 45 17 -19 19	9 40 17 -23 23	9 50 17 -23 23	8 45 15 -23 23	7 45 13 -23 23
1064 nm 1.0D+13	1064 nm 1.0D+13	1064 nm 1.0D+13	1064 nm 1.0D+13	1064 nm 1.0D+13	1064 nm 1.0D+13	1064 nm 1.0D+13
20 -2.0D-01	20 -2.0D-01	20 -2.0D-01	20 -2.0D-01	20 -2.0D-01	20 -2.0D-01	20 -2.0D-01
-0.539 -3.6D-12	-0.539 -3.6D-12	-0.539 -3.6D-12	-0.539 -3.6D-12	-0.539 -3.6D-12	-0.539 -3.6D-12	-0.539 -3.6D-12
-2.0D-03	-2.0D-03	-2.0D-03	-2.0D-03	-2.0D-03	-2.0D-03	-2.0D-03
HG	HG	HG	HG	HG	HG	HG
3 1.472	1.472	1.472	1.472	1.472	3 1.472	1.472
5 0.645E-02	0.645E-02	0.645E-02	0.645E-02	0.646E-02	5 0.640E-02	0.646E-02
7 0.445E-02	0.445E-02	0.441E-02	0.442E-02	0.453E-02	7 0.431E-02	0.436E-02
9 0.207E-01	0.207E-01	0.208E-01	0.218E-01	0.219E-01	9 0.216E-01	0.216E-01
11 0.143E-01	0.143E-01	0.143E-01	0.152E-01	0.157E-01	11 0.189E-01	0.186E-01
13 0.195E-02	0.195E-02	0.193E-02	0.210E-02	0.221E-02	13 0.238E-02	0.363E-02
15 0.136E-02	0.136E-02	0.136E-02	0.124E-02	0.115E-02	15 0.209E-02	0.440E-03
17 0.199E-03	0.199E-03	0.200E-03	0.208E-03	0.242E-03	17 0.751E-04	0.162E-03
19 0.467E-04	0.468E-04	0.479E-04	0.395E-04	0.443E-04	19 0.803E-05	0.564E-04
21 0.235E-05	0.236E-05	0.000E-00	0.189E-05	0.206E-05	21 0.147E-05	0.455E-05
23 0.481E-07	0.000E-00	0.000E-00	0.393E-07	0.408E-07	23 0.437E-07	0.127E-06
(dc + ac)	(dc + ac)	(dc + ac)	(dc + ac)	(dc + ac)	(dc + ac)	(dc + ac)
2 0.448E-01	0.448E-01	0.448E-01	0.448E-01	0.448E-01	2 0.448E-01	0.448E-01
4 0.471E-03	0.471E-03	0.471E-03	0.471E-03	0.472E-03	4 0.471E-03	0.473E-03
6 0.173E-03	0.173E-03	0.172E-03	0.179E-03	0.187E-03	6 0.192E-03	0.188E-03
8 0.952E-03	0.952E-03	0.946E-03	0.102E-02	0.107E-02	8 0.872E-03	0.937E-03
10 0.164E-02	0.164E-02	0.163E-02	0.187E-02	0.220E-02	10 0.114E-02	0.154E-02
12 0.406E-02	0.406E-02	0.407E-02	0.382E-02	0.365E-02	12 0.321E-02	0.289E-02
14 0.691E-03	0.691E-03	0.683E-03	0.728E-03	0.852E-03	14 0.495E-03	0.118E-02
16 0.728E-03	0.728E-03	0.727E-03	0.766E-03	0.777E-03	16 0.614E-03	0.996E-03
18 0.144E-03	0.144E-03	0.150E-03	0.116E-03	0.111E-03	18 0.447E-04	0.292E-04
20 0.100E-04	0.103E-04	0.000E-00	0.736E-05	0.771E-05	20 0.814E-05	0.126E-04
22 0.313E-06	0.000E-00	0.000E-00	0.241E-06	0.256E-06	22 0.354E-06	0.761E-06
QE: (-0.538923893616128247,-0.37314744405253797 6E-11)					QE: (-0.538923893616220284,-0.3940642748095709 09E-11)	
QE: (-0.538923893616128136,-0.37315852660597192 1E-11)					QE: (-0.538923893615757876,-0.4254602262704302 46E-11)	
QE: (-0.538923893616115257,-0.37181988766352458 1E-11)						
QE: (-0.538923893616088501,-0.38255191924423403 2E-11)						
QE: (-0.538923893616148453,-0.39223700163275557 2E-11)						

Table 7.7: Continuation of the convergence tests in Table 7.6 with different basis set. The input parameters are given at the top of each column of the table.

input:	input:	input:	input:	input:
11 45 21 -25 25	11 45 21 -25 25	12 45 23 -25 25	10 45 19 -25 25	12 45 23 -30 30
1064 nm 1.0D+13	1064 nm 1.0D+13	1064 nm 1.0D+13	1064 nm 1.0D+13	1064 nm 1.0D+13
28 -2.0D-01	25 -2.0D-01	30 -2.0D-01	30 -2.0D-01	33 -2.0D-01
-0.539 -3.6D-12	-0.539 -3.6D-12	-0.539 -3.6D-12	-0.539 -3.6D-08	-0.539 -3.6D-12
-2.0D-03	-2.0D-03	-2.0D-03	-2.0D-03	-2.0D-03
HG	HG	HG	HG	HG
3 1.472	1.472	1.472	1.472	1.472
5 0.645E-02	0.645E-02	0.646E-02	0.646E-02	0.646E-02
7 0.456E-02	0.437E-02	0.459E-02	0.459E-02	0.459E-02
9 0.194E-01	0.213E-01	0.194E-01	0.193E-01	0.194E-01
11 0.156E-01	0.156E-01	0.156E-01	0.156E-01	0.157E-01
13 0.240E-02	0.216E-02	0.240E-02	0.239E-02	0.240E-02
15 0.146E-02	0.120E-02	0.142E-02	0.142E-02	0.142E-02
17 0.104E-03	0.148E-03	0.110E-03	0.109E-03	0.111E-03
19 0.821E-05	0.201E-04	0.866E-05	0.864E-05	0.875E-05
21 0.208E-06	0.851E-06	0.190E-06	0.190E-06	0.193E-06
23 0.224E-08	0.181E-07	0.154E-08	0.154E-08	0.158E-08
25 0.132E-10	0.217E-09	0.629E-11	0.629E-11	0.611E-11
27 0.000E_00	0.000E-00	0.000E-00	0.000E-00	0.134E-13
29 0.000E_00	0.000E-00	0.000E-00	0.000E-00	0.216E-16
(dc + ac)	(dc + ac)	(dc + ac)	(dc + ac)	(dc + ac)
2 0.448E-01	0.448E-01	0.448E-01	0.448E-01	0.448E-01
4 0.471E-03	0.471E-03	0.471E-03	0.471E-03	0.471E-03
6 0.175E-03	0.178E-03	0.177E-03	0.177E-03	0.177E-03
8 0.949E-03	0.921E-03	0.972E-03	0.973E-03	0.975E-03
10 0.970E-03	0.131E-02	0.105E-02	0.106E-02	0.106E-02
12 0.382E-02	0.365E-02	0.379E-02	0.379E-02	0.379E-02
14 0.518E-03	0.679E-03	0.548E-03	0.551E-03	0.550E-03
16 0.829E-03	0.757E-03	0.824E-03	0.822E-03	0.824E-03
18 0.942E-04	0.703E-04	0.896E-04	0.892E-04	0.897E-04
20 0.271E-05	0.269E-05	0.231E-05	0.229E-05	0.231E-05
22 0.327E-07	0.941E-07	0.220E-07	0.218E-07	0.222E-07
24 0.216E-09	0.185E-08	0.977E-10	0.958E-10	0.975E-10
26 0.000E_00	0.000E-00	0.000E-00	0.000E-00	0.225E-12
28 0.000E_00	0.000E-00	0.000E-00	0.000E-00	0.342E-15
30 0.000E_00	0.000E-00	0.000E-00	0.000E-00	0.560E-18
QE: (-0.538923893616107708,-0.388877048451015131E-11)				
QE: (-0.538923893616079064,-0.382735260263893045E-11)				
QE: (-0.538923893616123917,-0.390469382042378339E-11)				
QE: (-0.538923893616127136,-0.390386713089181642E-11)				
QE: (-0.538923893616125693,-0.390699148058865531E-11)				

input:	input:	input:	input:	input:
11 40 21 -25 25	11 50 21 -25 25	11 45 21 -25 25	11 45 21 -25 25	11 45 21 -25 25
1064 nm 1.0D+13	1064 nm 1.0D+13	1064 nm 1.0D+13	1064 nm 1.0D+13	1064 nm 1.0D+13
30 -2.0D-01	30 -2.0D-01	35 -2.0D-01	33 -2.0D-01	30 -2.0D-01
-0.539 -3.6D-12	-0.539 -3.6D-12	-0.539 -3.6D-12	-0.539 -3.6D-11	-0.539 -3.6D-11
-2.0D-03	-2.0D-03	-2.0D-03	-2.0D-03	-2.0D-03
HG	HG	HG	HG	HG
3 1.472	1.472	1.472	1.472	1.472
5 0.646E-02	0.646E-02	0.646E-02	0.646E-02	0.646E-02
7 0.459E-02	0.463E-02	0.459E-02	0.459E-02	0.459E-02
9 0.194E-01	0.194E-01	0.194E-01	0.194E-01	0.194E-01
11 0.156E-01	0.157E-01	0.157E-01	0.156E-01	0.156E-01
13 0.240E-02	0.239E-02	0.239E-02	0.240E-02	0.239E-02
15 0.142E-02	0.144E-02	0.142E-02	0.142E-02	0.142E-02
17 0.110E-03	0.118E-03	0.111E-03	0.110E-03	0.111E-03
19 0.875E-05	0.989E-05	0.875E-05	0.875E-05	0.879E-05
21 0.193E-06	0.240E-06	0.193E-06	0.193E-06	0.195E-06
23 0.157E-08	0.230E-08	0.157E-08	0.157E-08	0.160-08
25 0.652E-11	0.124E-10	0.652E-11	0.652E-11	0.668E-11
(dc + ac)	(dc + ac)	(dc + ac)	(dc + ac)	(dc + ac)
2 0.448E-01	0.448E-01	0.448E-01	0.448E-01	0.448E-01
4 0.471E-03	0.472E-03	0.471E-03	0.471E-03	0.471E-03
6 0.177E-03	0.179E-03	0.177E-03	0.177E-03	0.177E-03
8 0.975E-03	0.100E-02	0.975E-03	0.975E-03	0.975E-03
10 0.106E-02	0.120E-02	0.106E-02	0.106E-02	0.106E-02
12 0.379E-02	0.379E-02	0.379E-02	0.379E-02	0.379E-02
14 0.550E-03	0.552E-03	0.550E-03	0.550E-03	0.549E-03
16 0.824E-03	0.816E-03	0.824E-03	0.824E-03	0.823E-03
18 0.897E-04	0.915E-04	0.897E-04	0.897E-04	0.897E-04
20 0.231E-05	0.251E-05	0.231E-05	0.231E-05	0.232E-05
22 0.222E-07	0.269E-07	0.221E-07	0.222E-07	0.223E-07
24 0.990E-10	0.150E-09	0.990E-10	0.990E-10	0.100E-09
QE: (-0.538923893616126248,-0.390683181213489393E-11)				
QE: (-0.538923893616119809,-0.393706670612520662E-11)				
QE: (-0.538923893616125915,-0.390689958786153690E-11)				
QE: (-0.538923893616126137,-0.390691815165949861E-11)				
QE: (-0.538923893616125471,-0.390675213620766975E-11)				

Table 7.8: Continuation of the convergence tests in Table 7.6 with different basis set. The input parameters are given at the top of each column of the table.

input:	input:	input:	input:	input:
12 50 23 -30 30	12 55 23 -30 30	13 45 25 -30 30	12 55 23 -35 35	12 55 23 -25 25
1064 nm 1.0D+13	1064 nm 1.0D+13	1064 nm 1.0D+13	1064 nm 1.0D+13	1064 nm 1.0D+13
33 -2.0D-01	33 -2.0D-01	33 -2.0D-01	33 -2.0D-01	33 -2.0D-01
-0.539 -3.6D-12	-0.539 -3.6D-12	-0.539 -3.6D-12	-0.539 -3.6D-12	-0.539 -3.6D-12
-2.0D-03	-2.0D-03	-2.0D-03	-2.0D-03	-2.0D-03
HG	HG	HG	HG	HG
3 1.472	1.472	1.472	1.472	1.472
5 0.646E-02	0.646E-02	0.646E-02	0.646E-02	0.646E-02
7 0.459E-02	0.459E-02	0.459E-02	0.459E-02	0.459E-02
9 0.194E-01	0.194E-01	0.194E-01	0.194E-01	0.194E-01
11 0.157E-01	0.157E-01	0.157E-01	0.157E-01	0.157E-01
13 0.240E-02	0.240E-02	0.239E-02	0.240E-02	0.240E-02
15 0.142E-02	0.142E-02	0.142E-02	0.142E-02	0.142E-02
17 0.110E-03	0.110E-03	0.111E-03	0.110E-03	0.110E-03
19 0.873E-05	0.864E-05	0.875E-05	0.864E-05	0.864E-05
21 0.192E-06	0.190E-06	0.193E-06	0.190E-06	0.190E-06
23 0.157E-08	0.155E-08	0.158E-08	0.155E-08	0.155E-08
25 0.603E-11	0.599E-11	0.611E-11	0.599E-11	0.639E-11
27 0.131E-13	0.130E-13	0.134E-13	0.130E-13	0.000E-00
29 0.209E-16	0.205E-16	0.216E-16	0.208E-16	0.000E-00
31 0.000E-00	0.000E-00	0.000E-00	0.365E-19	0.000E-00
33 0.000E-00	0.000E-00	0.000E-00	0.702E-22	0.000E-00
35 0.000E-00	0.000E-00	0.000E-00	0.108E-24	0.000E-00
(dc + ac)	(dc + ac)	(dc + ac)	(dc + ac)	(dc + ac)
2 0.448E-01	0.448E-01	0.448E-01	0.448E-01	0.448E-01
4 0.471E-03	0.471E-03	0.471E-03	0.471E-03	0.471E-03
6 0.177E-03	0.177E-03	0.177E-03	0.177E-03	0.177E-03
8 0.975E-03	0.975E-03	0.975E-03	0.975E-03	0.975E-03
10 0.106E-02	0.106E-02	0.106E-02	0.106E-02	0.106E-02
12 0.379E-02	0.379E-02	0.379E-02	0.379E-02	0.379E-02
14 0.550E-03	0.549E-03	0.550E-03	0.549E-03	0.549E-03
16 0.824E-03	0.824E-03	0.824E-03	0.823E-03	0.824E-03
18 0.896E-04	0.893E-04	0.897E-04	0.894E-04	0.894E-04
20 0.231E-05	0.230E-05	0.231E-05	0.230E-05	0.230E-05
22 0.220E-07	0.220E-07	0.221E-07	0.220E-07	0.220E-07
24 0.966E-10	0.970E-10	0.975E-10	0.969E-10	0.984E-10
26 0.221E-12	0.223E-12	0.225E-12	0.223E-12	0.000E-00
28 0.329E-15	0.329E-15	0.341E-15	0.329E-15	0.000E-00
30 0.564E-18	0.539E-18	0.590E-18	0.577E-18	0.000E-00
32 0.000E-00	0.000E-00	0.000E-00	0.143E-20	0.000E-00
34 0.000E-00	0.000E-00	0.000E-00	0.287E-23	0.000E-00
QE: (-0.538923893616125027,-0.390752051418504909E-11)				
QE: (-0.538923893616123251,-0.390863565224797086E-11)				
QE: (-0.538923893616125582,-0.390702059088232495E-11)				
QE: (-0.538923893616123251,-0.390865155836494997E-11)				
QE: (-0.538923893616123251,-0.390862166487449032E-11)				

Table 7.9: A set of results for a convergence test for the harmonics emission rate from H-atom for the dc-field strength $2F_o = 2.4 \times 10^{-4}$ a.u. and the quasienergy of the ground state of the system. The input parameters are given on the top of each column. The corresponding quasienergies for each system is given at the end of the table.

input:	input:	input:	input:	input:
7 40 13 -25 25	8 40 15 -25 25	9 40 17 -25 25	9 40 17 -30 30	9 45 17 -25 25
1064 nm 1.0D+13	1064 nm 1.0D+13	1064 nm 1.0D+13	1064 nm 1.0D+13	1064 nm 1.0D+13
20 -2.0D-01	20 -2.0D-01	20 -2.0D-01	20 -2.0D-01	20 -2.0D-01
-0.539 -3.7D-11	-0.539 -3.7D-11	-0.539 -3.7D-11	-0.539 -3.7D-11	-0.539 -3.7D-11
-2.40D-04	-2.40D-04	-2.40D-04	-2.40D-04	-2.40D-04
HG	HG	HG	HG	HG
3 1.466	1.466	1.466	1.466	1.466
5 0.612E-02	0.612E-02	0.612E-02	0.612E-02	0.612E-02
7 0.259E-02	0.259E-02	0.259E-02	0.259E-02	0.259E-02
9 0.107E-01	0.107E-01	0.107E-01	0.107E-01	0.107E-01
11 0.118E-01	0.118E-01	0.118E-01	0.118E-01	0.118E-01
13 0.105E-01	0.105E-01	0.105E-01	0.105E-01	0.105E-01
15 0.406E-03	0.406E-03	0.406E-03	0.406E-03	0.406E-03
17 0.262E-03	0.262E-03	0.262E-03	0.262E-03	0.262E-03
19 0.114E-04	0.114E-04	0.114E-04	0.114E-04	0.114E-04
21 0.157E-06	0.156E-06	0.156E-06	0.157E-06	0.157E-06
23 0.100E-08	0.100E-08	0.100E-08	0.100E-08	0.100E-08
25 0.373E-11	0.373E-11	0.373E-11	0.357E-11	0.373E-11
27 0.000E-00	0.000E-00	0.000E-00	0.790E-14	0.000E-00
29 0.000E-00	0.000E-00	0.000E-00	0.117E-16	0.000E-00
(dc + ac)	(dc + ac)	(dc + ac)	(dc + ac)	(dc + ac)
2 0.645E-03	0.645E-03	0.645E-03	0.645E-03	0.645E-03
4 0.703E-05	0.703E-05	0.703E-05	0.703E-05	0.703E-05
6 0.184E-04	0.184E-04	0.184E-04	0.184E-04	0.184E-04
8 0.113E-03	0.113E-03	0.113E-03	0.113E-03	0.113E-03
10 0.405E-03	0.405E-03	0.405E-03	0.405E-03	0.405E-03
12 0.864E-02	0.864E-02	0.864E-02	0.864E-02	0.864E-02
14 0.188E-02	0.188E-02	0.188E-02	0.188E-02	0.188E-02
16 0.867E-03	0.867E-03	0.867E-03	0.867E-03	0.867E-03
18 0.368E-04	0.368E-04	0.368E-04	0.368E-04	0.368E-04
20 0.474E-06	0.474E-06	0.474E-06	0.474E-06	0.474E-06
22 0.268E-08	0.268E-08	0.268E-08	0.268E-08	0.268E-08
24 0.817E-11	0.817E-11	0.817E-11	0.799E-11	0.817E-11
26 0.000E-00	0.000E-00	0.000E-00	0.139E-13	0.000E-00
28 0.000E-00	0.000E-00	0.000E-00	0.151E-16	0.000E-00
30 0.000E-00	0.000E-00	0.000E-00	0.974E-20	0.000E-00

QE:(-0.538921620810842383,-0.347726829463144315E-11)
QE:(-0.538921620810842383,-0.34772655353621269E-11)
QE:(-0.538921620810842383,-0.34772598205119905 9E-11)
QE: (-0.538921620810842383,-0.34772512213971658 2E-11)
QE: (-0.538921620810842383,-0.34772418792238771 4E-11)

input:	input:	input:	input:
7 40 13 -25 25	7 40 13 -25 25	7 40 13 -25 25	7 40 13 -25 25
1064 nm 1.0D+13	1064 nm 1.0D+13	1064 nm 1.0D+13	1064 nm 1.0D+13
30 -2.0D-01	25 -2.0D-01	15 -2.0D-01	33 -2.0D-01
-0.539 -3.7D-11	-0.539 -3.7D-11	-0.539 -3.7D-11	-0.539 -3.7D-11
-2.40D-04	-2.40D-04	-2.40D-04	-2.40D-04
HG	HG	HG	HG
3 1.466	1.466	1.466	1.466
5 0.612E-02	0.612E-02	0.612E-02	0.612E-02
7 0.259E-02	0.259E-02	0.259E-02	0.259E-02
9 0.107E-01	0.107E-01	0.107E-01	0.107E-01
11 0.118E-01	0.118E-01	0.118E-01	0.118E-01
13 0.105E-01	0.105E-01	0.105E-01	0.105E-01
15 0.406E-03	0.406E-03	0.406E-03	0.406E-03
17 0.262E-03	0.262E-03	0.262E-03	0.262E-03
19 0.114E-04	0.114E-04	0.114E-04	0.114E-04
21 0.157E-06	0.157E-06	0.157E-06	0.157E-06
23 0.100E-08	0.100E-08	0.100E-08	0.100E-08
25 0.373E-11	0.373E-11	0.373E-11	0.373E-11
(dc + ac)	(dc + ac)	(dc + ac)	(dc + ac)
2 0.645E-03	0.645E-03	0.645E-03	0.645E-03
4 0.703E-05	0.703E-05	0.703E-05	0.703E-05
6 0.184E-04	0.184E-04	0.184E-04	0.184E-04
8 0.113E-03	0.113E-03	0.113E-03	0.113E-03
10 0.405E-03	0.405E-03	0.405E-03	0.405E-03
12 0.864E-02	0.864E-02	0.864E-02	0.864E-02
14 0.188E-02	0.188E-02	0.188E-02	0.188E-02
16 0.867E-03	0.867E-03	0.867E-03	0.867E-03
18 0.368E-04	0.368E-04	0.368E-04	0.368E-04
20 0.474E-06	0.474E-06	0.474E-06	0.474E-06
22 0.268E-08	0.268E-08	0.268E-08	0.268E-08
24 0.817E-11	0.817E-11	0.817E-11	0.817E-11

QE: (-0.538921620810842383,-0.347728852420090635E-11)
QE: (-0.538921620810842383,-0.347724513827138507E-11)
QE: (-0.538921620810842494,-0.347733669079582674E-11)
QE: (-0.538921620810842272,-0.347732833907631215E-11)

Table 7.10: A set of results for a convergence test for the harmonics emission rate from Yukawa Potential for the dc-field strengths $2F_o = 3.0 \times 10^{-5}$ a.u. and $2F_o = 2.0 \times 10^{-5}$ a.u. and the quasienergy of the ground state of the system. The input parameters are given on the top of each column. The corresponding quasienergies for each system is given at the end of the table.

input:	input:	input:	input:	input:
10 55 19 -25 25	10 55 17 -25 25	10 55 19 -25 25	10 55 19 -23 23	10 50 17 -25 25
2.D+1 1.06D+5	2.D+1 1.06D+5	1.5D+1 1.06D+5	2.D+1 1.06D+5	2.D+1 1.06D+5
2.5D+10 -5.D-2	2.5D+10 -5.D-2	2.5D+10 -5.D-2	2.5D+10 -5.D-2	2.5D+10 -5.D-2
-2.D-05	-2.D-05	-2.D-05	-2.D-05	-2.D-05
HG	HG	HG	HG	HG
3 0.6140E-01	3 0.6140E-01	3 0.6140E-01	3 0.6140E-01	3 0.6140E-01
5 0.1941E-01	5 0.1941E-01	5 0.1941E-01	5 0.1941E-01	5 0.1941E-01
7 0.2073E-02	7 0.2073E-02	7 0.2073E-02	7 0.2073E-02	7 0.2073E-02
9 0.5434E-01	9 0.5434E-01	9 0.5434E-01	9 0.5434E-01	9 0.5434E-01
11 0.274E-01	11 0.274E-01	11 0.274E-01	11 0.274E-01	11 0.274E-01
13 0.162	13 0.162	13 0.162	13 0.162	13 0.162
15 0.150	15 0.150	15 0.150	15 0.150	15 0.150
17 0.221E-01	17 0.221E-01	17 0.221E-01	17 0.221E-01	17 0.221E-01
19 0.122E-02	19 0.122E-02	19 0.122E-02	19 0.122E-02	19 0.122E-02
21 0.340E-04	21 0.340E-04	21 0.340E-04	21 0.338E-04	21 0.340E-04
23 0.568E-06	23 0.568E-06	23 0.568E-06	23 0.579E-06	23 0.568E-06
25 0.625E-08	25 0.625E-08	25 0.625E-08		25 0.625E-08
(dc+ac)	(dc+ac)	(dc+ac)	(dc+ac)	(dc+ac)
2 0.4753E-05	2 0.4766E-05	2 0.4751E-05	2 0.4766E-05	2 0.4768E-05
4 0.1076E-02	4 0.1076E-02	4 0.1076E-02	4 0.1076E-02	4 0.1081E-02
6 0.3531E-02	6 0.3530E-02	6 0.3531E-02	6 0.3531E-02	6 0.3530E-02
8 0.7377E-03	8 0.7377E-03	8 0.7377E-03	8 0.7377E-03	8 0.7377E-03
10 0.242E-01	10 0.242E-01	10 0.242E-01	10 0.242E-01	10 0.242E-01
12 0.428E-01	12 0.428E-01	12 0.428E-01	12 0.428E-01	12 0.428E-01
14 0.522E-01	14 0.522E-01	14 0.522E-01	14 0.522E-01	14 0.522E-01
16 0.130E-01	16 0.130E-01	16 0.130E-01	16 0.130E-01	16 0.130E-01
18 0.110E-02	18 0.110E-02	18 0.110E-02	18 0.110E-02	18 0.110E-02
20 0.445E-04	20 0.445E-04	20 0.445E-04	20 0.445E-04	20 0.445E-04
22 0.102E-05	22 0.102E-05	22 0.102E-05	22 0.104E-05	22 0.102E-05
24 0.150E-07	24 0.150E-07	24 0.150E-07		24 0.150E-07
Quasienergy :	(-0.37411910850224654 2E-01,-0.28630497009314098 6E-07)			
Quasienergy :	(-0.37411910850338202 2E-01,-0.28630566145043732 2E-07)			
Quasienergy :	(-0.37411910850902424 5E-01,-0.28632696909291311 76E-07)			
Quasienergy :	(-0.37411910850224786 0E-01,-0.28630497016646359 9E-07)			
Quasienergy :	(-0.37411910840846017 4E-01,-0.28628189348159261 7E-07)			

input:	input:	input:	input:	input:
10 55 19 -23 23	10 55 19 -25 25	10 50 19 -25 25	10 55 19 -25 25	10 55 17 -25 25
1.5D+1 1.06D+5	1.5D+1 1.06D+5	1.5D+1 1.06D+5	2.0D+1 1.06D+5	1.5D+1 1.06D+5
2.5D+10 -5.D-2	2.5D+10 -5.D-2	2.5D+10 -5.D-2	2.5D+10 -5.D-2	2.5D+10 -5.D-2
-3.D-05	-3.D-05	-3.D-05	-3.D-05	-3.D-05
HG	HG	HG	HG	HG
3 0.5960E-01	3 0.5960E-01	3 0.5960E-01	3 0.5960E-01	3 0.5960E-01
5 0.1200E-01	5 0.1200E-01	5 0.1200E-01	5 0.1200E-01	5 0.1200E-01
7 0.1180E-02	7 0.1180E-02	7 0.1180E-02	7 0.1180E-02	7 0.1180E-02
9 0.2910E-01	9 0.2910E-01	9 0.2910E-01	9 0.2910E-01	9 0.2910E-01
11 0.346E-01	11 0.346E-01	11 0.346E-01	11 0.346E-01	11 0.346E-01
13 0.702E-01	13 0.702E-01	13 0.702E-01	13 0.702E-01	13 0.702E-01
15 0.998E-01	15 0.998E-01	15 0.998E-01	15 0.998E-01	15 0.998E-01
17 0.181E-01	17 0.181E-01	17 0.181E-01	17 0.181E-01	17 0.181E-01
19 0.114E-02	19 0.114E-02	19 0.114E-02	19 0.114E-02	19 0.114E-02
21 0.349E-04	21 0.351E-04	21 0.351E-04	21 0.351E-04	21 0.351E-04
23 0.636E-06	23 0.624E-06	23 0.624E-06	23 0.624E-06	23 0.624E-06
	25 0.716E-08	25 0.716E-08	25 0.716E-08	25 0.716E-08
(dc+ac)	(dc+ac)	(dc+ac)	(dc+ac)	(dc+ac)
2 0.9420E-04	2 0.9420E-04	2 0.9420E-04	2 0.9420E-04	2 0.9420E-04
4 0.1670E-02	4 0.1670E-02	4 0.1670E-02	4 0.1670E-02	4 0.1670E-02
6 0.4240E-02	6 0.4240E-02	6 0.4240E-02	6 0.4240E-02	6 0.4240E-02
8 0.3930E-03	8 0.3930E-03	8 0.3930E-03	8 0.3920E-03	8 0.3920E-03
10 0.555E-01	10 0.555E-01	10 0.555E-01	10 0.555E-01	10 0.555E-01
12 0.712E-01	12 0.711E-01	12 0.712E-01	12 0.712E-01	12 0.712E-01
14 0.970E-01	14 0.970E-01	14 0.970E-01	14 0.970E-01	14 0.970E-01
16 0.286E-01	16 0.286E-01	16 0.286E-01	16 0.286E-01	16 0.286E-01
18 0.264E-02	18 0.264E-02	18 0.264E-02	18 0.264E-02	18 0.264E-02
20 0.110E-03	20 0.110E-03	20 0.110E-03	20 0.110E-03	20 0.110E-03
22 0.260E-05	22 0.254E-05	22 0.254E-05	22 0.254E-05	22 0.255E-05
	24 0.367E-07	24 0.367E-07	24 0.367E-07	24 0.367E-07
Quasienergy :	(-0.37411917743035635 9E-01,-0.25780685022277750 6E-07)			
Quasienergy :	(-0.37411917743035504 0E-01,-0.25780685017016878 6E-07)			
Quasienergy :	(-0.37411917739734096 3E-01,-0.25788298874154139 6E-07)			
Quasienergy :	(-0.37411917740481838 4E-01,-0.25779287359514258 1E-07)			
Quasienergy :	(-0.37411917741150851 9E-01,-0.25781903392366967 1E-07)			

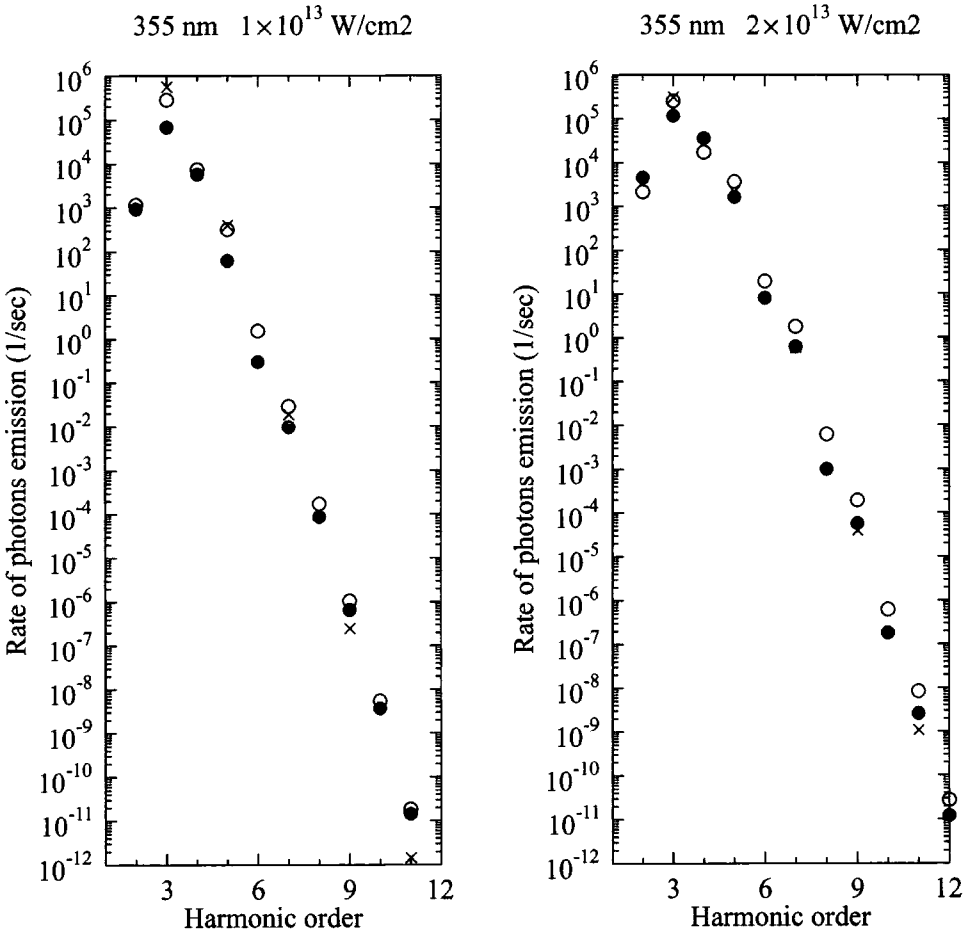

Figure 7.2: Rate of photons emission for hydrogen in a dc-field together with an ac-field with respect to harmonic number. The ac-field intensity and wavelength are given above each picture. The symbols indicates different dc-field strength: $\times$; $F_o = 0.0$, $\circ$; $F_o = 10^{-3}$ a.u. and filled $\circ$; $F_o = 2 \times 10^{-3}$ a.u.

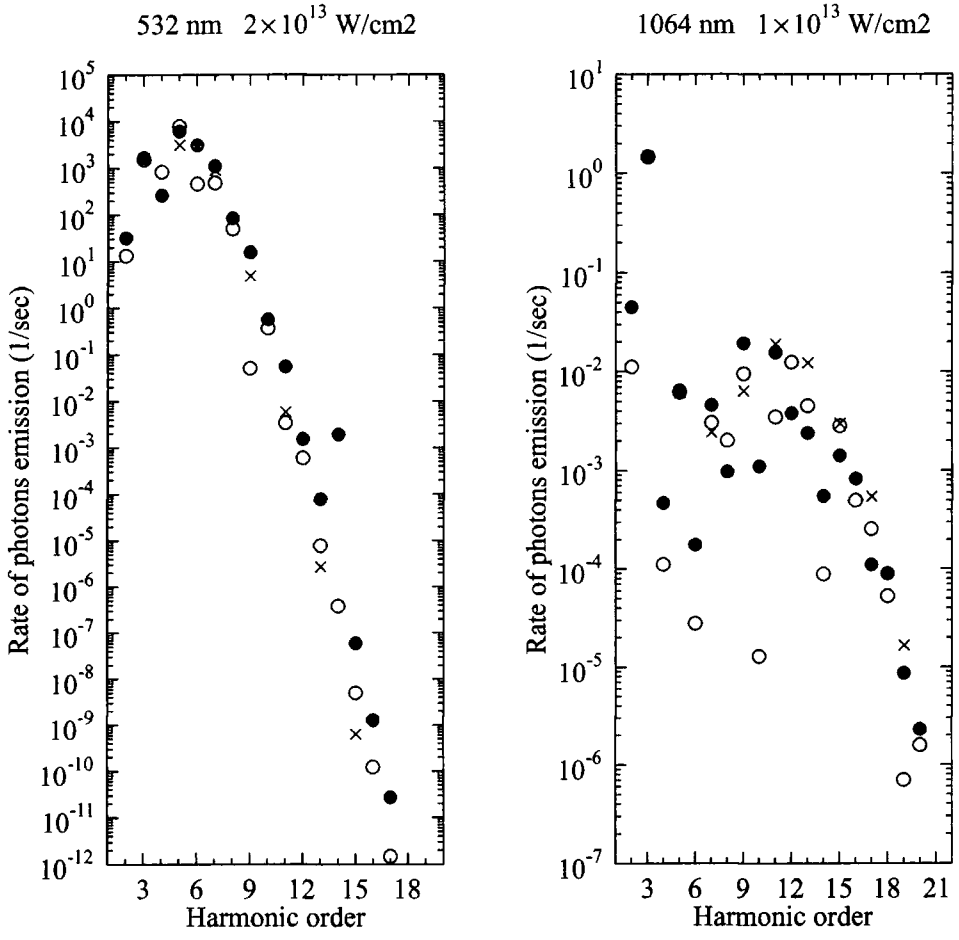

Figure 7.3: Rate of photons emission for hydrogen in a dc-field together with an ac-field with respect to harmonic number. The ac-field intensity and wavelength are given above each picture. The notation of the figures is the same as in Figure 7.2 for the first picture from left, but for the second one is as follows. $\times$; $F_o = 0.0$, $\circ$; $F_o = 0.5 \times 10^{-3}$ a.u. and filled $\circ$; $F_o = 10^{-3}$ a.u.

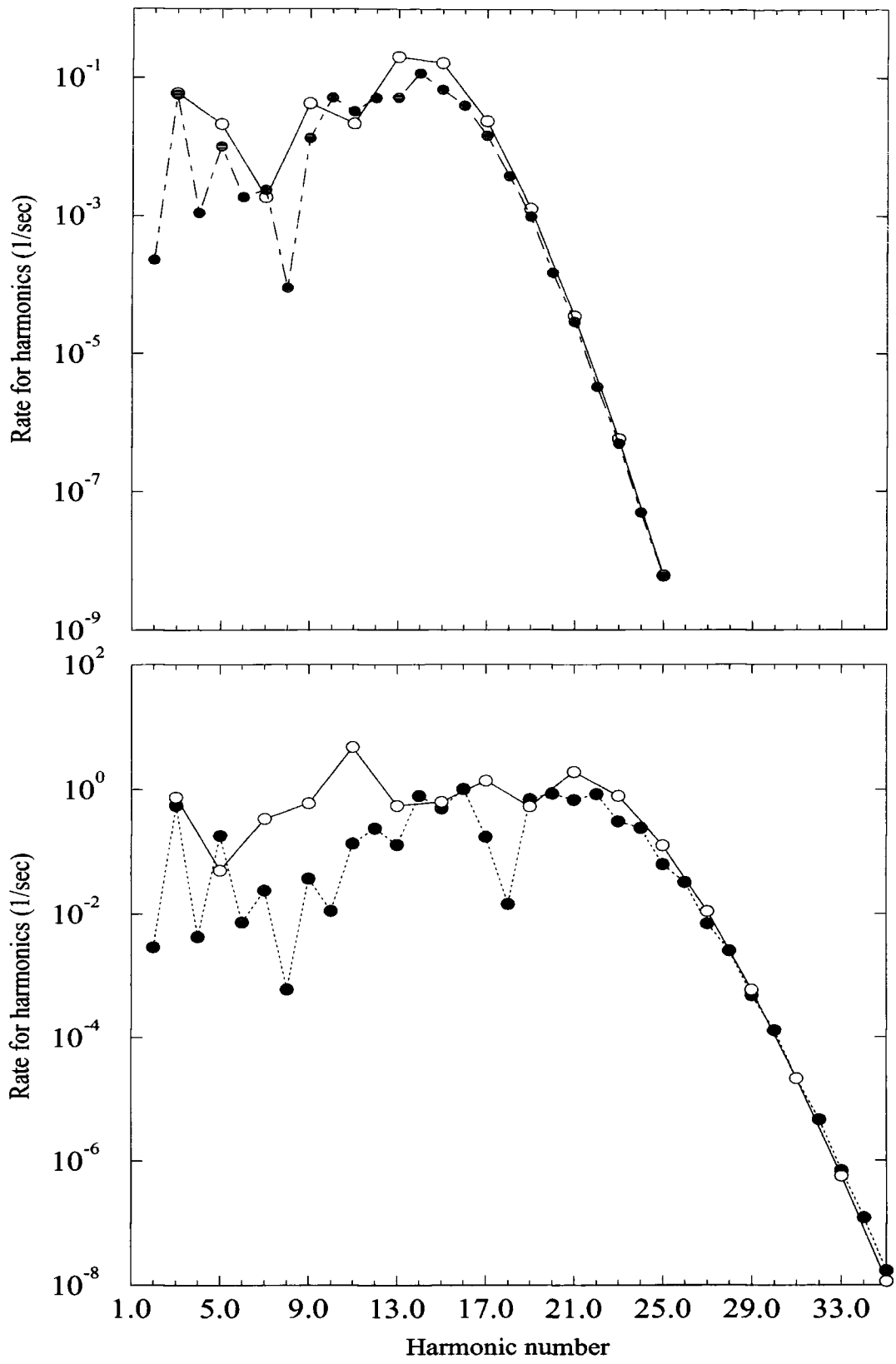

Figure 7.4: Rate of harmonic emission for a Yukawa potential with respect to Harmonic number in a dc-field with together an ac-field. The ac-field intensity and wavelength are I= 2.5×10^{10} W/cm^2 and 10.6μ m for the picture above, respectively and I= 5×10^{10} W/cm^2 and 10.6μ m for the picture below and , respectively and dc-field strength is $F_o = 2 \times 10^{-5}$ a.u. for the both pictures.

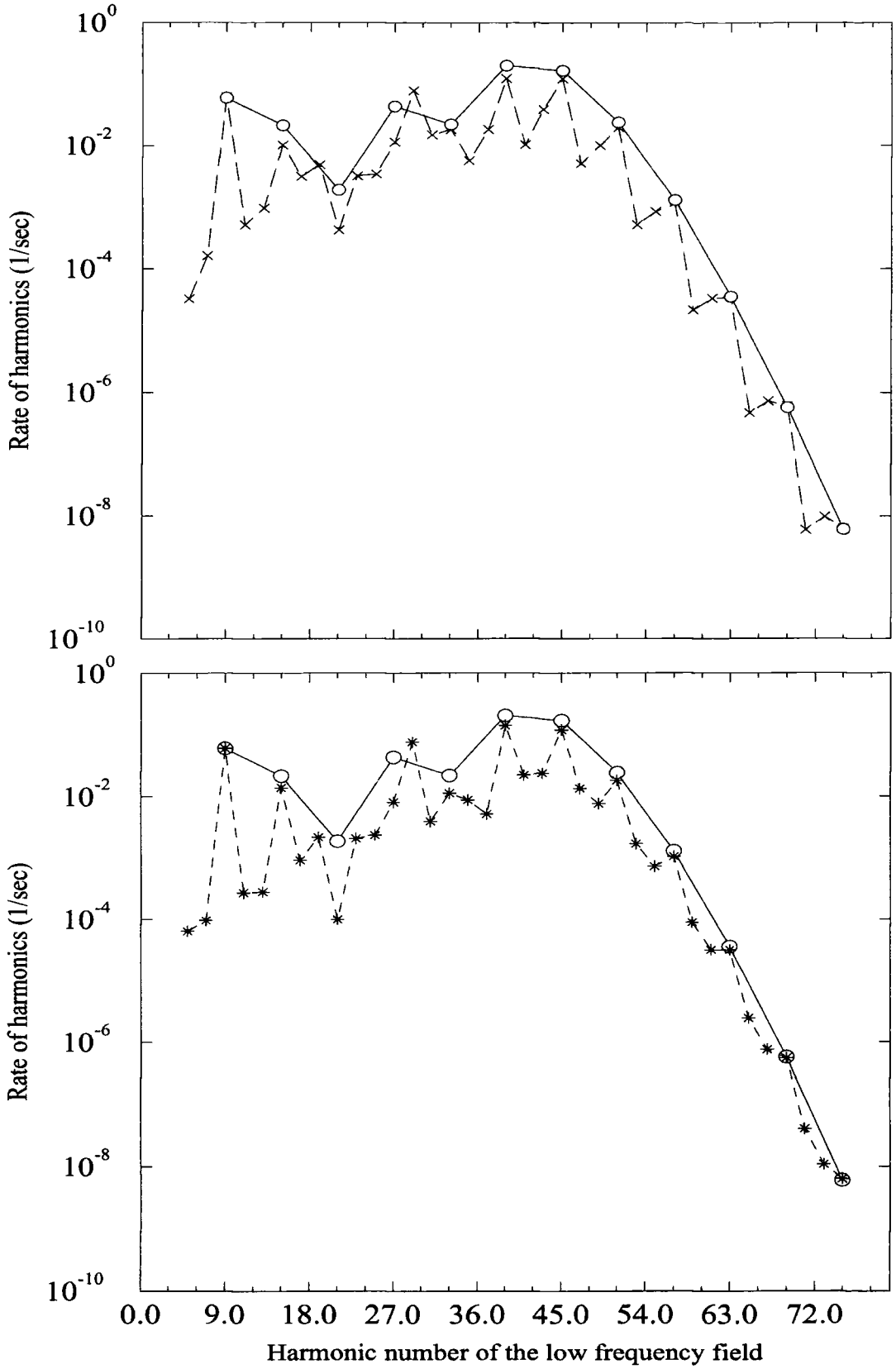

Figure 7.5: Rate of harmonic emission for hydrogen with respect to harmonic number in a commensurable two-colour field. The fundamental ac-field intensity and wavelength are I= 1.4×10^7 W/cm^2 and 31800 nm and the second field is its third harmonic. For the picture above the phase between the fields is $\phi = 180^o$ and for the below one $\phi = 0^o$.

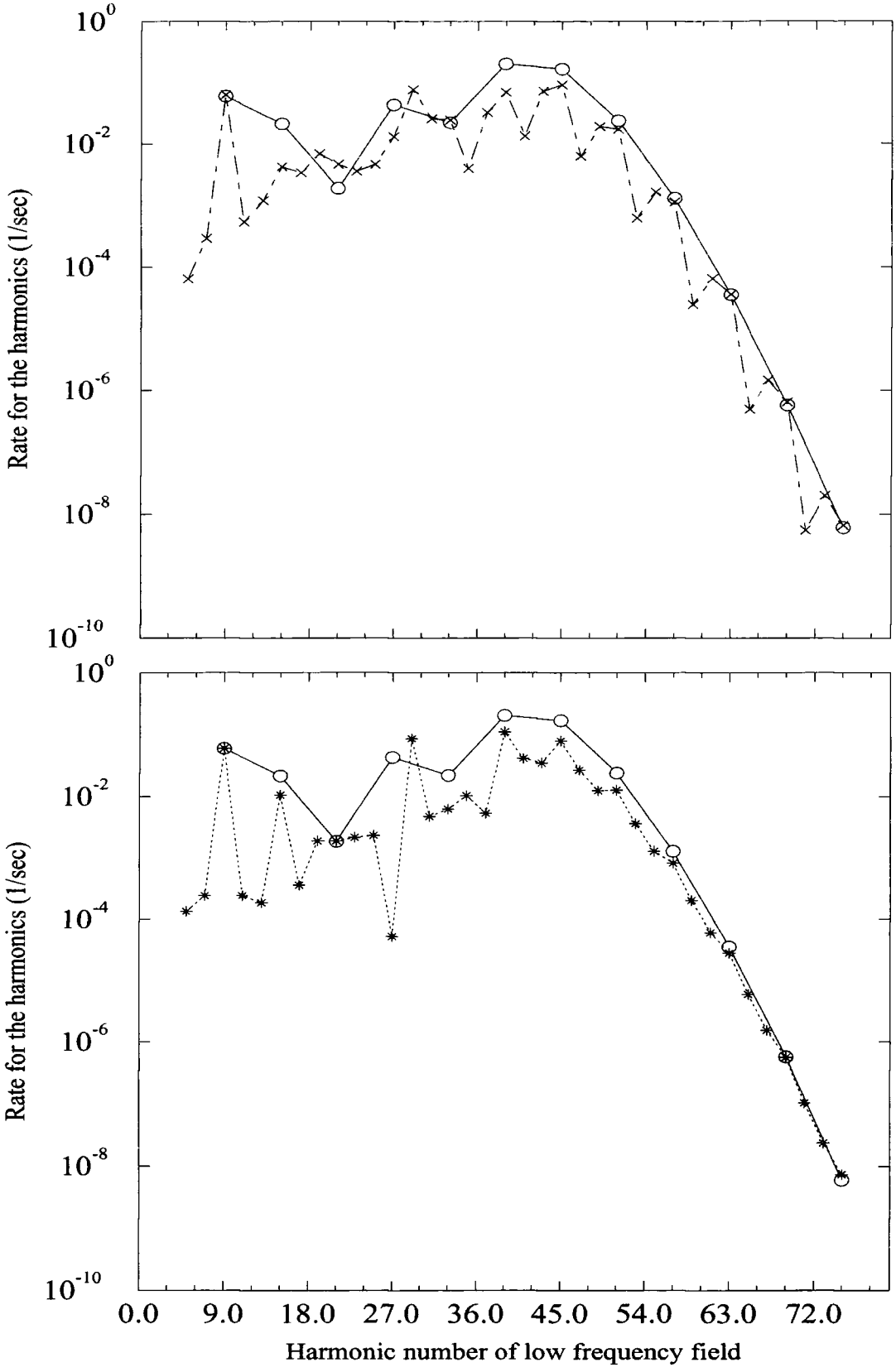

Figure 7.6: Rate of harmonic emission for hydrogen with respect to harmonic number in a commensurable two-colour field. The fundamental ac-field intensity and wavelength are I= 2.81×10^7 W/cm^2 and 31800 nm and the second field is its third harmonic. For the picture above the phase between the fields is $\phi = 180^o$ and for the below one $\phi = 0^o$.

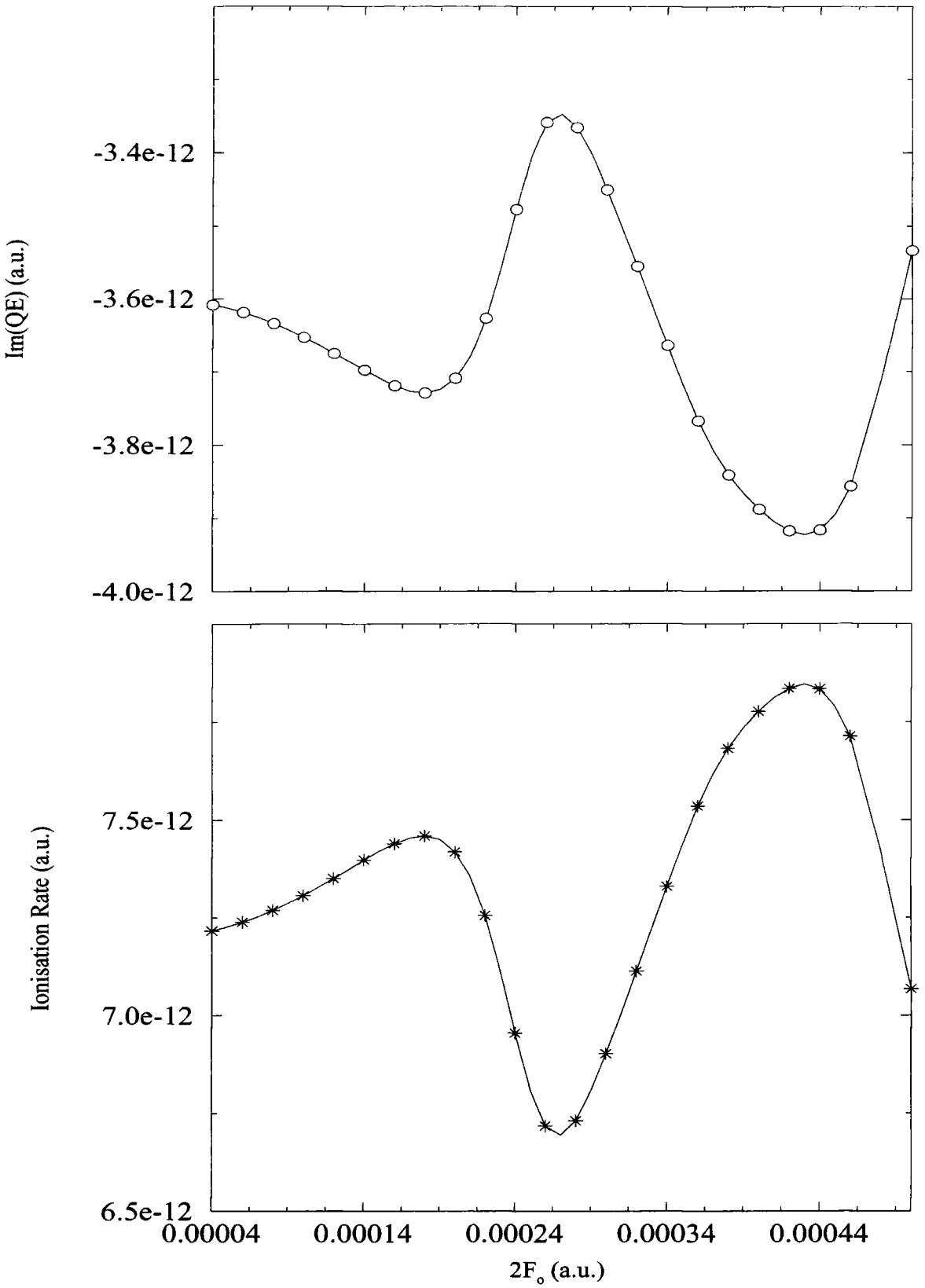

Figure 7.7: Variation of the quasi energy and the ionisation rate for hydrogen with respect to dc-field strength. The ac-field intensity and wavelength are I= 10^{13} W/cm^2 and 1064 nm, respectively.

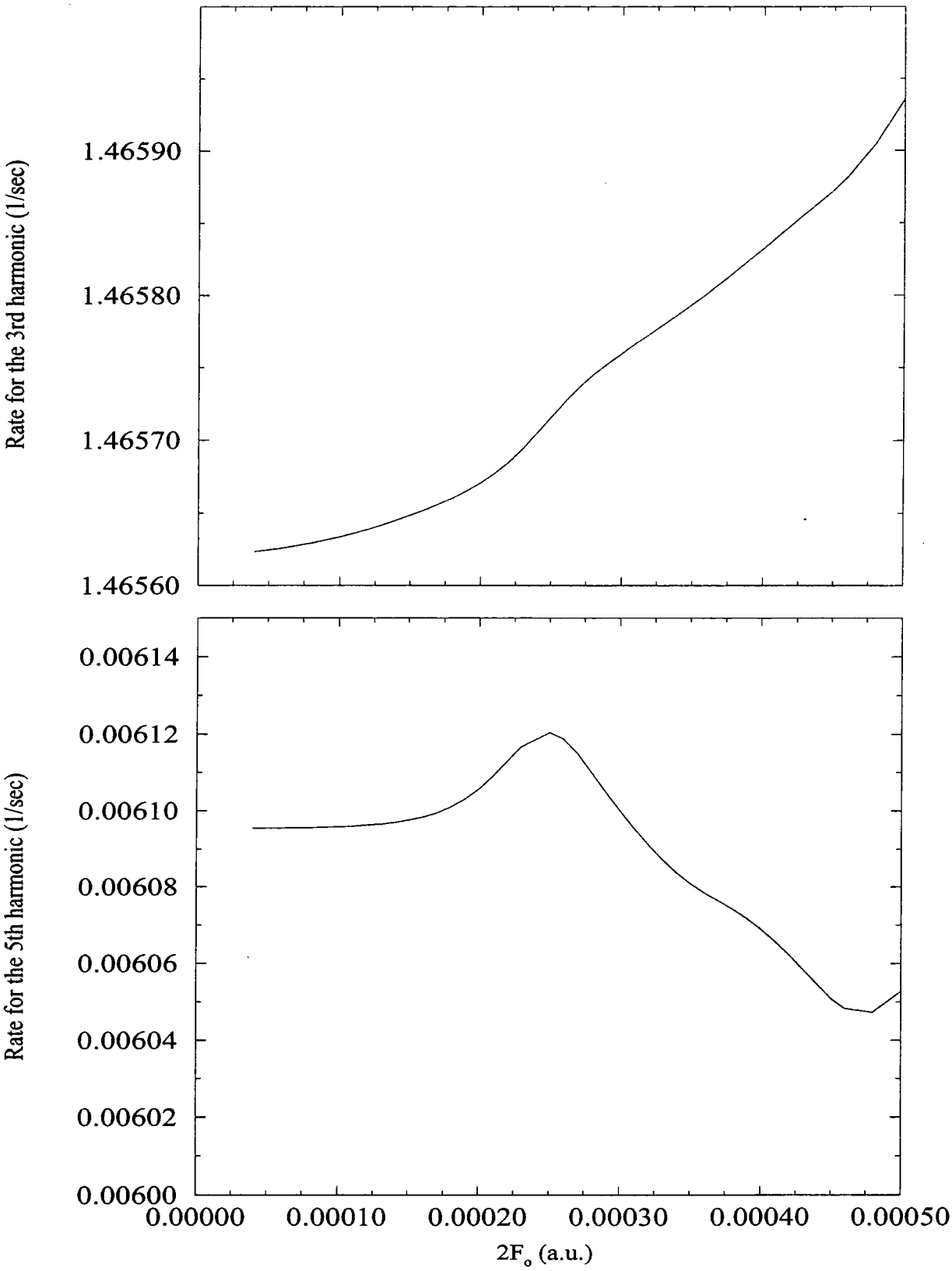

Figure 7.8: Variation of the rate for the 3rd (above) and 5th (bottom) harmonic from hydrogen with respect to dc-field strength. The ac-field intensity and wavelength are I= 10^{13} W/cm^2 and 1064 nm, respectively.

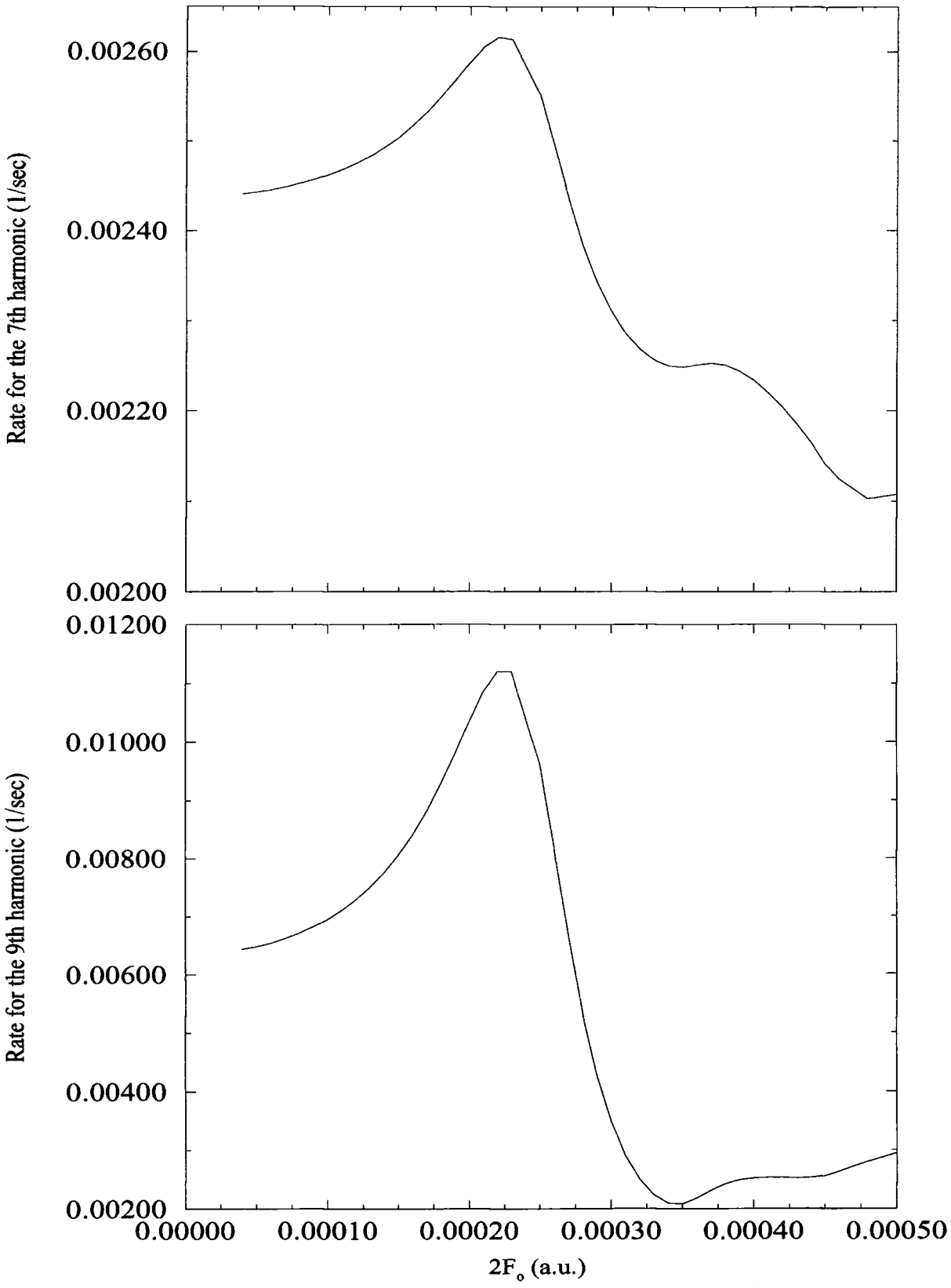

Figure 7.9: Variation of the rate for the 7th (above) and 9th (bottom) harmonic from hydrogen with respect to dc-field strength. The ac-field intensity and wavelength are I= 10^{13} W/cm^2 and 1064 nm, respectively.

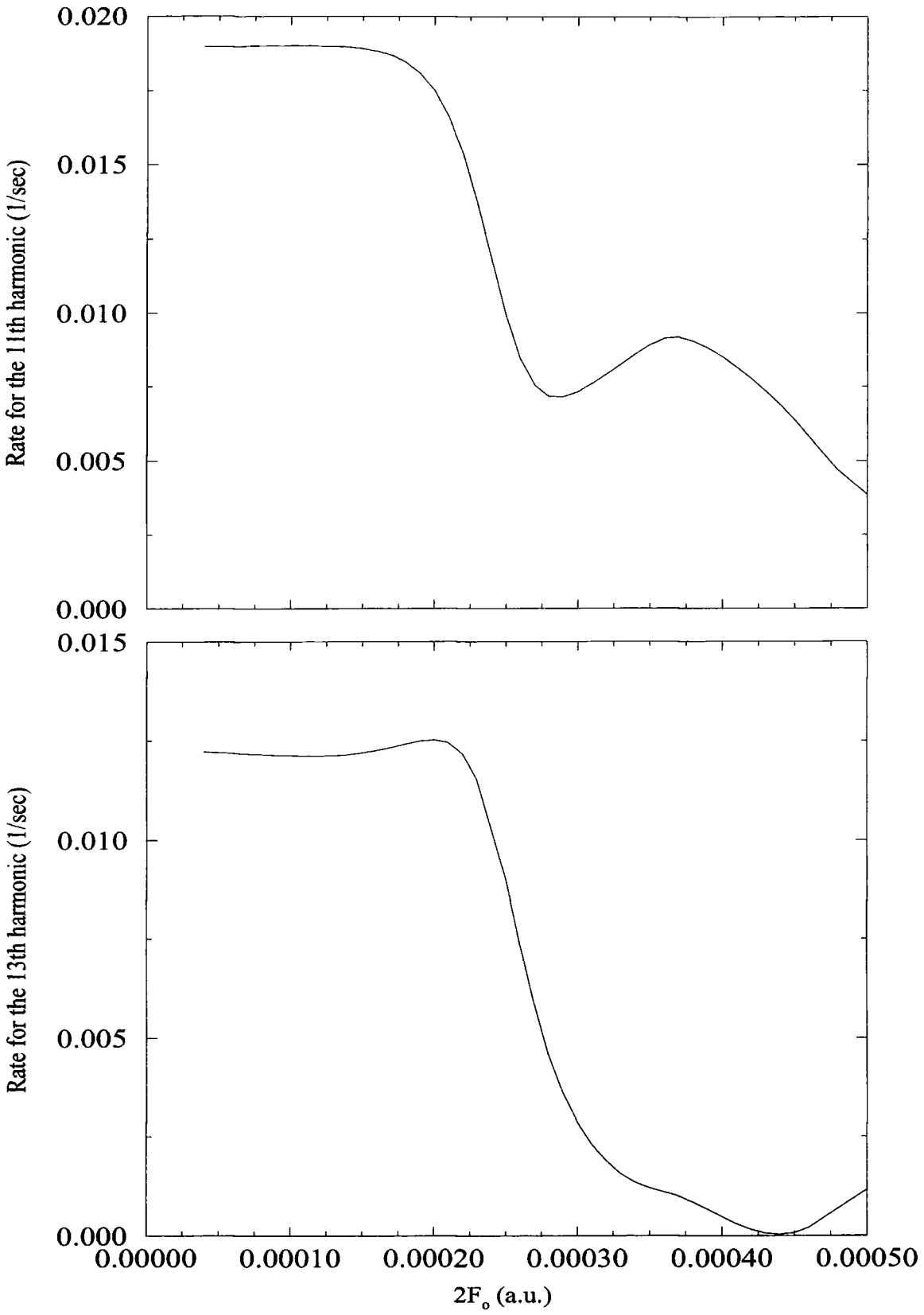

Figure 7.10: Variation of the rate for the 11th (above) and 13th (bottom) harmonic from hydrogen with respect to dc-field strength. The ac-field intensity and wavelength are I= 10^{13} W/cm^2 and 1064 nm, respectively.

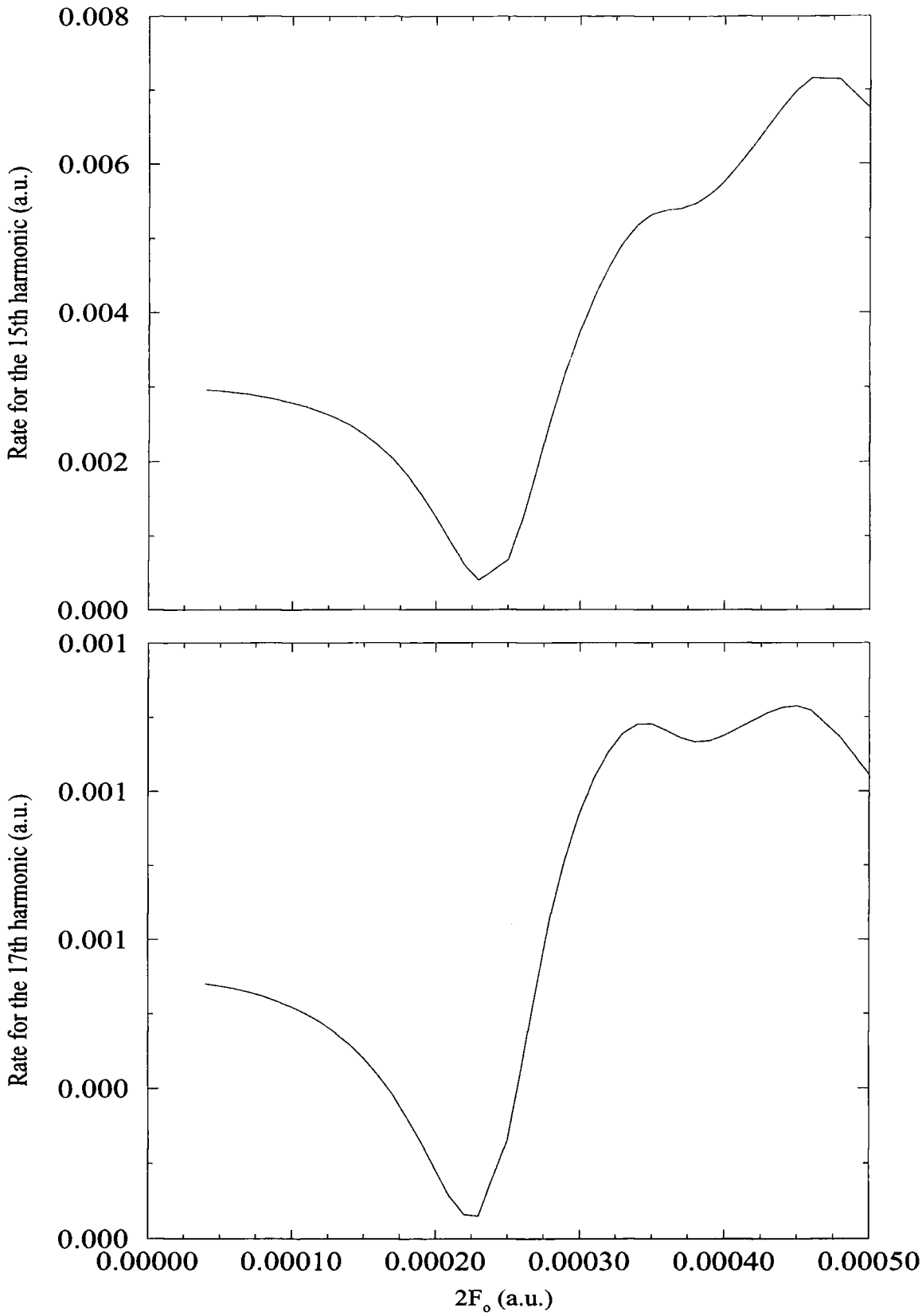

Figure 7.11: Variation of the rate for the 15th (above) and 17th (bottom) harmonic from hydrogen with respect to dc-field strength. The ac-field intensity and wavelength are I= 10^{13} W/cm^2 and 1064 nm, respectively.

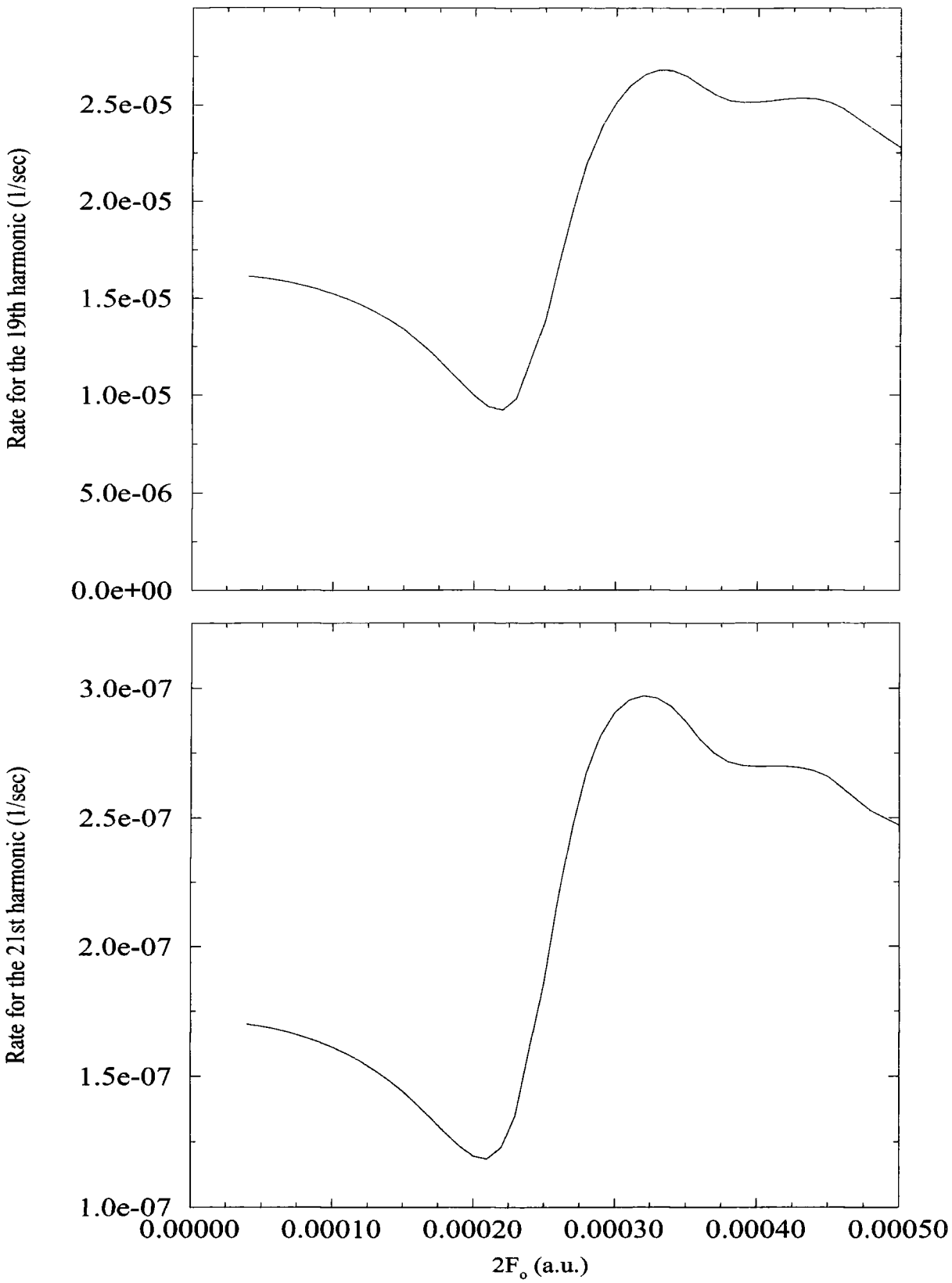

Figure 7.12: Variation of the rate for the 19th (above) and 21th (bottom) harmonic from hydrogen with respect to dc-field strength. The ac-field intensity and wavelength are I= 10^{13} W/cm^2 and 1064 nm, respectively.

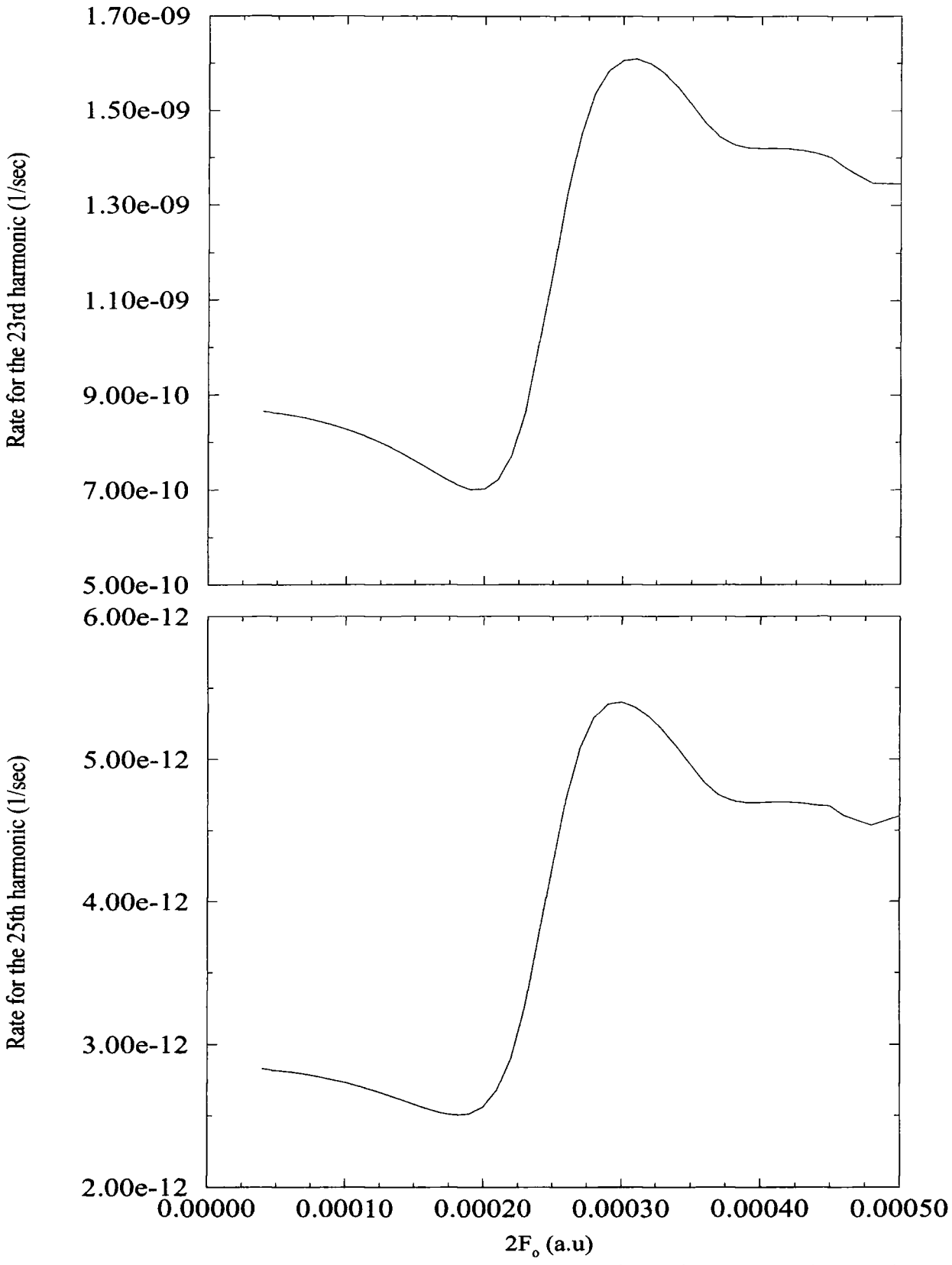

Figure 7.13: Variation of the rate for the 23rd (above) and 25th (bottom) harmonic from hydrogen with respect to dc-field strength. The ac-field intensity and wavelength are I= 10^{13} W/cm^2 and 1064 nm, respectively.

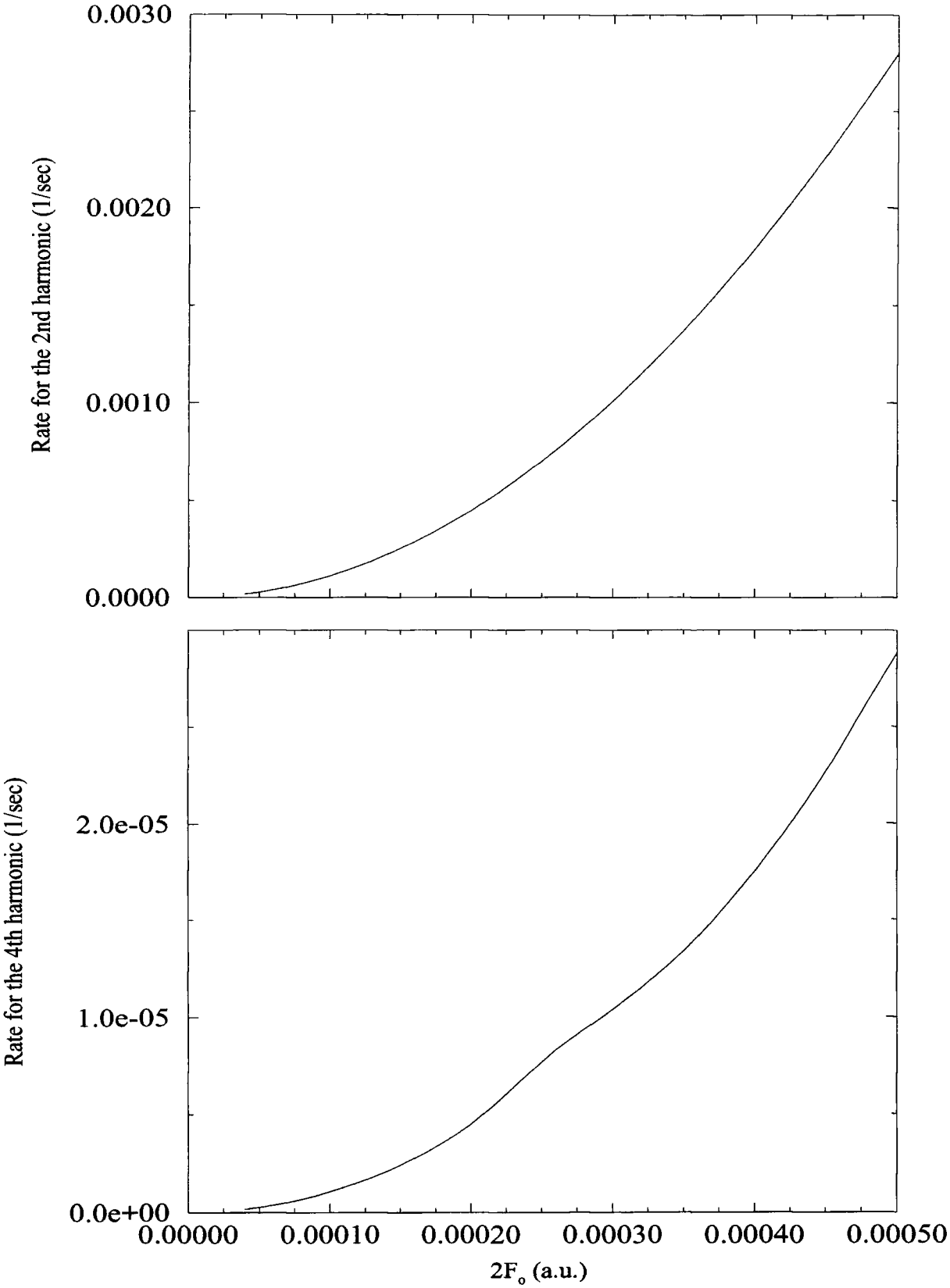

Figure 7.14: Variation of the rate for the 2nd (above) and 4th (bottom) harmonic from hydrogen with respect to dc-field strength. The ac-field intensity and wavelength are I= 10^{13} W/cm^2 and 1064 nm, respectively.

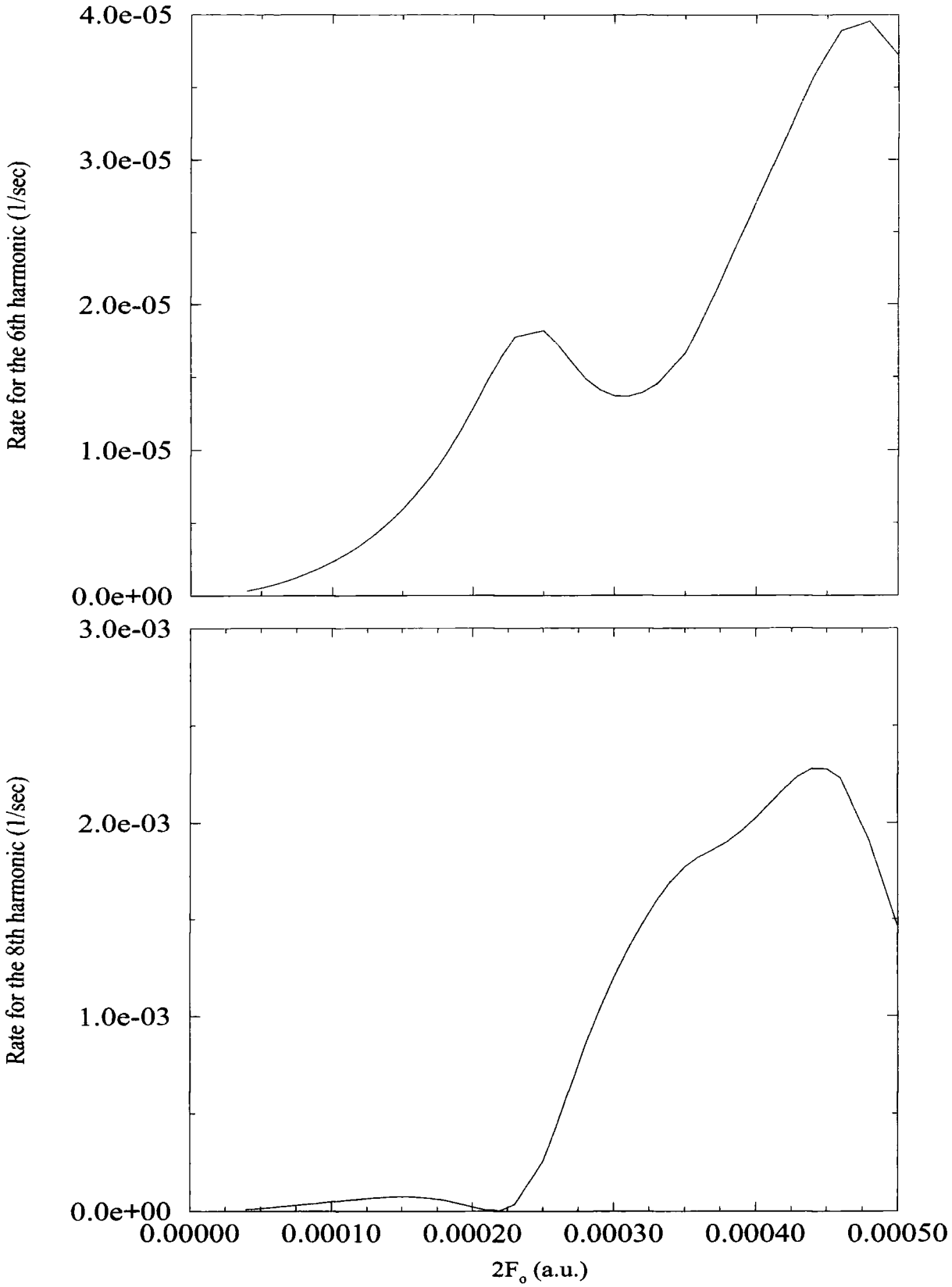

Figure 7.15: Variation of the rate for the 6th (above) and 8th (bottom) harmonic from hydrogen with respect to dc-field strength. The ac-field intensity and wavelength are I= 10^{13} W/cm^2 and 1064 nm, respectively.

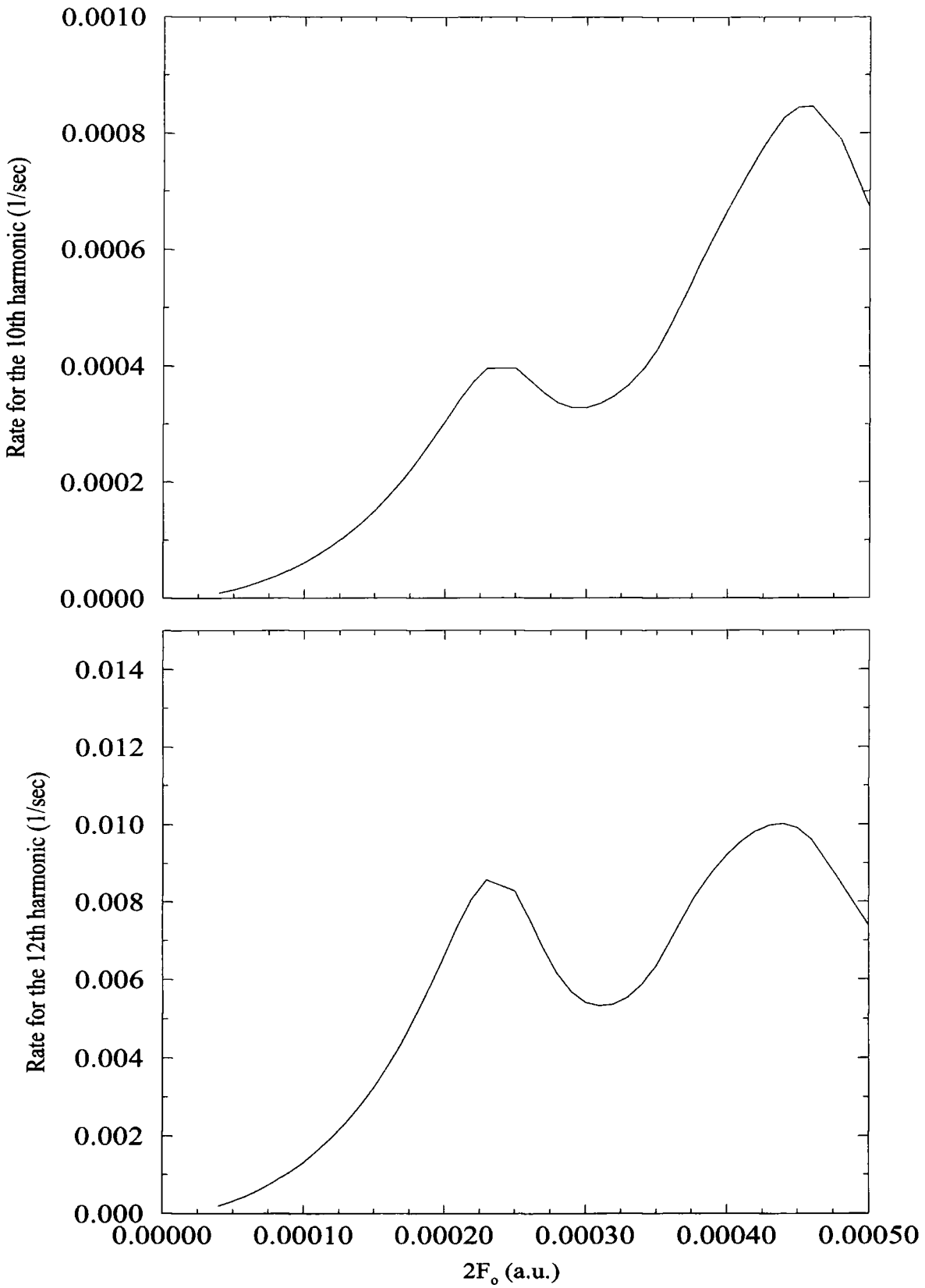

Figure 7.16: Variation of the rate for the 10th (above) and 12th (bottom) harmonic from hydrogen with respect to dc-field strength. The ac-field intensity and wavelength are I= 10^{13} W/cm^2 and 1064 nm, respectively.

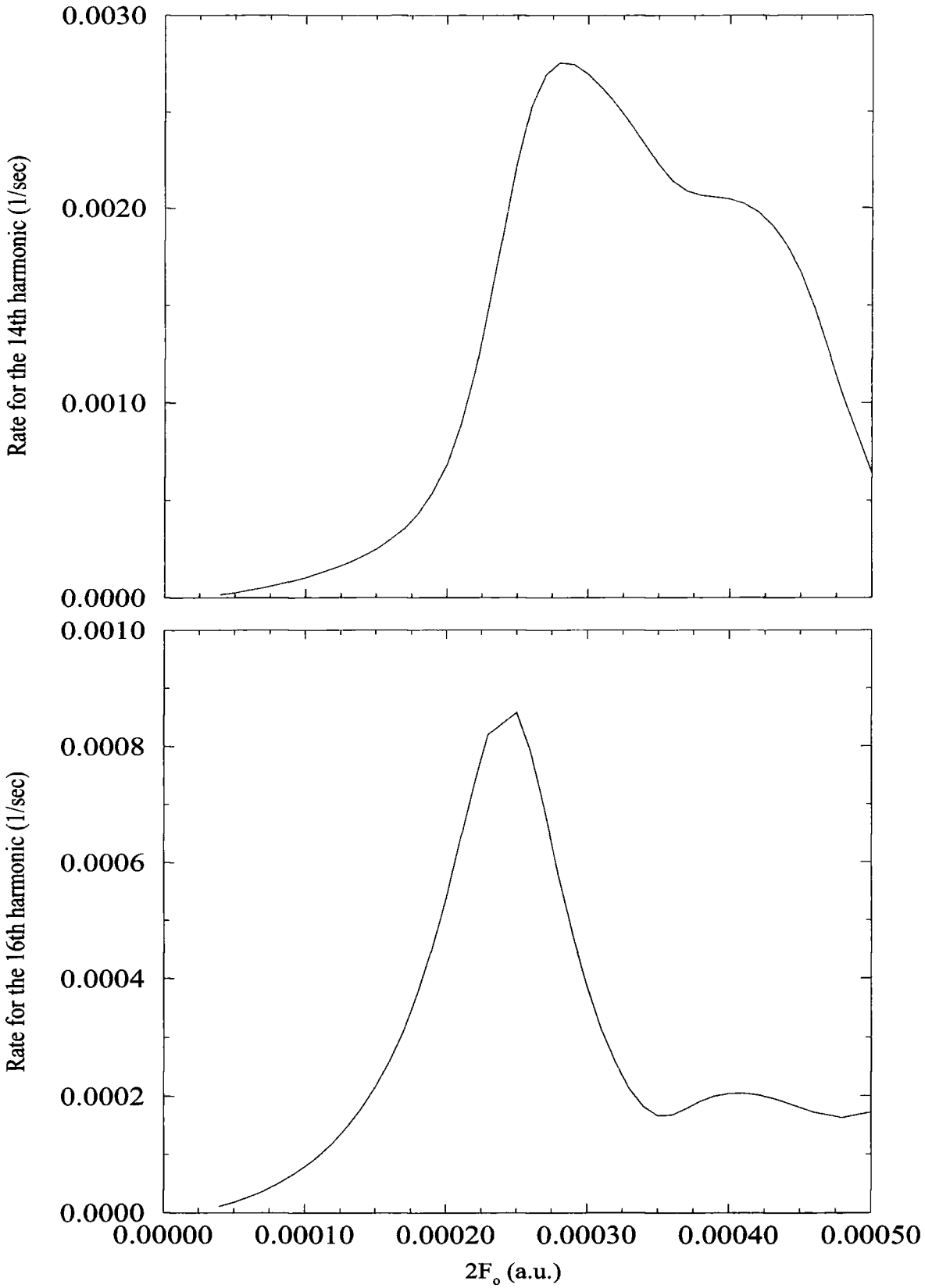

Figure 7.17: Variation of the rate for the 14th (above) and 16th (bottom) harmonic from hydrogen with respect to dc-field strength. The ac-field intensity and wavelength are I= 10^{13} W/cm^2 and 1064 nm, respectively.

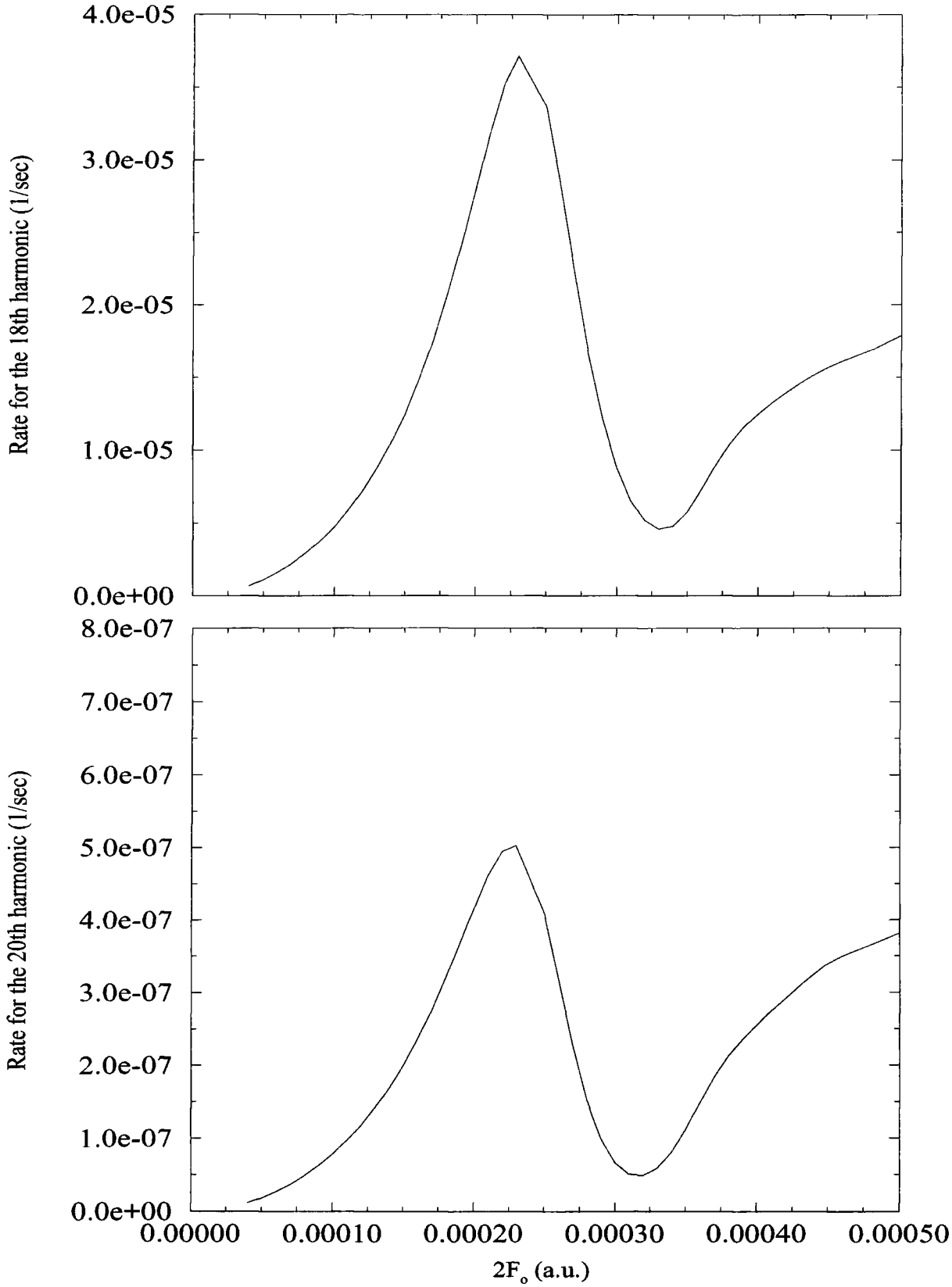

Figure 7.18: Variation of the rate for the 18th (above) and 20th (bottom) harmonic from hydrogen with respect to dc-field strength. The ac-field intensity and wavelength are I= 10^{13} W/cm^2 and 1064 nm, respectively.

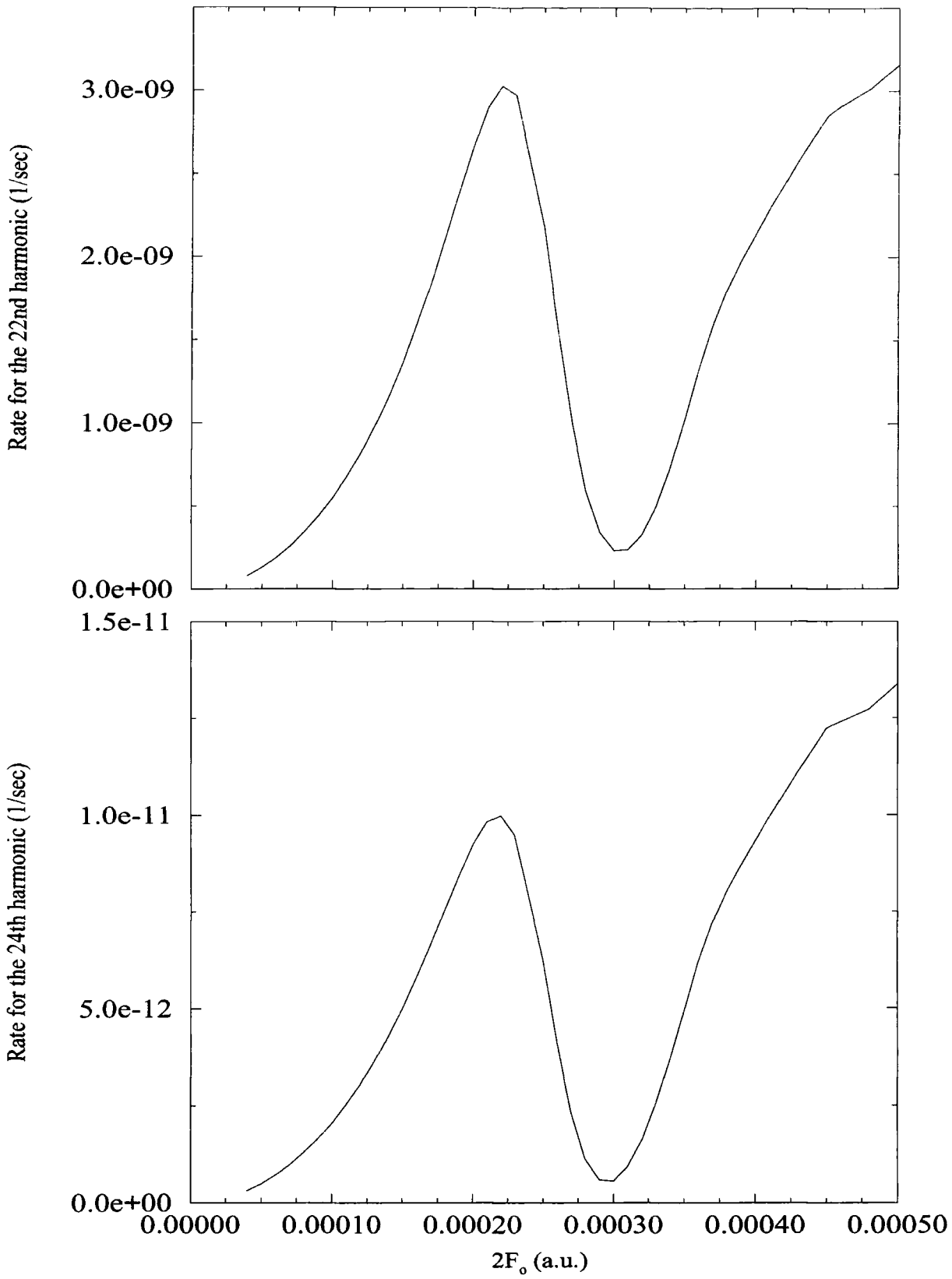

Figure 7.19: Variation of the rate for the 22th (above) and 24th (bottom) harmonic from hydrogen with respect to dc-field strength. The ac-field intensity and wavelength are I= 10^{13} W/cm^2 and 1064 nm, respectively.

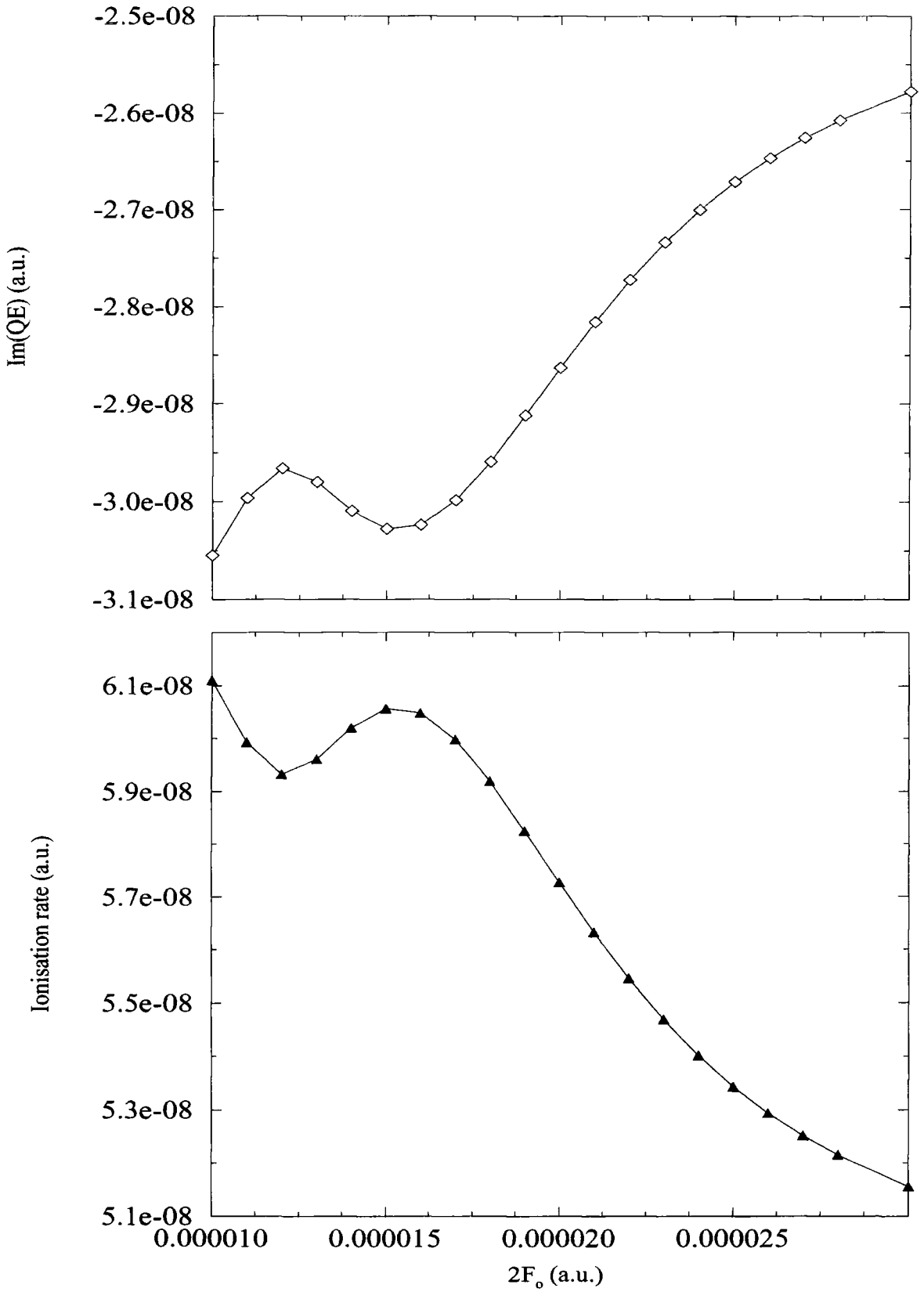

Figure 7.20: Variation of the quasienergy and the ionisation rate for a Yukawa potential with respect to dc-field strength. The ac-field intensity and wavelength are I= $2.50\times^{10}$ W/cm^2 and 10.6μm, respectively.

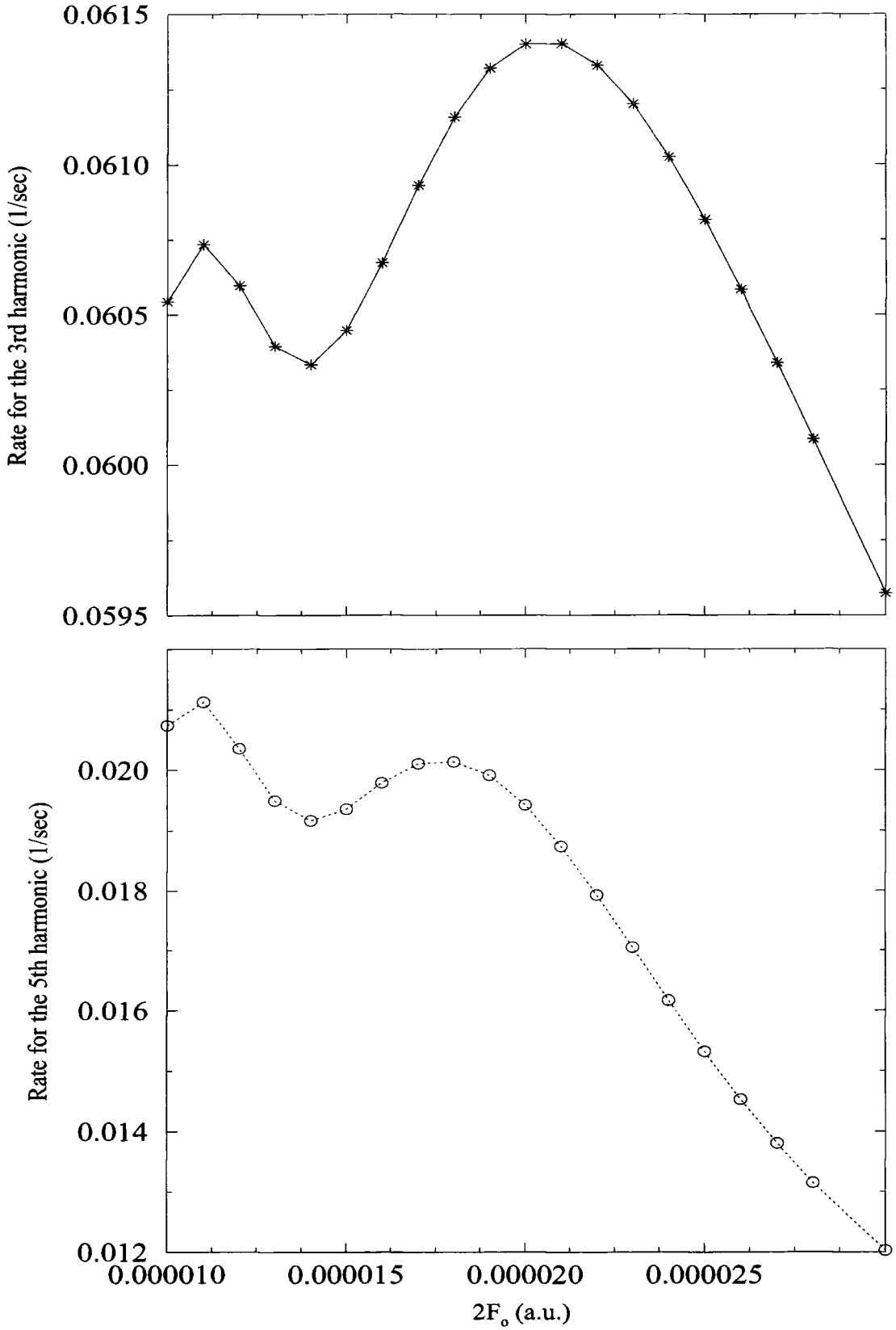

Figure 7.21: Variation of the rate for the 3rd (above) and 5th (bottom) harmonic from a Yukawa potential with respect to dc-field strength. The ac-field intensity and wavelength are I= $2.50\times^{10}$ W/cm^2 and 10.6μm, respectively.

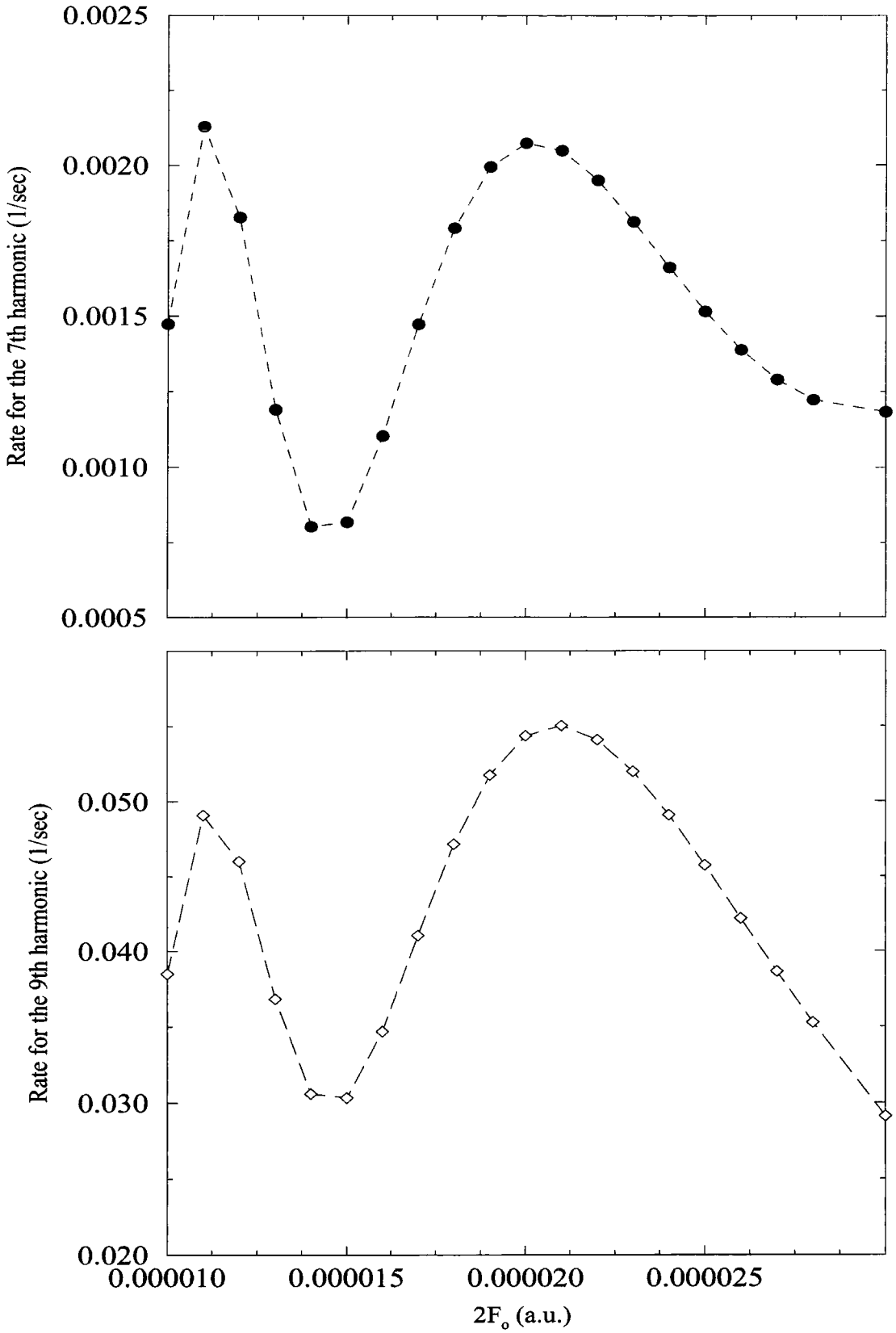

Figure 7.22: Variation of the rate for the 7rd (above) and 9th (bottom) harmonic from a Yukawa potential with respect to dc-field strength. The ac-field intensity and wavelength are I= $2.50\times^{10}$ W/cm^2 and 10.6μm, respectively.

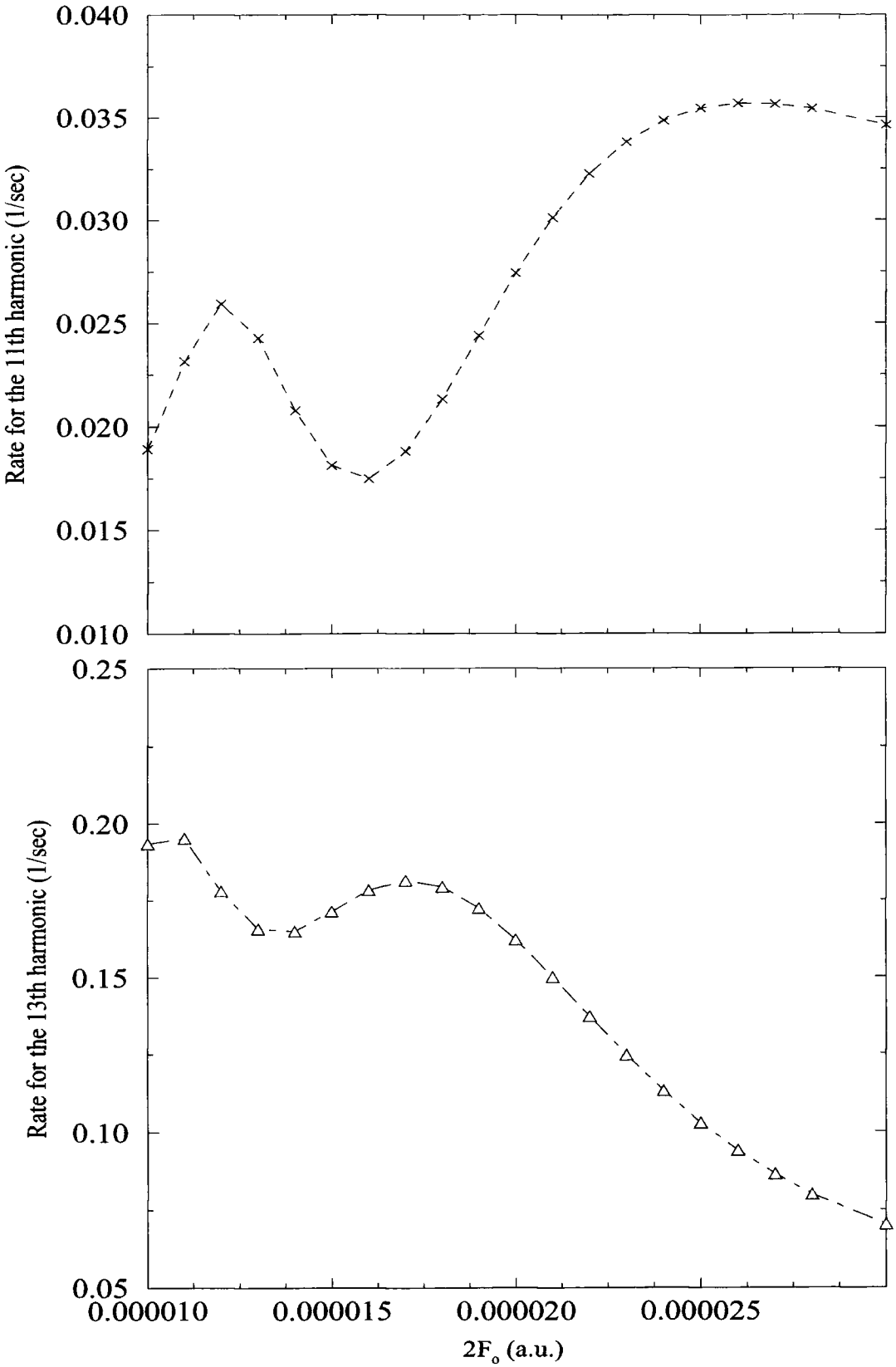

Figure 7.23: Variation of the rate for the 11rd (above) and 13th (bottom) harmonic from a Yukawa potential with respect to dc-field strength. The ac-field intensity and wavelength are I= $2.50\times^{10}$ W/cm^2 and 10.6μm, respectively.

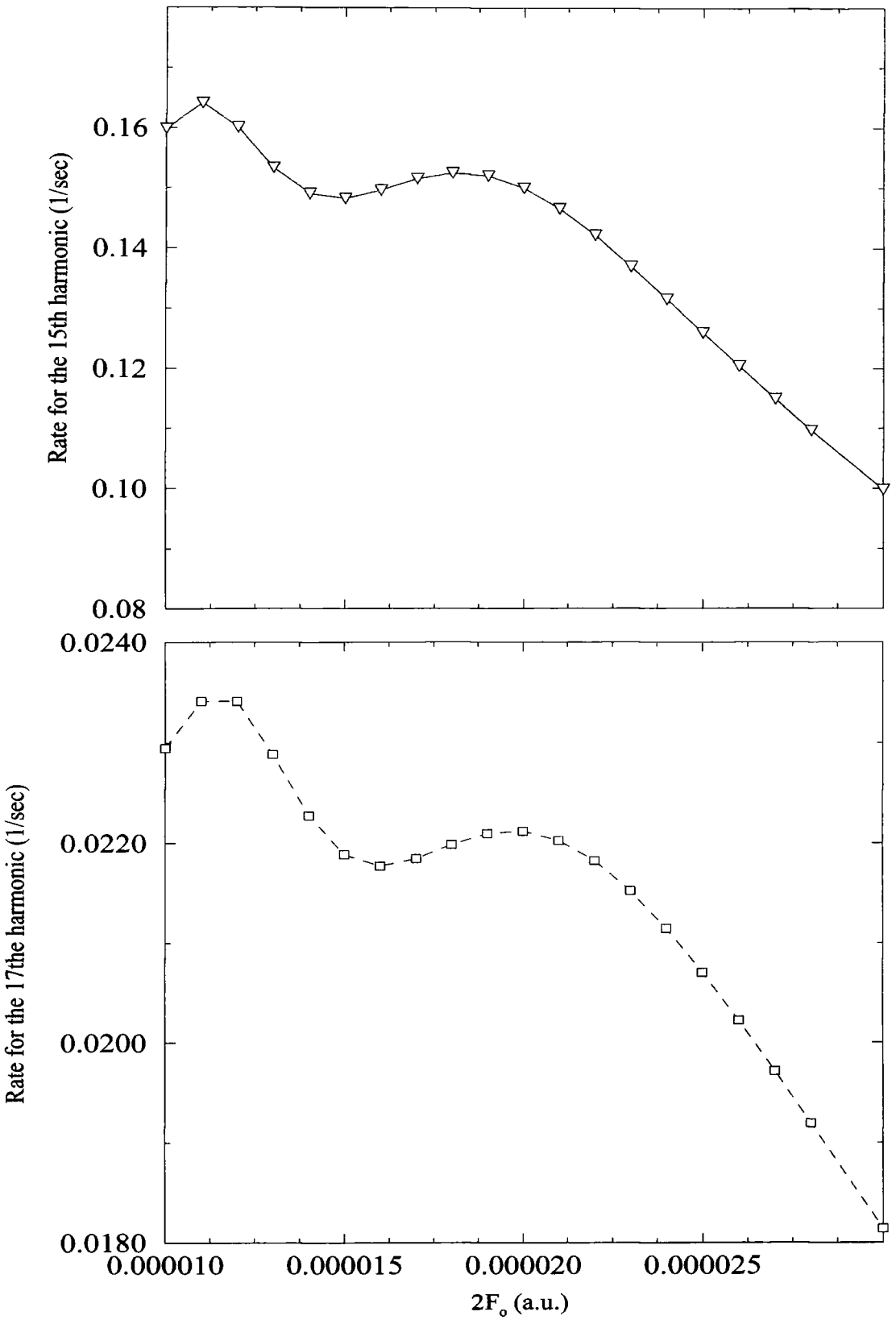

Figure 7.24: Variation of the rate for the 15rd (above) and 17th (bottom) harmonic from a Yukawa potential with respect to dc-field strength. The ac-field intensity and wavelength are I= $2.50\times^{10}$ W/cm^2 and 10.6μm, respectively.

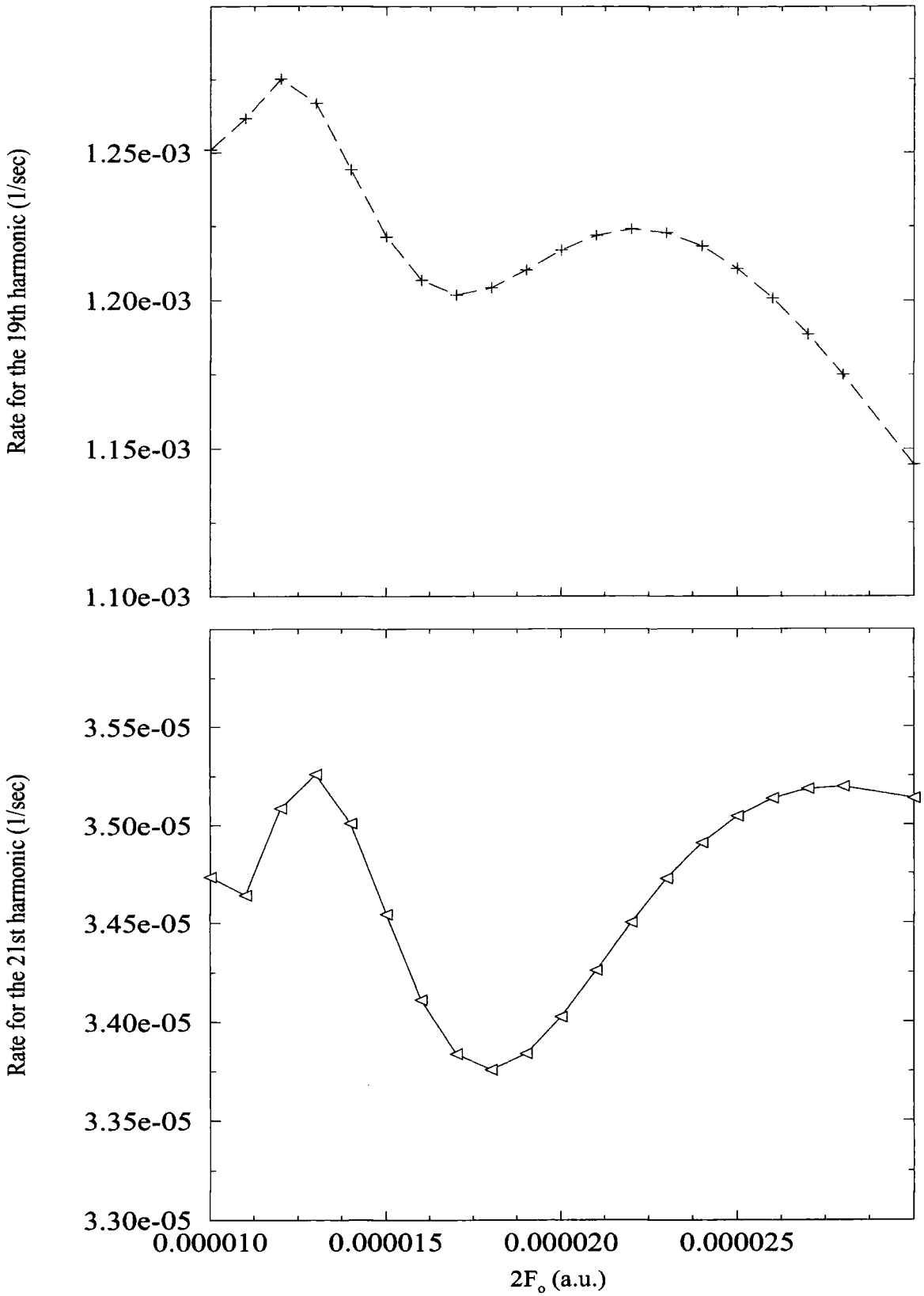

Figure 7.25: Variation of the rate for the 19rd (above) and 21th (bottom) harmonic from a Yukawa potential with respect to dc-field strength. The ac-field intensity and wavelength are I= $2.50\times^{10}$ W/cm^2 and 10.6μm, respectively.

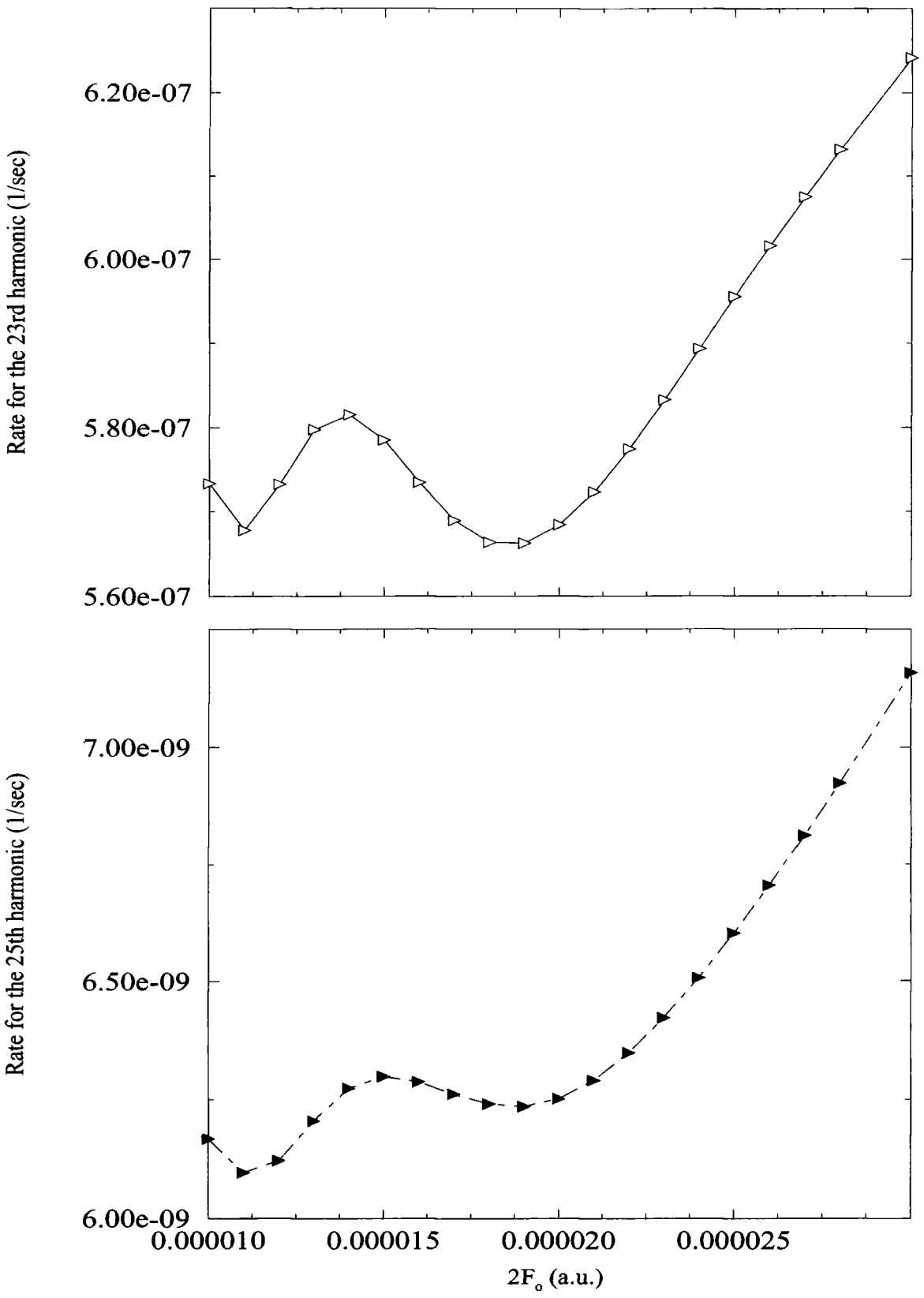

Figure 7.26: Variation of the rate for the 23rd (above) and 25th (bottom) harmonic from a Yukawa potential with respect to dc-field strength. The ac-field intensity and wavelength are I= $2.50\times^{10}$ W/cm^2 and 10.6μm, respectively.

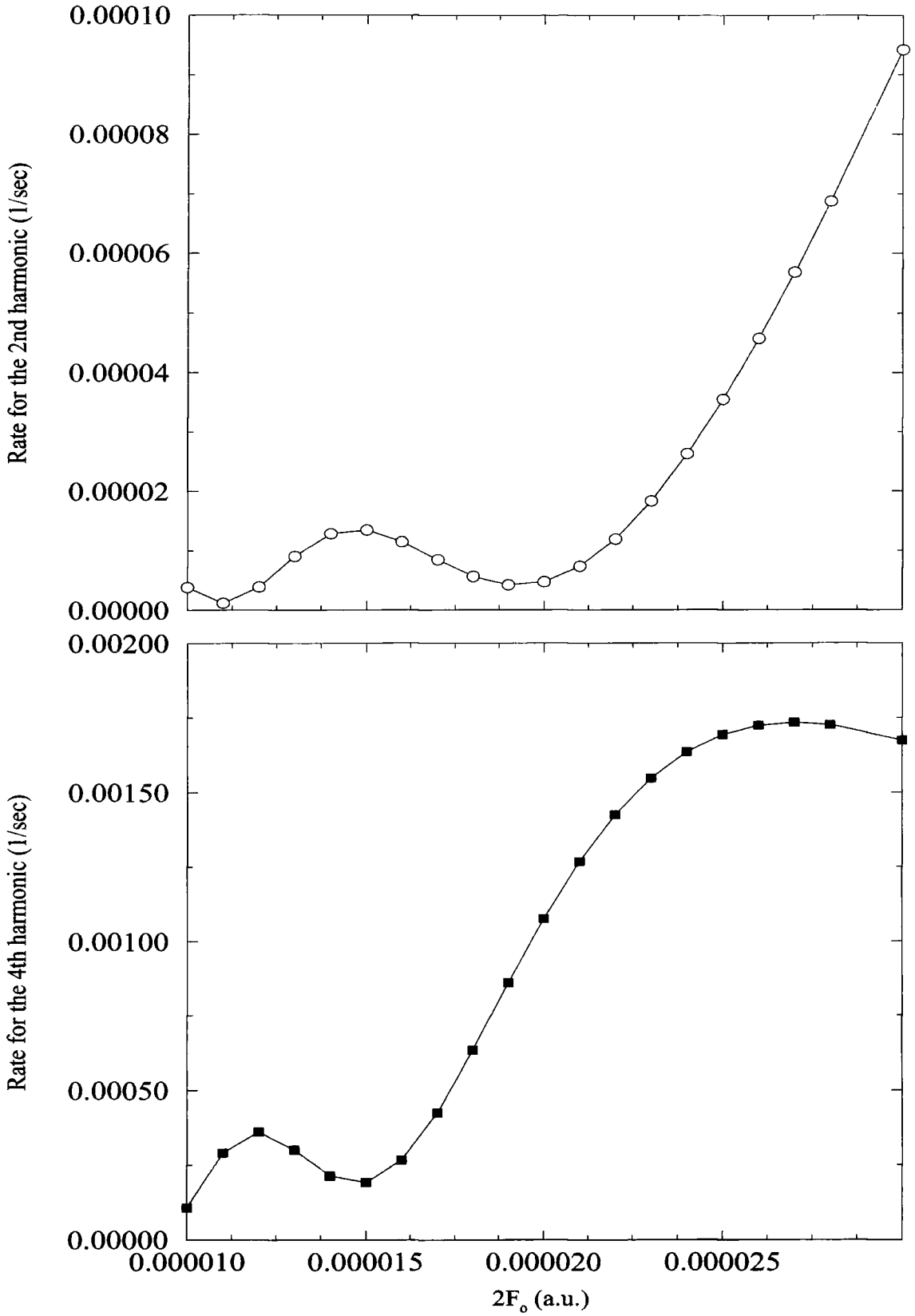

Figure 7.27: Variation of the rate for the 2nd (above) and 4th (bottom) harmonic from a Yukawa potential with respect to dc-field strength. The ac-field intensity and wavelength are I= $2.50\times^{10}$ W/cm^2 and 10.6μm, respectively.

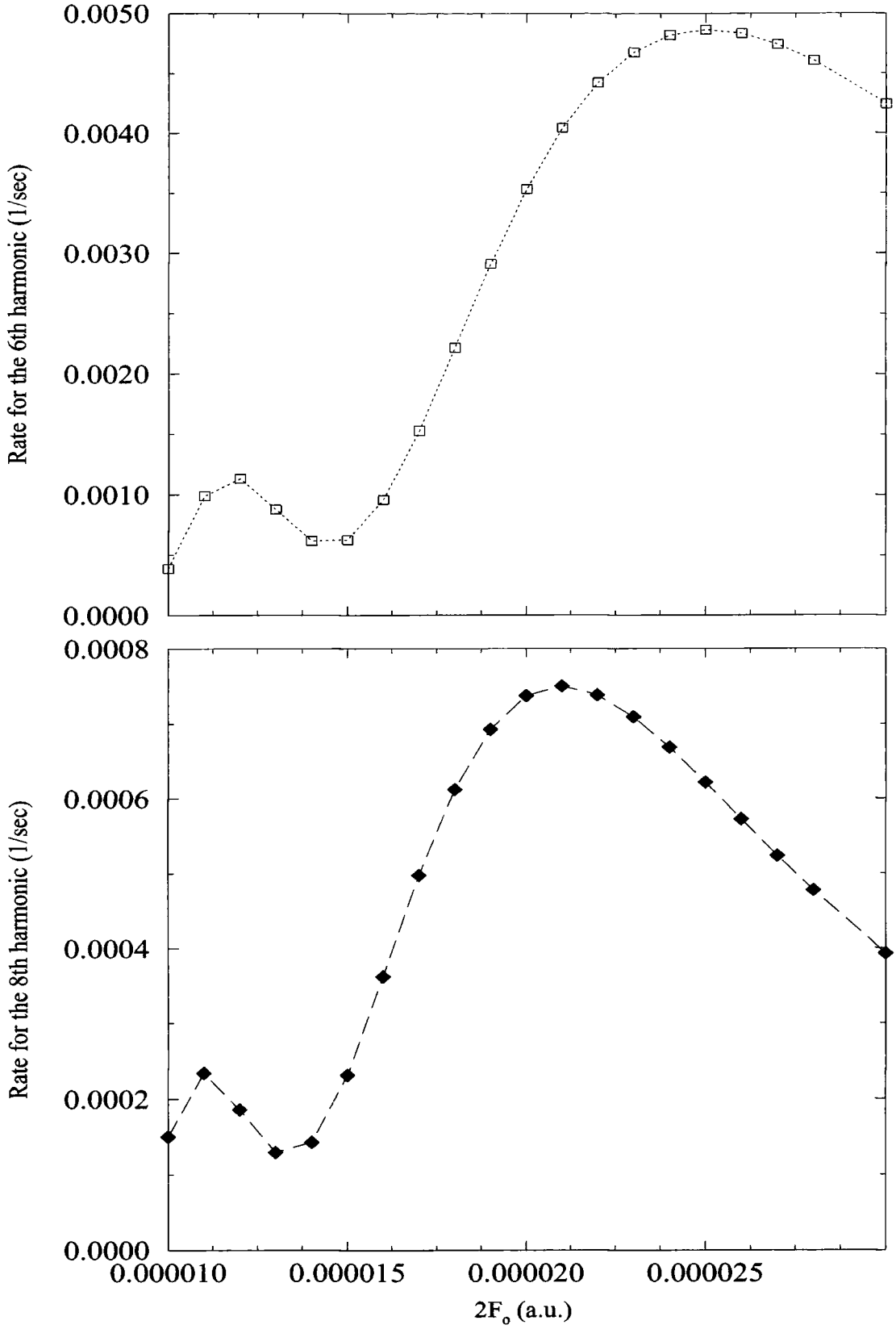

Figure 7.28: Variation of the rate for the 6th (above) and 8th (bottom) harmonic from a Yukawa potential with respect to dc-field strength. The ac-field intensity and wavelength are I= $2.50\times^{10}$ W/cm^2 and 10.6μm, respectively.

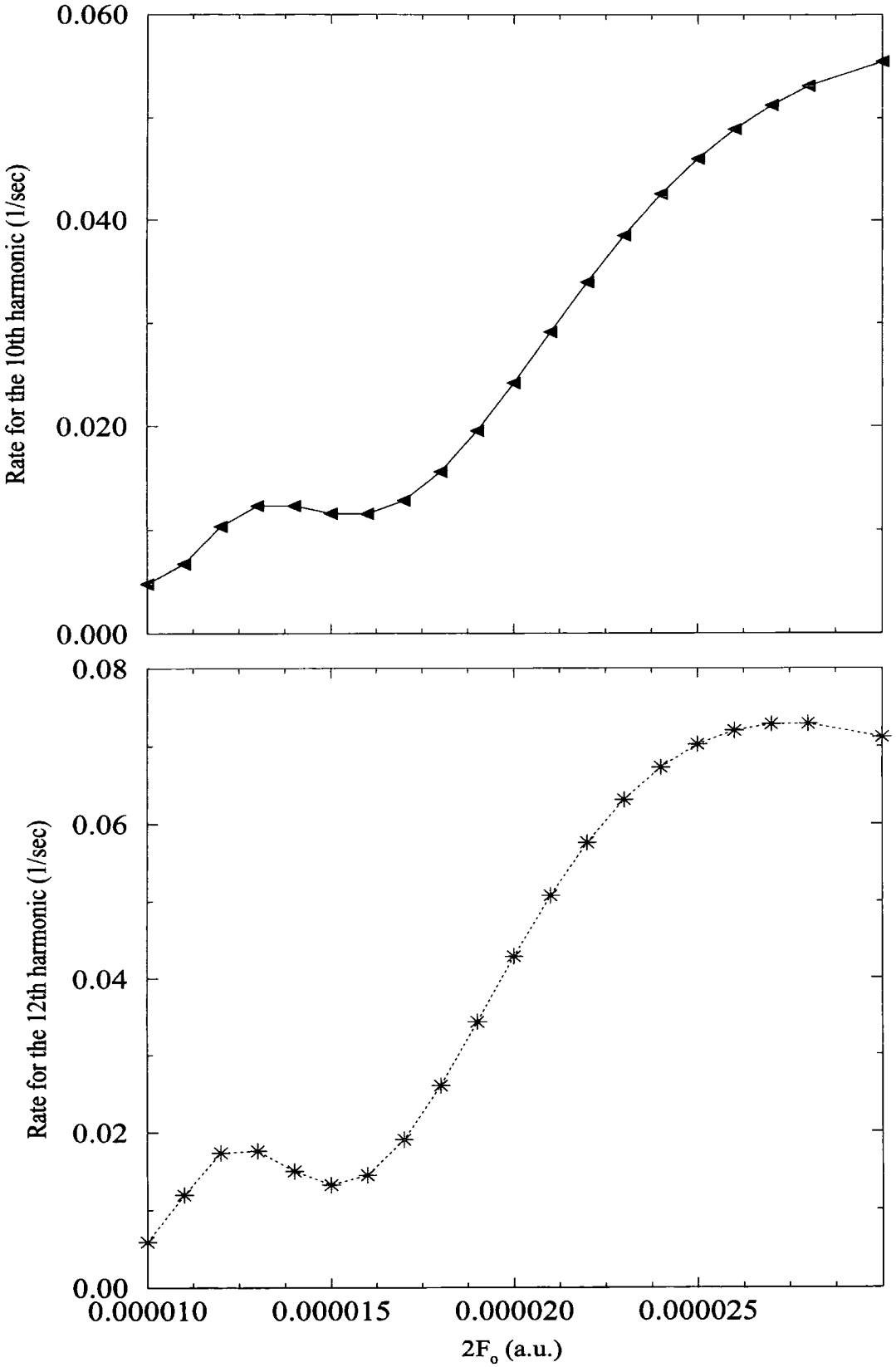

Figure 7.29: Variation of the rate for the 10th (above) and 12th (bottom) harmonic from a Yukawa potential with respect to dc-field strength. The ac-field intensity and wavelength are I= $2.50\times^{10}$ W/cm^2 and 10.6μm, respectively.

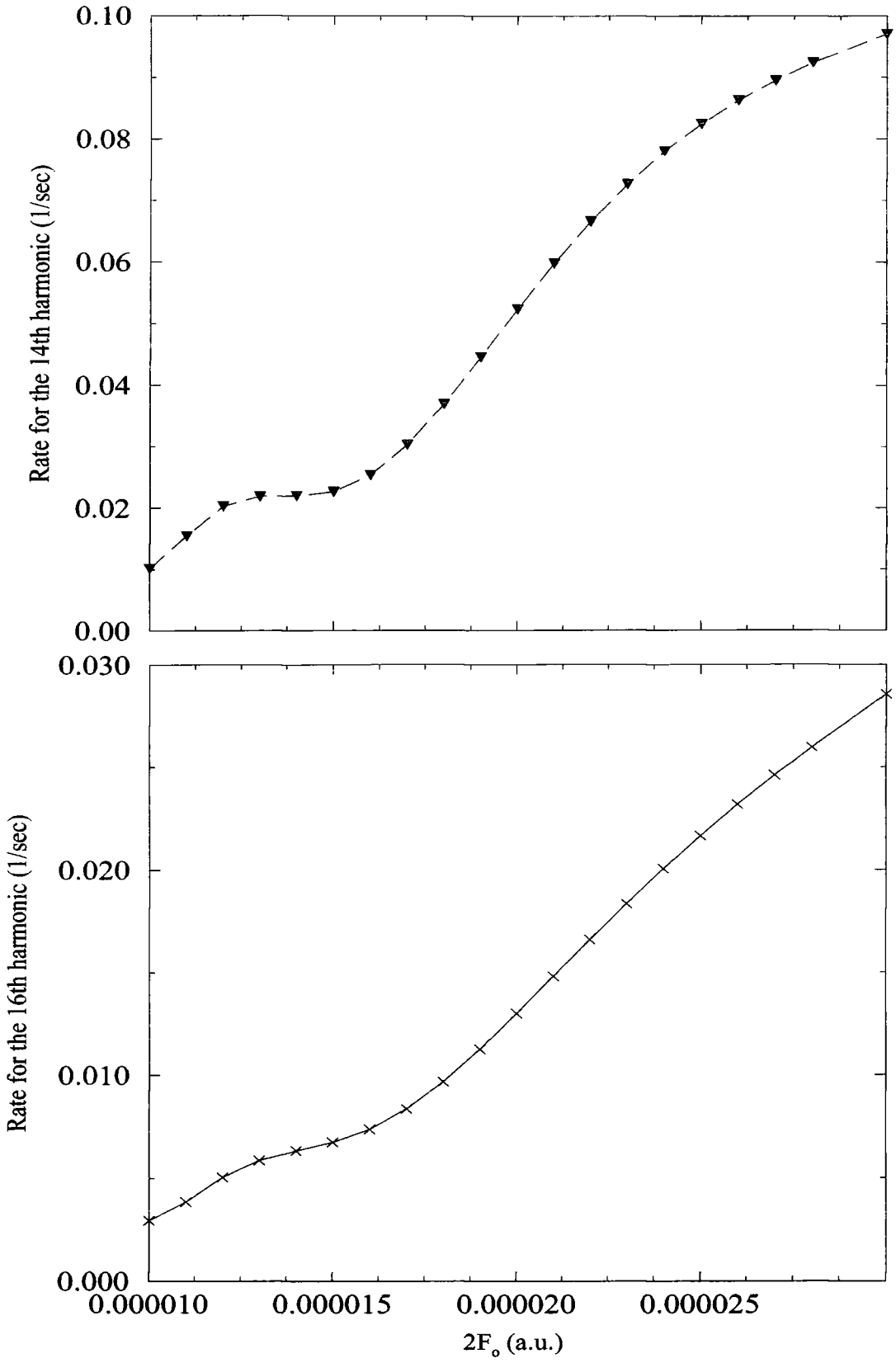

Figure 7.30: Variation of the rate for the 14th (above) and 16th (bottom) harmonic from a Yukawa potential with respect to dc-field strength. The ac-field intensity and wavelength are I= $2.50\times^{10}$ W/cm^2 and 10.6μm, respectively.

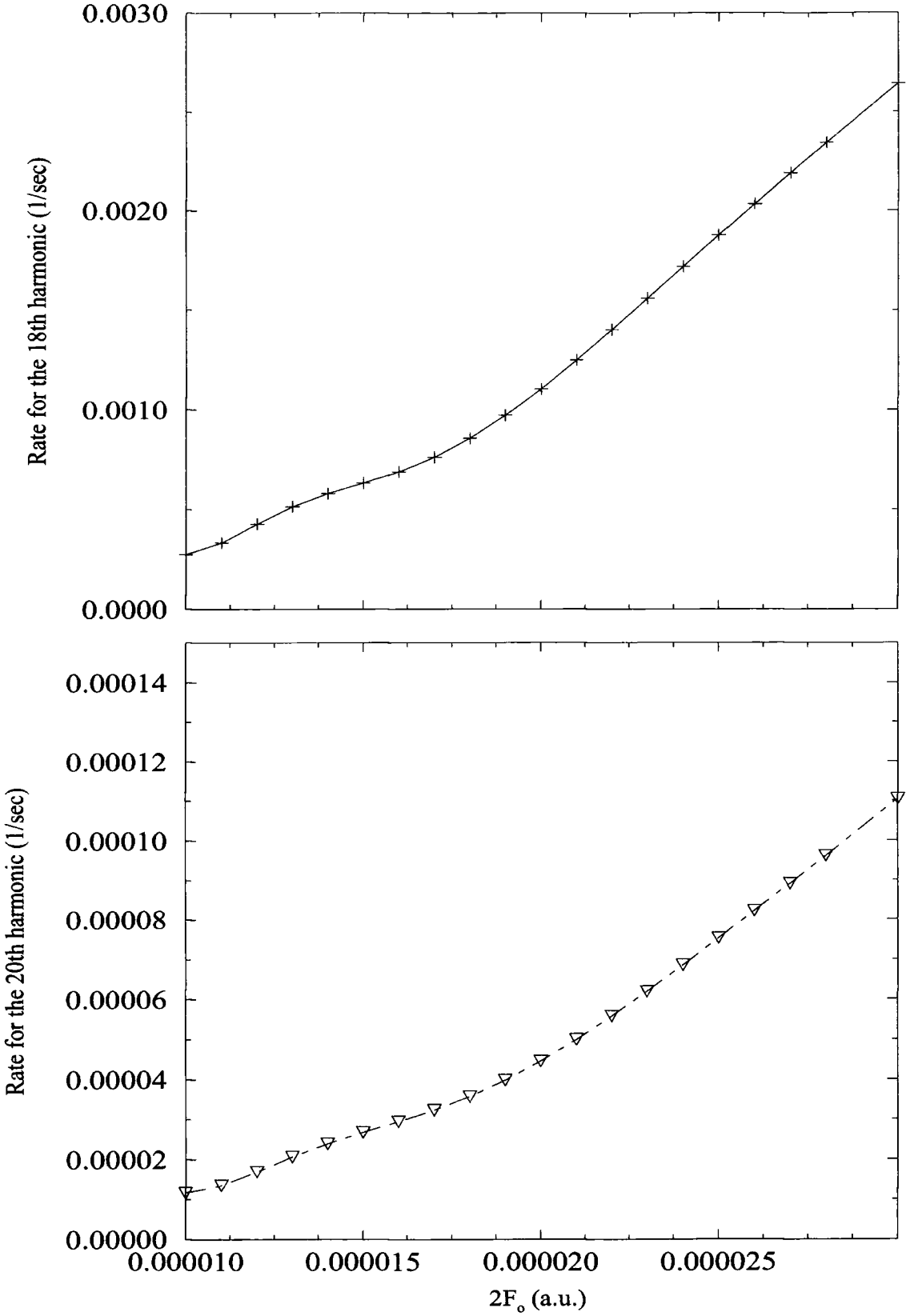

Figure 7.31: Variation of the rate for the 18th (above) and 20th (bottom) harmonic from a Yukawa potential with respect to dc-field strength. The ac-field intensity and wavelength are I= $2.50\times^{10}$ W/cm^2 and 10.6μm, respectively.

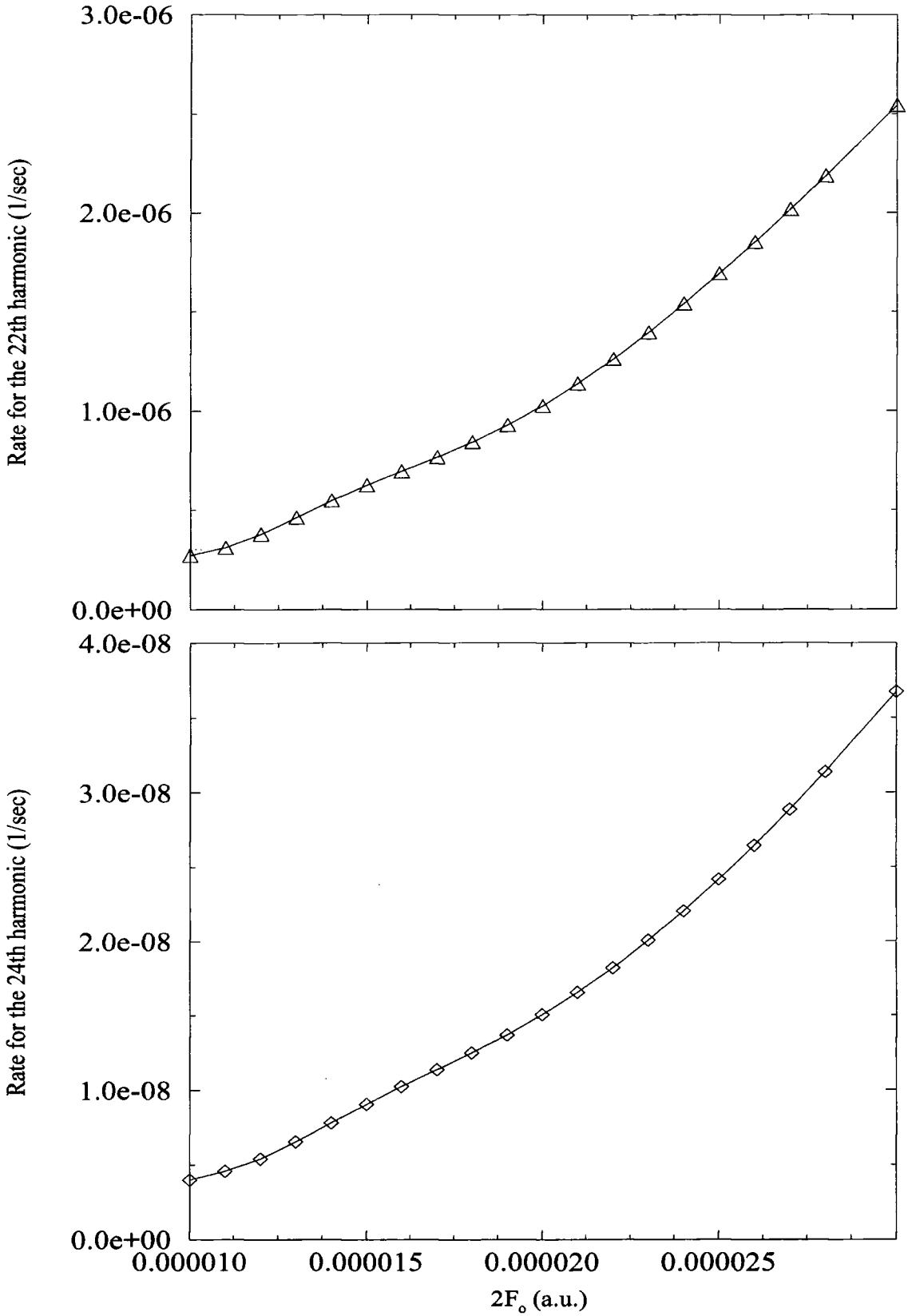

Figure 7.32: Variation of the rate for the 22th (above) and 24th (bottom) harmonic from a Yukawa potential with respect to dc-field strength. The ac-field intensity and wavelength are I= $2.50\times^{10}$ W/cm^2 and 10.6μm, respectively.

Bibliography

[1] S. Geltman, Phys. Lett. **4** 168 (1963).

[2] L. V. Keldish, Sov. Phys. JETP **47** 1307 (1964).

[3] J. L. Hall, E. J. Robinson, L. M. Branscomb Phys. Rev. Lett. **14** 1013 (1965).

[4] G. S. Voronov and N. B. Delone Sov. Phys. JETP **23** 54 (1966).

[5] P. Agostini, G. Barjot, J. F. Bonnal, C. Manus and J. Morellec J. Quantum Electron IEEE **QE-4** 667 (1968).

[6] *Atoms in intense laser fields*, edited by M. Gavrilla (Academic, New York,1992).

[7] P. Agostini, F. Fabre, G. Mainfray, G. Petite and N. K. Rahman Phys. Rev. Lett. **42** 1127 (1979).

[8] K. Burnett, V. C. Reed and P. L. Knight J. Phys. B. **26** 561 (1993).

[9] G. H. C. New and J. F. Ward, Phys. Rev. **185**, 57 (1969).

[10] J. Reintjes, C. Y. She, R. C. Eckardt, N. E. Karangelen, R. A. Andrews, and R. C. Elton, Phys. Rev. Lett. **37**, 1540 (1976).

[11] J. Reintjes, C. Y. She, R. C. Eckardt, N. E. Karangelen, R. A. Andrews, and R. C. Elton, Appl. Phys. Lett. **30**, 480 (1977).

[12] J. Wildenaur, J. Appl. Phys. **62** 41 (1987).

[13] A. McPherson, G. Gibson, H. Jara, U. Johann, T. S. Luk, I. A. McIntyre, K. Boyer, and C. K. Rhodes, J. Opt. Soc. Am. B. **4** 595 (1987).

[14] X. F. Li, A. L'Huillier, M. Ferray, L. A. Lompré, and G. Mainfray, Phys. Rev. A. **39** 5751 (1989).

[15] K. S. Budil, P. Salières and A. L'Huillier, T. Ditmire and M. D. Perry, Phys. Rev. A **48** R3437 (1989).

[16] W. Becker, S. Long, and J. K. McIver, Phys. Rev. **50** 1540 (1994).

[17] C. Lynga, A. L'Huillier and C-G Wahlström, J. Phys. B **29** 3293 (1996).

[18] I. H. Duru and H. Kleinert, Fortschritte der Physik **30** 401 (1982).

[19] H. Kelinert, Foundations of Physics, **23** 769 (1986).

[20] *Atoms in intense laser fields*, edited by M. Gavrilla (Academic, New York,1992), pp. 373-433.

[21] P. G. Burke, and K. T. Taylor, J. Phys. B **8** 2620 (1975).

[22] P. G. Burke, P. Franken and C. J. Joachain Europhys. Lett. **13** 617 (1990).

[23] P. G. Burke, P. Franken and C. J. Joachain J. Phys. B **24** 761 (1991).

[24] M. Plummer and J. F. McCann, J. Phys. B **28** L119 (1995).

[25] K. T. Taylor, J. S. Parker, D. Dundas, E. Smyth and S. Vivirito, *Multi-photon Processes*, edited by P. Lambropoulos and H. Walther (Published by Institute of Physics, by Galliard Ltd, 1997), pp. 56-67.

[26] J. Kupersztych, L. A. Lompré, G. Mainfray and C. Manus, J. Phys. B **21** L517 (1988).

[27] M. P. de Boer, J. H. Hoogenraad, R. B. Vrijen, L. D. Noordam and H. G. Muller, Phys. Rev. Lett. **71** 3263 (1993).

[28] M. P. de Boer, J. H. Hoogenraad, R. B. Vrijen, R. C. Constantinescu, L. D. Noordam and H. G. Muller, Phys. Rev. A **50** 4085 (1994).

[29] A. L'Huillier, L. A. Lompré, G. Mainfray, and C. Manus *Atoms in intense laser fields*, edited by M. Gavrilla (Academic, New York,1992), pp. 139-206.

[30] J. H. Shirley, Phys. Rev. **138** B979 (1965), V. Sov. Phys. JETP **24** 1041 (1966), Y. B. Zel'divich, Sov. Phys. JETP, **24** 1006 (1967);

[31] S. I. Chu, W. P. Reinhardt Phys. Rev. Lett. **39** 1195 (1977).

[32] R. M. Potvliege and R. M. Shakeshaft, Phys. Rev. A. **38** 1098 (1988).

[33] R. M. Potvliege and R. M. Shakeshaft, Phys. Rev. A. **38** 4597 (1988).

[34] R. M. Potvliege and R. Shakeshaft, Z. Phys. D. **11** 93 (1989).

[35] R. M. Potvliege and R. M. Shakeshaft, Phys. Rev. A. **40** 3061 (1989).

[36] M. Dörr, *Super-Intense Laser-Atom Physics*, Edited by H. G. Muller and M. V. Fedorov (Kluwer Academic Publishers in cooperation with NATO Scientific Affairs Division, Moskow, Russia, Augost 5-9, 1995), pp. 245-256.

[37] R. M. Potvliege, *Super-Intense Laser-Atom Physics*, Edited by H. G. Muller and M. V. Fedorov (Kluwer Academic Publishers in cooperation with NATO Scientific Affairs Division, Moskow, Russia, Augost 5-9, 1995), pp. 133-142.

[38] R. M. Potvliege and R. Shakeshaft, Adv. At. Mol. Phys. Suppl. **1** 373 (1992).

[39] R. Gebarowski, P.G. Burke, K.T. Taylor, M. Dörr, M. Bensaid, C.J. Joachain and C.J. Noble in *Electron and Photon Interactions with atoms, ions and molecules*, EC HCM Network, Paris, September 1-2 1995.

[40] C. J. Joachain, *Multiphoton Processes*, edited by P. Lambropoulos and H. Walther (Published by Institute of Physics, by Galliard Ltd, 1997), pp. 46-56.

[41] M. Dörr, C. J. Joachain, R. M. Potvliege, and S. Vučić, Phys. Rev. A. **49** 4852 (1994).

[42] H. G. Muller, P. Agostini, G. Petite, *Atoms in intense laser fields*, edited by M. Gavrilla (Academic, New York, 1992), pp. 1-41.

[43] A. Giusti-Suzor and P. Zoller Phys. Rev. A **36** 5178 (1987).

[44] S. I. Chu Adv. Chem. Phys. **73** 739 (1989).

[45] M. Plummer and J. F. McCann, J. Phys. B **28** 4073 (1995).

[46] R. M. Potvliege, R. Shakeshaft Phys. Rev. A **41** 1609 (1990).

[47] K. C. Kulander Phys. Rev. A **35** 445 (1987).

[48] J. Parker, K. T. Taylor, C. W. Clark and S. Blodgett-Ford, J. Phys. B **29** L33 (1996).

[49] S. C. Rae and K. Burnett, Phys. Rev. A **48** 2490 (1993).

[50] V. Véniard, R. Taïëb and A. Maquet, Phys. Rev. A **74** 4161 (1995).

[51] V. Véniard, R. Taïëb and A. Maquet, Phys. Rev. A **54** 721 (1996).

[52] M. Protopapas, P. L. Knight, and K. Burnett, Phys. Rev. A **49** 1945 (1994).

[53] A. Sanpera, Phys. Rev. A **49** 1967 (1994).

[54] K. Burnett, V. C. Reed, J. Cooper and P. L. Knight, Phys. Rev. A. **45** 3347 (1992).

[55] P.A. Franken, A.E. Hill, C.W. Peters, and G. Weinreich, Phys. Rev. Lett. **7** 118 (1961).

[56] P.D. Maker, R.W. Terhune, and C.M. Savage *Proceedings of the Third International Conference on Quantum Electronics, Paris, 1963*, edited by P. Grivet and N. Bloembergen (Colombia University Press, Newyork, 1964), p.1559; P.D. Maker and R.W. Terhune, Phys. Rev. **137**, A801 (1965).

[57] Y. Liang, M. V. Ammosov, and S. L. Chin, J. Phys. B. **27** 1269 (1994).

[58] P. Dietrich, N. H. Burnett, M. Ivanov, and P. B. Corkum, Phys. Rev. A. **50** R3585 (1994).

[59] N. H. Burnett, C. Kan, and P. B. Corkum, Phys. Rev. A. **51** R3418 (1995).

[60] F. A. Weihe, S. K. Dutta, G. Korn, D. Du, P. H. Bucksbaum and P.L. Shkolnikov, Phys. Rev. A **51** R3433 (1995).

[61] W. A. Weihe, P. H. Bucksbaum, J. Opt. Soc. Am. B. **13** 157 (1996).

[62] M. Kakehata, H. Takada, H. Yumoto, and K. Miyazaki, Phys. Rev. A **55** R861 (1997).

[63] K. C. Kulander and B. W. Shore, Phys. Rev. Lett. **62** 524 (1989).

[64] K. C. Kulander and B. W. Shore, J. Opt. Soc. Am. B. **7** 502 (1990).

[65] P. L. DeVries, J. Opt. Soc. Am. B. **7** 517 (1990).

[66] K. J. LaGattuta, J. Opt. Soc. Am. B. **7** 639 (1990).

[67] M. Dörr, R. M. Potvliege, R. Shakeshaft, J. Opt. Soc. Am. B **7** 433 (1990).

[68] M. Dörr, M. Terao-Dunseath, C.J. Noble, P.G. Burke and C.J. Joachain, J. Phys. B. **25** 2809 (1992).

[69] J. Purvis, M. Dörr, M. Terao-Dunseath, C.J. Joachain, P.G. Burke and C.J. Noble, Phys. Rev. Lett. **71** 3943 (1993).

[70] O. Latinne, N.J. Kylstra, M. Dörr, J. Purvis, M. Terao-Dunseath, C.J. Joachain, P.G. Burke and C.J. Noble, Phys. Rev. Lett. **74** 46 (1995).

[71] M. Dörr, J. Purvis, M. Terao-Dunseath, P.G. Burke, C.J. Joachain and C.J. Noble, Phys. B. **28** 4481 (1995).

[72] M. Lewenstein, P. Balcou, M. Yu. Ivanov, A. L'Huillier, and P. B. Corkum, Phys. Rev. A. **49** 2117 (1994).

[73] N. L. Manakov and V. D. Ovsyannikov, Sov. Phys. JETP **52** 895 (1980).

[74] P. Antoine, A. L'Huillier, M. Lewenstein, P. Salières and Carrè, Phys. Rev. A. **53** 1725 (1996).

[75] J. D. Jackson, *Classical Electrodynamics*, 2nd ed. (Wiley, New York, 1975).

[76] R. M. Potvliege *Private Communication.*

[77] R. M. Potvliege *Private Communication.*

[78] R. M. Potvliege *Private Communication.*

[79] R. M. Potvliege *Private Communication.*

[80] W. H. Press, B. P. Flannery, S. A. Teukolsky and W. T. Vetterling, *Numerical Recipies*, The Art of Scientific Computing (Fortran Version), (Cambrige University Press, Cambridge, 1989).

[81] D. W. Schumacher, F. Weilhe, H. G. Muller, and P. H. Bucksbaum, Phys. Rev. Lett. **73**, 1344 (1994); Y. Yian, C. Chen, and D. S. Elliot, *ibid* **69** 2353 (19192); M. Pont, D. Proulx, and R. Shakeshaft, Phys. Rev. A **44** 4486 (1991).

[82] K. J. Schafer and K. C. Kulander, Phys. Rev. A **45** 8026 (1992); G. Yao and S. I. Chu, J. Phys. B **25** 363 (1992).

[83] R. M. Potvliege and P. H. G. Smith, J. Phys. **24** L641 (1991).

[84] R. M. Potvliege and P. H. G. Smith, J. Phys. B **25** 2501.

[85] S. Watanabe, K. Kondo, Y. Nabekawa, A. Sagisaka, and Y. Kobayashi, Phys. Rev. Lett. **73** 2692 (1994).

[86] D. A. Telnov, J. Wang, and S. I. Chu, Phys. Rev. A **52** 3988 (1995).

[87] T. S. Ho, and S. I. Chu, J. Phys. B **17** 2101 (1984).

[88] M. Dörr, R. M. Potvliege, D. Proulx and R. Shakeshaft, Phys. Rev. A **44** 574 (1991).

[89] H. W. van der Hart, J. Phys. B **29** 2217 (1996).

[90] H. Rottke, B. Wolff-Rottke, D. Feldmann, K. H. Welge, M. Dörr, R. M. Potvliege, R. Shakeshaft, Phys. Rev. A. **49** 4837.

[91] M. D. Perry and J. K. Crane, Phys. Rev. A **48** R4051 (1993).

[92] S. Watanabe, K. Kondo, Y. Nabekawa, A. Sagisaka and Y. Koboyashi Phys. Rev. Lett. **73** 2692 (1994).

[93] H. Eichmann, S. Meyer, K. Riepl, C. Momma, and B. Wellegehausen, Phys. Rev. A **50** R2834 (1994).

[94] H. Eichmann, A. Egbert, S. Nolte, C. Momma, B. Wellegehausen, W. Becker, S. Long and J. K. McIver, Phys. Rev. A **51** R3414 (1995).

[95] S. Meyer, H. Eichmann, T. Menzel, S. Nolte, B. Wellegehausen, B. N. Chickov and C. Momma, Phys. Rev. A **76** 3336 (1996).

[96] M. B. Gaarde, P. Antoine, A. Persson, B. Carre, A. L'Huillier and C-G. Wahlström, J. Phys. B. **29** L163 (1996)

[97] A. Lago, G. Hilber and R. Wallenstein, Phys. Rev. A **36** 3827 (1987).

[98] S. Long, W. Becker and J. K. McIver, Phys. Rev. A **52** 2262 (1995).

[99] M. Protopapas, A. Sanpera, K. Burnett and P. L. Knight, Phys. Rev. A **52** R2527 (1995).

[100] M. Ivanov, P. B. Corkum, T. Zuo and A. Bandrauk, Phys. Rev. Lett. **74** 2933 (1995).

[101] V. Véniard, R. Taiëb and A. Maquet, *PECAM II* (Belfast, UK, July 1996).

[102] M. B. Gaarde, A. L'Huillier and M. Lewenstein, Phys. Rev. A **54** 4236 (1996).

[103] G. Z. Zhang, K. Hakuta and B. P. Stoicheff, Phys. Rev. Lett. **71** 3099 (1993).

[104] M. Bao and A. F. Starace, Phys. Rev. A **53** R3723 (1996).

[105] K. Hakuta, L. Marmet and B. P. Stoicheff, Phys. Rev. Lett. **66** 596 (1991).

[106] K. Hakuta, L. Marmet and B. P. Stoicheff, Phys. Rev. A. **45** 5152 (1992).

[107] G.F. Thomas, Phys. Rev. A **33** 1033 (1986).

[108] G.F. Thomas, J. Chem. Phys. **79** 4912 (1983).

[109] D. W. Noid and J. R. Stine, J. Chem. Phys. **76** 4957 (1982).

[110] S. I. Chu, J. V. Tietz and K. K. Datta, J. Chem. Phys. **77** 2968 (1982).

[111] R. Shakeshaft and X. Tang, Phys. Rev. A **36** 3193 (1987).

[112] M. Dörr, R. M. Potvliege, D. Proulx and R. Shakeshaft, Phys. Rev. A **42** 4138 (1990).

[113] J. L. Krause, K. J. Schafer and K. C. Kulander, Phys. Rev. A **45** 4998 (1992).

[114] J. L. Krause, K. J. Schafer and K. C. Kulander, Phys. Rev. Lett. **68** 3535 (1992).

[115] I. N. Aruttunyan and G. A. Askar'yan, Pis'ma Zh. Eksp. Teor. Fiz. **12** 378 (1970) [JETP Lett. **12** 259 (1970)].

[116] A. I. Nikishov, Zh. Eksp. Teor. Fiz. **62** 562 (1972) [Sov. Phys.-JETP **35** 298 (1972)].

[117] V. Z. Slonim and F. I. Dalidchik, Zh. Eksp. Teor. Fiz. **79** 751 (1980) [Sov. Phys. -JETP **52** 382 (1980)].

[118] N. L. Manakov and A. G. Fainshtein, Zh. Eksp. Teor. Fiz. **79** 751 (1980) [Sov. Phys.-JETP **52** 382 (1980)].

[119] B. Gao and A. F. Starace, Phys. Rev. A **42** 5580 (1990).

[120] Q. Wang and A. F. Starace, Phys. Rev. A **48** R1741 (1993).

[121] N. Du, I. I. Fabrikant and A. F. Starace, Phys. Rev. A **48** 2968 (1993).

[122] Q. Wang and A. F. Starace, Phys. Rev. A **51** 1260 (1995).

[123] R. M. Potvliege *unpublished results.*